N°d'ordre NNT : 2024ISAL0120

THÈSE de DOCTORAT DE L'UNIVERSITÉ DE LYON

opérée au sein de :

L'institut National des sciences appliquées de Lyon

En cotutelle internationale avec :

L'Université de Sherbrooke

Ecole Doctorale N°160

Électronique, Électrotechnique et Automatique

Électronique, micro et nanoélectronique, optique et laser

Soutenue publiquement le 19/12/2024 par :

Chander Bhan CHANDER BHAN

Capteurs environnementaux à base de dispositifs photonique pour la surveillance de la qualité de l'air dans l'automobile

Photonics-based environmental sensors for automotive air quality monitoring

---

Devant le jury composé de :

HADJI Emmanuel	Directeur de Recherche (CEA)	**Rapporteur**
GHIBAUDO Elise	Professeure des Universités (croma)	**Rapporteur**
CANVA Michael	Directeur de recherche (Université Paris Sud)	**Invité**
JOURLIN Yves	Professeure des Universités (Saint-Etienne)	**Président**
VICET Aurore	Professeure des Universités (Montpellier)	**Examinateur**
OROBTCHOUK Régis	Maître de conférences HDR (INSA Lyon)	**Directeur de thèse**
CHARETTE Paul	Professeure des Universités (UdeS)	**Co-Directeur de thèse**
MONFRAY Stéphane	Doctor (STMicroelectronics)	**Invité**

Thèse accessible à l'adresse : https://theses.insa-lyon.fr/publication/2024ISAL0120/these.pdf © [C.B. Chander Bhan], [2024], INSA Lyon, tous droits réservés

Thèse accessible à l'adresse : https://theses.insa-lyon.fr/publication/2024ISAL0120/these.pdf © [C.B. Chander Bhan], [2024], INSA Lyon, tous droits réservés

INSTITUT NATIONAL DES SCIENCES APPLIQUÉES LYON

Département de la Formation par la Recherche et des Études Doctorales (**FEDORA**)

Bâtiment Charlotte Perriand 3e étage
17, av. des Arts
69621 Villeurbanne Cédex
fedora@insa-lyon.fr

Référence : TH1180_CHANDER BHAN Chander Bhan

L'INSA Lyon a mis en place une procédure de contrôle systématique via un outil de détection de similitudes (logiciel Compilatio). Après le dépôt du manuscrit de thèse, celui-ci est analysé par l'outil. Pour tout taux de similarité supérieur à 10%, le manuscrit est vérifié par l'équipe de FEDORA. Il s'agit notamment d'exclure les auto-citations, à condition qu'elles soient correctement référencées avec citation expresse dans le manuscrit.

Par ce document, il est attesté que ce manuscrit, dans la forme communiquée par la personne doctorante à l'INSA Lyon, satisfait aux exigences de l'Etablissement concernant le taux maximal de similitude admissible.

INSA LYON
Campus LyonTech La Doua
20, avenue Albert Einstein - 69621 Villeurbanne cedex - France
Tél. +33 (0)4 72 43 83 83 - Fax +33 (0)4 72 43 85 00
www.insa-lyon.fr

UNIVERSITÉ DE LYON
membre de

Thèse accessible à l'adresse : https://theses.insa-lyon.fr/publication/2024ISAL0120/these.pdf © [C.B. Chander Bhan], [2024], INSA Lyon, tous droits réservés

Département FEDORA – INSA Lyon - Ecoles Doctorales

SIGLE	ECOLE DOCTORALE	NOM ET COORDONNEES DU RESPONSABLE
ED 206 CHIMIE	**CHIMIE DE LYON** https://www.edchimie-lyon.fr Sec. : Renée EL MELHEM Bât. Blaise PASCAL, 3e étage secretariat@edchimie-lyon.fr	**M. Stéphane DANIELE** C2P2-CPE LYON-UMR 5265 Bâtiment F308, BP 2077 43 Boulevard du 11 novembre 1918 69616 Villeurbanne directeur@edchimie-lyon.fr
ED 341 E2M2	**ÉVOLUTION, ÉCOSYSTÈME, MICROBIOLOGIE, MODÉLISATION** http://e2m2.universite-lyon.fr Sec. : Bénédicte LANZA Bât. Atrium, UCB Lyon 1 Tél : 04.72.44.83.62 secretariat.e2m2@univ-lyon1.fr	**Mme Sandrine CHARLES** Université Claude Bernard Lyon 1 UFR Biosciences Bâtiment Mendel 43, boulevard du 11 Novembre 1918 69622 Villeurbanne CEDEX e2m2.codir@listes.univ-lyon1.fr
ED 205 EDISS	**INTERDISCIPLINAIRE SCIENCES-SANTÉ** http://ediss.universite-lyon.fr Sec. : Bénédicte LANZA Bât. Atrium, UCB Lyon 1 Tél : 04.72.44.83.62 secretariat.ediss@univ-lyon1.fr	**Mme Sylvie RICARD-BLUM** Laboratoire ICBMS - UMR 5246 CNRS - Université Lyon 1 Bâtiment Raulin - 2ème étage Nord 43 Boulevard du 11 novembre 1918 69622 Villeurbanne Cedex Tél : +33(0)4 72 44 82 32 sylvie.ricard-blum@univ-lyon1.fr
ED 34 EDML	**MATÉRIAUX DE LYON** http://ed34.universite-lyon.fr Sec. : Yann DE ORDENANA Tél : 04.72.18.62.44 yann.de-ordenana@ec-lyon.fr	**M. Stéphane BENAYOUN** Ecole Centrale de Lyon Laboratoire LTDS 36 avenue Guy de Collongue 69134 Ecully CEDEX Tél : 04.72.18.64.37 stephane.benayoun@ec-lyon.fr
ED 160 EEA	**ÉLECTRONIQUE, ÉLECTROTECHNIQUE, AUTOMATIQUE** https://edeea.universite-lyon.fr Sec. : Philomène TRECOURT Bâtiment Direction INSA Lyon Tél : 04.72.43.71.70 secretariat.edeea@insa-lyon.fr	**M. Philippe DELACHARTRE** INSA LYON Laboratoire CREATIS Bâtiment Blaise Pascal, 7 avenue Jean Capelle 69621 Villeurbanne CEDEX Tél : 04.72.43.88.63 philippe.delachartre@insa-lyon.fr
ED 512 INFOMATHS	**INFORMATIQUE ET MATHÉMATIQUES** http://edinfomaths.universite-lyon.fr Sec. : Renée EL MELHEM Bât. Blaise PASCAL, 3e étage Tél : 04.72.43.80.46 infomaths@univ-lyon1.fr	**M. Hamamache KHEDDOUCI** Université Claude Bernard Lyon 1 Bât. Nautibus 43, Boulevard du 11 novembre 1918 69 622 Villeurbanne Cedex France Tél : 04.72.44.83.69 direction.infomaths@listes.univ-lyon1.fr
ED 162 MEGA	**MÉCANIQUE, ÉNERGÉTIQUE, GÉNIE CIVIL, ACOUSTIQUE** http://edmega.universite-lyon.fr Sec. : Philomène TRECOURT Tél : 04.72.43.71.70 Bâtiment Direction INSA Lyon mega@insa-lyon.fr	**M. Etienne PARIZET** INSA Lyon Laboratoire LVA Bâtiment St. Exupéry 25 bis av. Jean Capelle 69621 Villeurbanne CEDEX etienne.parizet@insa-lyon.fr
ED 483 ScSo	**ScSo**[1] https://edsciencessociales.universite-lyon.fr Sec. : Mélina FAVETON Tél : 04.78.69.77.79 melina.faveton@univ-lyon2.fr	**M. Bruno MILLY** (INSA : J.Y. TOUSSAINT) Univ. Lyon 2 Campus Berges du Rhône 18, quai Claude Bernard 69365 LYON CEDEX 07 Bureau BEL 319 bruno.milly@univ-lyon2.fr

[1] ScSo : Histoire, Géographie, Aménagement, Urbanisme, Archéologie, Science politique, Sociologie, Anthropologie

Thèse accessible à l'adresse : https://theses.insa-lyon.fr/publication/2024ISAL0120/these.pdf © [C.B. Chander Bhan], [2024], INSA Lyon, tous droits réservés

Résumé

La pollution de l'air demeure un défi de santé publique, entraînant des problèmes de santé graves tels que des infections respiratoires aiguës, la maladie pulmonaire obstructive chronique, les AVC, les maladies cardiaques et le cancer du poumon. Cela est principalement dû à l'inhalation d'air contenant de fortes concentrations de polluants, en particulier les hydrocarbures polyaromatiques (HAP) et les particules comme le fluoranthène et le benzène, qui sont des polluants PM2.5 (particules d'une taille $\leq$ 2,5 μm) courants émis par les véhicules, les industries, la fumée de cigarette et les feux de forêt. Les solutions actuelles sur le marché pour mesurer ces polluants, telles que les compteurs de particules optiques et les dispositifs MEMS basés sur les principes de diffusion de la lumière, sont souvent peu fiables, offrant une sensibilité réduite pour les particules fines (tailles $\leq$ 0,1 μm). Par conséquent, il est nécessaire d'explorer des approches alternatives, telles que la manipulation de fluides sur puce par la lumière à l'aide de dispositifs photoniques intégrés, qui offrent une détection de taille de particule plus précise.

Cette thèse explore les dispositifs de circuits photoniques intégrés (PIC) basés sur une plateforme en nitrure de silicium (Si_xN_y), en mettant l'accent sur leur potentiel pour la détection de particules dans l'air, un élément clé des capteurs de l'indice de qualité de l'air (AQI). La haute sensibilité volumique des résonateurs à anneaux (MRR) dans ces dispositifs permet la détection de faibles concentrations de particules, tandis que les forces optiques permettent le piégeage spécifique à la taille des particules. Pour relever les défis liés au piégeage de particules diélectriques de moins de 100 nm, cette recherche explore diverses structures photoniques, y compris des guides d'onde diélectriques, des résonateurs en mode d'ordre supérieur (HOM) et des guides d'onde plasmoniques hybrides. cette étude comprend leur conception, leur fabrication et leur compatibilité avec des plateformes industrielles telles que DAPHNE de STMicroelectronics. L'analyse des forces optiques, réalisée à l'aide de méthodes telles que le tenseur de contrainte de Maxwell (MST) et l'approximation de dipôle discret (DDA), fournit un cadre rigoureux pour optimiser la conception et évaluer différentes structures.

L'étude se concentre sur quatre composants photoniques clés : les guides d'onde diélectriques, les résonateurs HOM, le couplage à taper inversé et les résonateurs en anneau plasmonique hybride. Le optimisé guide d'onde diélectrique, offre une solution facilement fabricable pour le piégeage de particules de 100 nm. Les résonateurs HOM présentent une meilleure tolérance aux erreurs de fabrication et peuvent potentiellement piéger plus de particules que leur mode fondamental en raison de leurs multiples intensités maximales. Des tapers inversés ont été conçus pour atteindre une efficacité de couplage élevée, cruciale pour un piégeage efficace avec les configurations disponibles. Le résonateur en anneau plasmonique hybride, bien qu'il n'ait pas été fabriqué en raison de sa complexité, a montré un potentiel pour obtenir de fortes forces optiques et une sensibilité élevée, en faisant un design prometteur pour les études futures.

Les dispositifs fabriqués ont été caractérisés à l'aide d'une configuration expérimentale sur banc optique, révélant des défis tels que des pertes supplémentaires dues aux réservoirs fluidiques en polydiméthylsiloxane (PDMS). Pour surmonter cela, un réservoir fluidique repositionnable utilisant un film TPU et des composants imprimés en 3D a été employé, démontrant une meilleure répétabilité et facilité d'utilisation. Les résultats préliminaires ont indiqué de forts facteurs Q pour les MRR dans des gaines en oxyde de silicium et en eau.

Thèse accessible à l'adresse : https://theses.insa-lyon.fr/publication/2024ISAL0120/these.pdf © [C.B. Chander Bhan], [2024], INSA Lyon, tous droits réservés

Dans l'ensemble, les résultats suggèrent que des dispositifs comme les guides d'onde HOM et plasmoniques hybrides présentent un potentiel significatif pour le piégeage optique avancé et les applications de détection de l'AQI.

Thèse accessible à l'adresse : https://theses.insa-lyon.fr/publication/2024ISAL0120/these.pdf © [C.B. Chander Bhan], [2024], INSA Lyon, tous droits réservés

Abstract

Air pollution remains a public health challenge, causing severe health issues such as acute respiratory infections, chronic obstructive pulmonary disease, stroke, heart disease, and lung cancer. This is primarily due to inhalation of air containing high levels of pollutants, particularly polyaromatic hydrocarbons (PAHs) and particulate matter like fluoranthene and benzene, which are common PM2.5 (particulate matter with size $\leq$ 2.5 μm) pollutants emitted from vehicles, industries, cigarette smoke, and wildfires. Current market solutions for measuring these pollutants, such as optical particle counters and MEMS devices based on light scattering principles, are often unreliable, providing less sensitivity with fine particles (sizes $\leq$ 0.1 μm). Consequently, there is a need for alternative approaches, such as on-chip fluids manipulation by light using photonic integrated devices, that offer more accurate particle size detection.

This thesis explores photonic integrated circuit (PIC) devices based on a silicon nitride (Si_xN_y) platform, emphasizing their potential for particulate matter detection in air, a key component for air quality index (AQI) sensors. The high bulk sensitivity of microring resonators (MRRs) in these devices enables the detection of small particle concentrations, while optical forces allow for size-specific particle trapping. To address the challenges associated with trapping dielectric particles smaller than 100 nm, the research explores various photonic structures, including dielectric strip waveguides, higher-order mode (HOM) ring resonators, and hybrid plasmonic waveguides. The investigation encompasses their design, fabrication, and compatibility with industrial platforms such as STMicroelectronics DAPHNE. The optical force analysis, conducted using methods like the Maxwell stress tensor (MST) and discrete dipole approximation (DDA), provides a rigorous framework for optimizing the design and evaluating different structures.

The study focuses on four integrated photonics key components: dielectric strip waveguides, HOM ring resonators, inverted taper coupling, and hybrid plasmonic ring resonators. The optimized dielectric strip waveguide offers an easily fabricable solution for trapping 100 nm particles. HOM resonators provide better tolerance to fabrication errors and can potentially trap more particles than their fundamental mode due to their multiple maxima intensities. Inverted tapers were designed to achieve high coupling efficiency, crucial for effective trapping with available setups. The hybrid plasmonic ring resonator, although not fabricated due to its complexity, showed potential for achieving high optical forces and sensitivity, making it a promising design for future studies.

The fabricated devices were characterized using an experimental optical bench setup, revealing challenges such as additional losses from polydimethylsiloxane (PDMS) fluidic reservoirs. To overcome this, a repositionable fluidic reservoir using TPU film and 3D-printed components were employed, demonstrating improved repeatability and ease of use. Preliminary results indicated high Q-factors for MRRs in both silicon oxide and water cladding.

Overall, the findings suggest that designs like HOM and hybrid plasmonic waveguides exhibit significant potential for advanced optical trapping and AQI sensing applications.

Thèse accessible à l'adresse : https://theses.insa-lyon.fr/publication/2024ISAL0120/these.pdf © [C.B. Chander Bhan], [2024], INSA Lyon, tous droits réservés

Acknowledgment / Remerciements

First and foremost, I wish to express my deepest gratitude to my thesis supervisors, Paul Charette, Stéphane Monfray, and Régis Orobtchouk, for their guidance, support, and invaluable insights throughout the course of this work. Your expertise and dedication have been instrumental in shaping this thesis, and I am profoundly grateful for the time and effort you devoted to my progress. I am also immensely thankful to Frédéric Bouef and the entire team at STMicroelectronics for their warm welcome and for the productive scientific discussions that significantly contributed to this research. Furthermore, I extend my sincere appreciation to the members of the jury for agreeing to evaluate my work and for their valuable feedback.

I consider myself fortunate to have conducted this thesis in collaboration with two laboratories, allowing me to gain both scientific and personal growth. This journey would not have been possible without the unwavering support of the teams at 3IT, Université de Sherbrooke (UdeS), and INL, INSA. I am deeply grateful to the entire Groupe Biophotonique team at 3IT for their warm welcome and fruitful contributions. Special thanks to Guillaume Beaudin and Jean-François Bryche for their continuous assistance with cleanroom work, modeling, and design. Your availability, even on weekends, was invaluable to the progress of my research.

I would also like to extend my gratitude to Laurence Convert, Rémi Dreyfus, Thierry Courcier, and Michael Canva for their expertise in COMSOL, microfluidic channels, and plasmonics. To my colleagues and friends, Marlo Vega, Raphael Gherman, Pauline Girault, Sarra Chabbar, Coline Beltrami, Marion Stalet, Maxime Grenier-Castillo, and Redouane Amrar, thank you for your support during challenging times, for the enjoyable moments we shared, and for helping me learn French and experience your cultures, making this journey unforgettable.

I would also like to express my appreciation to the other members of 3IT for their assistance in the LN2 cleanroom and LSCM. In particular, I am grateful to Samuel René De Cotret for training me in E-beam lithography and for correcting numerous errors, to Khalid Moumanis, Maïté Volatier and Pierre Langlois for their guidance and formations in the cleanroom, and to Jean-François Morissette for his help with designing and printing PDMS molds. Additionally, I extend my thanks to Abdelatif Jaouad and Caroline Roy for their support with material deposition and ellipsometry, and to Guillaume Bertrand for assisting with rapid thermal annealing. My heartfelt thanks to all who contributed to the cleanroom work and I apologize if I have inadvertently omitted any names.

I am also grateful to my fellow PhD colleagues at UdeS : Swayam Prakash Sahoo, Nikhil Garg, Hussein Hamieh, Shrivani Pandiya, Reethu Sebastian, Adi Tihic, and Davide Florini for making this journey enjoyable through late-night snow funs, movie nights, and Christmas dinners. I wish you all the best in your ongoing and future endeavors.

On the INL side, I extend my sincere thanks to the entire i-Lum team for their warm welcome and to the laboratory members who provided essential technical support. My deepest appreciation extends to Christian Séassal for his continuous support, attentiveness, and availability. I am also grateful to Magalie Faivre, Pascal Kleimann, and Louis Renaud from the DSE team for introducing me to the concept of the “repositionable fluidic setup,” which proved crucial during my characterization experiments. Special thanks to Taha Benyattou, Lotfi Berguiga, Bruno Masenelli, Virginie Lagarde, Pascal Decebal, and all the other team members I had the privilege to interact with during my time at INL.

Thèse accessible à l'adresse : https://theses.insa-lyon.fr/publication/2024ISAL0120/these.pdf © [C.B. Chander Bhan], [2024], INSA Lyon, tous droits réservés

I would like to extend my appreciation to Benjamin Fornacciari for his assistance with SEM and PECVD, to Giovanni Alaimo-Galli and Jean-Charles Roux for their help in the clean-room, and to Esteves Josué for his support with 3D printing of reservoirs. I am also thankful to Yvan Doyeux for his help with IT matters. To all the PhD students, postdocs, and former colleagues at INL : Jimmy, Eva, Michele, Charif, Alestair, Jérémy, Théo, Huiru, Zineb - I am deeply grateful for your support and the pleasure of sharing this journey with you.

Finally, I wish to express my heartfelt gratitude to my family. To my parents, Narender and Urmila, and my sister Sangeeta, for their constant support and encouragement throughout this journey. To my nieces, Sovika and Yuvani, thank you for your love and joy. Most importantly, I am deeply grateful to my wife, Ritu, for her unwavering support, patience, and understanding over these three years. Your belief in me has been my greatest strength. I also extend my appreciation to my close friends : Akash, Atul, Dinesh, Asish, Vinayak, Piyush, Rakshith, Suraj, Charitha, Jyoti, Mohit, Sahil, Harshita, and Twinkle for standing by me through both the joyful and challenging times.

Thèse accessible à l'adresse : https://theses.insa-lyon.fr/publication/2024ISAL0120/these.pdf © [C.B. Chander Bhan], [2024], INSA Lyon, tous droits réservés

Thèse accessible à l'adresse : https://theses.insa-lyon.fr/publication/2024ISAL0120/these.pdf © [C.B. Chander Bhan], [2024], INSA Lyon, tous droits réservés

Table of Contents

List of Figures xiii

List of Tables xxv

1 Introduction 3

1.1 Air pollution . . . 3

1.2 Measurement solutions . . . 4

1.2.1 Gravimetric method . . . 5

1.2.2 Optical methods . . . 6

1.2.3 A future generation solution for measurement . . . 7

1.3 Thesis planning . . . 10

2 Context and State of the Art 11

2.1 Optical Manipulation: Brief History, Definition, Trapping Regime . . . 11

2.1.1 Optical Force . . . 12

2.2 Computational Method . . . 13

2.2.1 Optical trapping regime . . . 13

2.2.2 Discrete Dipole Approximation (DDA) . . . 16

2.2.3 Maxwell stress Tensor (MST) . . . 19

2.3 Displacement of particles in a viscous liquid . . . 22

2.3.1 Stokes Law . . . 23

2.3.2 Surface viscosity . . . 23

2.3.3 Brownian Motion . . . 23

2.4 Modelling Methods . . . 25

Thèse accessible à l'adresse : https://theses.insa-lyon.fr/publication/2024ISAL0120/these.pdf © [C.B. Chander Bhan], [2024], INSA Lyon, tous droits réservés

2.5 Optical waveguide Structure . . . 26
2.5.1 Dielectric – strip or ridge waveguide . . . 26
2.5.2 Slot waveguide . . . 27
2.5.3 Hybrid plasmonic waveguide . . . 27
2.6 Resonant Cavity Enhancement . . . 29
2.7 Ring resonators Spectral characteristics . . . 30
2.8 Conclusion . . . 33

3 Modeling and Analysis of Photonic Integrated Circuit components 35
3.1 Basic Knowledge on Physics and Modeling of Waveguide . . . 35
3.1.1 Electromagnetic analysis of a Waveguide . . . 35
3.2 Modeling of Optical Trapping and Sensitivity . . . 45
3.2.1 Waveguide based optical trapping . . . 46
3.3 Sensitivity . . . 56
3.4 Potential depth study: F_{min} and D_{min} . . . 58
3.5 MRRs: Coupling factor, Losses, Power in the ring . . . 60
3.6 Concluding and Perspective to Design . . . 63

4 Designing: Photonic Integrated circuit 65
4.1 Waveguide Design . . . 65
4.1.1 Final waveguide sensor . . . 66
4.1.2 HOM and FM Waveguide . . . 69
4.2 Bending radius optimization . . . 71
4.3 Coupling section : Directional couplers . . . 74
4.3.1 Circular and Racetrack MRRs . . . 75
4.3.2 FM and HOM MRRs . . . 77
4.4 Edge couplers : linear tapers . . . 78
4.4.1 Inverted tapers . . . 80
4.4.2 adiabatic tapers . . . 81
4.5 CAD Layout . . . 83

Thèse accessible à l'adresse : https://theses.insa-lyon.fr/publication/2024ISAL0120/these.pdf © [C.B. Chander Bhan], [2024], INSA Lyon, tous droits réservés

4.5.1 Main devices . . . 84
4.5.2 Bends and Spirals . . . 86
4.5.3 Alignment Marks and Labels . . . 86
4.6 Conclusion . . . 87

5 Device Fabrication **89**
5.1 Device fabrication at DAPHNE, STMicroelectronics . . . 89
5.2 Device fabrication at 3IT University of sherbrooke . . . 91
5.2.1 Deposition of Passive materials . . . 91
5.2.2 E-beam lithography . . . 93
5.2.3 Etching . . . 101
5.3 Fluidic setup . . . 104
5.4 Conclusion . . . 106

6 Characterisation **107**
6.1 Optical setup . . . 107
6.2 Experimental Results . . . 109
6.2.1 Linear propagation losses . . . 110
6.2.2 Bending losses . . . 115
6.2.3 MRRs spectral characteristics . . . 119
6.3 Optical trapping . . . 122
6.4 Conclusion . . . 126

7 Conclusion and Summary **127**

8 Annexes **131**
Annexe A : Brownian Motion . . . 131
Annexe B : Marcatilli's method for Directional coupler . . . 134
Annexe C : Dispersion of PECVD Silicon nitride, 3IT . . . 136

9 RÉSUMÉ LONG EN FRANCAIS **139**

Thèse accessible à l'adresse : https://theses.insa-lyon.fr/publication/2024ISAL0120/these.pdf © [C.B. Chander Bhan], [2024], INSA Lyon, tous droits réservés

Thèse accessible à l'adresse : https://theses.insa-lyon.fr/publication/2024ISAL0120/these.pdf © [C.B. Chander Bhan], [2024], INSA Lyon, tous droits réservés

List of Figures

1.1 Size comparison between human hair and particulate matter [2]. 3

1.2 Modern gravimeter M & NEMS: (a) Gravimetric method used with resonator structure [16] (b) MEMS air-microfluidic particulate matter (PM) sensor based on Film Bulk Acoustic Resonators [17] (c) PM2.5 Sensor Based on Surface Acoustic Wave [18]. 5

1.3 Optical methods to measure PM: (a) illustration of optical light scattering and extinction methods (b) illustration of optical particle counters (c) graphical illustration Holography working principle [23]. 6

1.4 Dielectrophoresis: (a) Principle [24] (b) dielectrophoresis (Volt $<$ 1) with nano-electrode gap of 9 nm to trap 10 nm size particle [25] (c) resonant MEMS sensor utilizing both dielectrophoresis and microcantilever resonant for the detection dielectric particles in aged lubricating oils [26]. 7

1.5 Optical Manipulation by Light: (a) Trapping of a 5 nm particle with a plasmonic bow-tie nanoantenna, (b) Design of a plasmonic bow-tie nanoantenna on a Si_xN_y trench waveguide for Rayleigh optical particle trapping, (c) Trapping of 320 nm particles with a 1D photonic crystal, and (d) Trapping of 1 μm particles with silicon MRRs. 8

2.1 Brief history of Optical Manipulation. 12

2.2 Schematic comparison between far field and near field optical manipulation. 13

2.3 Optical Trapping regimes: The horizontal scale bar shows the average object size and the corresponding light wavelength (Figure taken from research by Onofrio M Maragò [48]). 14

2.4 Approximation model condition 14

2.5 Gradient Force: (a) schematic diagram of strip Si_xN_y waveguide (b) vector plot of gradient force calculated using DDA at 1310 nm wavelength with power of 1 W, the binary color grading in this plot presents the evanescent field amplitude of the fundamental mode in a waveguide. 18

2.6 Polarizability of a dielectric particle in a water medium, comparing both Clausius-Mossotti relation (α_{CM}) and Draine approach (α_{rad}) for polarizability. 19

Thèse accessible à l'adresse : https://theses.insa-lyon.fr/publication/2024ISAL0120/these.pdf © [C.B. Chander Bhan], [2024], INSA Lyon, tous droits réservés

2.7 A comparison between COMOSL MST, Abraham-Minkowski stress tensor (optical pressure) , and Lorenz-Mie theory (an analytical model) model : (a) A COMSOL 3D model (b) radiation force F_z on 1 and 3 μm spheres for $1.3 < n_s < 1.4$ with $1\ mW$ of optical power in the TE mode and (c) radiation force as function of number of mesh element [75] 21

2.8 Force exerted on a particle: (a) solid friction with reference to both optical forces exerting on a particle. (b) illustrates the fluid friction forces with reference to optical forces. In the vicinity of the surface, the viscosity increases as the particle approaches it. (redrawn from Stéphanie gaugiran's thesis [79]). 24

2.9 Strip waveguide: (a) schematic diagram of strip waveguide (b) TE field profile (c) Field values at center of the waveguide (dashed red line on picture (b)) along the x-axis 26

2.10 slot waveguide: (a) schematic diagram of slot waveguide (b) TE field profile (c) Field values at center of the waveguide (dashed red line on picture (b)) along the x-axis 27

2.11 Hybrid Plasmonic waveguide: (a) schematic diagram of HPWG waveguide (b) mode field profile (c) Field values at center of the waveguide (dashed red line on picture (b)) along the x-axis 28

2.12 Various types of photonic and plasmonic resonators used for the optical trapping of nanomaterials, represented on a graph as a function of the resonant mode volume scale and the quality factor of the resonance [102]. 30

2.13 Micro-ring resonator common configurations 31

2.14 The transmission of an all-pass ring resonator with significant parameters. The orange curve represents the transmission without perturbation, and the blue curve represents a shift due to a refractive index change during perturbation. 32

3.1 An optical fibre with high index material (n_{core}) surrounded by low index material (n_{clad}) 36

3.2 Types of common planar and non-planar waveguide structure 36

3.3 TIR Condition & K Vector Triangle: (a) TIR condition for propagating light in a slab waveguide, and (b) K vector triangle establishing the relationship between β and K_x, where β is the propagation constant along the z-direction, and K_x is the vertical propagation component along the x-direction. 37

3.4 slab waveguide : (a) schematic diagram of slab waveguide with RI index profile along x and Y axis (b) solution to the second order differential equation for a slab waveguide for x and y-axis 40

3.5 Schematic diagram for establishing boundary value problem. 41

Thèse accessible à l'adresse : https://theses.insa-lyon.fr/publication/2024ISAL0120/these.pdf © [C.B. Chander Bhan], [2024], INSA Lyon, tous droits réservés

3.6 Solution of the boundary value problem for a rectangular waveguide: (a) Solutions in each region of the rectangular waveguide, and (b) Electric field distribution and mode profiles in the x-y plane for electromagnetic modes, as determined from the solution for the rectangular waveguide [110]. 43

3.7 EIM working principle 44

3.8 $b - V$ curve Comparison for Effective index method, Perturbation approach, 1_{st} order analytical solution 44

3.9 COMSOL FEM 2D mode solver : (a) Schematic diagram with RI and dimension of a strip waveguide (b) TE mode profile with n_{eff} 46

3.10 3D COMSOL model : (a) 3D model with PML boundary condition at the input and out ports (b) Normalized perturbed E field in XY and ZX profile for TE polarization. 47

3.11 2D lumerical FDE model : (a) a schematic diagram of strip waveguide (b) uniform rectangular mesh model in FDE (c) F_{grad} vector plot in XY axis with the fundamental TE mode, where mode-profile is shown with grey scale . . 47

3.12 Comparison of MATLAB FDFV, Lumerical FDE, and COMSOL FEM: (a) Schematic and Blender model representing the strip waveguide from the literature, and (b) F_{grad} as a function of dielectric particle radius for all three models developed in this thesis. 48

3.13 F_{grad} for two different refractive index contrasts of a strip waveguide: (a) Schematic diagram of a Si strip waveguide with perturbed normalized TE mode field profiles and F_{grad}, and (b) Schematic diagram of a Si_xN_y strip waveguide with perturbed normalized TE mode field profiles and F_{grad} evaluated using the COMSOL 3D model. 49

3.14 F_{grad} vector plot in XY profiles for HOM and FM waveguide with schematic diagram of both waveguide structure (evaluated with Lumerical FDE model). 50

3.15 n_{eff} versus w_{core} of a slot waveguide with a fixed gap of 40 nm. 51

3.16 TE electric field profile (E_y) at $y = 0$ along x-axis for a three different slot waveguide ($w_{core} = 250$, 300 and 350 nm) with varying slot gap. 52

3.17 F_{grad} (pN) as a function of slot gap ($120 \leq g \leq 400$) with w_{core} of 350 nm . . 52

3.18 Power in the cladding (η) as a function of core width for a strip waveguide : a schematic diagram with TE mode profile of radiation mode. 53

3.19 Comparison table and mode-field profile of Fundamental TE radiation mode, plasmonic SPP mode and HPWG super modes (combining dielectric and plasmonic modes). 54

3.20 HPWG with Normalized E profile (10^6 V/m) for 100 nm gap. a) Plasmonic walls has sharp corners that has 9.4 $\times$ 10^6 V/m electric field with peak effect b) used a corner with radius of curvature with 15 nm and reduced the Electric field by half of it 54

Thèse accessible à l'adresse : https://theses.insa-lyon.fr/publication/2024ISAL0120/these.pdf © [C.B. Chander Bhan], [2024], INSA Lyon, tous droits réservés

3.21 (a) contour plot of n_{eff} as a function of gap (g) and dielectric core width in HPWG b) shows the F_{grad} (y-axis left) and propagation losses (y-axis right) in the HPWG as a function of dielectric core width used in the HPWG. c) Schematic diagram of optimized HPWG for Racetrack MRRs d) optical gradient force for two dielectric particles placed on the top of waveguide for optimized designed HPWG as a function of gap (g) 55

3.22 F_{grad} comparison as a function of gap size for HPWG, slot, and strip waveguides. The blue and orange dashed lines represent F_{grad} for the slot and HPWG waveguides, respectively, in the gap range $120 \leq g \leq 400$ nm (yellow background) and $g \leq 120$ nm (grey background). The grey dashed line represents F_{grad} for the strip waveguide, as illustrated in the schematic diagram in the figure. 56

3.23 Comparison of S for HPWG, slot and strip waveguides a) Schematic diagram of Racetrack MRRs where dotted pattern shows the area where three different waveguide is used to evaluate the S b) S and losses curves as a function of slot gap for slot and HPWG waveguide. The black solid lines represents the strip waveguide sensitivity of 220 nm/RIU 57

3.24 Potential well depth curve along x-axis in water cladding : (a) F_{grad} as a function of distance from core/cladding interface at various levels of optical power (b) Potential well depth (U_x) as a function of distance from the core/cladding interface at various levels of optical power (c) Proportion of trapped particles (D_x) in trap-size (e_x)as function of optical power. 59

3.25 Potential depth (10 K_BT) contour lines as function of F_{grad} along x-axis for different optical powers 59

3.26 Potential well depth curve along x-axis in air cladding : (a) gradient force as a function of distance from core/cladding interface at various levels of optical power (b) Potential well depth (U_x) as a function of distance from the core/cladding interface at various levels of optical power (c) Proportion of trapped particles (D_x) in trap-size (e_x)as function of optical power. 60

3.27 A schematic diagram of racetrack ring resonators with a directional coupler. 61

3.28 Power in the ring ratio (P_{ring}/P_{bus}) as function of Linear propagation losses for two different optimized industrial (ST) and university bending losses using the device fabricated in previous thesis (race track ring resonators) with dimension of horizontal linear section L_x = 10 μm and vertical linear section L_y = 5 μm (19.3% of the total length) and Bending radius = 20 μm (80.7% of the total length). The critical coupling is considered here at resonating wavelength (λ_{res}) of 1.311 62

4.1 n_{eff} as a function of core width, where thickness of the strip waveguide is fixed at 300 nm. 67

Thèse accessible à l'adresse : https://theses.insa-lyon.fr/publication/2024ISAL0120/these.pdf © [C.B. Chander Bhan], [2024], INSA Lyon, tous droits réservés

4.2 F_{grad} as a function of core width for a strip waveguide with a 100 nm dielectric particle. The F_{grad} is evaluated at a normalized power of 1 W with the fundamental mode propagating in the strip waveguide, using the COMSOL FEM model. 67

4.3 Estimation of the approximate refractive index of a fluid surrounding particles using effective medium theory. 68

4.4 Optimization of final waveguide core width : F_{grad} (solid blue line) and wavelength shift (orange line) for varying core width : F_{grad} calculated here are for 100 nm dielectric particle with 1 W of normalized power. 69

4.5 Optimization of HOM and FM waveguide core width : (a) represents the TE mode-profile of FM mode with $E_y(x)$ profile at y = 0.15 μm with one maxima in the waveguide and (b) represents the TE mode-profile of HOM mode with $E_y(x)$ profile at y = 0.15 μm with two maxima in the waveguide. 70

4.6 Conformal mapping technique: (a) Relationship between 2D Cartesian straight boundaries and new (u,v) cylindrical coordinate boundaries, where the RI has an exponential dependence on the R_{bend}. (b) Meshing and RI mapping of the bending strip waveguide with a R_{bend} = 50 μm, core width of 570 nm, and thickness of 300 nm in the conformal mapping model (developed at INL). (c) TE bending mode and radiation losses (8.49 dB/90°) for the structure shown in (b). 71

4.7 FVFD bending mode solver: (a) Representation of the global cylindrical coordinate and local coordinate systems used in the fully vectorial mode solver. (b) Meshing and RI mapping of the bending strip waveguide with a R_{bend} of 50 μm, core width of 570 nm, and thickness of 300 nm in the FVFD model (developed at INL). (c) TE bending mode and radiation losses (1.18 dB/90°) for the structure shown in (b). 72

4.8 Optimization of Bending radius : (a) illustrates the losses as the function of bending radius in Si strip waveguide buried under SiO_2 at 1550 nm [135] (b) illustrates the losses as the function of bending radius in Si_xN_y strip waveguide in H_2O cladding as shown in the schematic diagram at 1310 nm wavelength. 73

4.9 Directional coupler working principle: The green, blue, and red curves represent the even, odd, and total mode fields propagating in the dielectric coupled waveguide system when the waveguides are placed close enough to each other. 74

4.10 VarFDTD and FDTD coupling waveguide model comparison with the literature's analytical method: (a) Illustration of the VarFDTD and FDTD model in Lumerical, utilizing ports, a Gaussian source, and a monitor to observe the modes. (b) Self-coupling coefficient as a function of the coupling gap between the bus and ring waveguides. The literature structure [142] (depicted in the schematic diagram within the graph) is used for comparison with the FDTD and VarFDTD models developed in this thesis. 75

Thèse accessible à l'adresse : https://theses.insa-lyon.fr/publication/2024ISAL0120/these.pdf © [C.B. Chander Bhan], [2024], INSA Lyon, tous droits réservés

4.11 Coupling coefficients (τ, κ) as function of coupling gap in circular MRRs: The schematic diagram of the coupling area with all critical dimensions including X-Y field profiles of coupling region is shown on the left side. The τ, κ, a as a function of the coupling gap are depicted on the right side. 76

4.12 Coupling coefficient (τ, κ) as function of coupling gap in racetrack MRRs: The schematic diagram of the coupling area with all critical dimensions including X-Y field profile of coupling region is shown on the left side. The τ, κ, a as a function of the coupling gap is depicted on the right side. 76

4.13 Coupling coefficients (τ, κ) as function of coupling gap in HOM MRRs: The schematic diagram of the coupling area with all critical dimensions including X-Y field profiles of coupling region is shown on the left side. The τ, κ, a as a function of the coupling gap are depicted on the right side. 77

4.14 Coupling coefficients (τ, κ) as function of coupling gap in FM MRRs: The schematic diagram of the coupling area with all critical dimensions including X-Y field profiles of coupling region is shown on the left side. The τ, κ, a as a function of the coupling gap are depicted on the right side. 78

4.15 Common types of tapers used in literature to enhance the coupling efficiency : (a) schematic comparison of linear, exponential and quadratic taper shape [144] (b) parabolic taper purposed by Hettrick [145] (c) Linear Si inverted taper for butt-coupling setup [144] and Si_xN_y inverted taper [146]. 79

4.16 n_{eff} as function of core width at the input of inverted tapers with fixed thickness of 0.300 μm. 80

4.17 X-Y TE Mode-field profile of both input waveguide cross-section at the input of the inverted taper (right side) and Gaussian source (left side) with spot size of 1.5 μm. 81

4.18 Power overlap efficiency as function of the linear taper length. 82

4.19 Design and schematic diagram of racetrack MRRs using adiabatic tapers with all its critical dimensions. 82

4.20 GDSfactory package. 83

4.21 Complete CAD for circular MRRs including spiral and snake bend for measuring experimental losses. 84

4.22 Schematic diagram of different MRRs included in the CAD design for different photonic chips. 85

4.23 Spirals and snake bends: Different colors are used to differentiate the various components within the devices. 86

4.24 Alignment marks. 87

Thèse accessible à l'adresse : https://theses.insa-lyon.fr/publication/2024ISAL0120/these.pdf © [C.B. Chander Bhan], [2024], INSA Lyon, tous droits réservés

5.1 Fabrication steps implemented at the photonic platform, DAPHNE, STMicroelectronics, to fabricate HOM microring resonators: The 4 steps illustrated in the figure demonstrate the waveguide configurations that can be achieved with the platform. 90

5.2 Colored SEM Image of HOM and HPWG MRR: (a) HOM MRRS where red strip lines shows the Si_xN_y strip waveguide on the SiO_2 substrate (gray color) (b) HPWG MRRs (taken from Michele Thesis [97]). 90

5.3 3D mapping thickness of LPCVD and PECVD Si_xN_y film deposited with standard recipes at LN2, 3IT : The legends shown in the pictures represents the thickness measured (in A°) with the responding color to it. 91

5.4 PECVD Tool for passive material deposition (SiO_2, Si_xN_y) at LN2, 3IT. . . . 92

5.5 Corner analysis of final strip waveguide fabricated with PECVD Si_xN_y (RI = 1.936) of 570 $\times$ 300 nm on SiO_2 (RI = 1.4462) substrate of 2 μm with H_2O (RI = 1.31) superstrate at 1310 nm wavelength. 93

5.6 PECVD SiO_2 and Si_xN_y material thickness and RI : Deposition of SiO_2 and Si_xN_y on all wafer RI of PECVD Si_xN_y measured with an ellipsometer (HORIBA UVISEL Plus) in the infrared wavelength. 94

5.7 Raith 5200 electron pattern beam generator (EPBG) at LN2, 3IT. 94

5.8 spin coater with schematic diagram of hot plate used to spin resist at LN2, 3IT. 95

5.9 correlation between beam step and spot size: (a) represents the underexposed pattern with smaller size of the spot-size and large step size, (b) and (c) represents overexposed pattern in case of large beam spot-sizes (adapted from [150]). 96

5.10 Graphical representation of Fracturing and multipass of ring with floating field ordering to avoid the stitching error :(a) LRFT fracturing mode with ring structure (b) the yellow and blue color represents two beam shot in each pass in multipass mode. 97

5.11 Beamer flow chart used in GenISys Beamer application to perform fracturing on the pattern. 98

5.12 Determination of doses required with two samples: (a) resist contrast curve, where the green rectangular structure represents the resist pattern exposed to determine the exposure dosses. (b) Different MRRs with varying doses to achieve clear coupling gaps of 200 and 400 nm. 99

5.13 Sequential development steps for a photonic chip, including time allocation for each phase. 99

5.14 Optical and electron microscopy of the resist profile after development: (a) Optical microscope image of the bending device, spirals, MRRs, and the coupling region of MRRs. (b) SEM cross-section image of the resist waveguide patterned on the Si_xN_y layer after development. 100

Thèse accessible à l'adresse : https://theses.insa-lyon.fr/publication/2024ISAL0120/these.pdf © [C.B. Chander Bhan], [2024], INSA Lyon, tous droits réservés

5.15 Influence on n_{eff} and evanescent field with trapezoidal profile of waveguide : (a) Electric field on y axis (TE) as a function of length of core width at centre. (b) TE mode-profiles of designed straight waveguide, fabricated design (trapz wg 2) and other option that can be achieved (trapz wg 1). 100

5.16 STS advance oxide ICP etcher at LN2, 3IT : plasma chamber and all the gases inlets are on the backside of the wall that are controlled by engineers. 101

5.17 Profilometer profile and electron microscope image of device after etching: (a) illustrates the profilometer profile of the sides of MRRs. (b) the cross-section of the strip waveguide after acetone and plasma oxidation. (c) coupling region after plasma oxidation and acetone cleaning. 102

5.18 SEM image of adiabatic taper (strip waveguide) after piranha to remove the dotten resist pattern on it. 103

5.19 PECVD tool at INL used to deposit SiO_2 at the edges of the photonic chip: (a) The PECVD tool (b) The RI graph across the visible wavelength range of PECVD SiO_2 deposited with this tool 104

5.20 PECVD SiO_2 inverted tapers 104

5.21 Fluidic reservoir fabrication steps using PDMS: Steps 1-6 illustrate all the standard steps involved in fabricating a PDMS reservoir using a mold (shown in step 4). Step 7 represents the adhesion of the reservoir to the SiO_2 substrate, with adhesion strength demonstrated in 7(c). 105

5.22 Fluidic reservoir fabrication steps using TPU film: (a) Illustration of the fluidic reservoir structure with TPU film, including repositioning and adhesion leakage testing. (b) and (c) Complete schematic diagrams of the reservoir structure and the silicon photonic chip with the reservoir mounted on the optical bench for characterization. 105

6.1 Optical coupling mechanism to the photonic chip on optical bench test . . . 107

6.2 Experimental optical bench test at INL,Lyon with butt-coupling mechanism. . 108

6.3 SEM image after PECVD deposition of SiO_2 on the edges of a photonics chip with a cross-sectional view of an adiabatic taper with a core width of 2 μm.109

6.4 Sample holder on the experimental optical bench setup with a fluidic reservoir on top of the chip: (a) 3D Blender model of the sample holder, and (b) a photonic chip with a fluidic reservoir (TPU film + 3D printed reservoir) placed on the sample holder. 110

6.5 Linear propagation losses of a standard PECVD Si_xN_y (3IT) strip waveguide with a cross-sectional width of 610 nm and thickness of 300 nm, buried under PECVD SiO_2: (a) Output power spectrum of spirals and linear waveguides, and (b) Linear propagation losses as a function of wavelength, along with the losses $\pm$ standard error. 111

Thèse accessible à l'adresse : https://theses.insa-lyon.fr/publication/2024ISAL0120/these.pdf © [C.B. Chander Bhan], [2024], INSA Lyon, tous droits réservés

6.6 A comparative analysis of the linear propagation losses as a function of wavelength, including shaded regions representing the error on independent and dependent variables, is presented for standard Si_xN_y strip waveguides under a SiO_2 cladding. The analysis covers three different cases: (a) standard PECVD Si_xN_y of 3IT, (b) standard PECVD Si_xN_y of ST [134], and (c) standard PECVD Si_xN_y of INL [134]. 112

6.7 Linear propagation losses of a standard PECVD Si_xN_y (3IT) strip waveguide with a cross-sectional width of 610 nm and thickness of 300 nm under water cladding for TE polarization: (a) and (c) output power spectra of spirals and linear waveguides for two different chips, and (b) and (d) Linear propagation losses as a function of wavelength, along with independent and dependent variable errors in water cladding for two different photonic chips. 113

6.8 Leakage losses estimated with FDFV mode solver due to silicon substrate for both SiO_2 and water cladding of a standard PECVD Si_xN_y (3IT) strip waveguide for TE polarization 115

6.9 Power spectrum for each bending snake with different bending radii as a function of wavelength: (a) Schematic and CAD diagram of the bending snakes used to measure bending losses, including their dimensions and labels representing the bending radius. (b) Power spectrum as a function of wavelength. 116

6.10 Power at 1310 nm wavelength as function of Bending radius to represent the relation between total bending losses as function of bending radius. 116

6.11 Normalization method to estimate radiation losses 117

6.12 Experimental and simulated radiation losses (dB/90°) for a 90° circular bending radius of a strip waveguide under SiO_2 cladding: (a) Radiation losses as a function of wavelength for a bending radius of 50 μm, and (b) Schematic diagram and TE mode profile of bending mode at 1310 nm for 50 µm bending radius. 118

6.13 Experimental and simulated radiation losses (dB/90°) for a 90° circular bending radius of a strip waveguide under water cladding: (a) Radiation losses as a function of wavelength for a bending radius of 70 μm, and (b) TE mode profile of bending mode of 70 µm bending radius at 1310 nm and 1550 nm. . 118

6.14 Output power spectra observed with an optical spectrum analyzer for a racetrack MRR with coupling gap of 350 nm under SiO_2 cladding, with the normalized transmission spectra highlighted in blue around the wavelength ranges of 1310 nm and 1550 nm. 119

6.15 Peaks method to determine the frequency spectral characteristics of MRRs: (a) Normalized transmission with respect to wavelength, (b) Selected peaks using peak detection methods, and (c) Lorentzian fit along with the experimental data points. 120

Thèse accessible à l'adresse : https://theses.insa-lyon.fr/publication/2024ISAL0120/these.pdf © [C.B. Chander Bhan], [2024], INSA Lyon, tous droits réservés

6.16 Output power spectra observed with an optical spectrum analyzer for a racetrack MRR with coupling gap of 400 nm under SiO_2 cladding, with the normalized transmission spectra highlighted in blue around the wavelength ranges of 1310 nm and 1550 nm. 121

6.17 Power spectrum observed with an optical spectrum analyzer for a racetrack MRR with coupling gap of 450 nm under water cladding, with the normalized transmission spectrum highlighted in blue around the wavelength ranges of 1310 nm. 121

6.18 Normalized transmission for racetrack HOM MRRs with a coupling gap of 600 nm under water cladding, in the wavelength range of 1290–1340 nm. The schematic diagram illustrates the critical dimensions of the MRRs. . . . 123

6.19 Experimental optical trapping setup 124

6.20 Images extracted from a recorded video (using a phone) displayed on a monitor, at different time frames, for the characterization of two devices with dielectric polystyrene particles of 4.8 μm and 1 μm. 125

8.1 Schematic diagram of the coupling region of MRR (a) top view (b) cross-section view at z=0 (redrawn from Pauline girault article [141]) 134

8.2 Comparison between experimental and Modified Psi (right) and delta (left): (a) modified delta (delta-360 °) as function of wavelength, (b) modified delta (delta-90 °) as function of wavelength. 136

8.3 Comparison between experimental and model's results for Psi (right) and delta (left). 137

8.4 Sellmeier dispersion model of Si_xN_y (left) and SiO_2 (right) as function of wavelength. 137

8.5 Forouhi-Bloomer model of Si as function of wavelength. 137

9.1 Comparaison de taille entre un cheveu humain et les particules en suspension [2]. 140

9.2 Manipulation optique par la lumière : (a) Piégeage d'une particule de 5 nm avec une nanoantenne plasmonique en forme de nœud papillon, (b) Conception d'une nanoantenne plasmonique en forme de nœud papillon sur un guide d'onde en tranchée SIN pour le piégeage optique de particules de Rayleigh, (c) Piégeage de particules de 320 nm avec un cristal photonique 1D, et (d) Piégeage de particules de 1 μm avec des résonateurs à anneaux en silicium (MRRs). 142

9.3 Régimes de piégeage optique : La barre d'échelle horizontale montre la taille moyenne des objets et la longueur d'onde correspondante (figure tirée des recherches d'Onofrio M. Maragò [48]). 145

9.4 Condition d'application des modèles d'approximation. 145

Thèse accessible à l'adresse : https://theses.insa-lyon.fr/publication/2024ISAL0120/these.pdf © [C.B. Chander Bhan], [2024], INSA Lyon, tous droits réservés

9.5 Tracé du vecteur F_{grad} dans les profils XY pour les guides d'ondes HOM et FM avec une vue en coupe et le profil en intensité du mode des deux guides d'onde schématique de la structure des deux guides d'ondes (évalué avec le modèle FDE de Lumerical). 150

9.6 Comparaison de F_{grad} en fonction de la taille de l'ouverture pour les HPWG. Les lignes en pointillés bleue et orange représentent F_{grad} pour les guides d'onde classiques fente et HPWG, respectivement, dans la plage d'écart $120 \leq g \leq 400$ nm (arrière-plan jaune) et $g \leq 120$ nm (arrière-plan gris). La ligne en pointillés grise représente F_{grad} pour le guide d'onde classique à nervure, comme illustré dans le diagramme schématique de la figure. 151

9.7 Comparaison de S pour les HPWG, les guides d'onde diélectriques à fente et standard : a) Diagramme schématique des MRRs en forme de piste où le motif en pointillés montre la zone où trois types de guides d'ondes différents sont utilisés pour évaluer S ; b) Courbes de S et de pertes en fonction de la taille de l'écart pour les guides d'onde diélectriques à fente et HPWG. Les lignes noires pleines représentent la sensibilité du guide d'ondes à standard de 220 nm/RIU. 152

9.8 n_{eff} en fonction de la largeur du coupleur effilé avec une épaisseur fixe de 0,300 μm. 153

9.9 Efficacité de recouvrement de puissance en fonction de la longueur linéaire du coupleur. 154

9.10 Courbe de la valeur du puit de potentiel en fonction de la distance x dans le milieu extérieur d'eau : (a) F_{grad} en fonction de la distance par rapport à l'interface cœur/extérieur à différents niveaux de puissance optique (b) Profondeur du puits potentiel (U_x) en fonction de la distance par rapport à l'interface cœur/extérieur à différents niveaux de puissance optique (c) Proportion de particules piégées (D_x) dans la taille du piège (e_x) en fonction de la puissance optique. 156

9.11 Optimisation de la largeur finale du cœur du guide d'onde : F_{grad} (ligne bleue solide) et décalage de longueur d'onde (ligne orange) pour différentes largeurs de cœur : les valeurs de F_{grad} calculées ici sont pour une particule diélectrique de 100 nm avec une puissance normalisée de 1 W. 156

9.12 Schéma des différents MRRs inclus dans la conception CAO pour différents puces photoniques. 158

9.13 Processus de fabrication : guide d'onde en Si_xN_y. 159

9.14 Profil au profilomètre et image au microscope électronique du dispositif après gravure : (a) illustre le profil au profilomètre des côtés des MRRs. (b) la coupe transversale du guide d'onde après nettoyage à l'acétone et oxydation plasma. (c) région de couplage après nettoyage à l'acétone et oxydation plasma. 159

Thèse accessible à l'adresse : https://theses.insa-lyon.fr/publication/2024ISAL0120/these.pdf © [C.B. Chander Bhan], [2024], INSA Lyon, tous droits réservés

9.15 Effet sur n_{eff} et champ évanescent avec un profil trapézoïdal du guide d'onde : (a) Champ électrique E_y (TE) en fonction de la largeur du noyau au centre. (b) Profils de mode TE du guide d'onde droit conçu, du design fabriqué (trapz wg 2) et d'autres options possibles (trapz wg 1). 160

9.16 Étapes de fabrication du réservoir fluidique utilisant un film TPU : (a) Illustration de la structure du réservoir fluidique avec film TPU, comprenant les tests de repositionnement et d'étanchéité. (b) et (c) Schémas complets de la structure du réservoir et de la puce photonique en silicium avec le réservoir monté sur le banc optique pour la caractérisation. 161

9.17 Test optique expérimental sur banc à INL, Lyon, avec un mécanisme de couplage par la tranche. 162

9.18 Support d'échantillon sur le dispositif optique expérimental avec un réservoir fluidique sur le dessus de la puce : (a) modèle 3D du support d'échantillon créé avec Blender, et (b) une puce photonique avec un réservoir fluidique (film TPU + réservoir imprimé en 3D) placé sur le support d'échantillon. . . . 162

9.19 Pertes de propagation linéaires d'un guide d'ondes en Si_xN_y standard PECVD (3IT) avec une largeur de section transversale de 610 nm et une épaisseur de 300 nm, enfoui sous du SiO_2 PECVD : (a) Spectre de puissance de sortie des spirales et des guides d'ondes linéaires, et (b) Pertes de propagation linéaires en fonction de la longueur d'onde, accompagnées des pertes $\pm$ erreur standard 163

9.20 Pertes de propagation linéaires d'un guide d'onde en Si_xN_y standard PECVD (3IT) avec une largeur de section transversale de 610 nm et une épaisseur de 300 nm sous gainage d'eau pour la polarisation TE : (a) et (c) spectres de puissance de sortie des spirales et des guides d'onde linéaires pour deux puces différentes, et (b) et (d) pertes de propagation linéaires en fonction de la longueur d'onde, ainsi que les erreurs des variables indépendantes et dépendantes dans un gainage d'eau pour deux puces photoniques différentes. 165

9.21 Pertes de radiation expérimentales et simulées (dB/90°) pour un rayon de courbure circulaire de 90° d'un guide d'onde à bande étroite sous revêtement de SiO_2 : (a) Pertes de radiation en fonction de la longueur d'onde pour un rayon de courbure de 50 μm, et (b) Schéma et profil du mode TE de la courbure à 1310 nm pour un rayon de courbure de 50 µm. 167

9.22 Pertes de radiation expérimentales et simulées (dB/90°) pour un rayon de courbure circulaire de 90° d'un guide d'onde sous gaine d'eau : (a) Pertes de radiation en fonction de la longueur d'onde pour un rayon de courbure de 70 μm, et (b) Profil du mode TE de la courbure pour un rayon de courbure de 70 µm à 1310 nm et 1550 nm. 168

9.23 Spectre de puissance observé avec un analyseur de spectre optique pour un résonateur à anneau en forme de piste (MRR) avec un écart de couplage de 450 nm sous un revêtement en eau, avec le spectre de transmission normalisé mis en évidence en bleu autour des plages de longueurs d'onde de 1310 nm. 169

Thèse accessible à l'adresse : https://theses.insa-lyon.fr/publication/2024ISAL0120/these.pdf © [C.B. Chander Bhan], [2024], INSA Lyon, tous droits réservés

List of Tables

1.1 Comparison of most common PM sensing techniques (adapted from [23]) . 9

2.1 Most common computation methods for optical force calculations. 16

2.2 Comparison table for modelling methods utilized in this thesis 25

2.3 Optical forces in different waveguide structures 29

2.4 Optical forces in Photonic cavities 31

5.1 Standard PECVD Low frequency Si_xN_y and SiO_2 recipes at LN2, 3IT by researcher and engineers. 92

5.2 Spin coating parameters used to spin the resist ARN7520 on the samples. . 95

5.3 SiNSlow recipe for etching Si_xN_y and resist ARN7520. 102

5.4 Standard PECVD high frequency SiO_2 parameters. 104

6.1 Linear propagation losses at wavelength of 1310 nm for standard Si_xN_y strip waveguides under a SiO_2 cladding fabricated at ST, INL and 3IT. 113

9.1 Comparaison des techniques de détection des PM les plus courantes (adapté de [23]) 141

9.2 Méthodes de calcul les plus courantes pour le calcul des forces optiques. . . 146

9.3 Tableau de comparaison des méthodes de modélisation utilisées dans cette thèse. 147

9.4 Forces optiques dans différentes structures de guides d'ondes. 148

9.5 Forces optiques dans des cavités photoniques. 149

Thèse accessible à l'adresse : https://theses.insa-lyon.fr/publication/2024ISAL0120/these.pdf © [C.B. Chander Bhan], [2024], INSA Lyon, tous droits réservés

Thèse accessible à l'adresse : https://theses.insa-lyon.fr/publication/2024ISAL0120/these.pdf © [C.B. Chander Bhan], [2024], INSA Lyon, tous droits réservés

Acronyms

Acronym	Definition
CMOS	Complementary metal–oxide–semiconductor
CMP	Chemical mechanical processing
DAPHNE	Datacom Advanced Photonic Nanoscale Environment
DDA	Discrete Dipole approximation
DEPs	Di-electrophoresis
ER	Extinction Ratio
FDTD	Finite Difference Time Domain
FEM	Finite element method
FSR	Free Spectral range
FP	Fabry–Pérot
FVFD	Fully Vectorial Full Differential
FWHM	Full Width Half Maximum
HPWG	Hybrid plasmonic waveguide
MRR	Micro-ring resonators
MST	Maxwell Stress Tensor
MZI	Mach–Zehnder interferometer
OF	Optical Force
PM	Particulate Matter
PAHs	Poly Aromatic Hydrocarbons
Q/V	Quality factor/mode-volume
TE	Transverse electric
TM	Transverse Magnetic
WHO	World Health Organisation

Thèse accessible à l'adresse : https://theses.insa-lyon.fr/publication/2024ISAL0120/these.pdf © [C.B. Chander Bhan], [2024], INSA Lyon, tous droits réservés

Thèse accessible à l'adresse : https://theses.insa-lyon.fr/publication/2024ISAL0120/these.pdf © [C.B. Chander Bhan], [2024], INSA Lyon, tous droits réservés

Chapter 1

Introduction

1.1 Air pollution

Globally, air pollution kills about seven million people per year. WHO data indicates that nine out of ten people breathe air containing a high level of pollutants which exceeds WHO guidelines [1]. Air pollution from ambient (outdoor) and household sources is responsible for 7 million premature deaths a year and presents a major threat to health and climate [1, 2, 3]. The cause of this mortality is exposure to particulate matter (PM) present in the air due to pollution. Acute respiratory infections, chronic obstructive pulmonary disease, stroke, heart disease, and lung cancer can all be causally linked to air pollution. PM consists of chemicals such as sulfates, nitrates, carbon, or mineral dust and organic compounds such as Poly Aromatic Hydrocarbons (PAHs). Various sources of PM include vehicle emissions, industrial emissions, cigarette smoke, and burning organic matter (such as wildfires).

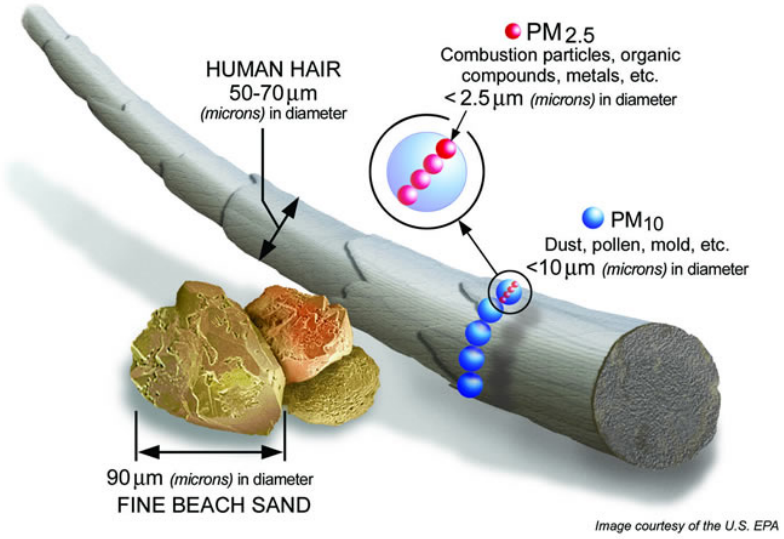

Figure 1.1: Size comparison between human hair and particulate matter [2].

More than 95% of emissions from diesel, petrol, and natural gas combustion, open waste

Thèse accessible à l'adresse : https://theses.insa-lyon.fr/publication/2024ISAL0120/these.pdf © [C.B. Chander Bhan], [2024], INSA Lyon, tous droits réservés

burning pollution, biomass burning pollution, and coal combustion at cook-stoves and boilers, fall under PM2.5[1]. Figure 9.1 illustrates the size comparison of fine particulate matter with human hair. In comparison to human hair, PM2.5 particles are 30 times smaller.

In the urban environment, PAHs are one of the most significant toxic air pollutants. They have been extensively studied in the context of health and environmental effects due to their well-known carcinogenic and mutagenic properties [4, 5]. Moreover, even if a new generation of vehicle engines and fuels are being developed to reduce particulate emission, it's still important to have high sensitivity sensing devices so that air pollution can be precisely evaluated [6, 7, 8].

Airborne particulate can be divided into three categories in the atmosphere:

- coarse particles (diameter $1.8 - 10$ μm)
- fine particles (diameter $0.1 - 1.8$ μm)
- ultra-fine particles (diameter < 0.1 μm)

Air pollution contains heterogeneous concentrations of airborne particles, but metals and polycyclic aromatic hydrocarbons (PAHs) are typically distributed almost uniformly, with seasonal variations in concentration [9]. Monitoring nanoparticles, such as PAHs, in media like the atmosphere and various liquids is crucial for public health, food quality assurance, and the efficient operation of machinery in the automotive industry. Moreover, multiple studies have shown that PM2.5 particles have a size distribution with a peak around 0.1 μm [6, 10]. Therefore, in our study, we consider PAHs as polystyrene particles of size 0.1 μm for simulation and characterization purposes.

1.2 Measurement solutions

In this section, we provide a brief introduction to PM (particulate matter) sensing instruments that have been historically developed, are currently in use, and are commercially available on the market. The most popular method for determining particle size is through the use of aerodynamic classifiers, such as cascade impactors [11]. This method measures the aerodynamic mobility (inertia) of a particle carried by an accelerating air flow and derives the aerodynamic diameter by taking the square root of the product of 18 times the Stokes number and air viscosity, divided by the product of particle density and flow velocity. This approach, known as Aerodynamic Particle Sizing (APS), typically involves a nozzle and a time-of-flight module [12] to generate the accelerating air flow required to determine the aerodynamic diameter.

Another commonly used method for particle sizing, found in the literature, involves the Scanning Mobility Particle Sizer (SMPS). This technique measures the deviation of an electrostatically charged particle subjected to an electric field, using an electrostatic classifier [13, 14]. However, APS and SMPS systems are limited to measuring particle sizes in the range of 0.5 to 1 μm and are often bulky and expensive.

[1] PM2.5 are the fine inhalable particles, with diameters that are generally 2.5 micrometers and smaller

Thèse accessible à l'adresse : https://theses.insa-lyon.fr/publication/2024ISAL0120/these.pdf © [C.B. Chander Bhan], [2024], INSA Lyon, tous droits réservés

There are two commonly used types of technologies for monitoring fine and ultrafine particles in the surrounding environment:

1. Gravimetric method
2. Optical

1.2.1 Gravimetric method

The gravimetric method is a common technique for measuring airborne particulates by collecting air samples on a filter, typically made of glass fiber or Teflon, and weighing the filter before and after collection. The difference in weight between the two measurements determines the amount of particulate matter in the sampled air. However, this method has several limitations, including high costs and the large size of the required instrumentation [15].

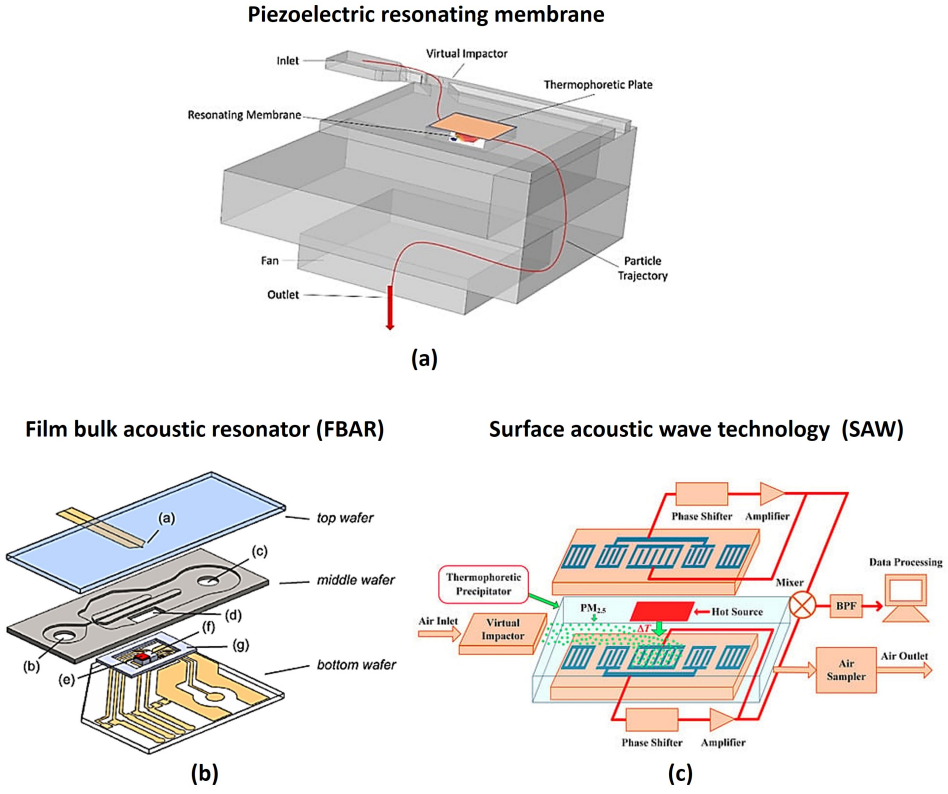

Figure 1.2: Modern gravimeter M & NEMS: (a) Gravimetric method used with resonator structure [16] (b) MEMS air-microfluidic particulate matter (PM) sensor based on Film Bulk Acoustic Resonators [17] (c) PM2.5 Sensor Based on Surface Acoustic Wave [18].

Modern approaches to gravimetric methods enable the mass measurement of single particles using Micro and Nano Electro-Mechanical Systems (MEMS and NEMS), such as oscillating piezoelectric cantilevers [19, 20], Film Bulk Acoustic Resonators (FBARs) [17], and Surface Acoustic Wave (SAW) resonators [21, 18]. These advanced methods utilize thermophoretic velocity, generated by a temperature gradient created by an external heat source as

Thèse accessible à l'adresse : https://theses.insa-lyon.fr/publication/2024ISAL0120/these.pdf © [C.B. Chander Bhan], [2024], INSA Lyon, tous droits réservés

shown in Figure 1.2 with 3 modern gravimetric MEMS, to divert selected particles onto the resonating membrane, making them sensitive to temperature changes.

1.2.2 Optical methods

Optical methods enable real-time measurement of airborne particulates and are generally based on the absorption and scattering of light by particles. One such approach is the extinction method, which measures the loss of optical intensity as a single light source passes through a cloud of particles, based on the Beer-Lambert law of attenuation. However, extinction methods have low sensitivity due to a poor signal-to-offset ratio and are not effective in measuring fine particles.

Another common method for measuring air particulates is laser scattering, which uses a laser beam that scatters off particles in the air, measuring the intensity of the scattered light to determine the size, concentration, and distribution of particles. However, these sensors rely on several assumptions to estimate particle density and size distribution, which can lead to unreliable and inaccurate results [22].

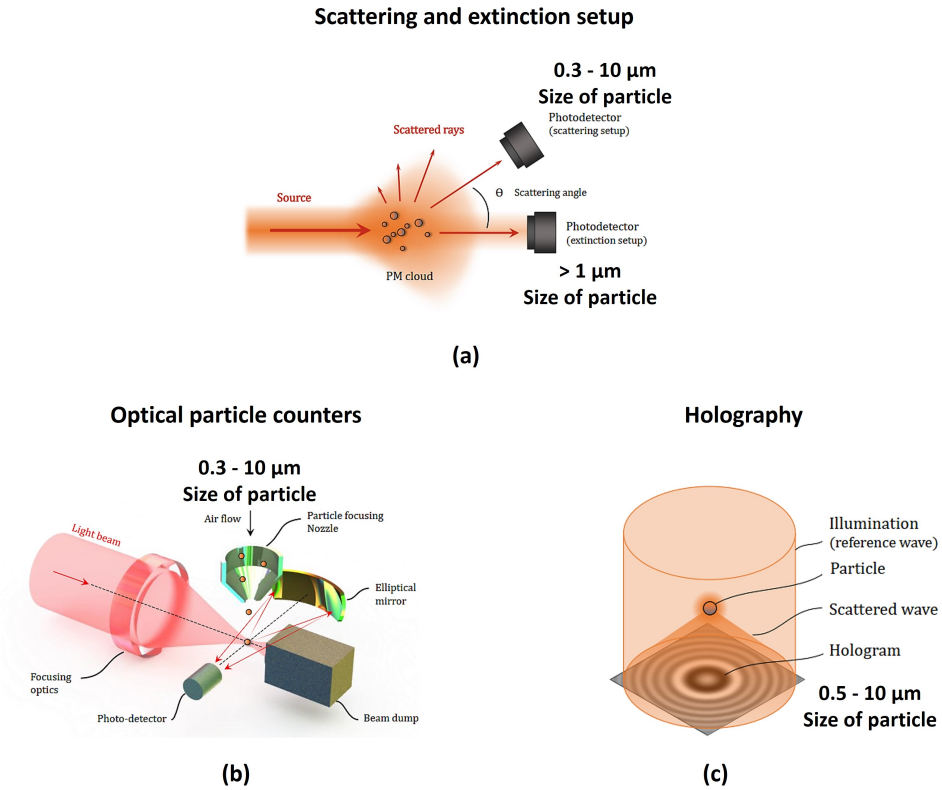

Figure 1.3: Optical methods to measure PM: (a) illustration of optical light scattering and extinction methods (b) illustration of optical particle counters (c) graphical illustration Holography working principle [23].

Other methods, such as Optical Particle Counters (OPCs) and holography, use similar principles but can detect individual particles. OPCs utilize high numerical aperture detection optics to improve sensitivity, whereas holography uses holograms created by lens-less CMOS image sensors to determine particle number and size distribution. However, methods like

Thèse accessible à l'adresse : https://theses.insa-lyon.fr/publication/2024ISAL0120/these.pdf © [C.B. Chander Bhan], [2024], INSA Lyon, tous droits réservés

OPC, holography, and light scattering are generally only effective for detecting particles larger than 300 nm and have low sensitivity for fine particles. The figure below illustrates different optical counters, their schematic diagrams, and their ability to detect various particle size ranges.

Implementing technologies that reduce cost and size while providing greater precision and selectivity could address the limitations of current methods. In the next section, we explore optical forces and dielectrophoresis as futuristic solutions. These advanced techniques allow researchers to study these particles in much greater detail than the measurement methods discussed above.

1.2.3 A future generation solution for measurement

Di-electrophoresis

Dielectrophoresis (DEP) is another method for measuring and manipulating small particles, such as air particles. DEP is based on the principle of using electric fields to exert forces on particles, which can be used to move, trap, and sort particles based on their electrical properties. One of the main advantages of DEP is that it can be used with a wide range of particle sizes, from sub-micron to millimeter-scale [24]. Additionally, DEP can be used with a wide range of particle materials, including biological cells. However, the main disadvantages of DEP is that it requires high frequency alternating electric fields and unable to analyze the particle properties, makes it not the complete ideal solution for monitoring air particulate. Figure 1.4 illustrates the principle of dielectrophoresis and what has been accomplished with current dielectrophoresis technology and how a solution could be developed to overcome the disadvantage with DEP published.

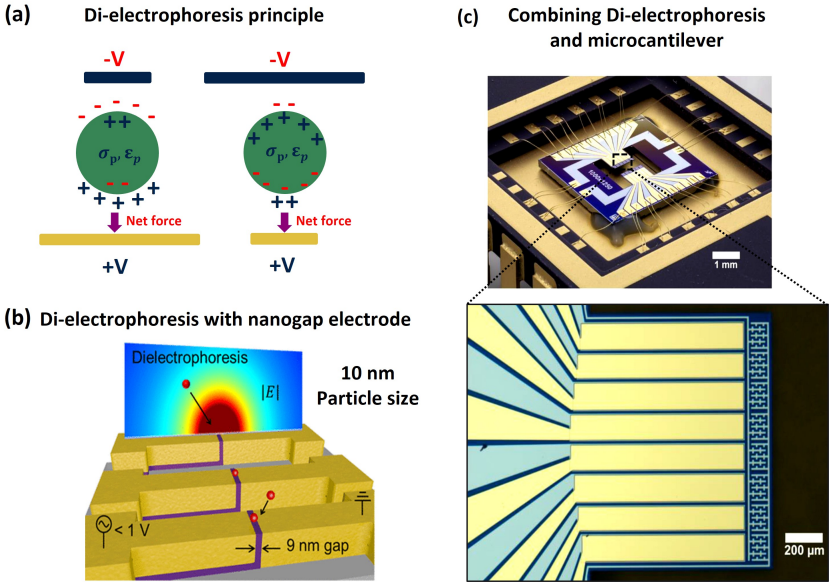

Figure 1.4: Dielectrophoresis: (a) Principle [24] (b) dielectrophoresis (Volt < 1) with nano-electrode gap of 9 nm to trap 10 nm size particle [25] (c) resonant MEMS sensor utilizing both dielectrophoresis and microcantilever resonant for the detection dielectric particles in aged lubricating oils [26].

Thèse accessible à l'adresse : https://theses.insa-lyon.fr/publication/2024ISAL0120/these.pdf © [C.B. Chander Bhan], [2024], INSA Lyon, tous droits réservés

On-Chip Fluids Manipulation by Light

An optical tweezer is an instrument used for manipulating and measuring small particles. Two of the most significant advantages of optical tweezers are their precision and resolution, which enable detailed measurements of particle size, shape, and location. Additionally, optical tweezers can manipulate and sort particles based on their physical properties, such as charge or refractive index [27]. However, optical tweezers have several disadvantages, including the requirement for a high-power laser, limitations imposed by diffraction, and thermal diffusion of nanoparticles. These factors make them expensive and challenging to use.

Near-field optical manipulation offers advantages over classical optical tweezers. For instance, the use of a cavity, such as a ring resonator, enhances the circulating field, which can be significantly stronger than the incident field [28]. Recently, optical microcavities have gained popularity as "sensors-on-a-chip" due to their capability of detecting nanoparticles and molecules without the need for labels [29, 30, 31]. Several researchers have demonstrated the manipulation of nanoparticles and microparticles using integrated near-field optical trapping based on the evanescent fields of photonic and plasmonic devices on lab-on-a-chip platforms as shown in Figure 1.5, which are low-cost, portable, and highly sensitive systems [32, 33, 34, 35, 36].

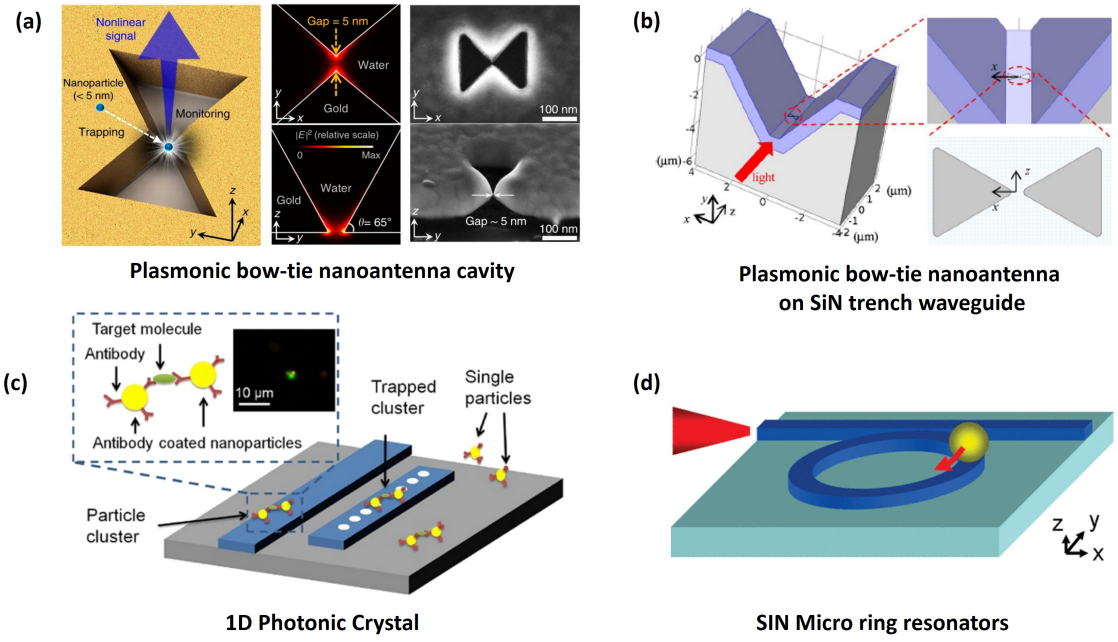

Figure 1.5: Optical Manipulation by Light: (a) Trapping of a 5 nm particle with a plasmonic bow-tie nanoantenna, (b) Design of a plasmonic bow-tie nanoantenna on a Si_xN_y trench waveguide for Rayleigh optical particle trapping, (c) Trapping of 320 nm particles with a 1D photonic crystal, and (d) Trapping of 1 μm particles with silicon MRRs.

Table 9.1 presents a comparison of the common PM sensing techniques reported in the literature. It can be observed that methods based on gravimetric and light scattering principles exhibit poor sensitivity to particle sizes below 100 nm. Current literature highlights emerging solutions that utilize on-chip fluid manipulation by light, offering new approaches to enhance sensitivity for particles smaller than 100 nm. Leveraging a CMOS platform,

Thèse accessible à l'adresse : https://theses.insa-lyon.fr/publication/2024ISAL0120/these.pdf © [C.B. Chander Bhan], [2024], INSA Lyon, tous droits réservés

measurements can be conducted more rapidly with integrated photonic chips, as this platform facilitates complete integration of lasers, photodetectors, and microfluidic channels on a single chip. Therefore, in this thesis, we focus on developing a prototype capable of trapping 100 nm dielectric particles using a photonic integrated device compatible with existing industrial platforms.

In this work, characterizing the fabricated devices requires the use of microfluidic channels for air. However, fabricating air-based channels presents significant challenges compared to water-based channels, primarily due to issues such as bubble formation, design complexity, and surface effects (e.g., absorption and adsorption). Given the lack of expertise in developing microfluidic channels for air, we opted to use a water-filled microfluidic reservoir for the initial prototype. As a result, all modeling and device designs in this thesis were based on dielectric particles suspended in water, rather than air.

Types of sensor	size ranges	Advantage	Disadvantage
Gravimetric	$>$ 150 nm	cheap, simple to deploy	analysis time consuming
M & NEMS	$>$ 5 nm	real time measurement, CMOS compatibility	sensitive to temperatures
APS	0.5 - 20 μm	High accuracy and resolution	Expensive and bulky
SMPS	2.5 nm - 1 μm	High accuracy and resolution	Expensive and bulky
Light scattering principle	300 nm - 10 μm	cheap, high portability	poor sensitivity to sub-micron particles ($<$ 0.1 μm)
Optical particle counter	300 nm - 10 μm	cheap	poor sensitivity to sub-micron particles ($<$ 0.1 μm)
Holograph	500 nm - 10 μm	high portability	analysis is computationally expensive
Dielectrophoresis	$<$ 10 nm	high trapping forces, CMOS compatibility	requires high frequency alternating electric fields
On-chip fluids manipulation by light	$<$ 5 nm	CMOS compatibility	optical forces diminishes with lower size of particles

Table 1.1: Comparison of most common PM sensing techniques (adapted from [23])

Thèse accessible à l'adresse : https://theses.insa-lyon.fr/publication/2024ISAL0120/these.pdf © [C.B. Chander Bhan], [2024], INSA Lyon, tous droits réservés

1.3 Thesis planning

This manuscript is structured as follows:

Chapter 2, provides the theoretical background on optical trapping, including various computational methods available in the literature for determining the optical forces on dielectric nanoparticles in fluid environments. Additionally, the chapter introduces different modeling methods that allow for the study of various waveguide structures, including recent designs based on the mode-lift concept and patents between STMicroelectronics, 3IT, and INL. We also present a state-of-the-art literature comparison in terms of optical trapping forces achieved with different devices, which helps guide our choice of the final design and structures to be utilized in this thesis.

Chapter 3, explains the basic concept of waveguide modeling and details the modeling of optical forces on dielectric particles using the Discrete Dipole Approximation (DDA) and Maxwell Stress Tensor (MST) methods. These two methods are employed to study different structures and concepts aimed at enhancing the optical force for 100 nm dielectric particles. We demonstrate how ring resonators are used to achieve high optical trapping forces. Additionally, we discuss the main aspects that must be optimized to maximize optical trapping forces while maintaining high sensitivity.

Chapter 4, describes the optimization and design concepts for an optimal final device, including various components such as inverted tapers, bending sections, sensing areas, adiabatic tapers, etc. These devices are designed for fabrication at the 3IT platform, as described in Chapter 5.

Chapter 5, outlines the fabrication process at the 3IT platform for the devices designed in Chapter 4.

Chapter 6, presents the experimental characterization of devices that were previously fabricated in earlier theses and those fabricated in this thesis.

Chapter 7, concludes this manuscript with a summary and discusses prospects for further development of integrated environmental sensors.

Thèse accessible à l'adresse : https://theses.insa-lyon.fr/publication/2024ISAL0120/these.pdf © [C.B. Chander Bhan], [2024], INSA Lyon, tous droits réservés

Chapter 2

Context and State of the Art

The previous chapter highlighted the significance of accurately assessing air quality. As discussed earlier, optical forces have been identified as potential methods for measuring air quality. This thesis focuses on the use of optical forces, which allow for both sensing and trapping capabilities. This chapter provides an overview of the historical development of optical manipulation, recent advancements in optical trapping techniques for manipulating dielectric nanoparticles, and various computational methods for evaluating the magnitudes of optical forces.

2.1 Optical Manipulation: Brief History, Definition, Trapping Regime

In 1619, Kepler proposed the existence of mechanical action of light on matter. In his view, the tails of comets always face away from the sun because of solar radiation pressure. In the 18th century, Euler confirmed this hypothesis by showing that a light wave exerts pressure on a body placed across its propagation direction [37]. In the late 19th century, with Maxwell's theory of electromagnetism, it was shown that the momentum flux of a light beam is proportional to its intensity. Therefore, the radiation pressure of the beam pushes objects along its propagation direction, resulting in radiation pressure [38].

In 1873, Crookes built an apparatus (Crookes radiometer or "light mill") to observe the effect of light pressure [39]. In the Crookes radiometer, there are two vanes [1]: an absorbing surface and a reflecting surface. Crookes believed he could demonstrate radiation pressure by observing light repelling the absorbing faces of the mill wings.

Arthur Schuster observed that there was a radiation force on the glass bulb of the Crookes radiometer in the opposite direction to the rotation of the vanes he demonstrated. In 1901, Peter Lebedev [40] discovered that, in fact, the radiometer exclusively works when there is low-pressure gas in the apparatus, and the vanes stay static in a hard vacuum. Moreover, at the beginning of the 20th century, Lebedev [41] in Russia and Nicols and Hull [42] in the

[1] a broad blade attached to a rotating axis or wheel which pushes or is pushed by wind or water and forms part of a machine or device such as a windmill, propeller, or turbine.

Thèse accessible à l'adresse : https://theses.insa-lyon.fr/publication/2024ISAL0120/these.pdf © [C.B. Chander Bhan], [2024], INSA Lyon, tous droits réservés

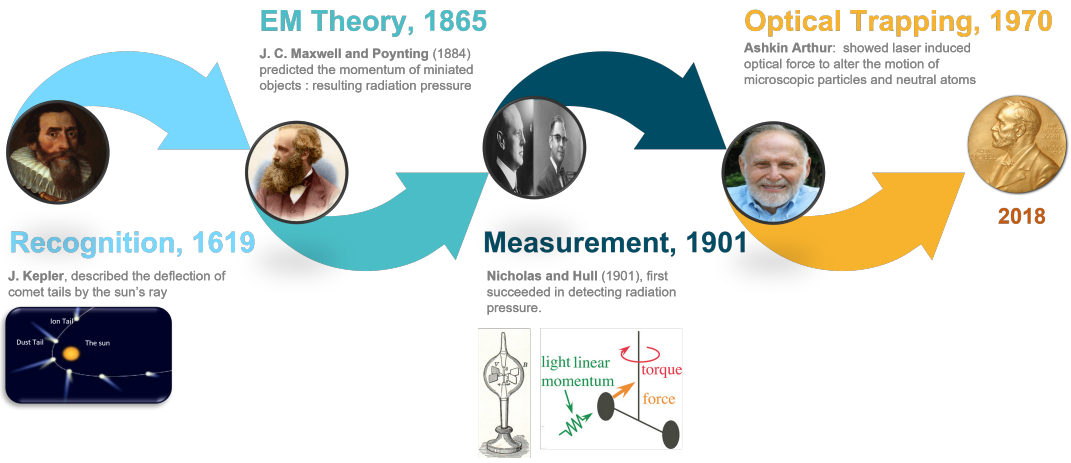

Figure 2.1: Brief history of Optical Manipulation.

U.S. succeeded in demonstrating the effects of radiation pressure on macroscopic objects.

The exploitation of these forces seemed difficult to envisage before the invention of the laser in the 1960's [43]. Arthur Ashkin was the first, in 1970, to demonstrate experimentally the influence of these forces on microscopic particles [44]. Later he demonstrated the combined influence of the radiation pressure and the gradient force on the motion of micrometer particles, neutral atoms, and biological specimens [45, 46]. For his work that lead to the invention of the optical tweezers, he was awarded the Nobel Prize in Physics 2018.

2.1.1 Optical Force

A particle experiences an optical force when the radiation pressure of light interacts with it in the form of absorption, reflection, or refraction. Optical forces are the result of the momentum conservation and consist of three forces ***gradient force, scattering forces, and spin-curl forces***. The spin-curl force acts when the field's polarization is not homogeneous. As compared to scattering and gradient forces, spin-curl forces are generally relatively small. Therefore, in most cases, we do not calculate the spin-curl force unless a non-homogeneous fields is present.

1. **Gradient force (trapping force)**: when a particle is positioned within a non-uniform electric field, the polarization of the particle changes with location. This results in a conservative force. Gradient forces are in the direction of the spatial light gradient.

2. **Scattering force (radiation pressure)**: The momentum of electromagnetic radiation is transferred to particles through optical scattering and absorption. Thus, it is a non-conservative forces. The scattering forces are in the direction of the light propagation.

The gradient force decreases with decreasing particle size. In conventional far-field optical tweezers, for smaller particles, a high optical power laser (tightly focused beam) is required in order to achieve an adequate gradient force to overcome Brownian motion and, therefore, to trap particles. However, high-power lasers cause particle heating and optical damage, which is often detrimental. Near-field optical trapping by evanescent fields generated from photonic structures (photonic crystal cavities, ring resonators) is capable of

Thèse accessible à l'adresse : https://theses.insa-lyon.fr/publication/2024ISAL0120/these.pdf © [C.B. Chander Bhan], [2024], INSA Lyon, tous droits réservés

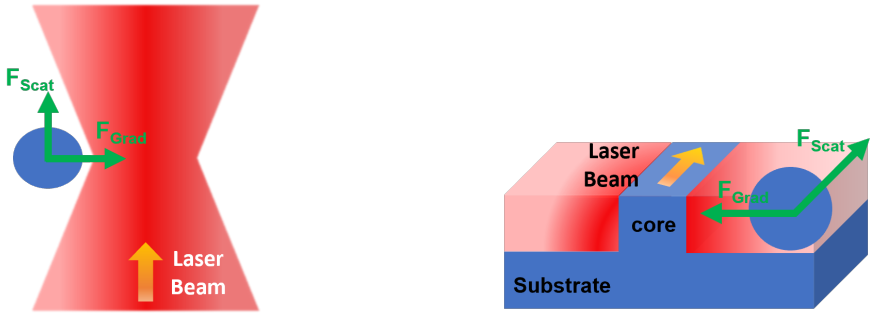

a) Far Field Optical Manipulation

b) Near Field Optical Manipulation

Figure 2.2: Schematic comparison between far field and near field optical manipulation.

providing a large trapping force enhancement and precise position control, with potentially less power. This is useful for the guidance and trapping of single nanoparticles. Figure 2.2 is a schematic comparison between near-field and far-field optical manipulation [47].

2.2 Computational Method

Modeling the optical forces exerted on a particle, arising from the conservation of electromagnetic momentum, is essential for understanding the underlying physics and optimizing design parameters. With the rapid advancement of optical tweezers, the theoretical framework for calculating optical forces has also evolved significantly. Over the past decades, several methods have been proposed in the literature to determine the optical forces on particles of varying sizes and shapes. Each method possesses its own advantages and limitations. These methods are categorized based on their applicability to different optical trapping regimes that depends upon the size parameter ($k_m a$), as detailed below.

2.2.1 Optical trapping regime

Researchers have proposed various optical trapping techniques to trap and manipulate objects at the nanometer scale, as illustrated in Figure 2.3. In this figure, objects are classified into different optical trapping regimes to simplify the understanding of their size in relation to the wavelength. There are three primary optical trapping regimes:

- Rayleigh regime ($k_m a < 1$)
- Lorenz-mie regime or intermediate regime ($k_m a \sim 1$)
- Ray optics or geometrical optics regime($k_m a >> 1$)

In general, a full electromagnetic calculation is required to accurately predict the optical trapping behavior of microscopic objects of various sizes and shapes. These comprehensive electromagnetic calculations can be solved using methods such as the Finite Difference

Thèse accessible à l'adresse : https://theses.insa-lyon.fr/publication/2024ISAL0120/these.pdf © [C.B. Chander Bhan], [2024], INSA Lyon, tous droits réservés

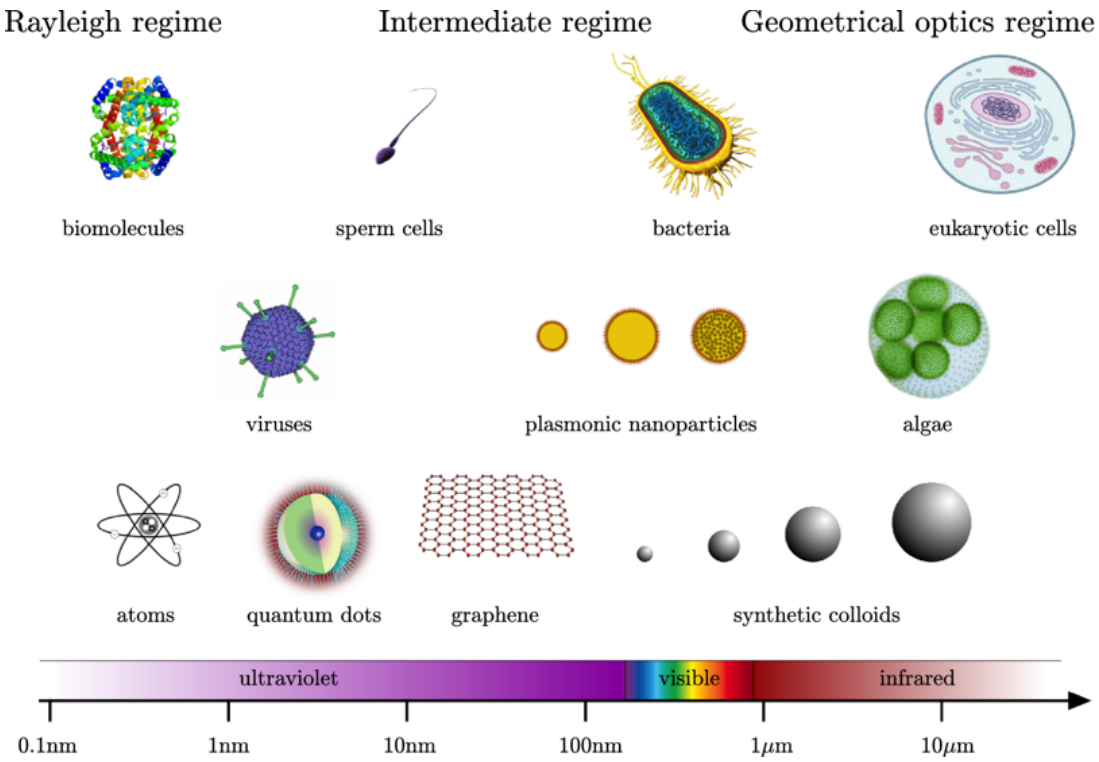

Figure 2.3: Optical Trapping regimes: The horizontal scale bar shows the average object size and the corresponding light wavelength (Figure taken from research by Onofrio M Maragò [48]).

Time Domain (FDTD) or the Finite Element Method (FEM). However, approximating models can provide quick physical insights into complex problems and improve computational efficiency [47], though they often come with limitations. It is crucial to understand the validity limits of these approximation models before applying them [49].

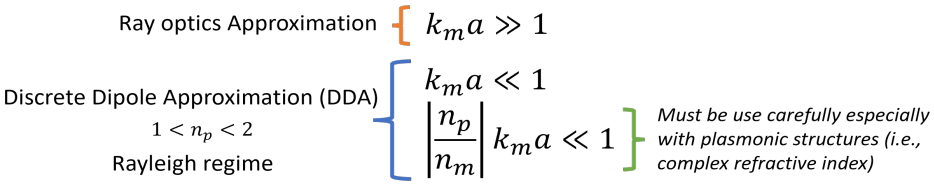

Figure 2.4: Approximation model condition

The *size parameter* ($K_m a$) in equation 9.1 is often used to determine the range of validity of an approximation method.

$$k_m a = \frac{2\pi n_m}{\lambda_0} a \tag{2.1}$$

where k_m is the wavevector or propagation constant of the light wavefront in the medium, λ_0 is the operating wavelength, n_m and a is refractive index (RI) and radius of spherical nanoparticle respectively [48]. Figure 2.4 illustrates the condition to choose the appropriate approximation model's.

Thèse accessible à l'adresse : https://theses.insa-lyon.fr/publication/2024ISAL0120/these.pdf © [C.B. Chander Bhan], [2024], INSA Lyon, tous droits réservés

In the intermediate regime, where the particle size is comparable to the wavelength, a complete electromagnetic calculation is necessary to accurately predict the behavior of optical trapping [48]. For spherical particles, the Lorenz–Mie theory [50, 51] can be employed to generate accurate numerical results for nearly any size and refractive index. This theory expands the field inside and outside the particle into a series of spherical vector wave functions, with the expansion coefficients determined by matching the boundary conditions at the particle's surface. The complexity increases for non-spherical particles, such as cylindrical ones, where T-matrix methods—an extended version of the Generalized Lorenz–Mie Theory (GLMT)—are applied. A more accurate comparison between computational T-matrix methods, combined with extended boundary conditions, point-matching methods, and the Discrete Dipole Approximation (DDA), is provided in [52, 53].

For our studies, we focus on dielectric spherical particles with a size of 0.1μ m, where the fields are considered homogeneous inside the particles. As shown in Figure 2.4, to study optical forces within this particle size range, the DDA method (valid for $k_m a < 1$) provides a reasonable approximation for computing optical forces and is computationally efficient.

However, since the DDA is limited to a specific range of particle sizes, a more rigorous calculation is necessary to study the effects of varying particle sizes and for complex structures such as hybrid plasmonic waveguides (described later). The Maxwell Stress Tensor (MST) method, implemented using Finite Difference Time Domain (FDTD) or Finite Element Method (FEM), is the most commonly used numerical approach for calculating optical forces for particles of any size and shape. The chosen methods, DDA and MST, are further detailed in the upcoming subsections to provide a deeper understanding of the underlying physics and how these methods were developed and utilized in the model. Additionally, a comprehensive comparison Table 2.1 of different computational methods for calculation optical forces is provided, highlighting their respective advantages and disadvantages.

Thèse accessible à l'adresse : https://theses.insa-lyon.fr/publication/2024ISAL0120/these.pdf © [C.B. Chander Bhan], [2024], INSA Lyon, tous droits réservés

Method	Advantage	Disadvantage
Ray optics (Geometrical optics)	Simple, fast, and suitable for large particles ($k_m a >> 1$)	Not accurate for small particles + ignores wave phenomena like diffraction and interference
Generalized Lorenz–Mie Theory	Highly accurate for spherical particles of any size [54]	Less flexible for non-spherical geometries or complex materials.
Discrete dipole approximation (Rayleigh regime)	Good for particles of arbitrary shape	Limited to Rayleigh size and by discretization error
T-matrix method	Accurate for axisymmetric particles (cylindrical) and efficient for multiple scattering problems	Less accurate for highly irregular shapes
Maxwell stress tensor	Accurate for particles of any size; can model complex shapes, polarizations, and materials.	Computationally expensive and requires significant resources for complex geometries and large domains

Table 2.1: Most common computation methods for optical force calculations.

2.2.2 Discrete Dipole Approximation (DDA)

The DDA methods was purposed by Purcell and Pennypacker to calculate the scattering and absorption of electromagnetic radiation by particles or clusters of particles [55]. When the particle is smaller than the wavelength of the light, it can be approximated as a dipole. The method assumes that the optical field can be represented as a sum of dipole fields, each with its own dipole moment. An optical force exerted on a particle can be calculated simply and straightforwardly by using this approximation.

The accuracy of the DDA depends upon a number of factors, including the size of the scattering particle (discussed in section 2.2.1) and the discretized volume of the particle. The size of the cells (mesh in the simulation) must satisfy the condition $kd|m| < 0.5$, where $k = 2\pi/\lambda$, d is the size of the cells, and m is the complex refractive index of a particle [56]. The electric field E and the induced dipole moment P under linear polarization are connected by

$$\overrightarrow{P} = \alpha \overrightarrow{E_o} \tag{2.2}$$

where, α is the polarizability of the medium, $\overrightarrow{E_o}$ unperturbed electric field (contribution of induced polarization of particle is excluded). The force exerting on a particle by an external electromagnetic field is defined as:

$$\overrightarrow{F} = (\nabla \overrightarrow{E}) \cdot \overrightarrow{P} \tag{2.3}$$

Thèse accessible à l'adresse : https://theses.insa-lyon.fr/publication/2024ISAL0120/these.pdf © [C.B. Chander Bhan], [2024], INSA Lyon, tous droits réservés

So, the time-averaged optical force [57, 58, 59, 60] is given by,

$$< \overrightarrow{F} >= \frac{1}{4}\mathit{Re}(\alpha) \cdot \nabla E_o^2 + \frac{\sigma_{ext}}{c} \cdot S_i \tag{2.4}$$

Where, α gives the polarizability, σ_{ext} extinction coefficient and ∇E_o^2 gradient of the electric field. The first term represents gradient force, and the second term corresponds to scattering force. It is important to note that the optical forces are proportional to the polarizability of the dielectric particle, which increases with particle size.

From equation 2.4 the gradient force can be defined as:

$$< F_{grad} > \approx \pi\varepsilon_2 \frac{(\varepsilon_{medium} - \varepsilon_{particle})}{(\varepsilon_{medium} + 2\varepsilon_{particle})} r^3 . \nabla E_o^2 \tag{2.5}$$

$$\nabla E_o^2 = \nabla (E_x E_x^* + E_y E_y^* + E_z E_z^*)^2 \tag{2.6}$$

An electric field with a sharp gradient leads to an increase in trapping force. The particle's ability to be trapped is determined by its polarizability. In order to trap an object, it is also essential that the gradient force in the light propagation direction be large enough to compensate for the scattering force. Consequently, the trapping force largely depends on the polarization of the incident light, gradient of electric field and the polarizability of the particle.

Figure 2.5 shows gradient forces calculated for a strip waveguide along the x and y-axes for polystyrene particles of 100 nm size at an operating wavelength of 1.310 μm. Figure 2.5.(b) presents a combined vector and fundamental mode field profile plotted with binary color gradients. It can be seen in the figure that there are stronger forces near the maximum intensities, which can be seen in the gradient vector plot.

From equation 2.4 the scattering force can be defined as:

$$\overrightarrow{F_{scat}} = \frac{\sigma_{ext}}{c} \cdot S_i \tag{2.7}$$

where, S_i = $E_i \times H_i^*$ is the poynting vector that indicates the amount of directional energy passing per unit area per unit time.

The σ_{ext} extinction coefficient in the equation 2.7 consists of two components scattering cross-section (σ_{scat}) and absorption cross-section (σ_{abs}):

$$\sigma_{ext} = \sigma_{scat} + \sigma_{abs} \tag{2.8}$$

1. The scattering cross-section σ_{scat} is related to the scattering of the light beam propagating in a waveguide

$$\sigma_{scat} = \frac{k_0^4}{6\pi\varepsilon_0^2} |\alpha_{rad}|^2 \tag{2.9}$$

[2]"Simulation is performed using a Full vectorial Finite difference Method (FVFD)-2D on MATLAB developed by Régis OROBTCHOUK and using Lumerical (FDE) to confirm the field values. To simulate the sensing device the 3D SiN ring resonator is converted into a 2D slab i.e., only the transversal profile of the ring is simulated"

Thèse accessible à l'adresse : https://theses.insa-lyon.fr/publication/2024ISAL0120/these.pdf © [C.B. Chander Bhan], [2024], INSA Lyon, tous droits réservés

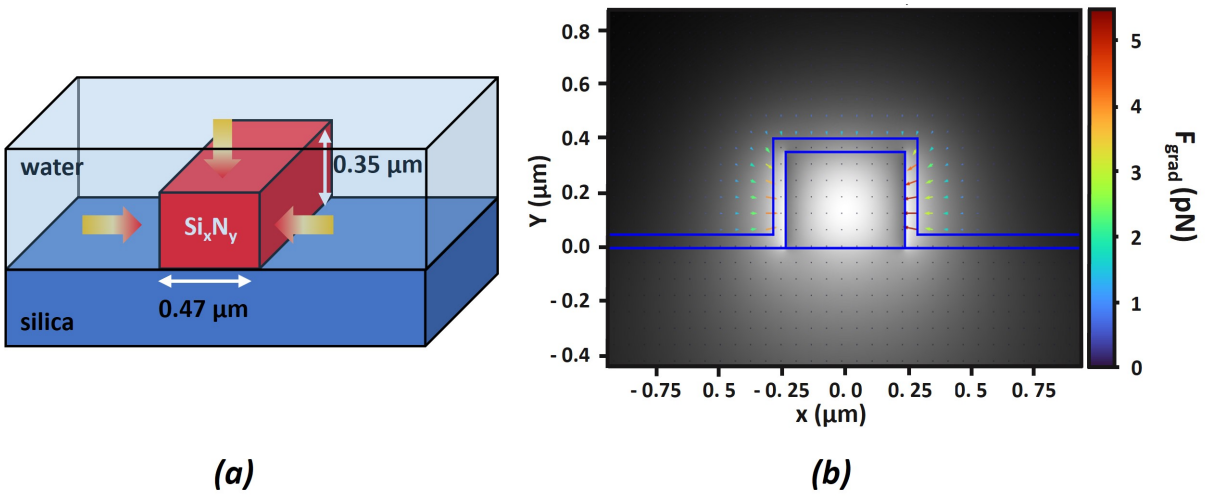

1

Figure 2.5: Gradient Force: (a) schematic diagram of strip Si_xN_y waveguide (b) vector plot of gradient force calculated using DDA at 1310 nm wavelength with power of 1 W, the binary color grading in this plot presents the evanescent field amplitude of the fundamental mode in a waveguide.

where α_{rad} is the polarizability defined by Draine [61] as expressed in Equation 2.12.

2. The absorption cross-section σ_{abs} is given by :

$$\sigma_{abs} = \frac{k_0}{\varepsilon_0} imag(\alpha_{rad}) - \frac{k_0^4}{6\pi\varepsilon_0^2}|\alpha_{rad}|^2 \tag{2.10}$$

In the case of the Rayleigh, dielectric particles ($\sigma_{ext} \approx \sigma_{scat}$). In the case of metallic particles, the absorption coefficient dominates the scattering cross-section ($\sigma_{ext} \approx \sigma_{abs}$).

Polarizability of particle : The Clausius-Mossotti relation is commonly used for predicting the dielectric properties of materials and has a number of important applications in fields such as optics and electrical engineering. Despite a few limitations, the Clausius-Mossotti relation is a valuable tool for predicting the dielectric properties of materials, and it is used in a variety of applications.

In the quasi-static limit $(\lambda >> r)$, the polarizability of the spherical Rayleigh particle with radius r surrounded by a medium is given by Clausius-Mossotti relation [62],

$$\alpha_{CM} = 3V\varepsilon_{particle} \cdot \frac{(\varepsilon_{medium} - \varepsilon_{particle})}{(\varepsilon_{medium} + 2\varepsilon_{particle})} \tag{2.11}$$

where V is the volume of the spherical particle ($V = 4/3\pi r^3$)and $\varepsilon_{particle}$ and ε_{medium} are the dielectric permittivity of the particle and medium of the particle.

Corrections to the static approximation : The clausius-Mossotti's relation is exact only when it is static. Despite its use in optical experiments, it does not account for phase shifts between incident and scattered waves (in other words, own induced scattered field by a particle). Various polarizability models [61, 63] have been proposed to fill these gaps. We

Thèse accessible à l'adresse : https://theses.insa-lyon.fr/publication/2024ISAL0120/these.pdf © [C.B. Chander Bhan], [2024], INSA Lyon, tous droits réservés

will focus on the one by Draine [61] which, by adding a "radiative reaction" term to the total electric field, leads to a new form of polarizability:

$$\alpha_{rad} = \frac{\alpha_{CM}}{1 - \frac{i}{6\pi}\kappa^3 \alpha_{CM}} \tag{2.12}$$

where κ is wavevector, i is the imaginary part of the complex polarizability and α_{CM} represents the polarizability of Clausius-Mossotti's relation.

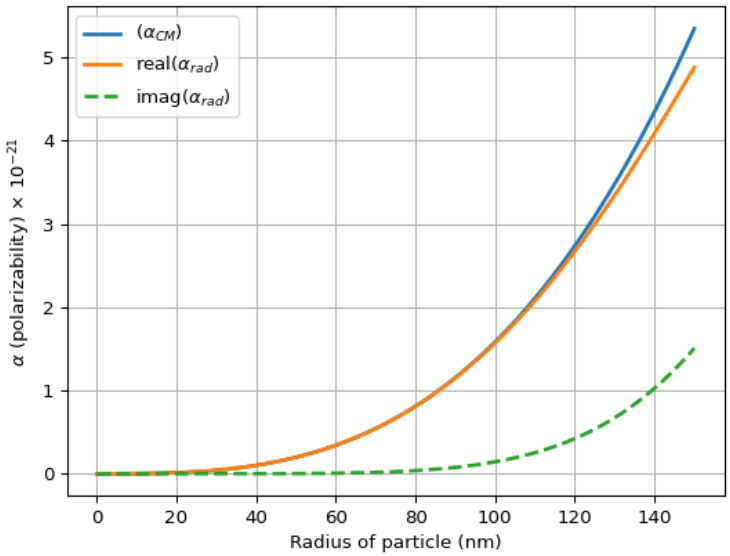

Figure 2.6: Polarizability of a dielectric particle in a water medium, comparing both Clausius-Mossotti relation (α_{CM}) and Draine approach (α_{rad}) for polarizability.

This thesis emphasizes the possibility of trapping dielectric particles rather than metal particles, therefore in Polarizability of dielectric particles we have not considered skin effect such as in case of metal particle, where the relationship for polarizability is different from what was stated above, particularly due to the skin effect phenomenon that limits the effective volume of the particle.

2.2.3 Maxwell stress Tensor (MST)

A general theory of optical stress on a particle or object by electromagnetic field can be solved using the MST, which is derived directly from Maxwell's equation and the Lorentz force law [64]. In an electromagnetic field, the force F acting on a body in a vacuum can be calculated by integrating the stress tensor over an enclosed surface S of the body using the divergence theorem, where the MST is defined as follows:

$$\overleftrightarrow{T} = [\varepsilon_0 EE + \mu_0 HH - \frac{1}{2}(\varepsilon_0 E^2 + H^2)\overleftrightarrow{I}], \tag{2.13}$$

where $\overleftrightarrow{I}$ is identity tensor, EE denotes the dyadic product.

Thèse accessible à l'adresse : https://theses.insa-lyon.fr/publication/2024ISAL0120/these.pdf © [C.B. Chander Bhan], [2024], INSA Lyon, tous droits réservés

$$\overleftrightarrow{T} = \begin{bmatrix} T_{11} & T_{12} & T_{12} \\ T_{21} & T_{22} & T_{23} \\ T_{31} & T_{32} & T_{33} \end{bmatrix} \tag{2.14}$$

where,
$T_{11} = \varepsilon_0(E_x^2 - E^2/2) + \mu_0(H_x^2 - H^2/2)$,
$T_{22} = \varepsilon_0(E_y^2 - E^2/2) + \mu_0(H_y^2 - H^2/2)$
$T_{33} = \varepsilon_0(E_z^2 - E^2/2) + \mu_0(H_z^2 - H^2/2)$
$T_{12} = \varepsilon_0 E_x E_y + \mu_0 H_x H_y$,
$T_{13} = \varepsilon_0 E_x E_z + \mu_0 H_x H_z$,
$T_{23} = \varepsilon_0 E_y E_z + \mu_0 H_y H_z$,
$T_{21} = T_{12}, T_{31} = T_{13}, T_{32} = T_{23}$

The time-averaged optical force is given as:

$$< F > = \oint_s < T > \dot{n} dS \tag{2.15}$$

The electromagnetic fields E_i and H_i $(i = x, y, z)$ in a tensor matrix can be numerically solved by using the FDTD or FEM. The MST is a mathematical formulation that describes stresses and forces within a material or system in terms of the electric and magnetic fields present in the system. However, it does not account for light's energy, momentum, or interactions with the medium. Therefore, it is only accurate in a vacuum.

This is a controversy that began in 1909 when Hermann Minkowski proposed that the momentum of light in a medium should be given by :

$$\rho = \frac{energy\ of\ the\ light}{speed\ of\ light\ in\ the\ medium} \tag{2.16}$$

A Minkowski stress tensor describes stresses and forces within a material or system in terms of energy and momentum. The model takes into account the energy and momentum of the light, as well as the interactions between the light and the medium. Thus, the Minkowski stress tensor provides a more accurate and complete description of optical forces acting on a particle in a medium [65, 66, 67, 68].

For a homogeneous body, the force acts only in the sphere's (particle) boundary layer. The volume force density f in a charge-free nonmagnetic medium, without electrostriction [3], is expressed as:

$$f = \frac{1}{2} E^2 \nabla \varepsilon \tag{2.17}$$

The Minkowski stress tensor is express as [69, 70]:

$$T_{ij} = \varepsilon_m E_i E_j^* + \mu_m H_i H_j^* - \frac{1}{2}(\varepsilon E_k E_k^* + \mu H_k H_k^*)\delta_{ij} \tag{2.18}$$

[3] Electrostriction is a property of all electrical non-conductors, or dielectrics, that causes them to change their shape under the application of an electric field

Thèse accessible à l'adresse : https://theses.insa-lyon.fr/publication/2024ISAL0120/these.pdf © [C.B. Chander Bhan], [2024], INSA Lyon, tous droits réservés

$$< F > = \int_V f dV = \oint_s < T > \dot{n} dS \tag{2.19}$$

The surface integration of equations 2.18 by 2.19 provides the optical force exerted on an object in a medium, where, ε_m and μ_m are the permittivity and permeability of the medium respectively; E_i and E_j are the components of electric field E, H_i and H_j are the components of magnetic induction field and δ_{ij} is the Kronecker delta.

The electromagnetic forces (optical forces in this case) calculated using COMSOL's built-in function rely on the Minkowski stress tensor by default to compute the internal and external pressure acting on a particle in the presence of an electromagnetic field. This approach has been validated in numerous studies, where COMSOL's Maxwell Stress Tensor (MST) function has been used to calculate optical forces on particles in water within various structures, such as rib [71] and strip waveguides [72], tapered strip waveguide [73] , and Y-branches [74].

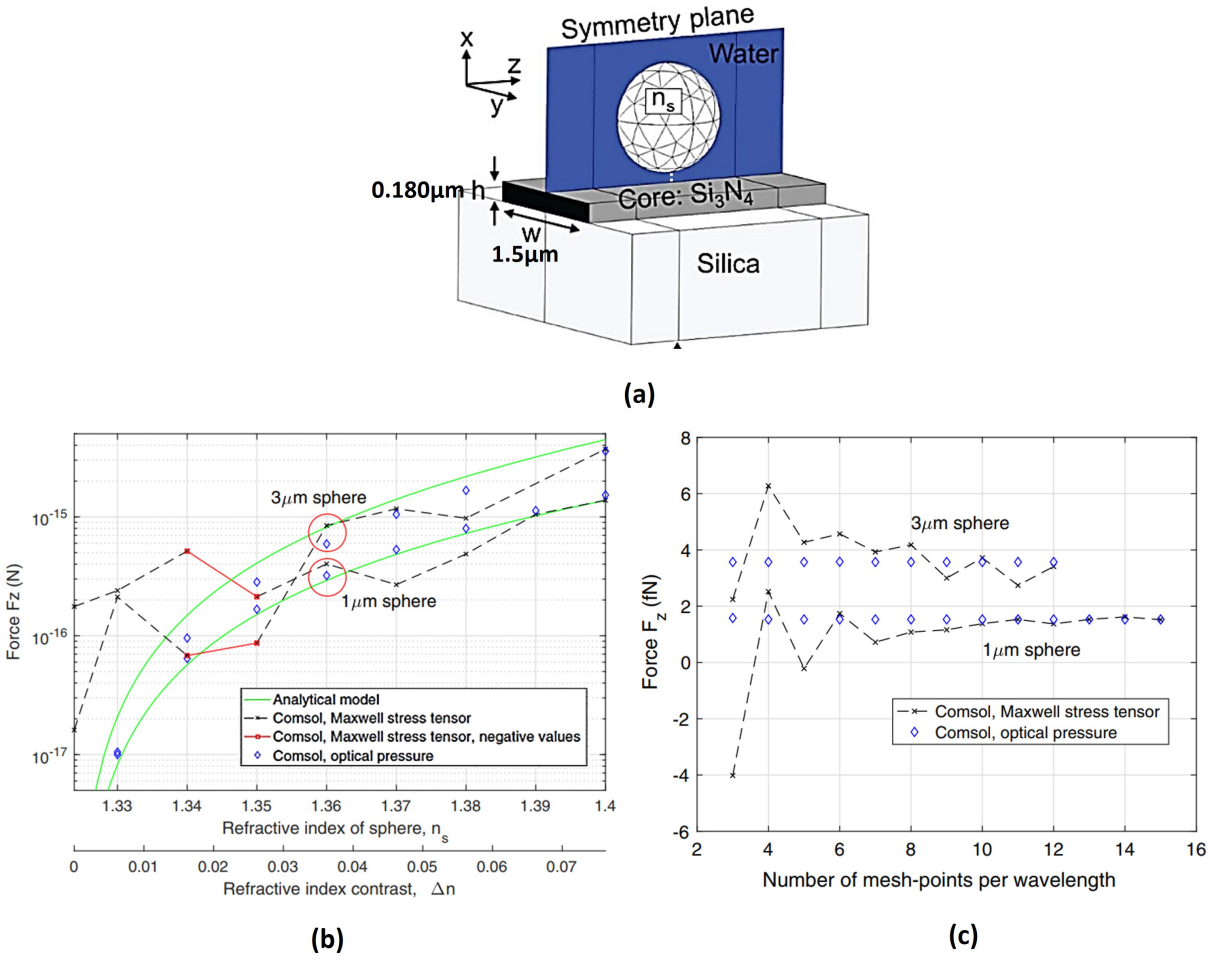

Figure 2.7: A comparison between COMOSL MST, Abraham-Minkowski stress tensor (optical pressure) , and Lorenz-Mie theory (an analytical model) model : (a) A COMSOL 3D model (b) radiation force F_z on 1 and 3 μm spheres for $1.3 < n_s < 1.4$ with $1\ mW$ of optical power in the TE mode and (c) radiation force as function of number of mesh element [75]

.

However, it is crucial to note that COMSOL's built-in function requires a significantly fine

Thèse accessible à l'adresse : https://theses.insa-lyon.fr/publication/2024ISAL0120/these.pdf © [C.B. Chander Bhan], [2024], INSA Lyon, tous droits réservés

mesh when the refractive index (RI) of the particle is close to that of the surrounding medium, as demonstrated in the work by Olav Gaute HellesØ [75]. In his paper, he compared three alternative methods : Maxwell stress tensor, Abraham-Minkowski stress tensor, and Generalized Lorenz-Mie theory (an analytical model) to calculate optical forces in water caused by the evanescent field of a Si_3N_4 waveguide for dielectric spheres of 1 and 3 μm in size . The Abraham-Minkowski surface pressure (optical pressure), which is derived using Equation 2.20, was implemented in COMSOL for comparison.

$$\sigma = -\frac{1}{4}\epsilon_0|E_t|^2(\varepsilon_m - \varepsilon_p) + \frac{|D_r|^2}{4\varepsilon_0}(\frac{\varepsilon_p - \varepsilon_m}{\varepsilon_m\varepsilon_p}) \tag{2.20}$$

where $D_r = \varepsilon_0\varepsilon_p E_r$, E_t and E_r are the tangential and radial components of E. ε_m and ε_p is the relative permittivity of the medium and the particle, respectively. The integration of the σ over the surface of the object gives the optical force exerted on the object.

As observed in Figure 2.7, COMSOL's MST built-in function can produce negative values for radiation forces when the refractive index of the particle is very close to that of the surrounding medium (e.g., water). However, increasing the mesh density can significantly enhance the accuracy of optical force calculations, as illustrated in Figure 2.7(c). In this study, since we are working with polystyrene dielectric particles with a refractive index of approximately 1.57, and given the availability of high-RAM computational resources, we employed COMSOL's built-in MST function for rigorous numerical calculations of optical forces.

Additionally, while the MST method can also be implemented in Lumerical Ansys using the Finite-Difference Time-Domain (FDTD) method, COMSOL offers a more versatile platform that enables the integration of other physical models, such as dielectrophoresis (DEP), which is important in our case. For this reason, we opted to continue our work using the COMSOL model. As a result, the COMSOL MST built-in function was employed for precise optical force calculations, while the DDA method will be used to approximate the optical forces on particles in the 100 nm range and for studies involving multiple points of optical force calculations to examine potential wells (detailed in Chapters 3 and 4).

When studying the external forces exerted on particles in a fluid, such as optical forces, it is also necessary to account for other forces that may influence particle trapping. These forces include viscosity, drag, and thermal forces. Proper consideration of these forces is essential to accurately calculate trapping forces and understand particle behavior. In the next section, we will explore the forces acting on a particle in a viscous liquid and how to overcome them to achieve stable optical trapping.

2.3 Displacement of particles in a viscous liquid

Once the optical forces have been expressed, we must study the particle's interaction with the fluid surrounding it and the influence of effects such as Brownian motion must be taken into consideration. To account for such effects, the equations must be extended to include the drag force, Brownian forces, and other thermal fluctuations. This will enable us to understand the particle's dynamics in a complex fluid environment. Throughout this section,

Thèse accessible à l'adresse : https://theses.insa-lyon.fr/publication/2024ISAL0120/these.pdf © [C.B. Chander Bhan], [2024], INSA Lyon, tous droits réservés

unless otherwise stated, the flow has been assumed to be steady, laminar, and Newtonian throughout.

2.3.1 Stokes Law

In a viscous liquid, particle displacement becomes more complex because it depends on both particle characteristics and flow characteristics. Based on the size of the objects, the support medium can be viewed either as a continuous or as a discontinuous fluid medium subject to statistical fluctuations. Aerosol physics has extensively studied these phenomena [76].

If we consider very large particles relative to the mean free path of water molecules($\approx 0.25\ nm$) at rest, we can write the fluid friction force exerted on a particle of radius a as follows:

$$\overrightarrow{F}_{viscous} = 6\pi a f_{kn} \eta \overrightarrow{v} \tag{2.21}$$

where η is the dynamic viscosity of the fluid, $\overrightarrow{v}$ is the velocity and coefficient f_{kn} describes the drag reduction on a particle due to the velocity slip at the interface. Milkian's expression [77] has been modified by Kim et al. [78] for nanoparticle aerosols to define this relation:

$$f_{kn} = \frac{1}{1 + Ak_n} \quad with \quad A = 1.165 + \exp\left(-\frac{0.997}{k_n}\right) \tag{2.22}$$

The Knudsen number (k_n) is very low for most of the nanoparticles in liquids.(e.g., $k_n = 0.05$ for $a = 5$ nm) The Knudsen coefficient for most of the Rayleigh nanoparticle is equal to 1.

2.3.2 Surface viscosity

There are deviations from Stokes' law due to the presence of a surface at a finite distance from the particle. An example of this surface would be the wall of a chamber, a guide, or the surface of another particle as illustrated in Figure 2.8. In this case, the stokes' formula can be generalized by defining an effective viscosity (η) depending on the viscosity of the liquid (η_0), the diameter of the particle (a), and distance from the surface (h).

$$\eta = \eta_0[1 - \frac{9}{16}(\frac{a}{h}) + \frac{1}{8}(\frac{a}{h})^3 - \frac{45}{256}(\frac{a}{h})^4 - \frac{1}{16}(\frac{a}{h})^5] - 1 \tag{2.23}$$

When the distance between the particle and the surface is comparable to the particle's radius, the surface viscosity plays a significant role. The effective viscosity of a spherical particle placed over a microscope slide is about three times greater than that of the fluid.

2.3.3 Brownian Motion

Microscopic objects are also subject to thermal forces in addition to the effects of fluid friction. Brownian motion is a continuous and disorderly displacement of particles within a liquid that was discovered in 1827. This movement results from the collisions of the molecules composing the liquid on the particle.

Thèse accessible à l'adresse : https://theses.insa-lyon.fr/publication/2024ISAL0120/these.pdf © [C.B. Chander Bhan], [2024], INSA Lyon, tous droits réservés

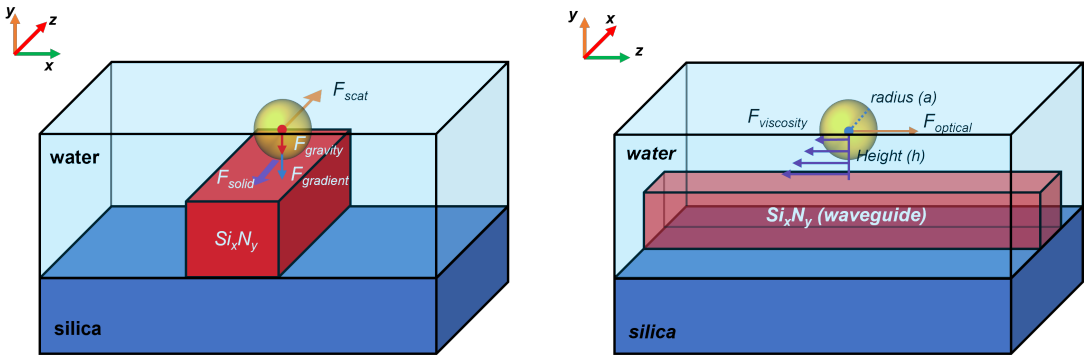

Figure 2.8: Force exerted on a particle: (a) solid friction with reference to both optical forces exerting on a particle. (b) illustrates the fluid friction forces with reference to optical forces. In the vicinity of the surface, the viscosity increases as the particle approaches it. (redrawn from Stéphanie gaugiran's thesis [79]).

To overcome Brownian motion, it is necessary to maintain a strong optical gradient force, i.e., high enough to reach a potential energy (10 K_BT) greater than three times the Brownian motion kinetic energy in each degree of freedom (1/2 K_BT), as per the rule of thumb described by Ashkin [45]. Using U_{grad} as the potential energy of the gradient force, T as the medium temperature, and K_B as the Boltzmann constant, the condition of trapping in the x direction can be written as follows [80, 81]:

$$\exp \frac{-U_{grad}}{K_BT} << 1 \quad with \quad U = \int_0^{\infty} F_{grad}(x)dx \tag{2.24}$$

Integrating the F_{grad} to infinity would lead to an infinite potential, which is unrealistic in any scenario. Therefore, infinite in the integration above Equation 2.24 of gradient forces to find the potential energy, refers to the 1/e of the maxima of the evanescent field.

Throughout the preceding discussion, we have assumed that the particle's motion is disturbed only by fluid friction (viscosity) and Brownian motion. There is also the possibility of solid friction[4] playing a role. It is apparent that forces acting perpendicularly to a waveguide, such as gradient forces, gravity, or Archimedes thrusts, solid friction can be generated on the waveguide surface as a result.

Consequently, the particle may be slowed down or may roll on the guide's surface. Also, a very thin layer of liquid underneath the particle might limit these effects. In all the theoretical approaches, we will not consider the influence of solid friction on particle displacement as a first approximation. When interpreting the experimental results, we will, however, take care not to overlook them.

[4]solid friction: static friction, sliding friction, rolling friction

Thèse accessible à l'adresse : https://theses.insa-lyon.fr/publication/2024ISAL0120/these.pdf © [C.B. Chander Bhan], [2024], INSA Lyon, tous droits réservés

2.4 Modelling Methods

In this thesis, the modeling and simulation of integrated photonic components such as rectangular waveguides, optical trapping studies, sensitivity analyses, and bending modes are essential for designing and optimizing photonic devices. With the expanding research in integrated photonic platforms, numerous analytical, semi-analytical, and numerical methods have been developed to solve optical waveguide problems, including the Effective Index Method [82, 83], Marcatili's Method [84], Finite Difference Time Domain (FDTD) [85], Finite Element Method (FEM) [86], Finite Difference Eigensolver (FDE) and Fully Differential and Fully vectorial (FDFV) [87, 88], Mode-Matching Method [89], and Method of Moments (MoM) [90], among others. These different methods are thoroughly explained and compared in the literature [91, 92, 93]. These methods offer varying levels of accuracy, computational efficiency, and ease of implementation. In the next chapter, we describe several analytical approaches to provide insights into the key parameters that must be understood for effective modeling.

This section provides concise and summarized tables of the key methods used in the simulations for our various studies. The Table 2.2 presents a brief overview of the FDTD, FEM, FDM, FDFV, and Marcatili's approach, along with their advantages, disadvantages, and the specific cases where they were applied.

Method	**Advantage**	**Disadvantage**	**use in this study**	**Tools**
FDTD	High accuracy, can be used for 1D, 2D and 3D structures	High computational intensive	Inverted tapers, coupling section in MRRs	Lumerical
FEM	Flexible, high accuracy	High computational resource requirement	Optical trapping study	COMSOL
FDE	2D solver, rectangular mesh	Medium computational time	Potential well depth study for evaluation of minimum optical forces and power	integrated with Lumerical API and python function
Marcatili's approach	Simple, easy to use	rectangular geometries only	Directional couplers	scripted in Python
FDFV	2D solver with averaging at boundaries, Transparent boundary conditions	provide beta guess	Strip, slot, HPWG optical modes, Bending modes, optical forces	Scripted in MATLAB [87]

Table 2.2: Comparison table for modelling methods utilized in this thesis

Thèse accessible à l'adresse : https://theses.insa-lyon.fr/publication/2024ISAL0120/these.pdf © [C.B. Chander Bhan], [2024], INSA Lyon, tous droits réservés

2.5 Optical waveguide Structure

In our previous sections, we explained what is the optical force and how near-field optical trapping could be more beneficial than far-field optical trapping and what methods researchers have deployed to evaluate optical trapping, and how fluid dynamics is concerned with optical trapping. In this section, we will review various different waveguide structures, such as dielectric strip, slot, and hybrid plasmonic waveguides that we examined in this thesis to enhance the optical forces.

2.5.1 Dielectric – strip or ridge waveguide

The basic structure of a dielectric strip waveguide consists of a longitudinally extended high index optical medium, called the core, which is transversely surrounded by low-index media, called the cladding. A guided optical wave propagates in the waveguide along its longitudinal direction. The most straightforward structure used for optical trapping in near-field optical manipulation is a strip waveguide. The Figure 2.9 shows the schematic diagram of a strip waveguide along with the evanescent field profile at the center of the waveguide along x-axis that will be studied in this thesis.

The electromagnetic wave propagates in the waveguide according to field distributions that we call guided modes or simply modes. Each mode is characterized by an effective refractive index (n_{eff}) given by the ratio between the phase velocity of the mode and the vacuum. The number of guided modes in a guide depends on the geometry of the core and the optical refractive indexes (n) of the materials. The mode is confined when $n_{core} > n_{eff} > n_{substrate}$. Depending on the main component of the magnetic and electric field of a mode in the plane normal to the direction of propagation, it is characterized by its transverse magnetic (TM) or transverse electric (TE) polarization. The largest proportion of the light energy is normally confined in the core, unless the mode is very close to the cut-off ($n_{substrate}$). In the cladding, the amplitude of the evanescent field decreases exponentially with the distance from the interface between the core and cladding.

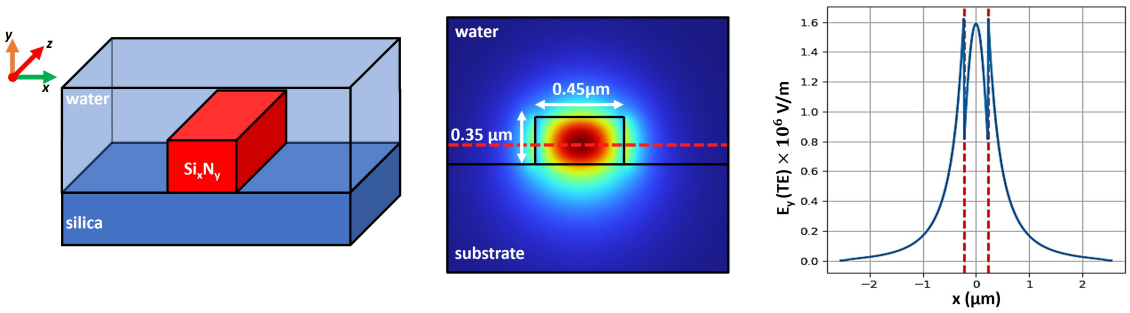

Figure 2.9: Strip waveguide: (a) schematic diagram of strip waveguide (b) TE field profile (c) Field values at center of the waveguide (dashed red line on picture (b)) along the x-axis

In our study, the particles will be introduced into deionized water as a cladding medium. As the evanescent field interacts with the particles, the mode effective index changes, and this can be studied using interferometers or resonators. In addition, adequate gradient force is

Thèse accessible à l'adresse : https://theses.insa-lyon.fr/publication/2024ISAL0120/these.pdf © [C.B. Chander Bhan], [2024], INSA Lyon, tous droits réservés

necessary to overcome the Brownian motion of the particle, which depends on the gradient of the field in the cladding.

The greater the difference between the index of the core and cladding, the sharper the gradient will be. In order to increase the gradient of the field in a strip waveguide, one approach is to use high-index core waveguides rather than low-index core waveguides (discussed in chapter 3). Another approachable method is by slot waveguides.

2.5.2 Slot waveguide

A optical slot waveguides were first discovered in 2004 at Cornell University [94]. They are composed of two strip waveguides with a narrow gap in between. Figure 2.10 indicates that the highest electric field is confined within the gap. If the two interfaces are sufficiently close, both electric fields profile in the low-index media interacts to create a guided mode.

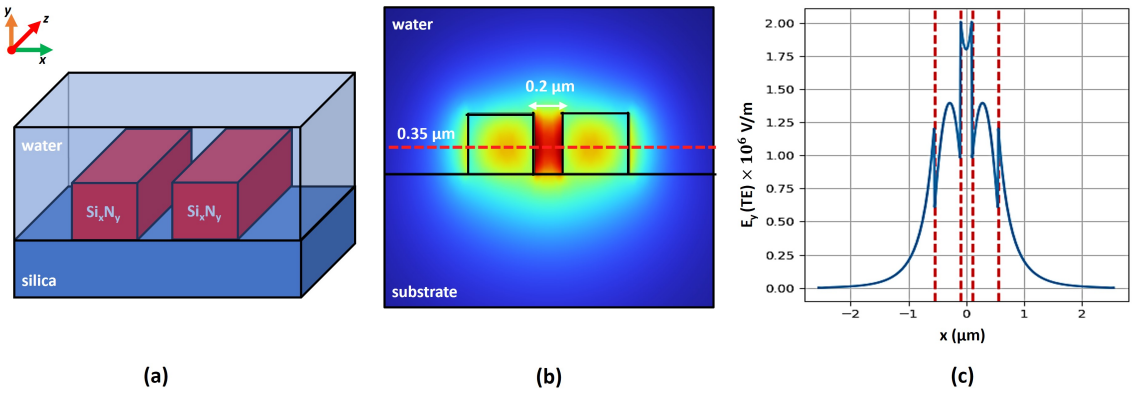

Figure 2.10: slot waveguide: (a) schematic diagram of slot waveguide (b) TE field profile (c) Field values at center of the waveguide (dashed red line on picture (b)) along the x-axis

A strong electric field exists in the lower index region only if the gap is very narrow (≈ 100 nm for a waveguide with a Si_xN_y and a cladding H_2O, at 1.31 μm [95]). In comparison to strip waveguides, slot waveguides provide a significantly greater evanescent field gradient in the cladding to interact with the analyte, but with a limited interaction area due to the narrow gap. This could be a constraint for our study.

2.5.3 Hybrid plasmonic waveguide

There are two types of surface plasmons:

1. **Surface plasmon polariton (SPP)** : They are electromagnetic excitations propagating along metal-dielectric interface, with evanescent field decaying perpendicularly on either side [96]. They are only confined in 1D and, as such, have a continuous frequency spectrum. The decay length is comparatively longer.

2. **Localized surface plasmon resonance (LSPR)** : This concept can be defined as collective electron charge oscillations on a metallic surface which are excited by light.

Thèse accessible à l'adresse : https://theses.insa-lyon.fr/publication/2024ISAL0120/these.pdf © [C.B. Chander Bhan], [2024], INSA Lyon, tous droits réservés

The decay length is comparatively shorter. LSPR confines modes in all three dimensions in a metal nanostructure.

There are two major reasons why we are interested in propagating plasmonic modes in this thesis. The LSPR mode has a sharp gradient but a small trapping volume. Using an SPP can produce long-range trapping, which can be useful for trapping particles over larger distances.

Hybrid plasmonic waveguides (HPWG) are produced by coupling between a dielectric mode and an SPP. If a dielectric and a plasmonic guide are sufficiently close to each other, the combined structure supports TE and TM supermodes whose properties can combine the advantages of both guides individually.

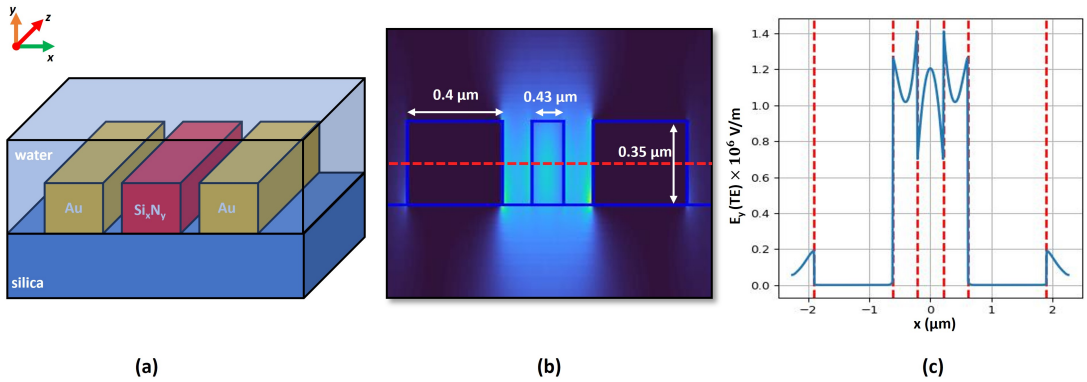

Figure 2.11: Hybrid Plasmonic waveguide: (a) schematic diagram of HPWG waveguide (b) mode field profile (c) Field values at center of the waveguide (dashed red line on picture (b)) along the x-axis

Figure 2.11.(a), illustrates the schematic diagram represents HPWG using the “mode-lift” concept [97] where a narrow core dielectric waveguide (0.430 μm) that is designed to only support radiation modes is between two metal walls so that the plasmonic modes at the metal/dielectric interfaces increase the effective refractive index of the hybridized mode, resulting in an overall guided mode (supermode). This concept allows to increase the gap ($\approx$ 400 nm) between dielectric and metal walls and provide an increased interaction volume with the analyte, resulting in high sensitivity (results for sensitivity and optical trapping are shown in chapter 3).

Furthermore, plasmonic trapping can enhance optical force by overcoming the classical diffraction limit. Using HPWG for the ring resonators cavities can lead to adequate quality factor with high sensitivity and high optical trapping comparatively to other waveguides structures mentioned above.

Based on the literature, the following Table 2.3 compares the different waveguide structures used to study the optical forces on dielectric polystyrene particles. The optical forces ($\approx 100\ pN/\mu m/mW$) by hybrid plasmonic structures are much higher than other waveguide structures. To achieve these forces in this study [98], they minimized the gap between the plasmonic metal and dielectric structure down to 20 nm. This introduced high losses of 1 dB/μm in the device. Moreover, the narrower gap such as 20 nm doesn’t allow to introduce the particle with size of 100 nm inside the gap.

Thèse accessible à l'adresse : https://theses.insa-lyon.fr/publication/2024ISAL0120/these.pdf © [C.B. Chander Bhan], [2024], INSA Lyon, tous droits réservés

waveguide type	waveguide materials	particle material, size	optical force / stiffness
Rib-pair array [99]	silicon	Polystyrene, 200 nm	$\sim 55\ pN/W$
Rib waveguide [72]	silicon nitride	glass, 500 nm	$\sim 153\ pN/W$
Slot waveguide (g = 100 nm) [100]	silicon	DNA, Polystyrene, 100 nm	$\sim 25\ pN/W$
Plasmonic strip [33]	gold	Polystyrene, 1 or $2\mu m$	$\sim 1.7\ pN/\mu m$
Hybrid plasmonic (gap = 20 nm) [98]	dielectric and gold	measured w.r.t thermomechanical noise and normalized to optical forces	$\sim 100\ pN/\mu m/mW$

Table 2.3: Optical forces in different waveguide structures

It is also important to note that optical forces in waveguide structures are influenced by the optical power coupled to them. As the power increases, the forces increase as well. In resonator cavities, the confined wavelength accumulates intensity over multiple round trips as a result of constructive interference. This results in a higher power in the cavity than in the waveguide that couples the light. Power in the cavity is directly related to the cavity's quality factor Q.

2.6 Resonant Cavity Enhancement

During our studies, we considered the ring resonator to be a cavity for trapping dielectric particles. Therefore, the theory is discussed with reference to the ring resonator, but it is important to note that cavity perturbation theory applies to all cavities similarly, except that formulas may vary based on their structural configuration.

For nanoparticle trapping, resonant devices such as ring resonators, photonic crystals, and Fabry–Pérot (FP) cavities are preferred due to their strong field enhancement and spatial confinement. The enhancement factor of resonant cavities scales with the ratio of the quality factor (Q) to the mode volume (V), denoted as Q/V [101]. High-Q nano-cavities with small mode volumes are particularly promising for optical trapping. An insightful comparison of Q/V for different cavities is illustrated in Figure 2.12.

Plasmonic cavities offer tight confinement and extremely low mode volumes, making them suitable for trapping very small nanoparticles. However, their evanescent fields are confined to highly localized regions, which limits their applicability in scenarios where a large concentration of trapped particles is required, such as in this thesis. On the other hand, photonic cavities like microring resonators (MRRs) offer significant advantages over plasmonic cavities, particularly in terms of integration with industrial CMOS platforms. MRRs

Thèse accessible à l'adresse : https://theses.insa-lyon.fr/publication/2024ISAL0120/these.pdf © [C.B. Chander Bhan], [2024], INSA Lyon, tous droits réservés

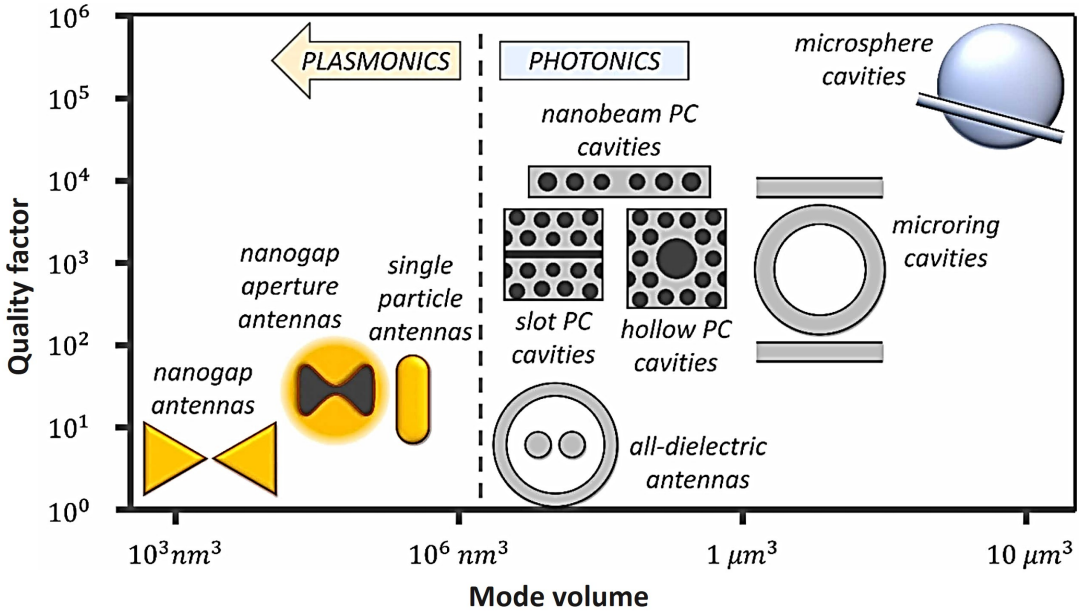

Figure 2.12: Various types of photonic and plasmonic resonators used for the optical trapping of nanomaterials, represented on a graph as a function of the resonant mode volume scale and the quality factor of the resonance [102].

can be seamlessly integrated with other optical components like modulators, detectors, and multiplexers, which is crucial for lab-on-chip systems and optofluidics.

The Table 2.4 below provides a comparison of optical forces obtained from various resonant cavities used in photonic devices. Photonic crystal cavities, due to their high quality factor (Q-factor) and small mode volume, exhibit stronger optical forces compared to ring resonators. However, achieving such high Q-factors in photonic crystal cavities is challenging in practice. Fabrication complexities, limited tuning ranges, sensitivity to imperfections, and difficulties in coupling light in and out of the cavities make photonic crystal cavities less practical for our application. Moreover, enhancing the quality factor of microring resonators (MRRs) by employing low-loss waveguides and minimizing bending losses presents a more feasible solution. For these reasons, we chose MRRs for this thesis.

The next section introduces two fundamental types of MRRs along with key spectral characteristics and parameters that are critical for MRR performance.

2.7 Ring resonators Spectral characteristics

The two most common configurations for optical ring resonators are all-pass and add-drop. The add-drop configuration could be used to trap and transport a particle in optical trapping, but this isn't the goal of the study. Further, it is possible to achieve a high extinction ratio (ER) by using add-drop configurations with a trade-off to the Q-factor. The all-pass ring resonator will be the focus of our study. Figure 2.13 illustrates both ring resonators configuration.

In ring resonators, the resonant wavelengths of light are [107]:

Thèse accessible à l'adresse : https://theses.insa-lyon.fr/publication/2024ISAL0120/these.pdf © [C.B. Chander Bhan], [2024], INSA Lyon, tous droits réservés

cavities type	waveguide material	particle: material, size	optical force / stiffness
Photonic crystal (guided mode) [103]	silicon	polystyrene, 520 nm	$\sim 500\ pN/W$
Photonic crystal (defect mode) [104]	silicon	polystyrene, 100 nm	$\sim 700\ pN/W$
Nanobeam cavity [105]	silicon	polystyrene, 100 nm	$\sim 300\ pN/W$
Ring resonator [28]	silicon	polystyrene, 1.1 μm	$\sim 150\ pN/W$
Ring resonator (add-drop) [106]	Si_xN_y	polystyrene, 1 μm	N/A

Table 2.4: Optical forces in Photonic cavities

$$\lambda_r = \frac{n_{eff}L}{m} \tag{2.25}$$

where λ_r is resonance wavelength, n_{eff} is the effective index of the cavity, L is optical path length and m is the azimuthal order. The azimuthal order is the integer corresponding to the resonance mode order.

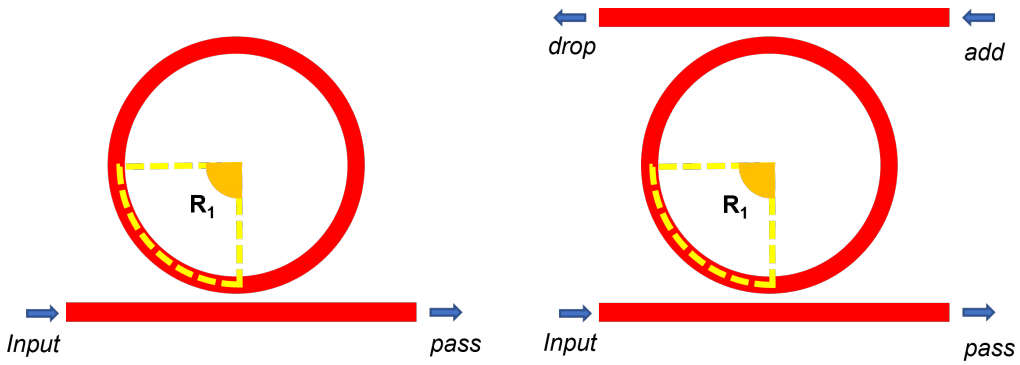

Figure 2.13: Micro-ring resonator common configurations

The distance between these resonances is determined by the Free Spectral Range (FSR), which depends on the length of the resonator.

$$FSR = \frac{\lambda^2}{n_g L} \tag{2.26}$$

where λ is the operating wavelength, n_g is the group index and $n_{eff}L$ is the optical path length of the ring resonator cavity.

The n_g corresponds to the relation with c/v_g which represents the velocity at which the envelope of the propagating pulse travels and is a characteristic of the dispersive medium or a waveguide[107]. In our study, we will work two types of rings: circular and racetrack ring resonator. The optical length for circular ring is defined by, $n_{eff}L = n_{eff}^{bend}(2\pi r_{bend})$ and for racetrack ring resonators is, $L = n_{eff}^{straight}(2(L_1 + L_2)) + n_{eff}^{bend}(2\pi r_{bend})$.

Thèse accessible à l'adresse : https://theses.insa-lyon.fr/publication/2024ISAL0120/these.pdf © [C.B. Chander Bhan], [2024], INSA Lyon, tous droits réservés

For the purpose of analyzing the performance of devices such as lasers, amplifiers, and detectors, two critical parameters are the 3 dB bandwidth, also known as Full Width Half Maximum (FWHM), and the quality factor (Q-factor). The FWHM is defined as the width of the resonance peak at half of its maximum amplitude. A detector with a smaller FWHM has a higher signal-to-noise ratio, making it more sensitive than one with a larger FWHM. In this thesis, we opted for a simpler design and focused our studies on all-pass ring resonators. For all-pass ring resonators, the FWHM is defined as:

$$FWHM = \frac{(1-\tau a)\lambda_{res}^2}{\pi n_g L \sqrt{\tau a}} \tag{2.27}$$

where τ is the self-coupling coefficient, a is round trip loss coefficient. The Q-factor, or quality factor, of a resonator is a measure of its damping or energy loss. It is defined as the ratio of the stored energy to the energy lost per cycle. A high Q-factor indicates low damping and a narrow resonance, while a low Q-factor indicates high damping and a wide resonance. In the case of a ring resonator, the Q-factor is a measure of the resonant behavior of the optical mode in the ring. It is related to the confinement of the light in the ring and losses of the resonator. The quality factor is expressed as :

$$Q = \frac{\lambda_{res}}{FWHM} \tag{2.28}$$

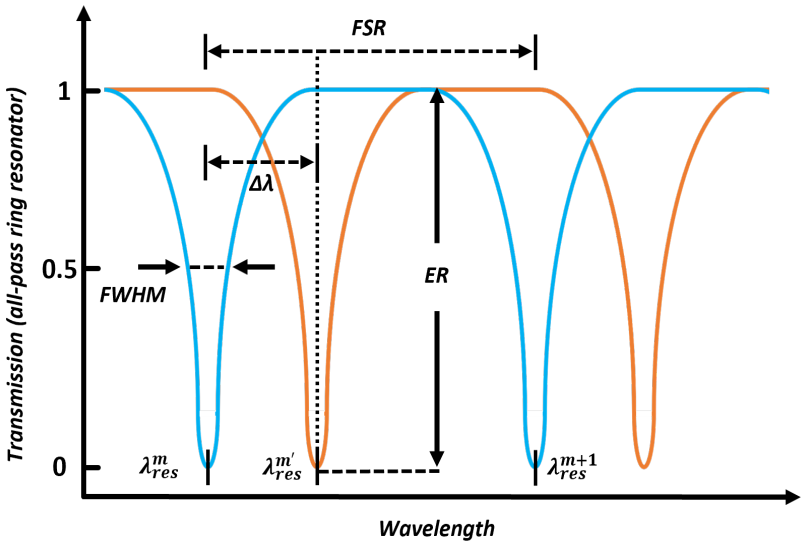

Figure 2.14: The transmission of an all-pass ring resonator with significant parameters. The orange curve represents the transmission without perturbation, and the blue curve represents a shift due to a refractive index change during perturbation.

Most often in case of sensors, the Q-factor is chosen to be as high as possible to have a steep slope in the resonance response which is related to the smallest detectable shift (also known as theinferior limit of detection). High Q-factor also helps to maximize the optical trapping power, it is therefor a very pertinent to study in the present context.

The contrast of the resonance peaks is examined by on-off Extinction Ratio (ER), which refers to the ratio of the minimum transmission R_{min} to the maximum transmission T_t

Thèse accessible à l'adresse : https://theses.insa-lyon.fr/publication/2024ISAL0120/these.pdf © [C.B. Chander Bhan], [2024], INSA Lyon, tous droits réservés

through the resonator when it is in the “on” state (resonant) and the “off” state (non-resonant). This ratio is used to quantify the quality of the resonator and its ability to selectively transmit a specific wavelength of light while rejecting others.

$$Q = \frac{T_t}{R_{min}} = \frac{(\tau + a)^2(1 - \tau a)^2}{(\tau - a)^2(1 + \tau a)^2} \tag{2.29}$$

2.8 Conclusion

In this chapter, we provided a foundational understanding and physical insights into the concept of optical forces in integrated photonic components by presenting a brief history and theory of optical forces, along with the computational methods used for their analysis. Through a comparative analysis of different computational methods, we concluded that the Discrete Dipole Approximation (DDA) is an effective analytical approach for providing fast and accurate solutions, particularly for potential well depth studies to overcome Brownian motion in fluid environments. In addition, the numerical Maxwell Stress Tensor (MST) method, based on the Finite Element Method (FEM) in COMSOL, offers rigorous calculations of optical forces, which are beneficial for studying different optical waveguide structures, such as strip, slot, and hybrid plasmonic waveguides.

Furthermore, in this chapter, we examined particle interactions with the surrounding fluid to understand the influence of other forces, such as Brownian motion, drag forces, and thermal fluctuations, which can affect optical forces. We also provided a comparison table with a brief introduction to the different modeling tools used in our studies, highlighting their advantages and disadvantages. Further, we explained the basic concepts, working principles, and optical modes of different waveguide structures that will be studied in this thesis to compare them in terms of the optical forces achieved in the state-of-the-art literature. Finally, we discussed how cavity perturbation approaches can enhance optical forces through field enhancement and spatial confinement, and we provided a comparison of optical trapping of dielectric particles using photonic cavities such as photonic crystal (PhC) cavities and microring resonators (MRRs). Due to fabrication complexity and limited tuning ranges of other cavities, we opted to focus on MRRs.

In conclusion, this chapter serves as a reference for the modeling methods related to the core physical phenomenon of “optical trapping” utilized in this thesis, as well as other modeling techniques for designing the fundamental building blocks of the final device. It provides a comprehensive conceptual understanding of the physics and models employed in Chapters 3 and 4, along with the state-of-the-art literature.

Thèse accessible à l'adresse : https://theses.insa-lyon.fr/publication/2024ISAL0120/these.pdf © [C.B. Chander Bhan], [2024], INSA Lyon, tous droits réservés

Thèse accessible à l'adresse : https://theses.insa-lyon.fr/publication/2024ISAL0120/these.pdf © [C.B. Chander Bhan], [2024], INSA Lyon, tous droits réservés

Chapter 3

Modeling and Analysis of Photonic Integrated Circuit components

In this chapter, we will develop an understanding of the modeling of the basic building blocks in photonic integrated circuits (PIC) that we will design in Chapter 4. From Chapter 2, we have acquired knowledge on PIC components that can be used in the design of our final device. Therefore, in this chapter, we will use the models developed in this thesis to explore various components such as different types of waveguides: strip, slot, Hybrid plasmonic waveguide (HPWG), Higher order modes (HOM), etc. These components will be compared in terms of optical trapping and sensitivity to select the most suitable one for the final device design. The chapter is divided into three sections. First, "Basic Knowledge on Physics and Modeling" describes the fundamental concepts and knowledge required to begin modeling, as well as the tools we will use. Second, "Modeling of Optical Trapping and Sensitivity" presents the modeling results of each device studied in the thesis, including a discussion of the final device, i.e., Micro-ring resonators (MRRs). Lastly, "Concluding and Perspective to Design" offers a summary and future outlook for the design.

3.1 Basic Knowledge on Physics and Modeling of Waveguide

3.1.1 Electromagnetic analysis of a Waveguide

A Waveguide is a sophisticated medium designed to transmit or guide light. Consider an optical fiber with a core surrounded by cladding as shown in Figure 3.1. The Refractive index (RI) of both the core and the cladding in x and y-axes are uniform along z-axis and it's denoted by n_{core} & n_{clad}, respectively. Light will be guided by the core if $n_{core} > n_{clad}$.

Furthermore, light can be confined in two dimensions (2D) or one dimension (1D) using non planar and planar waveguides, respectively. In planar waveguides or films, light is confined in one transverse direction, such as in slab waveguides where the core is sandwiched between two cladding materials, and light propagates in the lateral direction. Conversely, in non-planar waveguides, light is confined in two transverse directions, as seen in optical

Thèse accessible à l'adresse : https://theses.insa-lyon.fr/publication/2024ISAL0120/these.pdf © [C.B. Chander Bhan], [2024], INSA Lyon, tous droits réservés

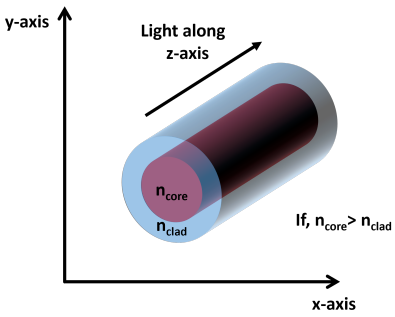

Figure 3.1: An optical fibre with high index material (n_{core}) surrounded by low index material (n_{clad})

fibers or channel waveguides. Moreover, some non-planar waveguides lack an analytical solution. To find solutions for complex geometries waveguides, we employ numerical methods such as the Beam propagation method (BPM) [108]. However, there are some approximation methods that will be discussed later in this section for simple dielectric rectangle waveguide. Figure 3.2 illustrates the various waveguide structures categorized under both planar and non-planar waveguides.

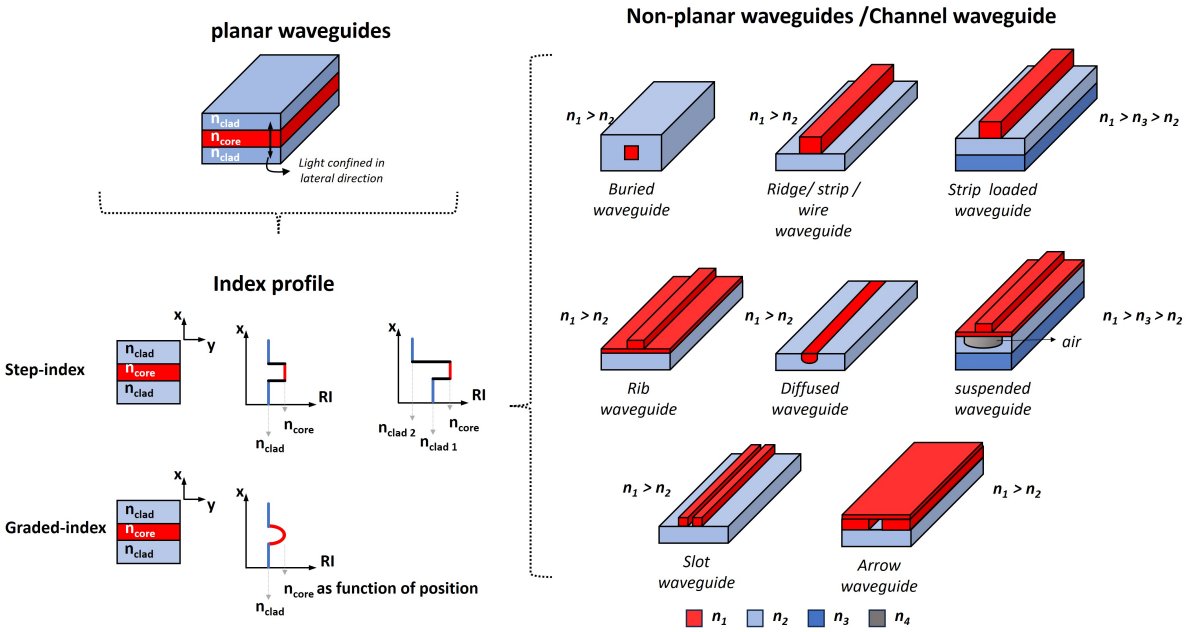

Figure 3.2: Types of common planar and non-planar waveguide structure

The propagation of light or energy flow in a waveguide can be characterized through modes. These modes are the characteristic solutions or transverse field patterns whose amplitude and polarization remain constant along the direction of propagation. A guided mode can only exist when a transverse resonance condition is satisfied, resulting in the repeatedly reflected wave having constructive interference with itself.

Consider a slab waveguide as shown in Figure 3.2. The wave inside the core will be totally reflected at the interfaces between n_1/n_2 and n_1/n_3 if the angle of incidence (θ) is greater than θ_2 and θ_3. This is commonly referred to as Total internal reflection (TIR). During this back-and-forth reflection of light, the wavefront will also be moving. For the energy to flow

Thèse accessible à l'adresse : https://theses.insa-lyon.fr/publication/2024ISAL0120/these.pdf © [C.B. Chander Bhan], [2024], INSA Lyon, tous droits réservés

through the waveguide, these wavefront must constructively interfere with themselves, thus forming a guided mode.

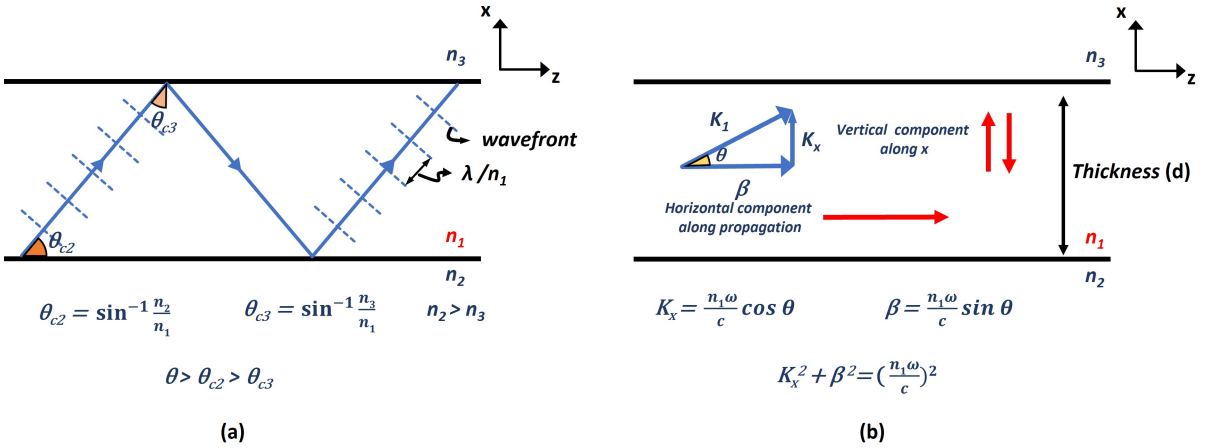

Figure 3.3: TIR Condition & K Vector Triangle: (a) TIR condition for propagating light in a slab waveguide, and (b) K vector triangle establishing the relationship between β and K_x, where β is the propagation constant along the z-direction, and K_x is the vertical propagation component along the x-direction.

Let's define the wavevector as it propagates through the waveguide using the K-vector triangle illustrated in Figure 3.3. The K-vector triangle helps to establish the relationship between the orthogonal component of the propagation constant (β) or horizontal or longitudinal component along the z-axis and transverse or vertical component K_x along x-axis with up/down creating a constructive interference. As we know when light travels from point A to B it accumulates phase shift. Therefore, the total phase shift for constructive interference of the optical field path will be equal to $2m\pi$ and equation will be :

$$2k_1 d cos\,\theta + \phi_2(\theta) + \phi_3(\theta) = 2m\pi \tag{3.1}$$

where the first term $2k_1 d cos\theta$ defines the phase shift due to two interface layer n_1/n_2 and n_1/n_3. $k_1 = \frac{n_1\omega}{c}$ is the wavevector of n_1 with angular frequency of ω and c as a speed of light. $\phi_2(\theta)$ and $\phi_3(\theta)$ is the phase shift between two interface of n_1/n_2 and n_1/n_3 respectively as function of θ.

As we know, phase shifts are dependent on polarization or electric field polarization. There are two types of polarization: Transverse Electric (TE) and Transverse Magnetic (TM). In TE polarization, the electric field (E) is parallel to the film plane (E_x = 0) whereas in TM polarization, the magnetic field (H) is parallel to the film plane (H_x = 0). It can be observed that with different polarization's, the phase shift is not the same for both TE and TM. Therefore, TE and TM waves will differ, and the guided mode solutions will be discrete.

Wave equation, field equation, Mode solution

To enhance the understanding on modes solution and how does modes shape evolves as it propagates, it's important to comprehend the mathematical equations starting from the 4

Thèse accessible à l'adresse : https://theses.insa-lyon.fr/publication/2024ISAL0120/these.pdf © [C.B. Chander Bhan], [2024], INSA Lyon, tous droits réservés

Maxwell equations defined below 3.2, 3.3 , 3.4, 3.5. Consider a linear, isotropic waveguide with dielectric constant spatially dependent.

$$\nabla \cdot \varepsilon E = 0 \tag{3.2}$$

$$\nabla \cdot H = 0 \tag{3.3}$$

$$\nabla \times E = -\mu_0 \frac{\partial H}{\partial t} \tag{3.4}$$

$$\nabla \times H = -\varepsilon \frac{\partial E}{\partial t} \tag{3.5}$$

As in isotropic medium the $\varepsilon(x, y)$ is spatially dependent. so the 3.2 will become 3.6.

$$\nabla \cdot E = -\frac{\nabla \varepsilon}{\varepsilon} \cdot E \tag{3.6}$$

By using 4 Maxwell Equations 3.2, 3.3 , 3.4, 3.5 together with equation 3.6 and vector identity double cross product ($\nabla \times \nabla \times = \nabla\nabla \cdot - \nabla^2$) and the temporal derivative is removed thanks to the plane wave decomposition in term of exp($j\omega t$) or exp(-$j\omega t$). we will have the 2 propagation equations :

$$\nabla^2 E + k^2 E = -\nabla(\frac{\nabla \varepsilon}{\varepsilon}.E) \tag{3.7}$$

$$\nabla^2 H + k^2 H = -\frac{\nabla \varepsilon}{\varepsilon} \times \nabla \times H \tag{3.8}$$

For a TE mode, $\nabla\varepsilon \perp E$ and the index profile of a step-index waveguide is piece-wise constant illustrated in Figure 3.2. so, we can write the homogeneous wave equation separately for each region as the $\nabla\varepsilon$ = 0 for each region. That means the waveguide mode whose amplitude and polarization profile will remain constant along the longitudinal z coordinate. Therefore, the electric and magnetic field of a mode will be written as :

$$E(r, t) = \mathcal{E}(x, y) \exp(\mathrm{i}\beta z - \mathrm{i}\omega t) \tag{3.9}$$

$$H(r, t) = \mathcal{H}(x, y) \exp(\mathrm{i}\beta z - \mathrm{i}\omega t) \tag{3.10}$$

where, $\mathcal{E}(x, y)$ and $\mathcal{H}(x, y)$ are the mode field profiles, and β is the propagation constant of the mode. Using equation 3.7,3.8, 3.9, 3.10 the longitudinal field component will become:

$$\frac{\partial^2 \mathcal{E}_z}{\partial x^2} + \frac{\partial^2 \mathcal{E}_z}{\partial y^2} + (k_i^2 - \beta^2)\mathcal{E}_z = 0 \tag{3.11}$$

Thèse accessible à l'adresse : https://theses.insa-lyon.fr/publication/2024ISAL0120/these.pdf © [C.B. Chander Bhan], [2024], INSA Lyon, tous droits réservés

$$\frac{\partial^2 \mathcal{H}_z}{\partial x^2} + \frac{\partial^2 \mathcal{H}_z}{\partial y^2} + (k_i^2 - \beta^2)\mathcal{H}_z = 0 \tag{3.12}$$

where, $k_i^2 = \omega^2 \mu_0 \epsilon_i = n_i^2 \frac{\omega^2}{c^2}$

Now, it's not necessary to solve for all the $\mathcal{E}_x, \mathcal{E}_y, \mathcal{H}_x, \mathcal{H}_y$ components because the transverse components can be found using $\mathcal{E}_z$, $\mathcal{H}_z$ with the help of boundary condition. So lets observe at a simple planar waveguide in x-y axis and the light is propagating in z-direction. so change in RI $\frac{\partial}{\partial y} = 0$ as its constant along the y -axis as shown in Figure 3.4.

Now in case of **TE mode** as discussed above $E_z = \mathcal{H}_y = 0$, $\frac{\partial \mathcal{H}_y}{\partial y} = 0$. Therefore, the only non-vanishing term would be $\mathcal{H}_x$, $\mathcal{E}_y$, $\mathcal{H}_z$ i.e. only one E non-vanishing field.

$$\frac{\partial^2 \mathcal{E}_y}{\partial x^2} + (k^2 - \beta^2)\mathcal{E}_y = 0 \tag{3.13}$$

where $k^2 = \omega^2 \mu_0 \epsilon(x) = \frac{\omega^2}{c^2} n^2(x)$,

using Equation 3.13 , the other $\mathcal{H}_x$, $\mathcal{H}_z$ will be equal to :

$$\mathcal{H}_x = -\frac{\beta}{\omega \mu_0} \mathcal{E}_y \tag{3.14}$$

$$\mathcal{H}_z = \frac{1}{i\omega\mu_0} \frac{\mathcal{E}_y}{\partial x} \tag{3.15}$$

Similarly, in case of **TM modes**, the non-vanishing term will be

$$\mathcal{H}_z = \frac{1}{i\omega\mu_0} \frac{\partial \mathcal{E}_y}{\partial x} \tag{3.16}$$

$$\mathcal{E}_x = \frac{\beta}{\omega \epsilon} \mathcal{H}_y \tag{3.17}$$

$$\mathcal{E}_z = -\frac{1}{i\omega\epsilon} \frac{\partial \mathcal{H}_y}{\partial x} \tag{3.18}$$

once we have defined the wave equation, the solution to the wave equation for TE mode will be look like :

$$E = \widehat{y} \mathcal{E}_y(x) e^{i(\beta z - \omega t)} \tag{3.19}$$

Equation 3.13 can be substitute in Equation 3.19 and after solving this second order differential equation two solution will be provided as sinusoidal and exponential :

$$\mathcal{E}_y = e^{\pm ix\sqrt{(k_i)^2 - \beta^2}} \tag{3.20}$$

The solution will be sinusoidal if $(k_i)^2 > \beta^2$ and it will be exponential if $(k_i)^2 < \beta^2$. Now, to have the guided mode the solution must be sinusoidal in the core and exponential in

Thèse accessible à l'adresse : https://theses.insa-lyon.fr/publication/2024ISAL0120/these.pdf © [C.B. Chander Bhan], [2024], INSA Lyon, tous droits réservés

the cladding. Therefore, $\beta > K_2 > K_3$ for exponential and $\beta < K_1$ for sinusoidal and the solution will be as illustrated in Figure 3.4 where its shows that two wavevector in the cladding K_2 and K_3 must have the same phase to have coupling of oscillation field between two media.

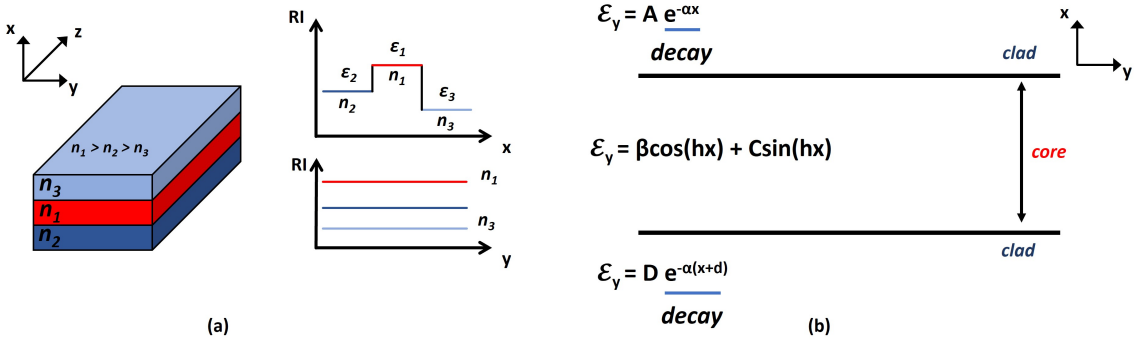

Figure 3.4: slab waveguide : (a) schematic diagram of slab waveguide with RI index profile along x and Y axis (b) solution to the second order differential equation for a slab waveguide for x and y-axis

Given understanding with waveguides, in literature we define waveguide mode properties by using three normalized dimensionless parameter [109]: V-number or normalised frequency that can explain the number of modes propagating in the waveguide without solving them numerically.

$$V = \frac{2\pi}{\pi} d\sqrt{n_1^2 - n_2^2} \tag{3.21}$$

The second is the b-number or normalized guided index that defines the β :

$$b = \frac{n_{eff}^2 - n_2^2}{n_1^2 - n_2^2} \tag{3.22}$$

where n_{eff} is the effective refractive index, a number quantifying the phase delay per unit length in a modes, relative to the phase delay in vacuum. The third is the asymmetry factor (a) that depends upon the TE or TM polarization of the mode as given below:

$$For\ \ TE\ \ Mode : a_E = \frac{n_2^2 - n_3^2}{n_1^2 - n_2^2} \tag{3.23}$$

$$For\ \ TM\ \ Mode : a_M = \frac{n_1^4}{n_3^4} \cdot \frac{n_2^2 - n_3^2}{n_1^2 - n_2^2} \tag{3.24}$$

In the case of symmetric waveguides as $n_3 = n_2$ and $a_E = a_M = 0$. Together all three can be used to form an eigenvalue equation from which the value of the effective index for each guided mode can be determined:

$$For\ \ TE : tan(\frac{hd}{2} - \frac{m\pi}{2}) = \frac{\sqrt{V^2 - h^2d^2}}{hd} \tag{3.25}$$

$$For\ \ TM : tan(\frac{hd}{2} - \frac{m\pi}{2}) = \frac{n_1^2}{n_2^2}[\frac{\sqrt{V^2 - h^2d^2}}{hd}] \tag{3.26}$$

Thèse accessible à l'adresse : https://theses.insa-lyon.fr/publication/2024ISAL0120/these.pdf © [C.B. Chander Bhan], [2024], INSA Lyon, tous droits réservés

where m is an integer (0,1,2..) defining the order of the mode in the waveguide. The mode will be at cutt-off when the propagating angle will be equal to the critical angle i.e., $V = V_c$ and after solving the equation the cutt-off condition would be $V_c = hd$ or if we define V_c in eigen value then :

$$tan[\frac{hd - m\pi}{2}] = 0 \tag{3.27}$$

so, m will be defined as the closest large number than bracket value or ceiling value of $[V/\pi]$. In case of a symmetric waveguide where $n_2 = n_3$ there will be always a solution whereas its not the case in an asymmetric waveguide where $n_2 \neq n_3$. Furthermore, the condition for single-mode will be defined as $V < \pi$.

We understand the fundamental concepts using a basic waveguide structure: a slab waveguide consisting of a thin infinite film in the z-direction sandwiched between two cladding layers. In a slab waveguide, as discussed earlier, the light is confined vertically by index contrast and propagates laterally (along the z-axis). Practically, we use rectangular or channel waveguides, as shown in the Figure 3.2. In these waveguides, we have boundary conditions in the x-y direction, with confinement in the vertical direction by index contrast and in the transverse direction by index contrast as well. Since we will be using strip waveguides in our final devices, it is essential to extend our understanding of β and n_{eff} for rectangular waveguides.

Approaches to calculate β or n_{eff} in rectangular waveguides

The pioneering work by Marcatili's [84, 110] provides the approximate analytical formulation of the rectangular waveguide design. In the rectangular waveguide, the boundary conditions are in both x and y directions. If we consider the simplest example of rectangular waveguide with embedded or buried structure as shown in Figure 3.5 . In this structure, the boundaries are considered are nicely defined in x-y direction as n_2, n_3 and n_4, n_5 respectively, whereas the corner domains have been ignored to avoid the complexity where the field x, y, z would be coupled to each other.

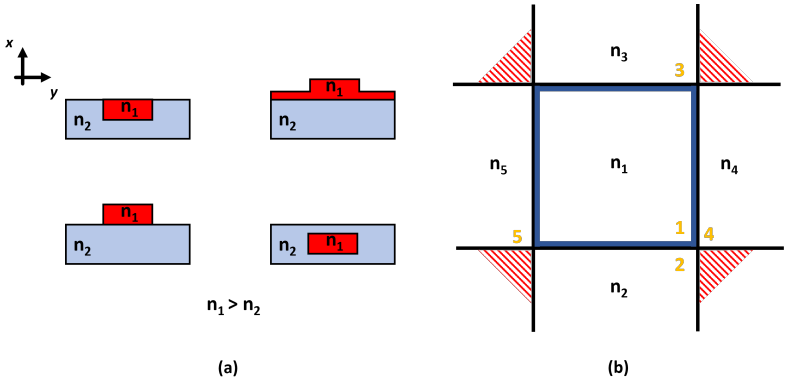

Figure 3.5: Schematic diagram for establishing boundary value problem.

Thèse accessible à l'adresse : https://theses.insa-lyon.fr/publication/2024ISAL0120/these.pdf © [C.B. Chander Bhan], [2024], INSA Lyon, tous droits réservés

so, the scalar wave equation to this structure would be :

$$\frac{\partial^2\psi}{\partial x^2} + \frac{\partial^2\psi}{\partial y^2} + [k_0^2 n^2(x,y) - \beta^2]\psi = 0 \tag{3.28}$$

where, $\psi = X(x)Y(y)$ is the wave function that shows the relation of "amplitude distribution along x" $X(x)$ and "amplitude distribution along y" $Y(y)$, k_0 is the free-space wave vector, β is the propagation constant and $n(x,y)$ is the RI. The general solution to the problem defined in Equation 3.28 will be :

$$\psi(x,y) = \psi_0 e^{-j(k_{x_i}x + k_{y_i}y)} \cdot e^{-j\beta z} + C \tag{3.29}$$

where, K_{x_i}, K_{y_i} are propagation constants w.r.t regions (1, 2, 3, 4, 5) defined in Figure 3.5. In case of step index profile, where in core $n(x,y) = n_1$. The possible allowed solution to the wave Equation 3.28 defined above will be

$$X(x) = Acos(K_x x + \phi_x) Y(x) = Bcos(K_y y + \phi_y) \tag{3.30}$$

where K_x and K_y are the separation constants and they should satisfy the boundary conditions where one is sharing x and the other is sharing the y boundary. Therefore propagation constant $\beta = k_0^2 n_1^2 - k_x^2 - k_y^2$. Now, outside the core region the guided mode solution must exponential decay. So, in region 3 the solution to the above Equation 3.28 will be for $x > 0$:

$$\psi_3(x) = e^{-\gamma_3 x} \tag{3.31}$$

where γ_3 is the decay constant and will be equal to $\sqrt{k_0^2(n_1^2 - n_3^2) - k_x^2}$.

The total field in the waveguide for $x > 0$ and $0 < y > b$ will be :

$$\psi(x,y) = Ccos(K_y y + \phi_y) e^{-\gamma_3 X} \tag{3.32}$$

where, C is constant. Similarly, the other region (2,4,5) solution could be written and its shown in the Figure 3.6.

As it can be seen that in all the corner domains there is only decaying solution. Moreover, with this boundary value problem we have seen how the propagating field and decaying field will look like but we are more interested in quantifying the solution and it comes with k_x, k_y, and β .

In a rectangular waveguide of 'a' core width and with 'b' height, the field is propagating E_x along x, H_y along y. The tangential E_x and H_y are continuous at $y = 0$, $y =$b and $x =$a, $x =$-a respectively. so the characteristic equation given by Marcatili's work for k_x, k_y, and normalized propagation constant b will be :

$$tan(k_x a) = n_1^2 \frac{k_x(n_2^2\gamma_3 - n_3^2\gamma_2)}{n_2^2 n_3^2 k_x - n_1^2\gamma_2\gamma_3} \tag{3.33}$$

Thèse accessible à l'adresse : https://theses.insa-lyon.fr/publication/2024ISAL0120/these.pdf © [C.B. Chander Bhan], [2024], INSA Lyon, tous droits réservés

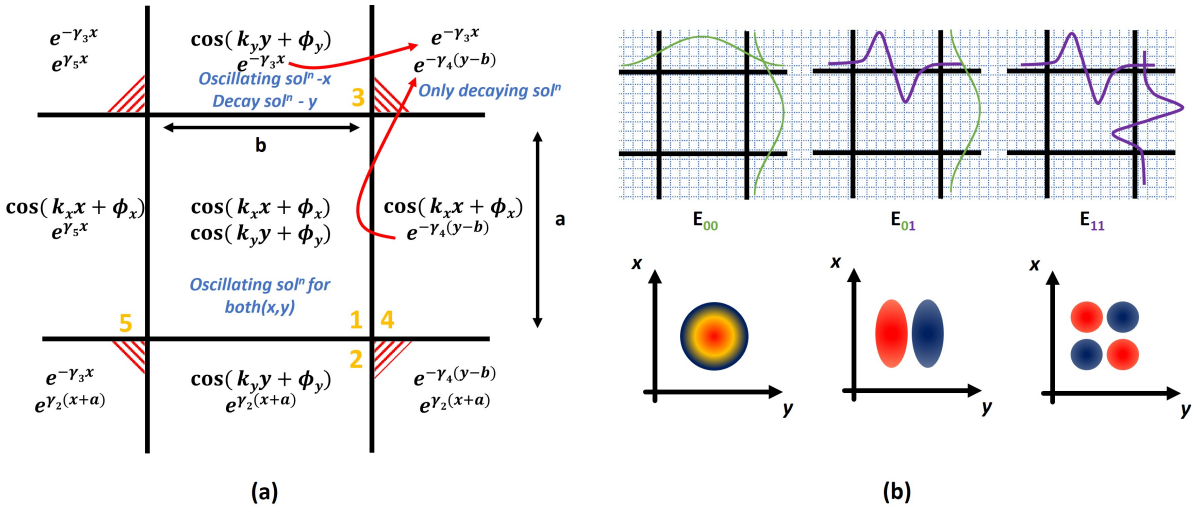

Figure 3.6: Solution of the boundary value problem for a rectangular waveguide: (a) Solutions in each region of the rectangular waveguide, and (b) Electric field distribution and mode profiles in the x-y plane for electromagnetic modes, as determined from the solution for the rectangular waveguide [110].

$$tan(k_y b) = \frac{k_y(\gamma_4 - \gamma_5)}{k_y^2 - \gamma_4 \gamma_5} \tag{3.34}$$

$$b = \frac{\beta^2 - k_0^2 n_2^2}{k_0^2 (n_1^2 - n_2^2)} \tag{3.35}$$

If we plot b and V from equation 3.35 and 3.21 respectively as shown in Figure 3.8, the analytical approach sometimes provides non-physical propagation constants for certain small ranges of V, which is not practically feasible, as light cannot suddenly propagate backward or forward due to changes in refractive index or size. Furthermore, for any symmetrical waveguide, whether a rectangular or strip waveguide buried under the same cladding as the substrate, there must be a single mode solution, as discussed in the previous section. In cases where the mode is close to cutoff—either when the dimensions are very small and the refractive index contrast is high, or the dimensions are large but the refractive index contrast is very low: the analytical method may yield non-physical values for β

To address this problem, the literature describes two methods: the “Perturbation Approach” [111] and the “Effective Index Method” [82]. In the perturbation approach, we consider an initial guess close to β and then find the β with minimal error. In this approach, the closest RI distribution ($n_0(x, y)$) is used to provide the infinite solution (Trial, radiation, higher-order, true solution..so on) but with finite propagating solution and as with perturbed state the error will be minimized. According to the Perturbation approach the correction of β is proportional to the difference in RI and written as followed:

$$\partial\beta^2 = \beta^2 - \beta_m^2 = k_0 \frac{\int_s (n^2(x,y) - n_0^2)\psi_m ds}{\int_s \psi_m^2 ds} \tag{3.36}$$

In these methods, as we approach the cutoff, the total number of modes reduces. Con-

Thèse accessible à l'adresse : https://theses.insa-lyon.fr/publication/2024ISAL0120/these.pdf © [C.B. Chander Bhan], [2024], INSA Lyon, tous droits réservés

sequently, the other solutions are eliminated from the trial solutions, leading to non-physical modes. In other words, the number of guided solution is reduced to find the right mode. This is similar to what happens with Fourier transformation: as the number of coefficients decreases, the reconstruction becomes difficult. This makes it challenging to find the β as it approaches the cutoff region, as illustrated in the Figure 3.8, which shows the negative β similar to the first-order analytical equation. However, the perturbation approach provides better accuracy compared to the analytical approach when far from the cutoff region.

In case of "Effective Index Method (EIM)", we convert 2-dimensional complex structure into two 1 - dimensional structure as slab waveguides shown in Figure 3.7.

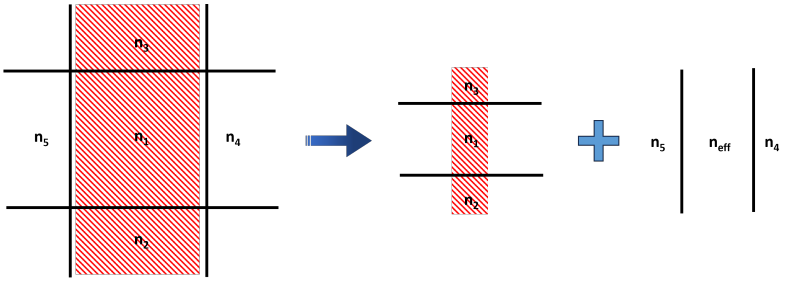

Figure 3.7: EIM working principle

where $n_{eff} = \frac{\beta}{k_0}$. Moreover, the effective index method might not provide the accurate n_{eff} but its accurate enough to the numerical methods that help to look for the waveguide modes and its faster than numerical method once its scripted in MATLAB and PYTHON language.

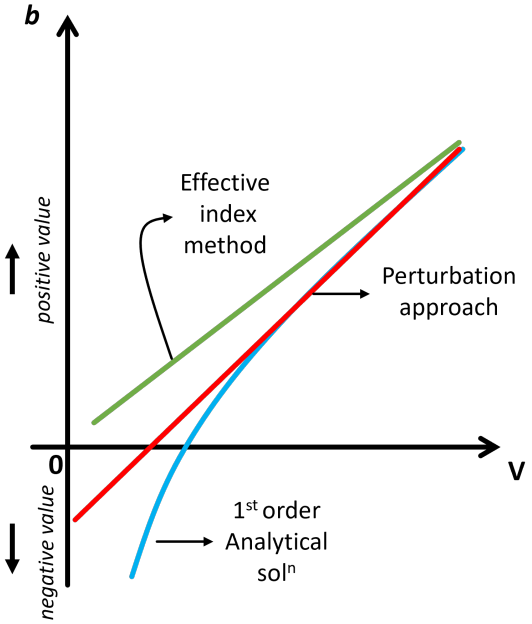

Figure 3.8: $b - V$ curve Comparison for Effective index method, Perturbation approach, 1_{st} order analytical solution

The methods described above such as the effective index method, perturbation methods, and Marcatili's approach are analytical techniques used to determine the modes and propagation constants for rectangular waveguides. However, the marcatili's approach assumes well confined modes and only work when cross-section of waveguide is large enough

Thèse accessible à l'adresse : https://theses.insa-lyon.fr/publication/2024ISAL0120/these.pdf © [C.B. Chander Bhan], [2024], INSA Lyon, tous droits réservés

than wavelength else the theory becomes inaccurate for the the mode. Moreover, these methods have limitations when applied to complex cross-sectional geometries, graded index profiles, ion-implanted waveguides, and other non-rectangular structures. The analysis of 3D rectangular waveguide is always mathematically complicated.

In many advanced studies, such as optical trapping, it is crucial to perform rigorous mode calculations to accurately solve the boundary value problems and determine the electromagnetic field values, as these can significantly influence the gradient of the field. For such precise analysis, numerical waveguide modal analysis is often employed. Common numerical methods used to compute electromagnetic modes include the Finite element method (FEM) [112], the Finite difference method (FDM) [113], the method of lines (MoL) [114], the film mode matching (FMM) [115], and Fine-difference time domain (FDTD) [85]. Among these, FEM offers several advantages due to its ability to utilize adaptive meshing, which improves accuracy in complex geometries and less computational intensive compare to FDTD. In the previous chapter, we have briefly compared these methods and justified our choice of FDM, FEM, and FDTD for the numerical analysis of our devices.

Once we have established a comprehensive understanding of the parameters that can influence modeling and identified the electromagnetic modes and methods for determining them, we can proceed to the core focus of this thesis: the modeling of optical trapping.

3.2 Modeling of Optical Trapping and Sensitivity

Optical forces consist of both gradient and scattering forces when a polarized, homogeneous field interacts with a particle (as explained in Chapter 2). Gradient forces, also known as trapping forces, are conservative forces that help trap particles or analytes toward regions of higher field intensity. Given our focus on sensing and trapping 100 nm dielectric particles in air (i.e., polyaromatic hydrocarbons), this modeling section will concentrate on exploring various waveguide structures to enhance the optical gradient force (F_{grad}).

In this section, we used various numerical models to analyze different parts of the photonic integrated circuit. Importantly, we conducted convergence tests for both mesh size and solver window size in each scenario to avoid unstable or nonphysical results. We began our modeling with the simplest and most popular design, the strip waveguide, and continued our exploration by varying material, structures (slot and hybrid plasmonic waveguides) and index contrast. Our study aimed to optimize the waveguide sensor for both sensitivity and optical trapping. Although these aspects are interconnected, we divided the analysis into two sections: “Optical Trapping” and “Sensitivity”.

As discussed in Chapter 2, recognizing the importance of various methods for calculating optical trapping, we chose to employ COMSOL Finite element method (FEM) [86] for precise calculations. Additionally, we used Lumerical’s Finite-Difference Eigenmode (FDE) solver [88] and the Fully Differential Fully Vectorial (FDFV) [87] method for analytical solutions, which facilitated faster computations in potential depth studies where multiple data points were required. We subsequently compared our model with established literature models to verify its accuracy.

Thèse accessible à l'adresse : https://theses.insa-lyon.fr/publication/2024ISAL0120/these.pdf © [C.B. Chander Bhan], [2024], INSA Lyon, tous droits réservés

3.2.1 Waveguide based optical trapping

To enhance F_{grad}, we need to consider multiple other parameters such as the index of the core waveguide, wavelength, and modes, among others. To understand all the possibilities of enhancing the optical forces with strip waveguides and their pros and cons, we start with the simplest example found in the literature [116]: a dielectric Si_xN_y (RI = 1.98) strip waveguide with core width of 1 μm and core thickness of 0.2 μm surrounded by cladding water (RI = 1.33) on SiO_2 (RI = 1.46) substrate of 2 μm solved with FEMLAB (former name of COMSOL). As shown in the Figure 3.9 below with the schematic diagram of similar structure as described in literature and fundamental TE mode at 1064 nm wavelength were evaluated using FEM numerical analysis in COMSOL 2D model with the Frequency Domain Module.

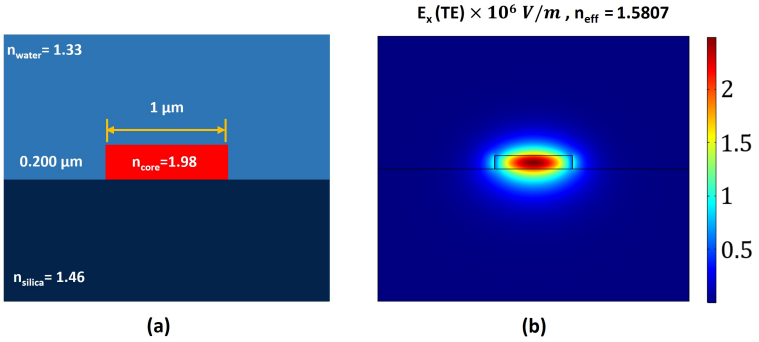

Figure 3.9: COMSOL FEM 2D mode solver : (a) Schematic diagram with RI and dimension of a strip waveguide (b) TE mode profile with n_{eff}

In this model to avoid back reflection and perturbation with the main field, a scattering boundary condition was used at the boundaries, with a mesh size of 10 nm. For higher accuracy in the calculation of the propagation constant, a mesh size of 5 nm was chosen in the waveguide section, along with a convergence study. In other regions, the mesh was set to 50 nm. For rigorous optical force calculations, we utilized the MST method in-built function within a 3D COMSOL model in the frequency domain.

In the 3D COMSOL model, the field is excited in the waveguide using a Gaussian source or port function in COMSOL with a power of 1 W. In contrast, in the 2D model, the mode is evaluated using the Helmholtz equation for electric fields, searching for a solution in the form of a wave traveling in the out-of-plane direction. The Figure 3.10 below shows the perturbed mode field profile due to particle interaction and F_{grad} calculated with the 3D COMSOL model for a 100 nm polystyrene particle using the MST for TE polarization.

To ensure accurate results, the model incorporates Perfectly Matched Layer (PML) boundary conditions at both the input and output ends of the waveguide, as shown in Figure 3.10.(a). This effectively mitigates reflections and enhances the reliability of simulations. As MST methods use the perturbed field so we calculated the F_{grad} by introducing a rigid, homogeneous dielectric polystyrene particle with a diameter of 100 nm and a RI of 1.57 [117] into the fluid medium and positioning it with a spacing of 5 nm between the particle and the walls of the waveguide.

To determine the minimum force (F_{min}) and minimum distance (D_{min}) required for stable trapping, we performed a potential well depth study 3.4 that utilizes multiple points of force

Thèse accessible à l'adresse : https://theses.insa-lyon.fr/publication/2024ISAL0120/these.pdf © [C.B. Chander Bhan], [2024], INSA Lyon, tous droits réservés

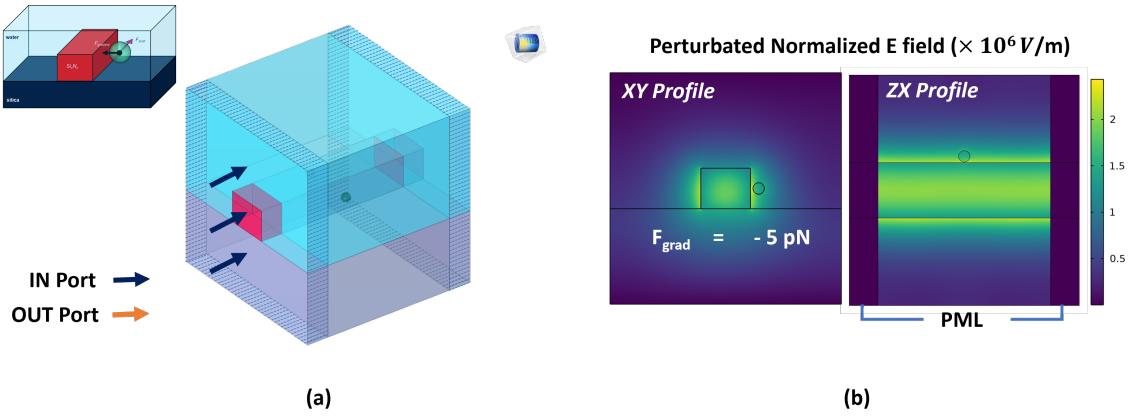

Figure 3.10: 3D COMSOL model : (a) 3D model with PML boundary condition at the input and out ports (b) Normalized perturbed E field in XY and ZX profile for TE polarization.

in the field. Conducting this study with a 3D COMSOL model can be highly computationally intensive. Therefore, we utilized the Discrete Dipole Approximation (DDA) analytical method using the Lumerical FDE model. In the FDE Eigensolver, Maxwell's equations are formulated as a matrix eigenvalue problem and solved on a cross-sectional mesh of the waveguide using sparse matrix techniques [88] to obtain the effective refractive index (n_{eff}) and mode profiles of the waveguide modes. To confirm our 2D modelling and analytical function developed in the thesis we also used the FDFV model, a home-made solver developed by Regis OROBTCHUK at INL [87], Lyon, using a propagation constant (β) guess to find the closest n_{eff} using a rectangular cross-sectional mesh without averaging the indexes at boundaries. Both methods utilize the same meshing techniques, and we obtained consistent values for the F_{grad} and electric field (E_x,E_y) profiles.

Furthermore, the FDE model was scripted in Python with an application programming interface (API) and multiple functions to facilitate reuse for further studies. The Figure 3.11 below shows the FDE Lumerical model (meshing and the results resembles by FDFV tool) used to find the unperturbed field of the desired mode, with DDA subsequently implemented to find the optical forces.

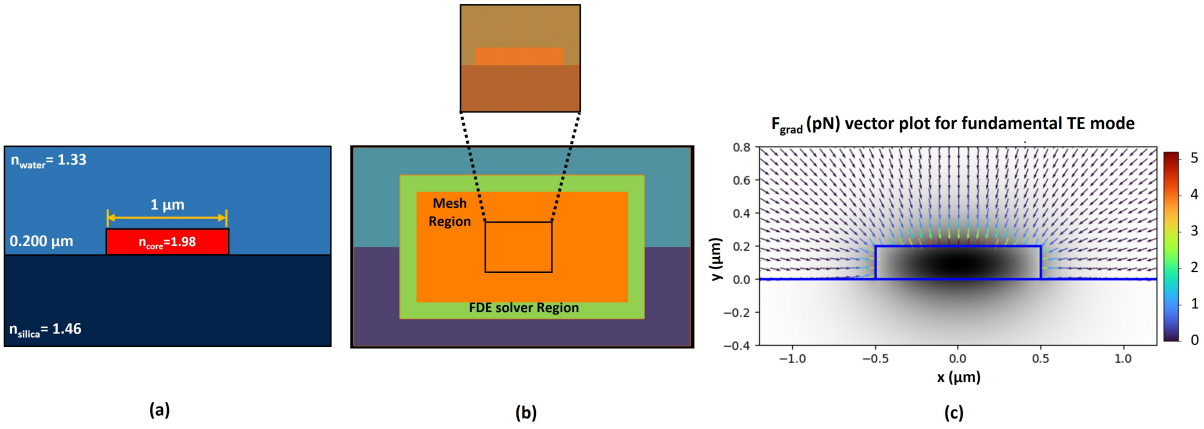

Figure 3.11: 2D lumerical FDE model : (a) a schematic diagram of strip waveguide (b) uniform rectangular mesh model in FDE (c) F_{grad} vector plot in XY axis with the fundamental TE mode, where mode-profile is shown with grey scale

Thèse accessible à l'adresse : https://theses.insa-lyon.fr/publication/2024ISAL0120/these.pdf © [C.B. Chander Bhan], [2024], INSA Lyon, tous droits réservés

Both the coarse and fine meshes used in the FDE and FDFV were 3 nm, as shown in the Figure 3.11 (b). To minimize the reflection, in both model Lumerical FDE and FDFV model uses the absorbing boundary condition (PML) and transparent boundary condition (TBC) respectively. Given that the thickness of the waveguide chosen here is 200 nm (as in literature reference [116]), the evanescent field exhibits a sharp gradient on top of the waveguide. This can be observed in the gradient vector plot, which represents the gradient force (pN) in the x-y direction for a 100 nm dielectric particle, calculated with a normalized power of 1 W. Moreover, since the gradient force is directed towards the maximum intensity of the evanescent field of the mode, a similar behavior can be observed when comparing the TE mode in the Figure 3.10 above with the gradient vector plot.

Finally, we compared all three methods with published results from the literature [116, 72] for a dielectric Si_xN_y strip waveguide in a water cladding as shown in Figure 3.12, where the F_{grad} is evaluated with respect to changes in the size of the particle. The meshes and boundary conditions for all models used here were explained above.

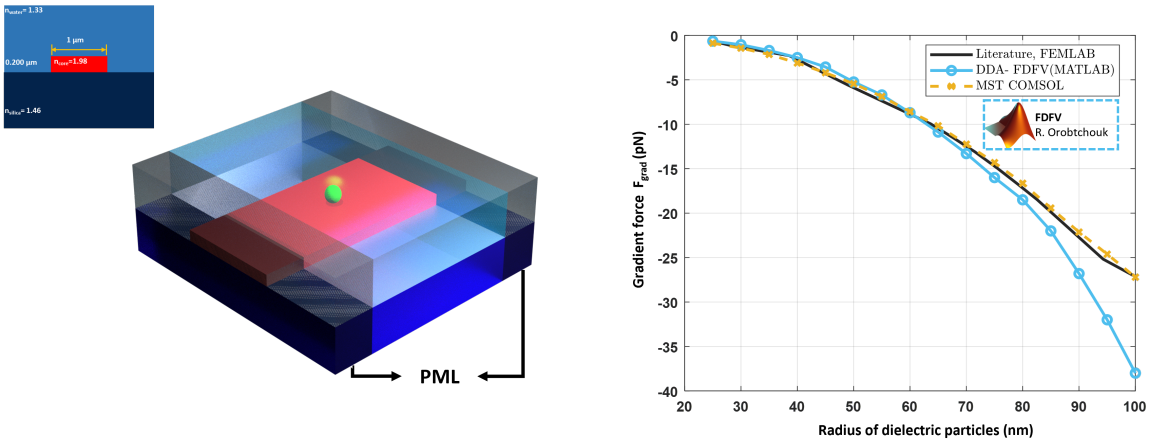

(a) (b)

Figure 3.12: Comparison of MATLAB FDFV, Lumerical FDE, and COMSOL FEM: (a) Schematic and Blender model representing the strip waveguide from the literature, and (b) F_{grad} as a function of dielectric particle radius for all three models developed in this thesis.

As observed in Figure 3.12, the model developed in this thesis, which combines the FDFV approach with the DDA function and the MST COMSOL model, shows strong agreement with existing models in the literature. However, the DDA-FDFV model demonstrates a deviation in optical gradient forces for particles with radii larger than 70 nm. This difference arises because the DDA method is only valid in Rayleigh regime where the size parameters is less than 1 ($k_m a < 1$), as discussed in detail in Chapter 2.

With the models established, we can now explore all possibilities for enhancing the F_{grad} to trap a dielectric particle. The F_{grad} depends on the gradient of the electric field (∇E_o^2) and the polarizability of the particle (α_{rad}), as shown in equation 2.5 in chapter 2. Since α_{rad} depends on the permittivity ($\varepsilon_{particle}$) and size of the particle, which remain constant throughout our study, the only feasible approach is to increase the ∇E_o^2. One way to achieve this is by increasing the index contrast of the waveguide. All the studies conducted to enhance optical forces, as shown below, were performed using 1 W of optical power and polystyrene dielectric particles with a size of 100 nm and a refractive index (RI) of 1.57

Thèse accessible à l'adresse : https://theses.insa-lyon.fr/publication/2024ISAL0120/these.pdf © [C.B. Chander Bhan], [2024], INSA Lyon, tous droits réservés

estimated using cauchy dispersion law defined in Equation 3.37 [117].

$$n_{real\ polystyrene} = 1.5725 + \frac{0.0031080}{\lambda^2} + \frac{0.00034779}{\lambda^4} \tag{3.37}$$

The thickness of the Si_xN_y waveguide was fixed at 350 nm with an RI of 1.94, chosen for compatibility with the DAPHNE platform from STMicroelectronics. The refractive indices of SiO_2 and water (H_2O) were considered to be 1.44 and 1.32, respectively, at a wavelength of 1310 nm, as determined by the Sellmeier dispersion fit described in Chapter 4. The wavelength of 1310 nm was selected as the operating wavelength of the device due to the availability of a high-power laser in the laboratory, which offers low material absorption and high energy at this wavelength.

Refractive index contrast

In optical waveguides, refractive index contrast defines the relative difference in RI between the core and cladding. In an optical dielectric waveguide, this contrast determines its characteristics. A higher index contrast can facilitate larger integration scales and new functionalities [118]. For optical trapping applications, a higher index contrast leverages the sharp gradient in the cladding area, resulting in stronger confinement.

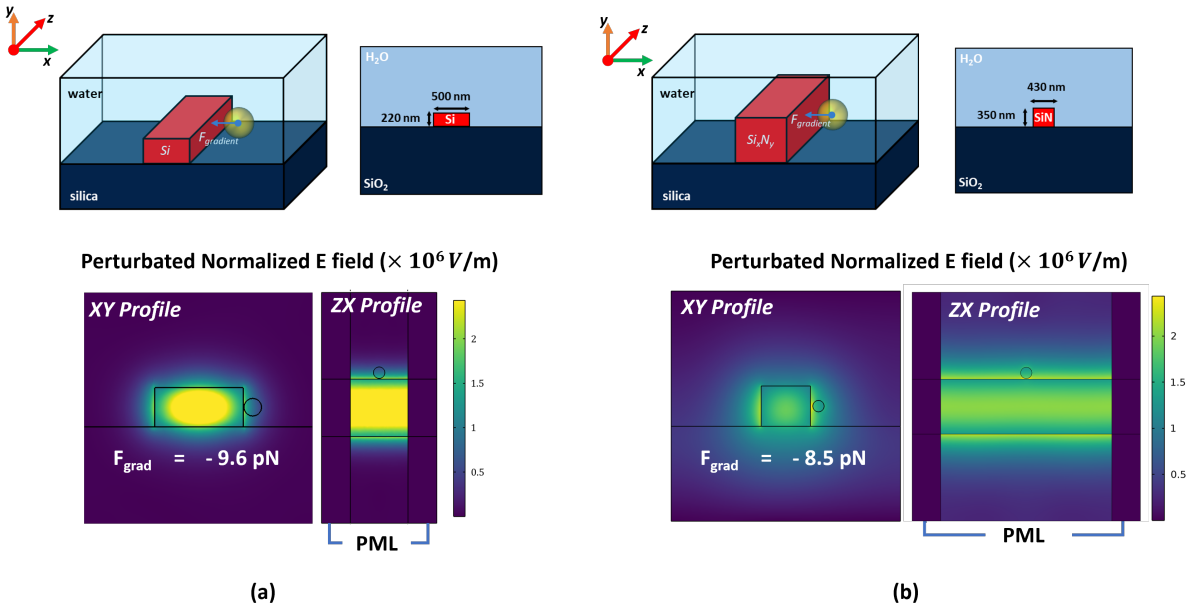

Figure 3.13: F_{grad} for two different refractive index contrasts of a strip waveguide: (a) Schematic diagram of a Si strip waveguide with perturbed normalized TE mode field profiles and F_{grad}, and (b) Schematic diagram of a Si_xN_y strip waveguide with perturbed normalized TE mode field profiles and F_{grad} evaluated using the COMSOL 3D model.

However, it is important to optimize the dimensions to ensure sufficient electric field presence in the cladding region to interact with the particle. For example, for a wider core width waveguides, as the field decays exponentially in the cladding, and therefore, there will be complete confinement and a negligible evanescent field in the cladding to interact. This will lead to negligible optical forces exerting on the particle.

We examined two index contrasts for our study using Si with RI of 3.50 at 1310 nm [119] and Si_xN_y under water cladding. For both dielectric waveguides, the optical F_{grad} were

Thèse accessible à l'adresse : https://theses.insa-lyon.fr/publication/2024ISAL0120/these.pdf © [C.B. Chander Bhan], [2024], INSA Lyon, tous droits réservés

almost similar. The schematic diagrams of both dielectric waveguides and their modes are illustrated in the Figure 3.13 above.

The F_{grad} for 100 nm dielectric particles in both Si and Si_xN_y waveguides are very close, with a difference of only 1.15 pN. However, Si is known for two-photon absorption (TPA), which results in higher losses compared to Si_xN_y waveguides. Additionally, the temperature expansion coefficient of Si is higher than that of Si_xN_y makes is more sensitive to temperature variation [120]. Therefore, we opted to work with Si_xN_y waveguides for our thesis.

Different optical modes : Higher order and fundamental modes strip waveguides
The F_{grad} is stronger towards the maximum intensity of the mode. Higher order modes (HOM) in dielectric waveguide with multiple maxima can facilitates trapping of large number of particles. Moreover, due to the wider core of waveguides it reduces the fabrication tolerances in fabricating such devices. In this thesis, we study the first order mode and fundamental mode for optical trapping application. Figure 9.5 below shows the schematic diagram and F_{grad} vector plot for both modes to compare.

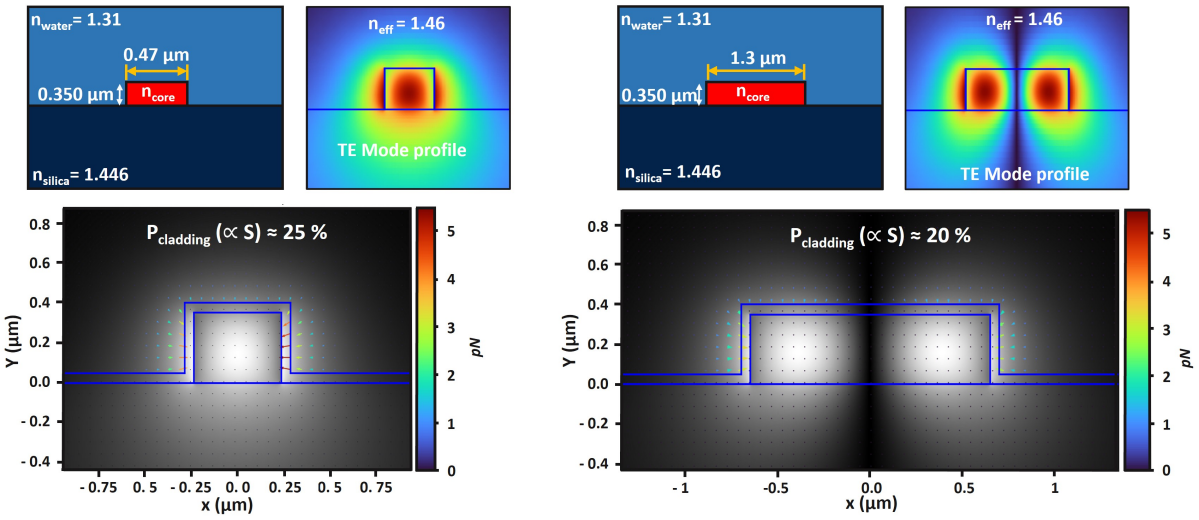

(a) Fundamental mode *(b) Higher order mode*

Figure 3.14: F_{grad} vector plot in XY profiles for HOM and FM waveguide with schematic diagram of both waveguide structure (evaluated with Lumerical FDE model).

As can be seen, both narrow (FM) and wider core (HOM) waveguides exhibit the same optical F_{grad} on their adjacent vertical walls. The optical forces here are calculated using the DDA method, which evaluates the force at the center of the particle. Therefore, close to the wall of the waveguide, the force values were intentionally set to zero up to the center of the particle (radius) shown with contour blue line in Figure 9.5. Additionally, in this figure the modes of both waveguides are shown with black and white contour plots to distinguish the behavior of the F_{grad} vector plot and the mode intensities. Due to the fact that multiple maxima in HOM could be beneficial in trapping multiple particles, we have considered this structure in our fabrication design.

Slot waveguides
slot waveguides enhance the evanescent field intensities in the gap by trapping light in a narrow, low-refractive-index slot between two high-refractive-index materials [94]. As dis-

Thèse accessible à l'adresse : https://theses.insa-lyon.fr/publication/2024ISAL0120/these.pdf © [C.B. Chander Bhan], [2024], INSA Lyon, tous droits réservés

cussed earlier in chapter 2, the high contrast in refractive index causes more of the electromagnetic field to enter the slot, increasing the electric field intensity due to the lower effective index. This results in a stronger evanescent field in the gap that can be used to enhance the optical force and sensing of a dielectric particle in our studies. However, designing and optimizing a slot waveguide is not the same as a strip waveguide. With the waveguide thickness fixed at 350 nm, the other dimensional parameters in a slot waveguide are the gap (g) and the width of a single core waveguide (w_{core})

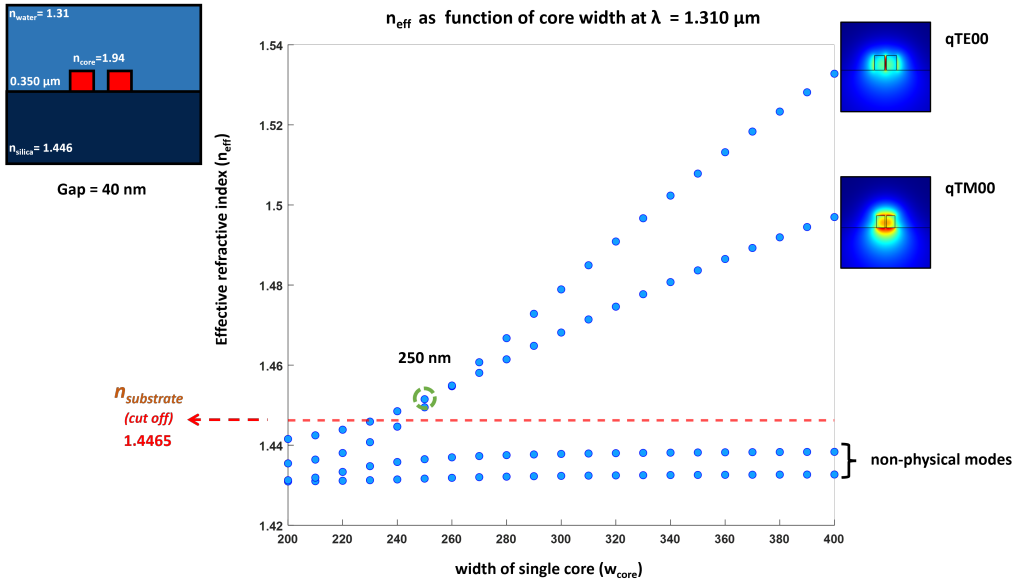

Figure 3.15: n_{eff} versus w_{core} of a slot waveguide with a fixed gap of 40 nm.

For sensitivity applications, we choose the mode closer to the radiation mode so that the power in the cladding would be higher. As shown in the Figure 3.15, for a fixed slot gap of 40 nm, the radiation mode is close to the w_{core} of 250 nm. However, it is important to note that the particle size is 100 nm, and for higher sensitivity, they must be able to reach the evanescent field in the slot waveguide gap. This leads to our further study of increasing the w_{core} to observe the maximum gap that can be achieved through the design.

In the Figure 3.16 below, three different w_{core} of the slot waveguide were evaluated with the fundamental TE mode, and the electric field of the centered profile ($y = 0$) is plotted to observe the maximum gap and electric field in the waveguide. Theoretically, as we know, when the core width increases, the confinement increases, and this also applies to slot waveguides. Fortunately, as the slot waveguide confines the light in the gap, the higher confinement will result in a higher electric field value in the gap, as shown for the three different core widths of 250 nm, 300 nm, and 350 nm with a 40 nm gap in Figure 3.16. Moreover, in slot waveguide with higher confinement it allows us to achieve the gap up to 400 nm with w_{core} of 350 nm.

To calculate the F_{grad} for a Si_xN_y slot waveguide, it is important to consider the optimum positions where optical forces would be higher, rather than comparing for any particle positioning in the cladding. Therefore, we considered two positions in our study: one right on top of the slot gap where the gap of the slot waveguide is smaller than or equal to the size of the particle i.e., $g \leq 120$ nm, and in the second scenario, where the gap is greater than the size of the particle, up to the maximum possible that the slot waveguide can achieve,

Thèse accessible à l'adresse : https://theses.insa-lyon.fr/publication/2024ISAL0120/these.pdf © [C.B. Chander Bhan], [2024], INSA Lyon, tous droits réservés

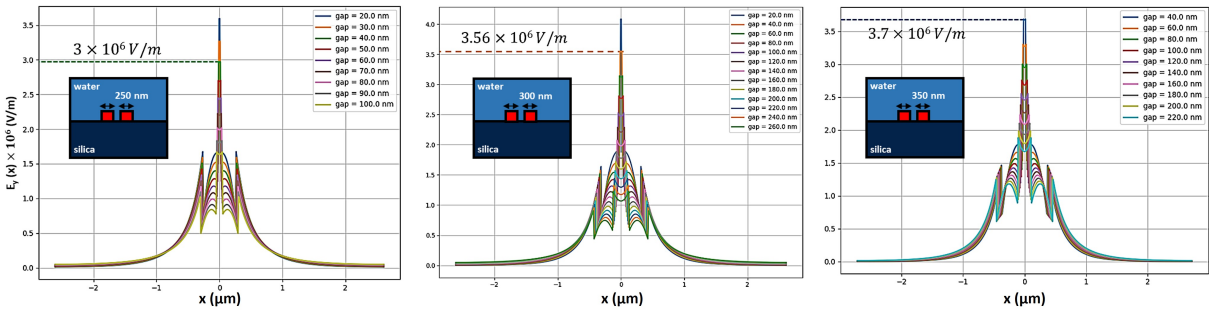

Figure 3.16: TE electric field profile (E_y) at $y = 0$ along x-axis for a three different slot waveguide ($w_{core} = 250$, 300 and 350 nm) with varying slot gap.

i.e., $120 \leq g \leq 400$ nm.

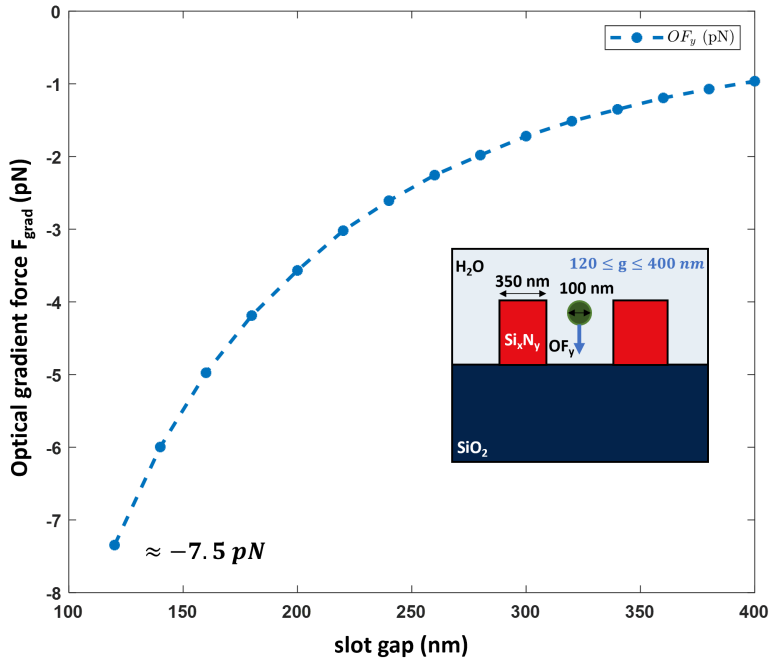

Figure 3.17: F_{grad} (pN) as a function of slot gap ($120 \leq g \leq 400$) with w_{core} of 350 nm

In the case of a $120 \leq g \leq 400$ nm gap, the particle can be positioned inside the slot gap, so it was placed right at the center top inside the slot to maximize the force exertion. This is illustrated in the Figure 3.17 below, which shows the F_{grad} calculated at 1 W optical power with Maxwell stress tensor (MST) model in COMSOL as the slot gap increases. In terms of optical forces, the optimized version of the slot waveguide does not offer any significant advantage compared to the strip waveguide. However, this is not the case for sensitivity, which will be discussed in the next section.

Hybrid plasmonic waveguides (HPWG)

In the case of the strip waveguide, to increase sensitivity, the dimensions (either core width or thickness) of the waveguide must be reduced to bring the mode closer to the radiation modes ($n_{eff} = n_{subs}$). This maximizes the power in the cladding, ultimately enhancing the effect of changes in the n_{eff} as it interacts with the analyte. As shown in the Figure 3.18 below, the power in the cladding (indicated by orange star marks) increases as the core width decreases. However, this also causes the n_{eff} to drop and approach the radiation

Thèse accessible à l'adresse : https://theses.insa-lyon.fr/publication/2024ISAL0120/these.pdf © [C.B. Chander Bhan], [2024], INSA Lyon, tous droits réservés

mode, leading to designs that are unrealistic to fabricate. Despite the simplicity of designing and studying strip waveguides, they have limitations in their potential to increase sensitivity.

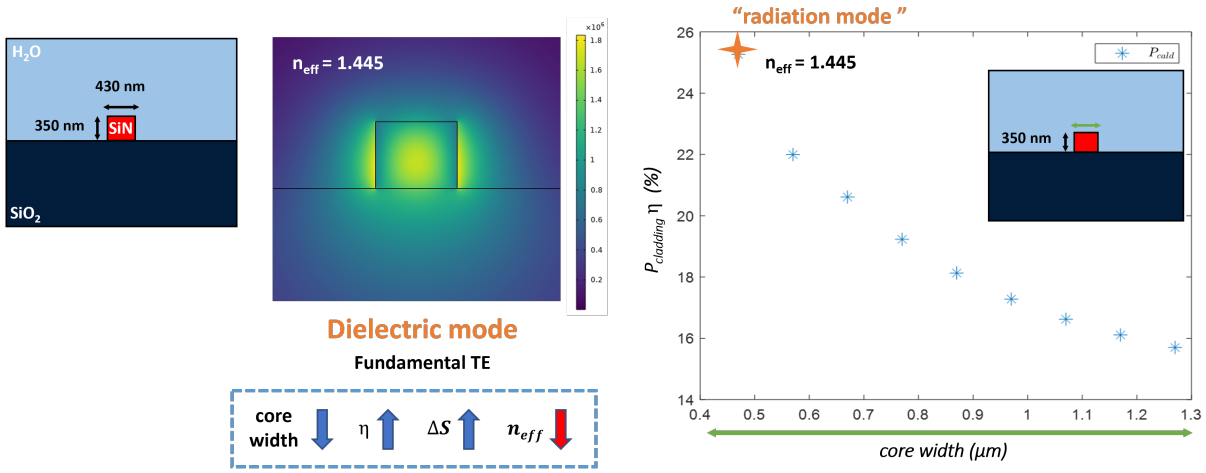

Figure 3.18: Power in the cladding (η) as a function of core width for a strip waveguide : a schematic diagram with TE mode profile of radiation mode.

Plasmonic metals are popular in the literature for enhancing optical trapping and sensitivity because they enable strong resonant enhancement of the local density of photon states at the surface, which increases the gradient of the electric field [121]. Researchers have proposed structures using plasmonic nanoholes and cavities to enhance optical trapping, but these structures possess high optical losses due to absorption [122, 123].

In a previous thesis, the team worked with hybrid plasmonic waveguides to increase sensitivity [124]. The hybrid plasmonic waveguide designed in the previous thesis was named "mode-lift" [125]. This design involves a narrow core dielectric waveguide, intended to support only radiation modes, placed between two metal walls. The plasmonic modes (SPP) at the metal/dielectric interfaces increase the n_{eff} of the hybridized mode, resulting in an overall guided mode (supermode). This concept increases sensitivity while reducing losses by up to six times compared to complete plasmonic modes, as shown in the Figure 3.19, where we have compared the pure low-loss dielectric radiation mode with plasmonic modes and supermodes by HPWG. The radiation mode losses in dielectric strip waveguide shown in the Figure 3.19 is calculated with Lumerical FDE mode and only shows the radiation losses (doesn't consider material absorption, wall roughness losses) where extinction coefficient of RI (k) is considered to be zero as we couldn't measure with ellipsometry (explained in chapter 5).

We considered the similar structure for our study using gold (Au) as a plasmonic metal in the infrared. Despite the enhancement with electric field, it exhibits unique features underlying their strong absorption and scattering of light in biomedical studies [126]. The refractive index of Au used in the modelling is 0.550 + 9.81i at 1.31 μm wavelength. To ensure surface plasmon polariton (SPP) modes in the plasmonic vertical walls, we deliberately selected plasmonic structures with widths of 0.43 μm exceeding the skin depth. Furthermore, to accommodate fabrication tolerances especially with gold deposition, we carefully considered the radius of curvature, setting it to 15 nm for plasmonic corners in the COMSOL model. This precautionary measure helps prevent the occurrence of peak effects, such as charge accumulation at right angles, which could otherwise complicate the calculation of optical

Thèse accessible à l'adresse : https://theses.insa-lyon.fr/publication/2024ISAL0120/these.pdf © [C.B. Chander Bhan], [2024], INSA Lyon, tous droits réservés

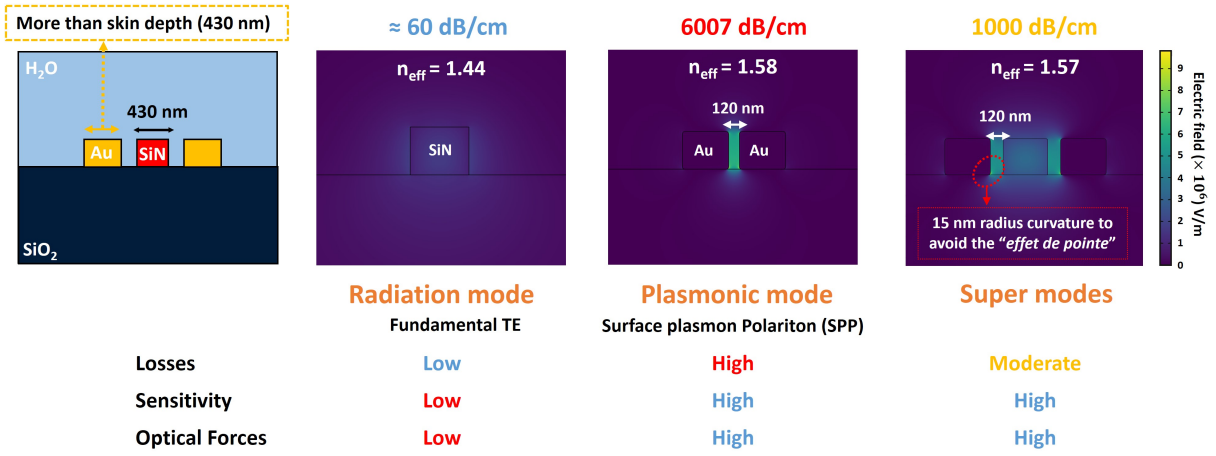

Figure 3.19: Comparison table and mode-field profile of Fundamental TE radiation mode, plasmonic SPP mode and HPWG super modes (combining dielectric and plasmonic modes).

forces and render them impractical as shown in Figure 3.20.

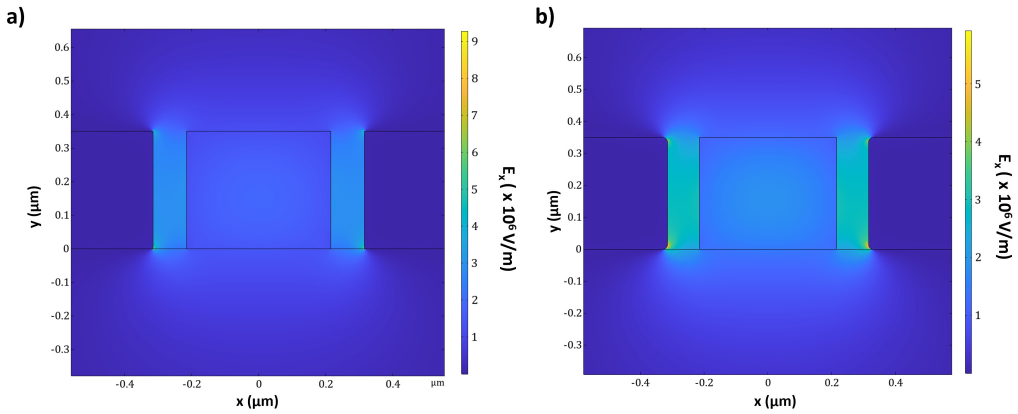

Figure 3.20: HPWG with Normalized E profile (10^6 V/m) for 100 nm gap. a) Plasmonic walls has sharp corners that has 9.4 $\times$ 10^6 V/m electric field with peak effect b) used a corner with radius of curvature with 15 nm and reduced the Electric field by half of it

In the context of nanoparticle optical trapping, significant optical forces are required to counteract fluidic forces such as Brownian motion, Thermophoretic forces, and viscosity drag...etc. To achieve such high optical forces, a smaller dielectric core width within the HPWG can be chosen as shown in Figure 3.21.(b), where the dielectric waveguide's cross-section is treated as a variable parameter, while maintaining a fixed gap of 20 nm between the dielectric waveguide and the plasmonic wall. Remarkably, configurations with a dielectric waveguide width of 20 nm can yield optical forces of approximately -50 pN.

However, it's essential to acknowledge that this design comes with considerable losses, reaching a remarkable 11000 dB/cm. These losses far exceed those encountered in complete dielectric waveguides. Consequently, the overall functionality of sensors employing such designs may experience a reduction due to increased losses.

Therefore, for practicality, we optimized the HPWG design by selecting the radiation mode, occurring at 430 nm core width of the dielectric waveguide, with associated losses of 3000

Thèse accessible à l'adresse : https://theses.insa-lyon.fr/publication/2024ISAL0120/these.pdf © [C.B. Chander Bhan], [2024], INSA Lyon, tous droits réservés

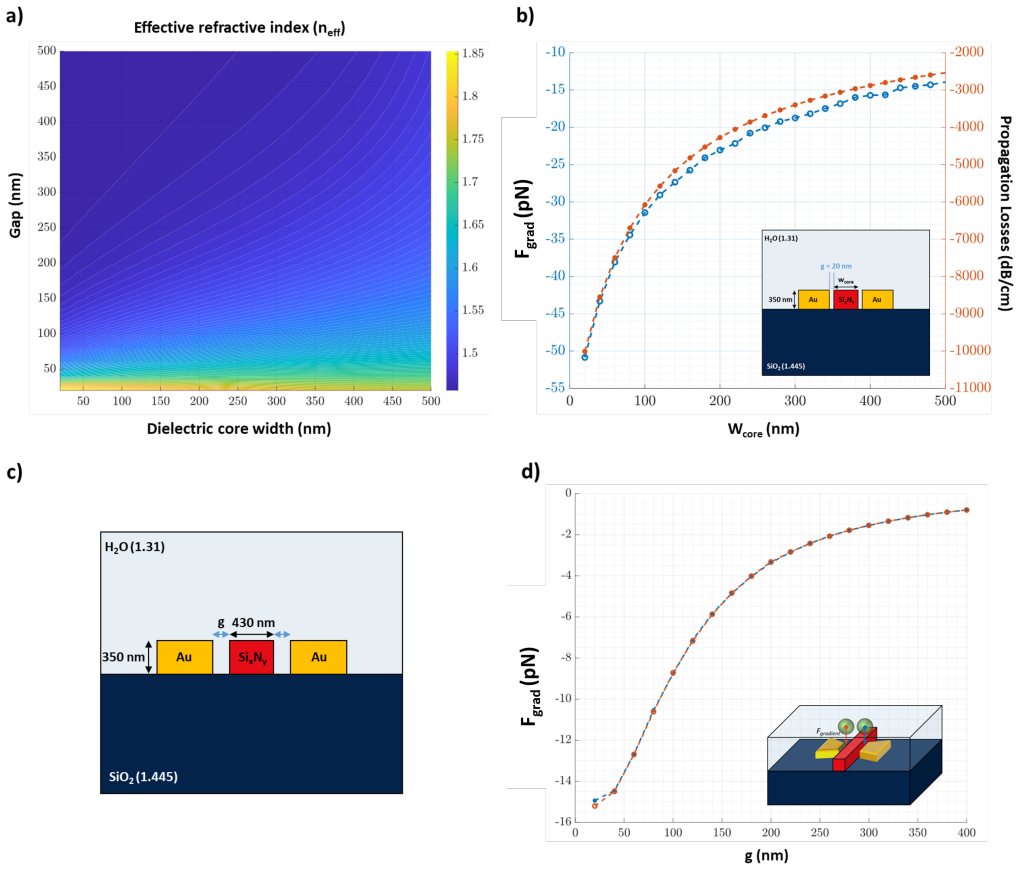

Figure 3.21: (a) contour plot of n_{eff} as a function of gap (g) and dielectric core width in HPWG b) shows the F_{grad} (y-axis left) and propagation losses (y-axis right) in the HPWG as a function of dielectric core width used in the HPWG. c) Schematic diagram of optimized HPWG for Racetrack MRRs d) optical gradient force for two dielectric particles placed on the top of waveguide for optimized designed HPWG as a function of gap (g)

Thèse accessible à l'adresse : https://theses.insa-lyon.fr/publication/2024ISAL0120/these.pdf © [C.B. Chander Bhan], [2024], INSA Lyon, tous droits réservés

dB/cm, as depicted in Figure 3.21.(a). Additionally, this HPWG design incorporates double slots to facilitate multiple trapping of particles, resulting in two distinct intensity maxima within the gaps as illustrates in the Figure 3.21.(c). The F_{grad} for both particles positioned at the top of the HPWG with gap of 20 nm is 15 pN that is impressively high compared to our previous structures (HOM, strip and slot) discussed earlier.

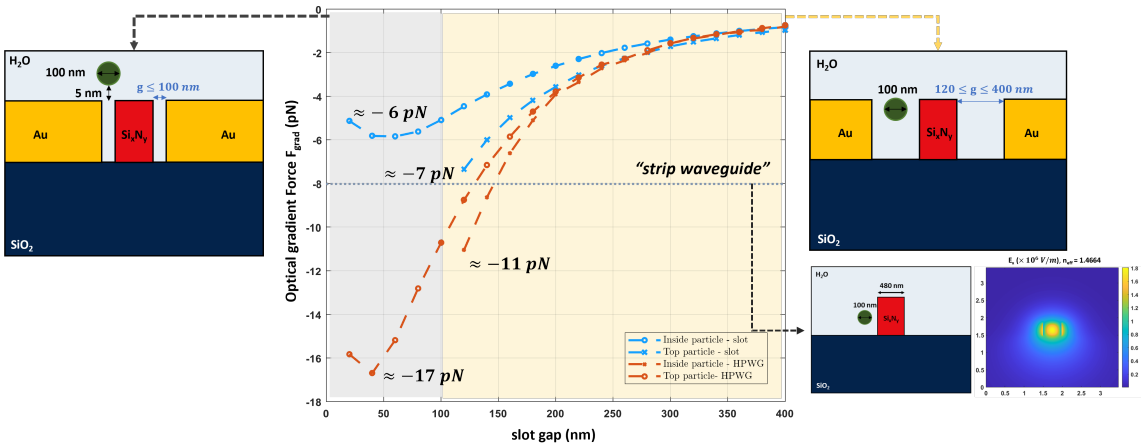

Figure 3.22: F_{grad} comparison as a function of gap size for HPWG, slot, and strip waveguides. The blue and orange dashed lines represent F_{grad} for the slot and HPWG waveguides, respectively, in the gap range $120 \leq g \leq 400$ nm (yellow background) and $g \leq 120$ nm (grey background). The grey dashed line represents F_{grad} for the strip waveguide, as illustrated in the schematic diagram in the figure.

Furthermore, it is imperative to comprehend the pivotal role of gap size, as smaller gaps facilitate stronger light-matter interactions, thus amplifying optical forces in HPWG compared to slot waveguides. For instance, as illustrated in Figure 3.22, for gaps smaller than 100 nm, the maximum optical force exerted on HPWG with a 20 nm gap is 17 pN, threefold higher than that of a slot waveguide. Conversely, for gaps exceeding 100 nm, the maximum optical force is approximately 1.5 times greater than that of a slot waveguide and this comparison decreases more as we go more up to 400 nm gap size. Compare to strip waveguides the optical gradient forces in HPWG are two-folds higher. While a 20 nm gap may be advantageous solely for optical trapping applications, in studies involving analyte measurement, it is crucial to consider both sensitivity and optical trapping capabilities of the device. Thus, assessing the bulk sensitivity of all three waveguides is essential for practical comparison

3.3 Sensitivity

Bulk sensitivity (S) relates to the change in the δn_{eff} of the mode to a change in cladding RI δn_{clad}. n_{eff} is more influenced when more power is concentrated in the cladding area and this increases the interaction with the analyte. To evaluate bulk sensitivity, we have considered racetrack MRR with 30% of the sensor (either of HPWG, slot and strip) as shown in the schematic diagram Figure 3.23, where the radius of the MRRs is fixed at 120 μm and other horizontal (L_x) and vertical straight section (L_y) dimension are chosen to be 20 and 90 μm respectively. The Bulk sensitivity is defined as [127]:

Thèse accessible à l'adresse : https://theses.insa-lyon.fr/publication/2024ISAL0120/these.pdf © [C.B. Chander Bhan], [2024], INSA Lyon, tous droits réservés

$$S = \frac{\Delta\lambda_{res}}{\Delta n_{clad}} = \frac{\lambda_{res}}{n_g}\frac{\delta n_{eff}}{\delta n_{clad}} \tag{3.38}$$

Where $\frac{\delta n_{eff}}{\delta n_{clad}}$ defines the change in the n_{eff} due to the change in the RI of cladding $(\delta n_{clad} = 0.0073)$, n_g is defined as the group index. λ_{res} is the resonant wavelength. The $\frac{\delta n_{eff}}{\delta n_{clad}}$ increases as the power in the cladding increases.

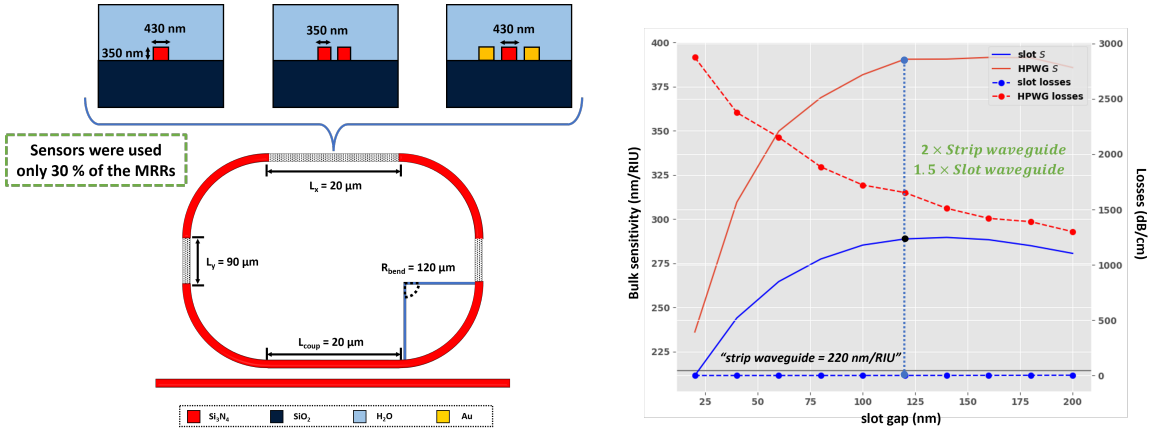

Figure 3.23: Comparison of S for HPWG, slot and strip waveguides a) Schematic diagram of Racetrack MRRs where dotted pattern shows the area where three different waveguide is used to evaluate the S b) S and losses curves as a function of slot gap for slot and HPWG waveguide. The black solid lines represents the strip waveguide sensitivity of 220 nm/RIU

It is noteworthy that both HPWG and slot waveguides exhibit minimum S with a 20 nm gap compared to a 120 nm gap, while the F_{grad} are comparatively higher for the 20 nm configuration. This phenomenon arises from the nature of F_{grad}, which align towards the peak intensity gradient, inducing particle charge and directing forces towards the intensity peak, regardless of the interaction volume of the field with the analyte. Conversely, S relies on a larger interactive volume with high electric field, enhancing sensor sensitivity. Hence, in our investigation, we opted for a 120 nm gap in conjunction with the optimized design of HPWG for practical comparisons. With a core width of 430 nm and a 120 nm gap, the HPWG proposed in this study outperforms slot waveguides by 1.5 times and strip waveguides by 2 times. Additionally, by incorporating a racetrack MRRs with HPWG losses, a respectable Q factor of 3000 can be achieved using the equation described in chapter 2. Furthermore, depending on the application, such a HPWG design can be tailored with narrower dielectric core widths and smaller gaps to enhance optical forces, at the expense of increased device losses.

From all the possibilities discussed above, we preferred to work with the dielectric Si_xN_y strip waveguide for our waveguide design and fabrication, considering the complexity, time constraints, and the overall design and fabrication timeline of the entire device.

Thèse accessible à l'adresse : https://theses.insa-lyon.fr/publication/2024ISAL0120/these.pdf © [C.B. Chander Bhan], [2024], INSA Lyon, tous droits réservés

3.4 Potential depth study: F_{min} and D_{min}

It is pertinent to comprehend that for nanoparticle trapping, as the size decreases, the trapping potential diminishes drastically, increasing the probability of particles escaping the trap due to Brownian motion. To overcome this, it is necessary to maintain a strong optical gradient force, i.e., high enough to reach a potential energy (10 K_BT) greater than three times the Brownian motion kinetic energy in each degree of freedom (1/2 K_BT), as per the rule of thumb described by Ashkin [45].

One can find the potential energy ($U(x)$) from the force calculated above along x-axis is with the following equation :

$$U(x) = \int_0^{\infty} F_{grad} \cdot dx \tag{3.39}$$

Integrating the F_{grad} to infinity would lead to an infinite potential, which is unrealistic in any scenario. Therefore, the integration must be limited to the penetration depth (x_e) of the evanescent field, where 37 $\%$ of the field is confined in the cladding region. Therefore the field equation 3.39 will look like :

$$U(x) = \int_0^{x_e} F_{grad} \cdot dx \tag{3.40}$$

The Figure 3.24.(a) below shows the F_{grad} calculated for different optical powers for a 100 nm dielectric particle along the x-axis, just beyond the waveguide's vertical wall. The F_{grad} values are presented for the center profile of TE Mode E_y (core height = 150nm). The Figure 3.24.(b) depicts the potential depth of the F_{grad} using the above equation3.40. As shown, the F_{grad} calculated for 24, 30, and 36 mW only have enough $U(x)$ to exceed the minimum stable trapping condition of 10 K_BT. However, it is also crucial to determine the amount of power required to fill the proportion of particles in the trap size, which is defined by the penetration depth of the evanescent field in the cladding. To assess this, one must evaluate the probability density as a function of trapping energy using the Maxwell-Boltzmann distribution and partition function, as shown below in Equation 3.41. Subsequently, the proportion of particles can be evaluated for the trap size(x_e) using Equation 3.42.

$$p(x) = \frac{e^{-\frac{u(x)}{K_BT}}}{e^{\int_0^{\infty} \frac{u(x)}{K_BT}}} \tag{3.41}$$

$$D(x) = \frac{\int_0^{x_e} p(x)dx}{\int_0^{\infty} p(x)dx} \tag{3.42}$$

The graph in the Figure 3.25.(c) shows the F_{min} (25 mW) required in the waveguide to achieve optical trapping of the particle within the trap-size. This F_{min} applies to the device designed with a water cladding, a core width of 470 nm, and a core height of 350 nm. Once we know the F_{min} required to trap the particle its important to know what would be the

Thèse accessible à l'adresse : https://theses.insa-lyon.fr/publication/2024ISAL0120/these.pdf © [C.B. Chander Bhan], [2024], INSA Lyon, tous droits réservés

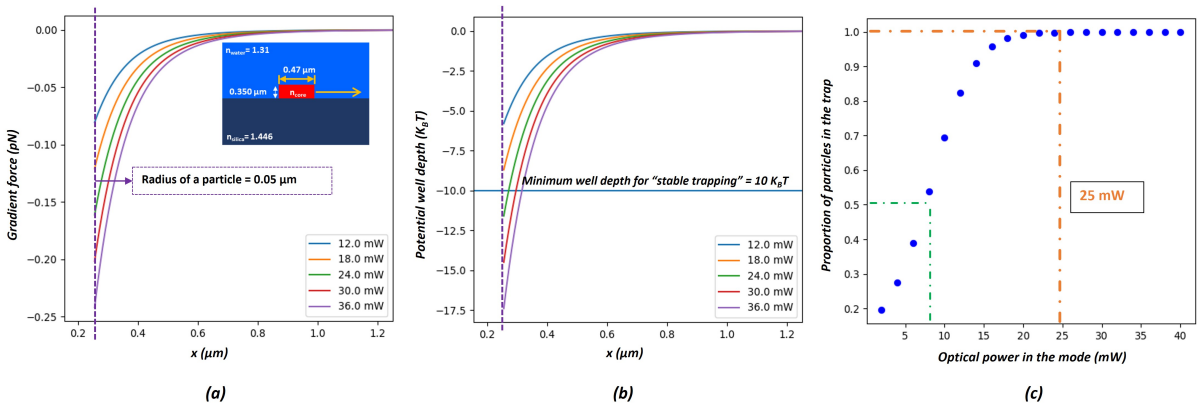

Figure 3.24: Potential well depth curve along x-axis in water cladding : (a) F_{grad} as a function of distance from core/cladding interface at various levels of optical power (b) Potential well depth (U_x) as a function of distance from the core/cladding interface at various levels of optical power (c) Proportion of trapped particles (D_x) in trap-size (e_x)as function of optical power.

minimum distance D_{min} where the particle must be present to observe the optical trapping experimentally.

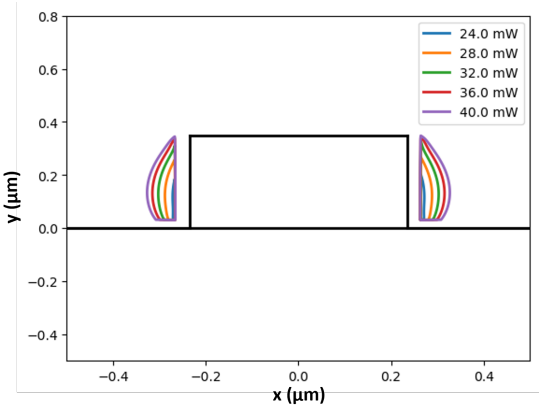

Figure 3.25: Potential depth (10 K_BT) contour lines as function of F_{grad} along x-axis for different optical powers

The D_{min} is defined as the distance from the vertical wall of the waveguide to the point where the potential depth maintains a stable trapping condition ($U_x > 10\ K_BT$). Therefore, the D_{min} where the particle can be trapped is 85 nm for 32 mW optical power and 95 nm for 40 mW, this distance increases with power due to the increasing F_{grad} as shown in the Figure 3.25.

Similarly, using the aforementioned theory, one can easily calculate the F_{grad} and U_x for a core waveguide in air cladding, as shown in the Figure 3.26. Here, the F_{min} required is 50 mW. This increase is primarily because, in air cladding, the core width must be larger to have the fundamental mode (close to radiation mode) that will be less confined in the core and closer to the substrate, as the air cladding RI is low as compare to water cladding.

Achieving high power within the device presents several challenges. Losses—such as coupling, material absorption, and propagation complicates the task of delivering sufficient

Thèse accessible à l'adresse : https://theses.insa-lyon.fr/publication/2024ISAL0120/these.pdf © [C.B. Chander Bhan], [2024], INSA Lyon, tous droits réservés

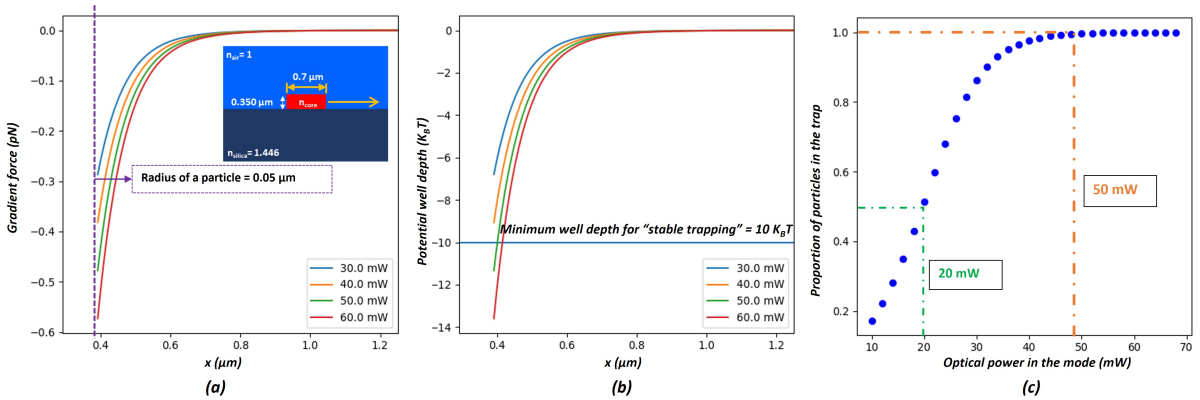

Figure 3.26: Potential well depth curve along x-axis in air cladding : (a) gradient force as a function of distance from core/cladding interface at various levels of optical power (b) Potential well depth (U_x) as a function of distance from the core/cladding interface at various levels of optical power (c) Proportion of trapped particles (D_x) in trap-size (e_x)as function of optical power.

power to the waveguide for effective optical trapping. In this thesis, we address these challenges by employing an inverted taper to enhance coupling efficiency and utilizing MRRs to achieve high power within the ring. This is facilitated by the constructive interference between the bus and ring waveguides when they are positioned in close proximity. To maximize power in the ring (P_{ring}), it is crucial to understand the coupling theory of ring resonators and the various parameters that influence it. In the following section, we will discuss the coupling between the bus waveguide and the racetrack ring.

3.5 MRRs: Coupling factor, Losses, Power in the ring

The ring resonators are the combination of the ring and straight bus waveguide. Figure 3.27 illustrates light guided along the waveguide is transferred to the racetrack ring via a similar coupling mechanism used in a directional coupler. The light is injected into a waveguide either through an angled grating or an edge coupler. There are several factors that influence the spectral characteristics of ring resonators, including coupling efficiency between the ring and straight waveguide, resonator losses, and propagation constants of the modes propagating in the different parts.

In the absence of backward reflection, the amplitudes of the guided modes in the respective waveguides can be represented in matrix form as follows:

$$\begin{bmatrix} B^+ \\ b^+ \end{bmatrix} = \begin{bmatrix} c \cdot t & -jc.\kappa \\ -jc \cdot \kappa & c \cdot t \end{bmatrix} \begin{bmatrix} A^+ \\ a^+ \end{bmatrix} \tag{3.43}$$

where κ and t are the coupling factor and the transmission coefficient respectively and c is the coupling loss. The determination of κ and t using mode solvers are explained in chapter 4. The energy criteria impose that $|t|^2 + |\kappa|^2$ = 1. therefore, the relation between and a^+ and b^+ follows as:

$$a^+ = b^+ e^{(-i\beta(p-L_{coup})+\alpha(p-L_{coup}))} \tag{3.44}$$

Thèse accessible à l'adresse : https://theses.insa-lyon.fr/publication/2024ISAL0120/these.pdf © [C.B. Chander Bhan], [2024], INSA Lyon, tous droits réservés

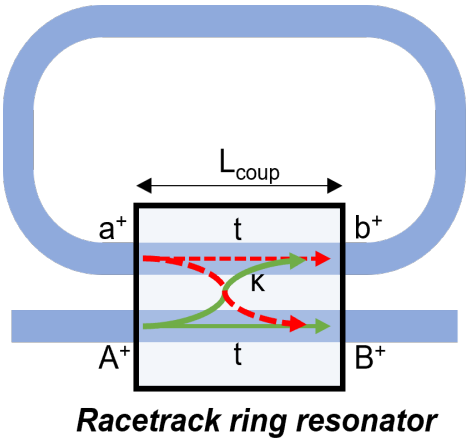

Figure 3.27: A schematic diagram of racetrack ring resonators with a directional coupler.

where β is the propagation constant, α is the resonator losses and p is the racetrack perimeter and L_{coup} is the coupling length. By substituting equation 3.44 in equation3.43, we obtain:

$$B^+ = \frac{\sqrt{1-|\kappa|^2} - e^{-(i\beta+\alpha)p}}{1-\sqrt{1-|\kappa|^2}e^{-(i\beta+\alpha)p}} A^+ \tag{3.45}$$

The transmission of the device is given by multiplying equation 3.45 with its complex conjugate:

$$T = \frac{B^+}{A^+} = \frac{|t|^2 + a^2 - 2a|t|cos(\phi)}{1 + (a|t|)^2 - 2a|t|cos(\phi)} \tag{3.46}$$

where $a = e^{\alpha p}$ is the single pass transition coefficient and $\phi = p\beta$ the single pass phase shift.

The ring shape of the resonator forms a closed loop, which allows the electromagnetic waves to circulate within the cavity, building up energy depending on the quantity of light coupled to the ring and the quantity that leaked with each pass. This contributes to a higher power density within the cavity. Ring resonators are therefore good candidates for optical trapping and sensors in integrated photonic devices. The P_{ring} for ring resonator is defined as follows:

$$P_{ring} = \frac{c^2|\kappa|^2 e^{-2\alpha p}}{1 + c^2 e^{-2\alpha p}(1-|\kappa|^2) - 2ce^{-\alpha p}\sqrt{1-|\kappa|^2}cos(\beta p)} P_{in,\ bus\ waveguide} \tag{3.47}$$

In equation 3.46 and 3.47 the phase (βp) is defined by $\beta_b 2\pi$. In case of racetrack ring resonator, this will be replaced by $2\beta_s(L_1+L_2)+\beta_b 2\pi$, where the β_b and β_s are the propagation constant of the bent and linear section in the racetrack ring resonator, respectively. In most of the cases with mode-solver the β_b already includes the radius of the ring.

In a ring resonator, there are three major coupling conditions: under-coupling ($t > a$) and over-coupling ($t < a$) and critical condition ($t = a$). Most notable is the critical coupling condition, in which the losses are exactly compensated by the coupling of the bus waveguides. This provides the maximum contrast between the resonant peaks. In critical coupling condition, $\sqrt{1-|\kappa|^2} = ce^{-\alpha p}$. so the P_{ring} at critical condition becomes:

Thèse accessible à l'adresse : https://theses.insa-lyon.fr/publication/2024ISAL0120/these.pdf © [C.B. Chander Bhan], [2024], INSA Lyon, tous droits réservés

$$P_{ring} = \frac{1}{|\kappa|^2} P_{in,\ bus\ waveguide} \tag{3.48}$$

As observed from the equation above, three major factors influence the P_{ring}: losses in the ring α, the self-coupling coefficient (τ), and coupling loss (α). The kappa factor (κ), or self-coupling coefficient (τ), can be improved through design optimization to achieve different coupling conditions, as explained below. The loss of the ring waveguide, which results from bending, absorption, scattering, and coupling losses, can be minimized by selecting an optimized design. Most studies overlook the presence of coupling loss in the bus-ring coupling region and assume that the loss of a microring is solely due to the microring waveguide itself [128]. However, it is important to note that in some cases, reducing the coupling gap can increase total losses in the ring due to increased coupling losses, thereby reducing overall performance [129]. To mitigate this, coupling radiation losses can be minimized by using a wider gap between the bus and ring waveguide, which must be carefully optimized (as discussed in the next chapter).

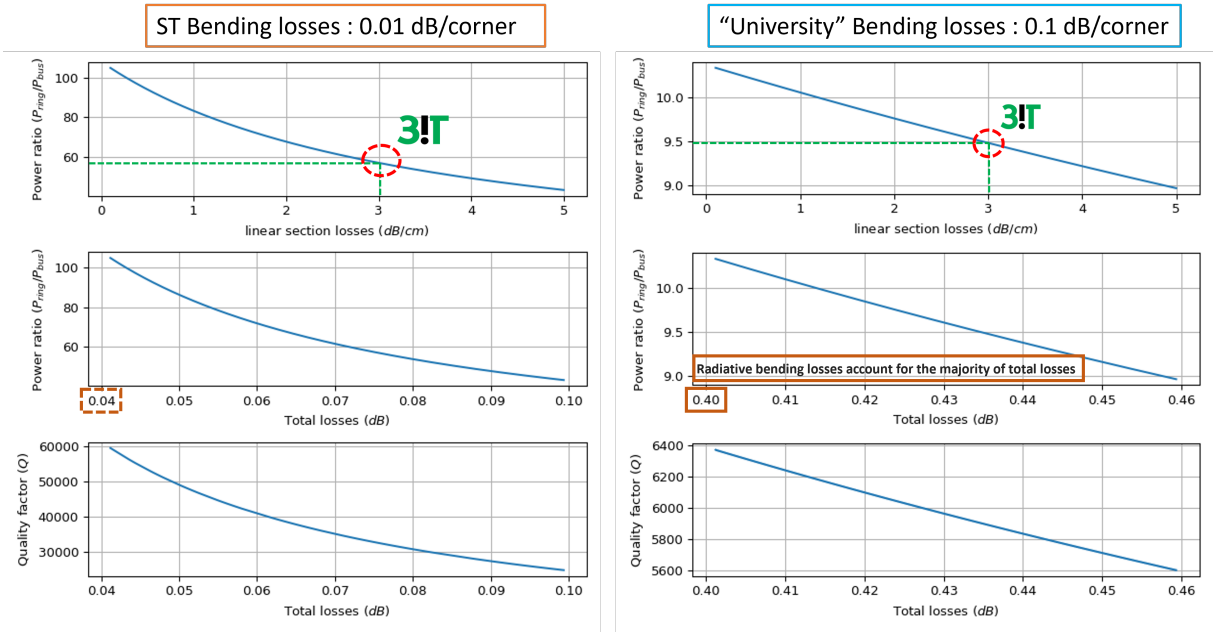

Figure 3.28: Power in the ring ratio (P_{ring}/P_{bus}) as function of Linear propagation losses for two different optimized industrial (ST) and university bending losses using the device fabricated in previous thesis (race track ring resonators) with dimension of horizontal linear section L_x = 10 μm and vertical linear section L_y = 5 μm (19.3% of the total length) and Bending radius = 20 μm (80.7% of the total length). The critical coupling is considered here at resonating wavelength (λ_{res}) of 1.311

One can assess the behavior of P_{ring} with respect to device losses using equations 3.47 and 3.48 for critical coupling conditions, while fixing MRR dimensions such as the horizontal and vertical straight sections and a bending radius (R_{bend}) to 20 μm taken from the previously fabricated and designed devices. It is noteworthy that the majority of the ring circumference consists of bending sections. For this thesis, as we have utilized both ST DAPHNE (Industry) fabricated devices and those fabricated at LN2, 3IT (university of sherbrooke) laboratories, so we have compared the P_{ring} for both scenarios as shown on the left and right sides of the Figure 3.28.

Thèse accessible à l'adresse : https://theses.insa-lyon.fr/publication/2024ISAL0120/these.pdf © [C.B. Chander Bhan], [2024], INSA Lyon, tous droits réservés

Both industrial (ST DAPHANE) and university (INL and 3IT) bending losses represent the performance of Si_xN_y deposited on two different platforms, each optimized to achieve minimal losses at the bending radius of the MRR. In this study, we analyzed devices fabricated using Si_xN_y deposited at both industrial and university platforms, focusing on the R_{bend} to minimize bending losses. The optimization of the R_{bend} plays a crucial role in reducing bending losses, which are a significant factor in the overall performance of the MRR.

The dashed red circles in Figure 3.28 represent the linear propagation losses estimated using the Payne and Lacey method, with a correlation length of 172 nm, a roughness of 5.5 $\times 10^{-}9$ (for e-beam lithography), and refractive indices of 1.9, 1.31, and 1.45 for the core, cladding, and substrate, respectively. As illustrated in Figure 3.28, industrially fabricated devices demonstrate a power ratio of 100:1 in the case of 0 dB/cm linear propagation losses (only accounting radiative bending losses), and 60:1 even under the worst-case scenario of 5 dB/cm linear propagation losses. On the other hand, devices fabricated using the university platform show a power ratio of 10:1 and 9:1 for 0 dB/cm (only accounting radiative bending losses) and 5 dB/cm linear propagation losses, respectively. Consequently, when fabricating the device, it is imperative to optimize the bending section to minimize bending losses. The Figure 3.28 further illustrates how bending losses, a critical component of the MRR, influence its overall performance by affecting the quality factor.

3.6 Concluding and Perspective to Design

In this chapter, we have explored and executed the necessary modeling tasks, establishing a solid foundation for the subsequent design phase. The MST and DDA models employed here not only encapsulate the theoretical underpinnings of our study but also revealed potential challenges and opportunities that may not have been apparent through qualitative analysis alone.

In the first phase of this chapter, we delved into the fundamental waveguide modeling concepts and physics required to initiate simulations. We discussed various methods for determining the propagation constant, including perturbation approaches, Marcatili's analytical approach, and the effective index method, to understand the basic concepts of optical waveguide and the required parameters to use for the modeling of more complex devices or multi-physic modelings.

In the second phase, we validated our models against existing literature to confirm their accuracy, using them as a testing ground for various hypotheses. This process allowed us to validate assumptions and refine our understanding of the optical trapping device. We explored multiple strategies to enhance waveguide-based optical trapping for dielectric nanoparticles in a water fluidic medium, including:

- **Refractive Index Contrast:** While the high index contrast of Si waveguides offers an optical gradient force that is 1.15 pN higher than that of Si_xN_y waveguides, this advantage is insufficient to offset the other challenges associated with silicon waveguides at higher optical powers, such as TPA, high thermal coefficients, and increased losses.

Thèse accessible à l'adresse : https://theses.insa-lyon.fr/publication/2024ISAL0120/these.pdf © [C.B. Chander Bhan], [2024], INSA Lyon, tous droits réservés

- **Higher-Order Modes (HOM) and Fundamental Modes (FM):** HOM waveguides offer multiple maxima and minima in intensity profiles, increasing the likelihood of optical trapping at multiple points. Additionally, due to their lower fabrication tolerances and wider cores, HOM waveguides are easier to fabricate compared to fundamental mode waveguides. Due to their simple designing and as they multiple maxima mode intensities that can to trap large number of particles we have considered this device in our design.
- **Slot and Hybrid plasmonic waveguides (HPWG):** The novel "mode-lift" concept introduced in HPWG not only enhances sensitivity but also improves optical trapping performance. Our rigorous modeling in COMSOL revealed that the optical force with HPWG is approximately three times greater than that of a slot waveguide and twice that of a strip waveguide. However, considering the complexity, time constraints, and the overall design and fabrication timeline of the entire device, we opted for the simpler dielectric strip waveguide design.

Lastly, we discussed the power requirements for achieving optical trapping for the desired particle size, utilizing a potential depth study. We also explored how to achieve the necessary power levels using micro-ring resonator (MRR) structures, including the challenges involved in this approach.

In summary, the modeling work completed in this chapter serves as a critical bridge to the design phase. Each design decision will be informed by the data and predictions generated through our models, ensuring that the final design is both optimal and feasible. The forthcoming design chapter will build upon the foundation laid by the modeling and hypotheses explored here. Additionally, we will design our final device in the next chapter, incorporating all the integrated components required to complete the final device.

Thèse accessible à l'adresse : https://theses.insa-lyon.fr/publication/2024ISAL0120/these.pdf © [C.B. Chander Bhan], [2024], INSA Lyon, tous droits réservés

Chapter 4

Designing: Photonic Integrated circuit

In this chapter, we will use the models and results discussed in the previous chapter to finalize the dimensions of each component in the final device. The chapter is organized into four main sections: “Waveguide Design”, “Bending radius optimization”, “Coupling Section” and finally, “CAD Layout”.

In the “Waveguide Design” section, we will begin by optimizing the dielectric strip waveguide for optical trapping (F_{grad}) and sensitivity studies. This will include finalizing the dimensions of final strip waveguide design, the HOM and FM strip waveguides. The optimized waveguide dimensions will then be used in the next section, where we will investigate and optimize the bending radius (R_{bend}) for MRRs to minimize the total losses of the device, as discussed in the previous chapter. After optimizing the R_{bend}, the next critical aspect of MRRs is coupling modes to the ring via the bus waveguide, which will be addressed in the “Coupling Section.”

In the “Coupling Section,” we will optimize the gap to achieve coupling in MRRs using varFDTD and FDTD Lumerical models. Additionally, we will use these models to optimize the length of the inverted taper to enhance coupling efficiency from the optical fiber to the input waveguide. After optimizing all components, we will utilize Python scripts and the GDSfactory library to design multiple CAD layouts of the devices, considering all potential fabrication scenarios. Moreover, in the final CAD design, we have included linear spirals and snake bends to measure the linear propagation and bending losses in the device.

4.1 Waveguide Design

In this section, we will optimize three strip waveguides. The first waveguide will be used for optical trapping of 100 nm dielectric particles, referred to as the “Final Waveguide Sensor.” The second will be a higher-order mode (HOM) strip waveguide sensor, designed for studying optical trapping independent of particle size, termed the “HOM Waveguide.” The third will be a fundamental mode (FM) strip waveguide sensor, used for comparing the performance of the HOM waveguide w.r.t sensitivity and optical trapping, referred to as the “FM Waveguide.”

Before proceeding with the modeling and optimization of waveguide parameters, it is ne-

Thèse accessible à l'adresse : https://theses.insa-lyon.fr/publication/2024ISAL0120/these.pdf © [C.B. Chander Bhan], [2024], INSA Lyon, tous droits réservés

cessary to determine the refractive index of each material used in the waveguide structure. The primary materials used in the modeling presented in this chapter are Si_xN_y, SiO_2, and water. The dispersion data for SiO_2 and water were sourced from the literature and subsequently fitted using the Sellmeier dispersion law, as shown in Equations 4.1 and 4.2, respectively. These fits were further validated in previous theses [97].

$$n_{SiO_2} = \sqrt{1 + \frac{0.6961663\lambda^3}{\lambda^2 - 0.0684043^2} + \frac{0.4079426\lambda^2}{\lambda^2 - 0.1162414^2} + \frac{0.8974794\lambda^2}{\lambda^2 - 9.896161^2}} \tag{4.1}$$

$$n_{H_2O} = \sqrt{1 + \frac{0.75831\lambda^2}{\lambda^2 - 0.01007^2} + \frac{0.0.08495\lambda^2}{\lambda^2 - 8.91377^2}} \tag{4.2}$$

The above Equation 4.1 and 4.2 represents the dispersion formulae for the real part of the RI of SiO_2 and water in wavelength range of 0.31-6.7 and 0.5-1.75 μm respectively. The RI of standard PECVD Si_xN_y was measured 1.936 at 1310 nm wavelength with ellipsometer and the RI curve as function of wavelength is provided in chapter 5.

4.1.1 Final waveguide sensor

As we have chosen the strip waveguide for our final design, and discussed earlier in the previous chapter, the optical trapping experiment will require high power in the waveguide. Therefore, we have explored two primary solutions. The first approach involves utilizing MRRs, where power in the ring can be significantly increased at critical coupling, although this requires careful optimization. The second approach involves using inverted tapers to enhance coupling efficiency, which are more effective compared to adiabatic tapers. We designed inverted tapers optimized for a thickness (eg_{core}) of 300 nm (detailed explanation provided later) using Si_xN_y.

Furthermore, since the industrial DAPHNE platform is optimized for only two eg_{core} of Si_xN_y, 350 nm and 600 nm, we preferred to continue designing and fabricating within the Laboratoire Nanotechnologies et Nanosystèmes (LN2) and Institut interdisciplinaire d'innovation technologique (3IT) facilities, where greater flexibility is offered for our design requirements. Considering that the FM is easier to couple with light from an optical fiber (due to better mode matching) and results in lower losses, we opted to work with the Fundamental mode of the strip waveguide for the final device.

Once we fixed the thickness of the waveguide at 300 nm, we then needed to optimize the core width (wg_{core}). To ensure we only study the Fundamental mode, we can identify a narrow range of core width where this mode is exclusively confined. Mode identification can be achieved using any available numerical or analytical method. The Figure 4.1 below shows all the fundamental TE and TM modes available in the Si_xN_y strip waveguide for different core widths while the core eg_{core} is fixed. Additionally, the modes are displayed with water cladding, as illustrated in the schematic diagram of the strip waveguide in the Figure 4.1.

From the Figure 4.1 above, by selecting the modes above the radiation mode ($n_{eff} \geq$ refractive index (RI) of substrate - SiO_2) and below the higher-order mode, one can narrow

Thèse accessible à l'adresse : https://theses.insa-lyon.fr/publication/2024ISAL0120/these.pdf © [C.B. Chander Bhan], [2024], INSA Lyon, tous droits réservés

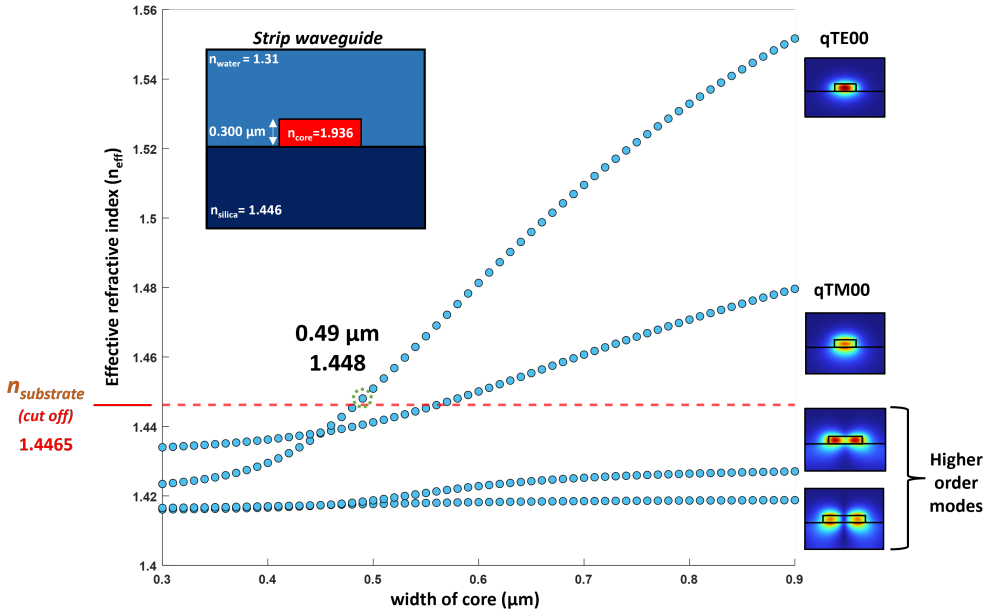

Figure 4.1: n_{eff} as a function of core width, where thickness of the strip waveguide is fixed at 300 nm.

down the window to further optimize the core width for optical trapping applications. It can be observed that there is no mode above the cut-off until 1 μm. Therefore, the optical gradient forces were calculated only for core widths between 0.49 and 1 μm, as shown with closed blue markers in the Figure 4.2.

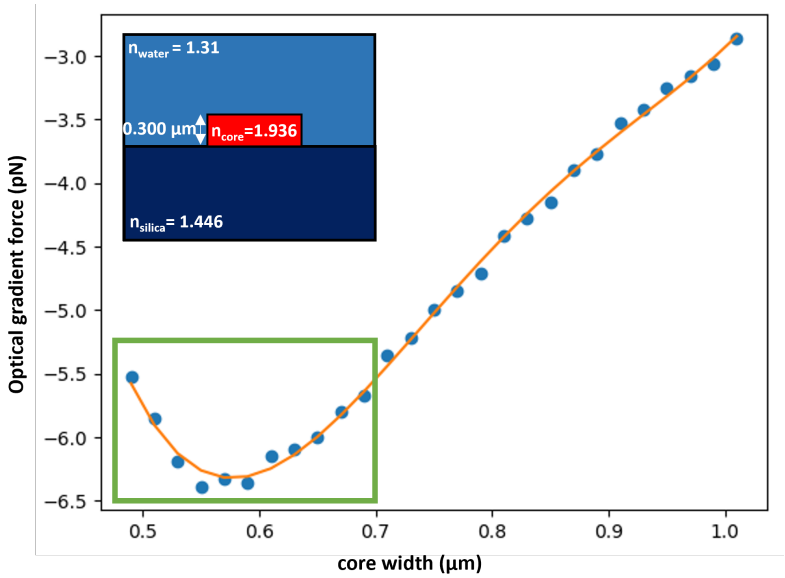

Figure 4.2: F_{grad} as a function of core width for a strip waveguide with a 100 nm dielectric particle. The F_{grad} is evaluated at a normalized power of 1 W with the fundamental mode propagating in the strip waveguide, using the COMSOL FEM model.

As seen in the green box in the Figure 4.2, the gradient of the decaying evanescent field increases up to a certain core width. Beyond this width, the mode in the waveguide becomes highly confined, and the amplitude of the electric field outside is not sufficient to maintain the same optical gradient force (F_{grad}) as with the narrower widths. Consequently, there

Thèse accessible à l'adresse : https://theses.insa-lyon.fr/publication/2024ISAL0120/these.pdf © [C.B. Chander Bhan], [2024], INSA Lyon, tous droits réservés

is a narrow window of core widths that interest us. Beyond a certain core width, both the sensitivity and F_{grad} decrease.

In micro ring resonators cavity, the sensitivity is determined by the wavelength shift caused by temperature, physical deformation, or changes in waveguide core and cladding composition. In a ring resonator, the resonating wavelength is determined by the following equation :

$$\lambda_{res} = \frac{n_{eff} L}{m} \tag{4.3}$$

where λ_r is resonance wavelength, n_{eff} is the effective index of the cavity, L is the length of the ring, and m is the azimuthal order. The azimuthal order refers to the number of times the light travels around the circumference of the ring before it is coupled out. (integer corresponding to the resonance mode order). The optical length ($n_{eff}L$) for circular ring is defined by, $n_{eff}L = n_{eff}^{bend}(2\pi r_{bend})$ and for racetrack ring resonators is, $L = n_{eff}^{linear}(2(L_x + L_y)) + n_{eff}^{bend}(2\pi r_{bend})$. n_{eff}^{linear} and n_{eff}^{bend} are defined and n_{eff} of linear and bending section respectively.

In the optical trapping case, the particle will be trapped around the waveguide, covering the maximum evanescent field. As a result of the change in composition of the cladding, the effective medium theory as illustrated in the Figure 4.3 can be used to calculate the approximate index of the fluid medium (n_{fluid}) followed by Equation 4.4.

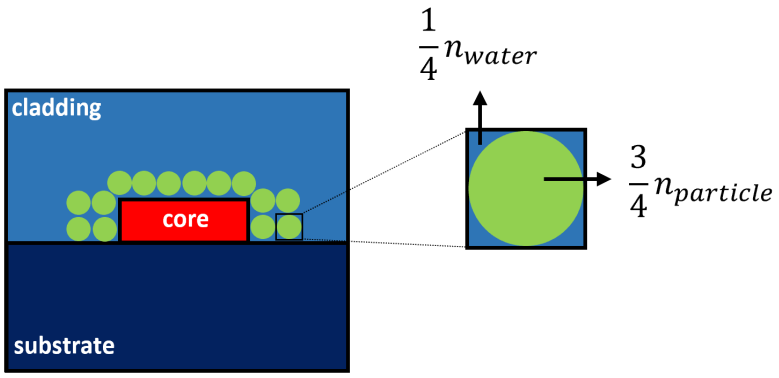

Figure 4.3: Estimation of the approximate refractive index of a fluid surrounding particles using effective medium theory.

$$n_{fluid} = \frac{3}{4}n_{particle} + \frac{1}{4}n_{water} \tag{4.4}$$

where, $n_{particle}$ and n_{water} is the RI of the nanoparticles and water respectively. The change in RI of the cladding will alter the mode n_{eff} of the ring, resulting in a change in wavelength shift, which can be expressed as follows:

$$\Delta\lambda_{res} = \frac{\Delta n_{eff}\lambda_{res}}{n_g} \tag{4.5}$$

where, Δn_{eff} is the change in the mode n_{eff} of the ring, λ_{res} is the resonating wavelength calculated above in equation. n_g is the group index, corresponds to the relation with c/v_g

Thèse accessible à l'adresse : https://theses.insa-lyon.fr/publication/2024ISAL0120/these.pdf © [C.B. Chander Bhan], [2024], INSA Lyon, tous droits réservés

which represents the velocity at which the envelope of the propagating pulse travels and is a characteristic of the dispersive medium or a waveguide [107].

As $\Delta\lambda_{res}$ is directly proportional to the sensitivity, we considered $\Delta\lambda_{res}$ as a sensitivity parameter and will be recalled as sensitivity in further discussion. To optimize the waveguide for both sensitivity and optical trapping applications, one could directly observe the relation between $\Delta\lambda_{res}$ and the F_{grad} with respect to the core width, as shown in the Figure 4.4.

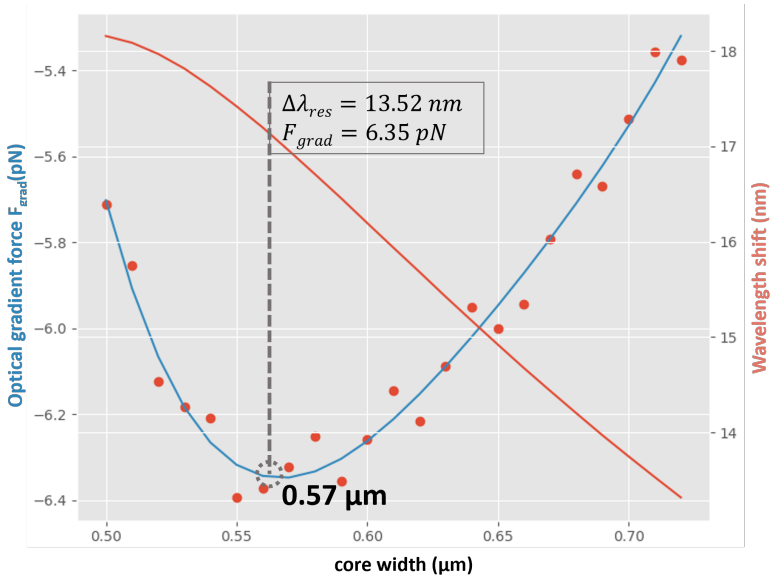

Figure 4.4: Optimization of final waveguide core width : F_{grad} (solid blue line) and wavelength shift (orange line) for varying core width : F_{grad} calculated here are for 100 nm dielectric particle with 1 W of normalized power.

It is apparent from the Figure 4.4 that a narrower core width (500 nm) provides higher sensitivity while a sharp gradient increases F_{grad} up to 590 nm of the core width. If only one of the parameters is essential, then it can easily be chosen but at the end goal, it is important for the device to have high trapping force and be sensitive. In this case, the gain percentage in F_{grad} must be equal to the loss percentage in sensitivity to determine the optimal core width. As a result, instead of losing the maximum of either parameter, it would be better to find the optimal point where the gain equals the loss.

This could be done by finding the relative difference percentage between two F_{grad} (changing from the initial positional to the position want to evaluate) and sensitivity levels for both positions. The least difference between the relative change will be the optimized width where force is maximised without compromising the sensitivity parameter. We have optimized our core width at 570 nm for Si_xN_y strip waveguides with a eg_{core} of 300 nm.

4.1.2 HOM and FM Waveguide

From the previous chapter, we observed that higher-order modes (HOM) offer the potential to enhance the trapping of a larger number of particles due to their multiple intensity maxima and minima. Interestingly, HOM waveguides have not been extensively studied for optical trapping applications in the literature. Therefore, we dedicated one photonic chip

Thèse accessible à l'adresse : https://theses.insa-lyon.fr/publication/2024ISAL0120/these.pdf © [C.B. Chander Bhan], [2024], INSA Lyon, tous droits réservés

specifically to HOM-based MRR devices, where we aim to compare their performance with fundamental mode (FM) MRRs.

To conduct a comprehensive comparative analysis between the FM and HOM MRR devices, both devices must share the same n_{eff} while exhibiting distinct mode profiles for the FM and HOM waveguides. This ensures that the comparison yields meaningful and reliable results. As illustrated in the Figure 4.5, the plot demonstrates the relationship between n_{eff} and core width for the strip waveguide, depicted schematically in the diagram.

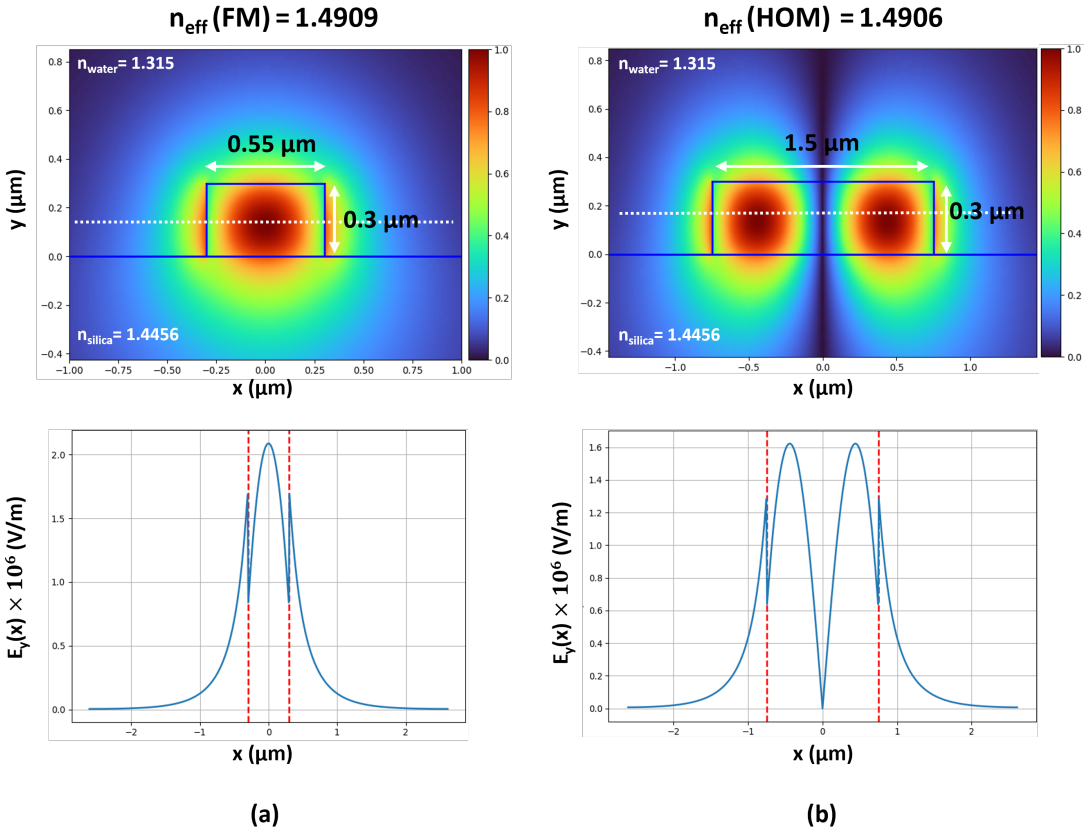

Figure 4.5: Optimization of HOM and FM waveguide core width : (a) represents the TE mode-profile of FM mode with $E_y(x)$ profile at y = 0.15 μm with one maxima in the waveguide and (b) represents the TE mode-profile of HOM mode with $E_y(x)$ profile at y = 0.15 μm with two maxima in the waveguide.

To design these devices, we selected the core width of the HOM waveguide to be 1.5 μm and the FM waveguide to be 0.55 μm, primarily to achieve similar n_{eff} (n_{eff} (FM) $\simeq$ n_{eff} (HOM) = 1.49), which is essential for a meaningful comparison. While this design approach may result in a reduction in F_{grad} forces, the goal here is not to optimize for trapping a specific particle size. However, if there will be a need to increase the F_{grad} forces in these devices, an alternative approach would be to increase the size of the particle using.

Thèse accessible à l'adresse : https://theses.insa-lyon.fr/publication/2024ISAL0120/these.pdf © [C.B. Chander Bhan], [2024], INSA Lyon, tous droits réservés

4.2 Bending radius optimization

Compared to linear waveguides, bent waveguides introduce additional losses, primarily bending radiation losses. These losses are particularly significant in MRRs, where the bending sections constitute the majority of the structure. Analyzing the modes and radiation losses in bent waveguides requires global cylindrical coordinates, unlike straight waveguides where Maxwell's equations are solved in a local Cartesian system. The propagation constant along the width of the bend is not uniform, complicating the analysis.

M. Heiblum proposed the use of conformal mapping to address this challenge [130]. The conformal mapping method applies a coordinate transformation to the wave equation, converting the curved boundaries of the structure in the original (x, y) coordinates into straight boundaries in the new (u, v) coordinates as shown in Figure 4.6.

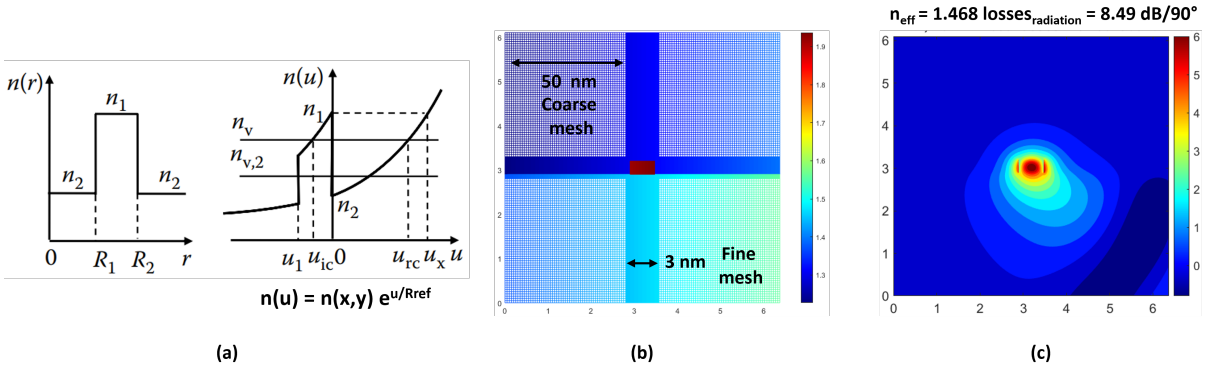

Figure 4.6: Conformal mapping technique: (a) Relationship between 2D Cartesian straight boundaries and new (u,v) cylindrical coordinate boundaries, where the RI has an exponential dependence on the R_{bend}. (b) Meshing and RI mapping of the bending strip waveguide with a R_{bend} = 50 μm, core width of 570 nm, and thickness of 300 nm in the conformal mapping model (developed at INL). (c) TE bending mode and radiation losses (8.49 dB/90°) for the structure shown in (b).

Explanation of radiation bending losses with conformal mapping. Refractive index of the cladding versus r increase and becomes higher than the effective index of the mode. This induces losses because the evanescent field in the cladding becomes propagative and then adds losses due to leakage of the power of the mode.

The bending losses calculated through conformal mapping demonstrate an exponential dependence on the R_{bend}, as predicted by Marcuse's approximation model [131].In conformal mapping, it can be observed that the RI of the cladding increases along the bend radius (R_{bend}) and becomes higher than the n_{eff} of the mode. This results in radiation losses, as the evanescent field in the cladding starts to propagate, leading to power leakage and increased losses for the mode. Moreover, in high-index contrast waveguides, such as Si / SiO_2 and Si_xN_y / SiO_2, this model tends to produce inaccurate loss values [132, 133]. For instance, the radiation losses estimated by the conformal mapping model developed at INL for a Si_xN_y strip waveguide with a R_{bend} of 50 μm were 8.49 dB/90°, which is significantly 100 times higher than values reported in previous experimental studies and literature for Si_xN_y waveguides even with 20 μm bending radius for core width of 600 nm [134].

Thèse accessible à l'adresse : https://theses.insa-lyon.fr/publication/2024ISAL0120/these.pdf © [C.B. Chander Bhan], [2024], INSA Lyon, tous droits réservés

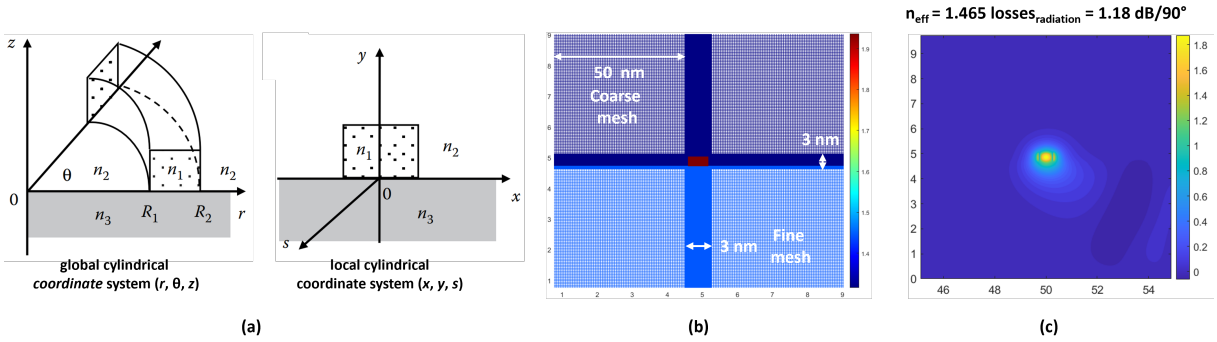

Figure 4.7: FVFD bending mode solver: (a) Representation of the global cylindrical coordinate and local coordinate systems used in the fully vectorial mode solver. (b) Meshing and RI mapping of the bending strip waveguide with a R_{bend} of 50 μm, core width of 570 nm, and thickness of 300 nm in the FVFD model (developed at INL). (c) TE bending mode and radiation losses (1.18 dB/90°) for the structure shown in (b).

This discrepancy arises because, in high-index contrast and tightly bent waveguides, the modes become highly hybridized (not pure TE or TM modes), making Marcuse's and other analytical approximations insufficient. In such cases, a full-vectorial numerical solution is necessary to accurately analyze the modal characteristics. To address this, we utilized the FDFV mode solver developed at INL [87], which incorporates transparent boundary conditions (TBC). The FDFV mode solver demonstrated convergence within a 4.5 μm $\times$ 4.5 μm window and used a coarse mesh of 50 nm and a fine mesh of 5 nm at the waveguide core, ensuring an accurate calculation of the bending losses of 1.18 dB/90° for R_{bend} of 50 μm in water cladding as shown in Figure 4.7.

Moreover, bending losses in waveguides are indeed more complex than linear losses, comprising multiple types that each contribute to the overall loss in different ways. These losses primarily include mode-mismatch losses, radiation losses, and linear losses.

1. Mode-mismatch losses: These losses occur due to the mismatch in mode profiles (that involves back reflection) between straight and curved sections of the ring. However, these losses are typically minimal and form a smaller part of the total bending losses. As the mode propagates from a straight to a curved section, the change in the waveguide structure causes some deviation in the mode shape, resulting in a slight loss.

2. Radiation losses: This is the largest contributor to bending losses. The curvature of the waveguide reduces the confinement of the mode, particularly on the outer edge of the bend, causing it to radiate away. These losses decrease as R_{bend} increases because the curve becomes gentler, allowing the mode to remain more confined by the waveguide core.

3. Linear losses: These are the same propagation losses that occur in straight waveguides due to material absorption, scattering, and other intrinsic waveguide factors. These losses are present whether the waveguide is straight or bent.

As the R_{bend} increases, radiation losses decreases. Additionally, the improved mode confinement towards the center of the bending waveguide facilitates smoother transitions between

Thèse accessible à l'adresse : https://theses.insa-lyon.fr/publication/2024ISAL0120/these.pdf © [C.B. Chander Bhan], [2024], INSA Lyon, tous droits réservés

the straight and curved sections, leading to better mode matching and further minimizing losses. However, as the bending section lengthens with a larger radius, the total propagation losses (due to absorption, scattering from surface roughness, etc.) increase in proportion to the waveguide length.

Thus, when plotting total bending losses as a function of R_{bend}, the curve typically shows a parabolic nature. At small radii, radiation losses dominate, leading to high overall losses. As the radius increases, radiation losses decrease, but the total propagation losses increase because the waveguide length grows. This results in a curve that initially drops and then rises again, reflecting the competing effects of radiation and propagation losses.

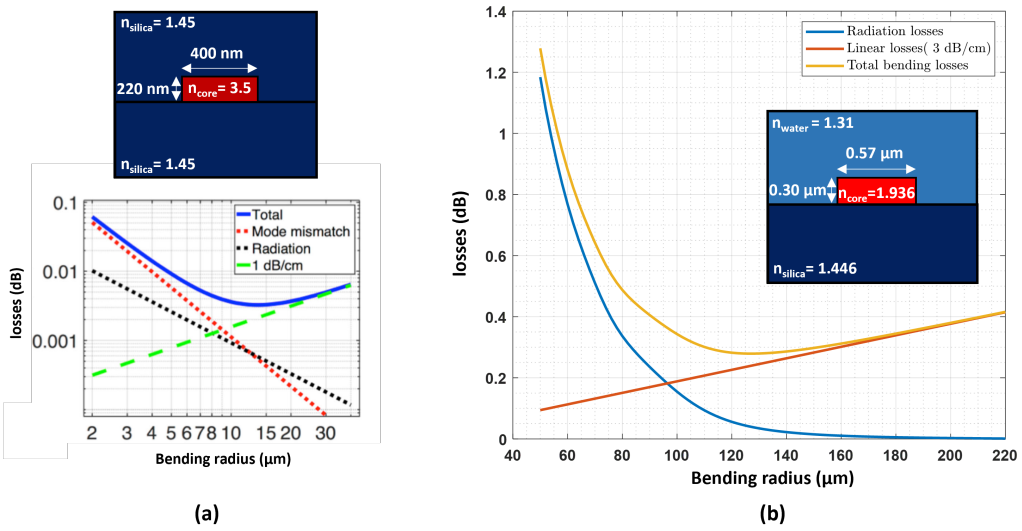

Figure 4.8: Optimization of Bending radius : (a) illustrates the losses as the function of bending radius in Si strip waveguide buried under SiO_2 at 1550 nm [135] (b) illustrates the losses as the function of bending radius in Si_xN_y strip waveguide in H_2O cladding as shown in the schematic diagram at 1310 nm wavelength.

Figure 4.8.(a) illustrates this relationship, showing a downward slope as radiation losses decrease with increasing R_{bend}, followed by an upward trend as the extended length of the bending section leads to higher propagation losses. Using Payne and lacey method [136] as described in chapter 2, we estimated the linear propagation losses to be approximately 3 dB/cm for PECVD Si_xN_y. Using FDFV mode solver, we plotted the relationship between total bending losses (linear + radiation losses) and R_{bend} to identify the optimized R_{bend}, where total bending losses are minimized, as shown in the Figure 4.8.(b). As can be seen in the Figure 4.8, at a R_{bend} of 120 μm, the total bending losses reach their minimum with radiation losses of 0.056 dB/90.

This behavior is typical for strip waveguides. However, for rib waveguides or hybrid plasmonic waveguides, the radiation losses themselves may exhibit a parabolic nature, as these structures introduce additional complexities in mode confinement and radiation behavior due to their unique geometries and material properties.

Leveraging the integrated platforms at LN2, 3IT, we decided to incorporate racetrack-shaped MRR's in our chips. Racetrack MRR's offer the distinct advantage of allowing an increase in the core width of the strip waveguide, which further reduces radiation losses and achieves higher optical power in the ring—essential for optical trapping applications. In our racetrack

Thèse accessible à l'adresse : https://theses.insa-lyon.fr/publication/2024ISAL0120/these.pdf © [C.B. Chander Bhan], [2024], INSA Lyon, tous droits réservés

MRR design, we created one sensing area. For these area, we utilized the previously optimized straight waveguide (cross-section : (570 $\times$ 300 nm) for efficient optical trapping. Additionally, we increased the core width to 610 nm in the bending sections. This adjustment helped reduce the radiation losses in the bending sections to 0.0014 dB/90° bend.

4.3 Coupling section : Directional couplers

Directional couplers are fundamental optical components that enable the transfer of power, either fully or partially, from one waveguide to another when they are placed in close proximity. To understand this concept, consider two identical single-mode dielectric waveguides, each supporting the same TE polarization mode, placed close enough for the propagating fields to interact, as illustrated in the Figure 4.9. When light is coupled into one of the waveguides, the proximity of the two waveguides results in the formation of supermodes—specifically, odd and even modes. These modes, depicted as blue and green fields in the Figure 4.9, the red curve field represent the total field as a combination of the overlap integral of the odd and even modes.

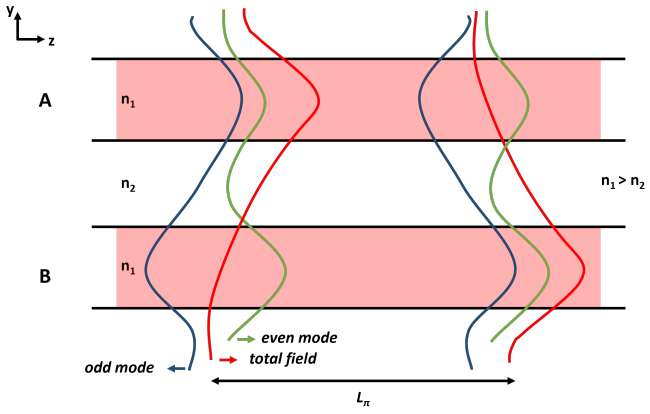

Figure 4.9: Directional coupler working principle: The green, blue, and red curves represent the even, odd, and total mode fields propagating in the dielectric coupled waveguide system when the waveguides are placed close enough to each other.

As light propagates through the waveguides, after a certain distance, known as the critical length, the total field will be fully transferred to the other waveguide. This critical length is defined as the point where the two modes are in phase opposition, causing all the power to be transferred to the adjacent waveguide. The critical length (L_π) can be mathematically defined by the equations provided below :

$$L_\pi = \frac{\pi}{\beta_{even} - \beta_{odd}} \tag{4.6}$$

In the literature, Coupled Mode Theory (CMT) [137, 138] and Marcatill's approach [84] are widely recognized as analytical approach for determining the coupling length and coupling coefficient (τ, κ) between rectangular waveguides. The self-coupling coefficient (τ) specifies the fraction of the amplitude transmitted on each pass of light through the coupler. The cross-coupling factor κ specifies the fraction of the amplitude transmitted on each pass

Thèse accessible à l'adresse : https://theses.insa-lyon.fr/publication/2024ISAL0120/these.pdf © [C.B. Chander Bhan], [2024], INSA Lyon, tous droits réservés

of light between bus to ring or ring to bus. In this thesis, we employed a refined version of Marcatill's method by Kuznetsov [139, 140] (detailed equations are provided in the annexes) to calculate the coupling factor (κ) and coupling length (L_c) between the bus and ring waveguide in the MRRs. Furthermore, this analytical approach was verified through varFDTD and FDTD simulations compared with the results of recent publication [141], as shown in Figure 4.10.

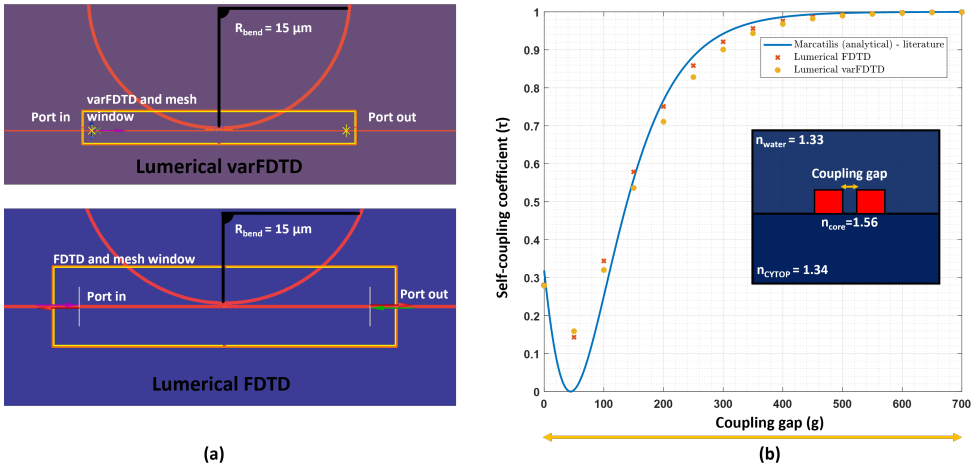

Figure 4.10: VarFDTD and FDTD coupling waveguide model comparison with the literature's analytical method: (a) Illustration of the VarFDTD and FDTD model in Lumerical, utilizing ports, a Gaussian source, and a monitor to observe the modes. (b) Self-coupling coefficient as a function of the coupling gap between the bus and ring waveguides. The literature structure [142] (depicted in the schematic diagram within the graph) is used for comparison with the FDTD and VarFDTD models developed in this thesis.

4.3.1 Circular and Racetrack MRRs

After developing the models, they were used to determine the range of coupling gaps required for the fabrication and design of both circular and racetrack MRRs. We utilized varFDTD simulations to model these devices, where computational intensity was significantly reduced by solving Maxwell's equation only for coupling area. This method allowed us to optimize the coupling gap and design the coupling section of the ring while accounting for fabrication tolerances.

For circular MRRs, the cross-sectional dimensions along the bus and ring waveguides were kept identical to facilitate efficient light coupling into the ring, as both would propagate the same mode, as previously discussed. In circular MRRs, the entire ring is employed as the sensing component, designed with a cross-section of 570 $\times$ 300 nm. Therefore, the bus waveguide was also designed with the same dimensions. The coupling simulations were performed using varFDTD in Lumerical, with a fine mesh of 5 nm throughout the coupling region, at a wavelength of 1310 nm, for different coupling gaps, as illustrated in the Figure 4.11.

Similar models were used in racetrack MRRs by adding a straight coupling length (L_c) in the coupling region. Racetrack MRRs offer advantages over circular MRRs, such as reduced bending losses by employing a wider core width in the bending sections, improved

Thèse accessible à l'adresse : https://theses.insa-lyon.fr/publication/2024ISAL0120/these.pdf © [C.B. Chander Bhan], [2024], INSA Lyon, tous droits réservés

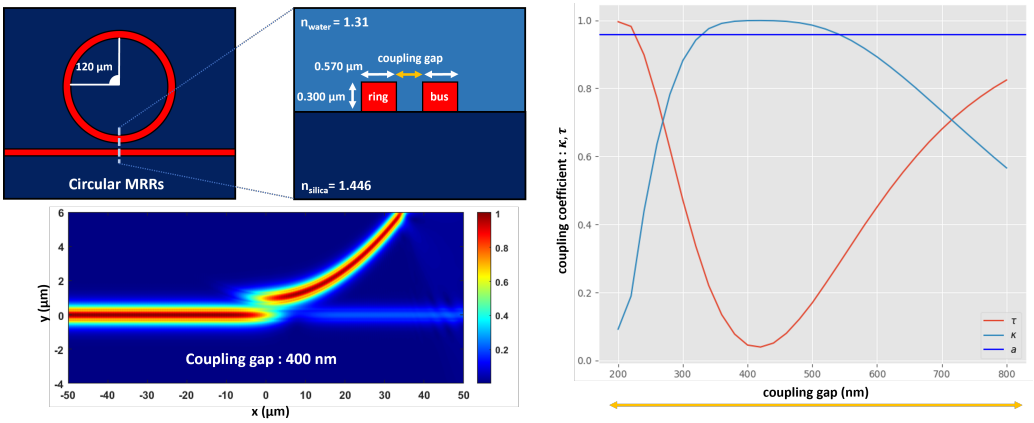

Figure 4.11: Coupling coefficients (τ, κ) as function of coupling gap in circular MRRs: The schematic diagram of the coupling area with all critical dimensions including X-Y field profiles of coupling region is shown on the left side. The τ, κ, a as a function of the coupling gap are depicted on the right side.

coupling efficiency, and greater fabrication tolerance. As shown in the Figure 4.12, the varFDTD modeling illustrates a graph between the coupling coefficient and the coupling gap. The relationship between the self-coupling coefficient and the coupling gap reveals the coupling condition of the ring resonator. In the racetrack coupling section, a L_c of 23 μm was considered.

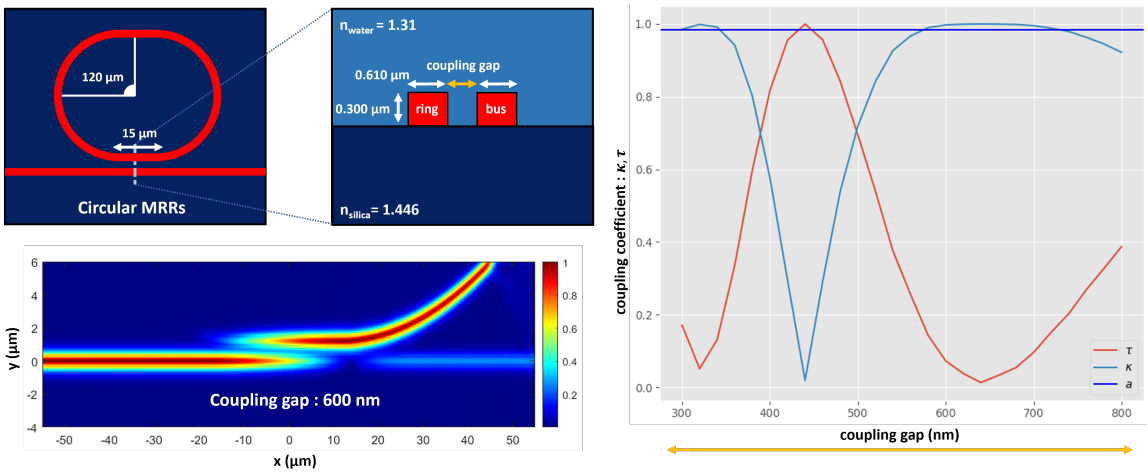

Figure 4.12: Coupling coefficient (τ, κ) as function of coupling gap in racetrack MRRs: The schematic diagram of the coupling area with all critical dimensions including X-Y field profile of coupling region is shown on the left side. The τ, κ, a as a function of the coupling gap is depicted on the right side.

For the specific design structure shown in the above two Figures 4.11 and 4.12, the circular MRRs achieved critical coupling at a coupling gap of 220 nm. In contrast, the racetrack MRRs, incorporating a directional coupler with a coupling length (L_c) of 23 μm, achieved critical coupling at a gap of 430 nm. Accounting fabrication challenges and potential variations, multiple MRRs were designed with a range of coupling gaps. Specifically, circular MRRs were designed with coupling gaps ranging from 200 to 750 nm, while racetrack MRRs were designed with gaps ranging from 250 to 600 nm.

Thèse accessible à l'adresse : https://theses.insa-lyon.fr/publication/2024ISAL0120/these.pdf © [C.B. Chander Bhan], [2024], INSA Lyon, tous droits réservés

4.3.2 FM and HOM MRRs

To excite the higher-order mode (HOM) in the bus waveguide, direct coupling via optical fiber is not feasible. This is because, in the butt-coupling setup, we use a single-mode optical lensed fiber that couples only the fundamental mode to the waveguide. Additionally, with adiabatic tapers at the beginning, it is ensured that no other modes are excited during propagation. Therefore, a viable method to achieve this is by using directional couplers. In the circular MRR configuration, the bus waveguide initially propagates the fundamental mode, which is then coupled into the higher-order mode within the ring resonator. Given the complexity of dealing with HOM, analytical methods are no longer accurate or feasible. Therefore, we employed the varFDTD and FDTD methods (as discussed previously) in this modeling to accurately determine the self-coupling coefficient as a function of the coupling gap, as illustrated in the Figure 4.13.

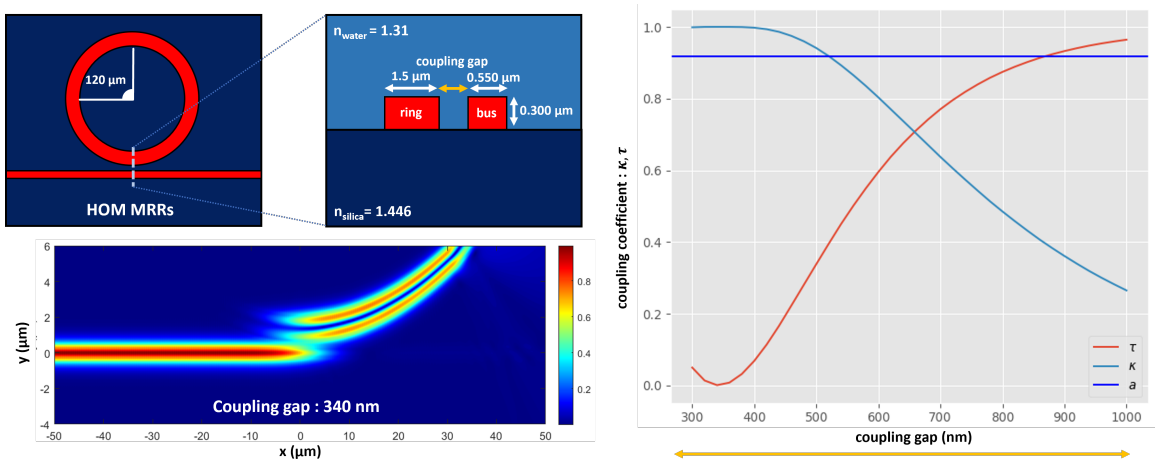

Figure 4.13: Coupling coefficients (τ, κ) as function of coupling gap in HOM MRRs: The schematic diagram of the coupling area with all critical dimensions including X-Y field profiles of coupling region is shown on the left side. The τ, κ, a as a function of the coupling gap are depicted on the right side.

Each photonic chip incorporated spiral and snake bends designed to experimentally measure the bending and linear propagation losses of the waveguides. For the HOM photonic chip, which requires excitation of the higher-order mode (HOM) from a fundamental mode waveguide, we have implemented directional couplers at the beginning of the spirals and snake bends as shown in Figure 4.23. These couplers are optimized to ensure the excitation of the HOM and will be used for precise characterization.

For this directional coupler, the coupling gap was fixed at 600 nm to minimize fabrication complexity and challenges. The optimal length of the directional coupler needed to achieve complete transfer of the fundamental mode (FM) into the higher-order mode (HOM) was determined to be 30 μm.

For another MRRs where only FM is considered in both bus and ring. This optimized design of the strip waveguide 4.1.2 aimed at sensitivity and optical trapping comparisons with HOM MRRs, features a core width of 0.55 μm and a thickness of 300 nm. Since the same mode is needed in both the ring and bus waveguide for FM MRRs, a schematic model and mode-field profile, including the relation of the coupling coefficient as a function of the coupling

Thèse accessible à l'adresse : https://theses.insa-lyon.fr/publication/2024ISAL0120/these.pdf © [C.B. Chander Bhan], [2024], INSA Lyon, tous droits réservés

gap, are depicted in the Figure 4.14.

Moreover, for the spiral and snake bends in the FM MRRs photonic chip, directional couplers are not required. This is because the FM mode can be directly excited using an optical lensed fiber at the butt-coupling setup during characterization, simplifying the design and minimizing additional loss sources.

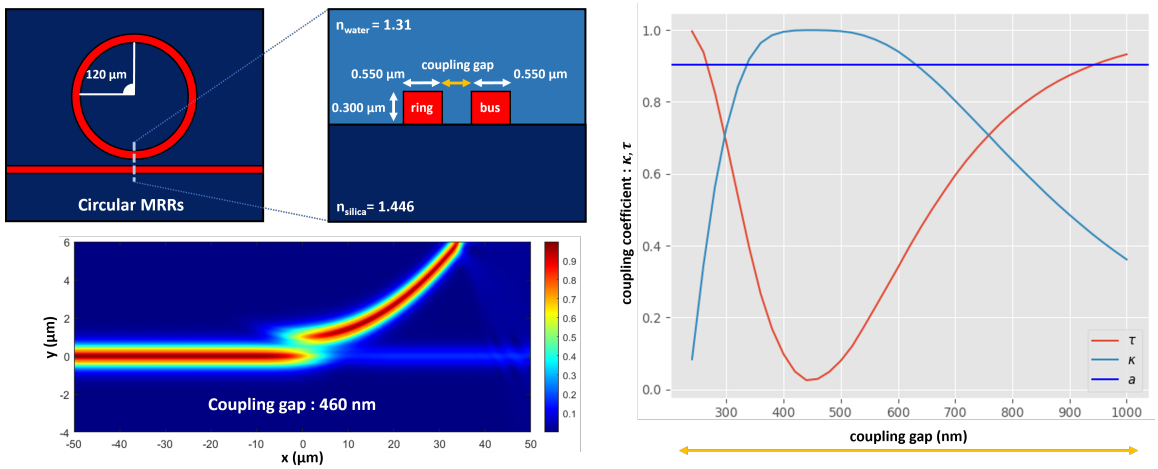

Figure 4.14: Coupling coefficients (τ, κ) as function of coupling gap in FM MRRs: The schematic diagram of the coupling area with all critical dimensions including X-Y field profiles of coupling region is shown on the left side. The τ, κ, a as a function of the coupling gap are depicted on the right side.

It is never fully reliable to base fabrication solely on a particular simulated optimized geometry, as the fabrication process often yields results that differ from the simulated ones due to various factors. Therefore, to account for fabrication challenges and ensure redundancy, we designed the photonic chips for HOM MRRs with a range of coupling gaps from 200 to 640 nm and 200 - 750 nm for FM MRRs. This variation around the optimal coupling gap ensures that we capture a broader spectrum of possible outcomes in the final design, providing more flexibility for successful device performance.

4.4 Edge couplers : linear tapers

In PICs, edge couplers play a crucial role in facilitating the efficient transfer of optical signals between waveguides of different sizes or between diverse optical components. These structures ensure minimal loss and mode distortion during transitions, making them essential for preserving signal integrity within the circuit [143]. As discussed in the previous chapter, enhancing coupling efficiency for high-power delivery in the device is critical. Consequently, efficient fiber-to-chip coupling is a key factor in optimizing overall system performance.

Edge couplers, also known as tapers, work by gradually transitioning the size and shape of a waveguide along its length, allowing smooth passage of the mode between regions with varying optical properties while minimizing mode distortion. These transitions can be achieved using different taper designs, such as exponential [144], parabolic [145], linear, or inverted shapes [146], as illustrated in the Figure 4.15.

Thèse accessible à l'adresse : https://theses.insa-lyon.fr/publication/2024ISAL0120/these.pdf © [C.B. Chander Bhan], [2024], INSA Lyon, tous droits réservés

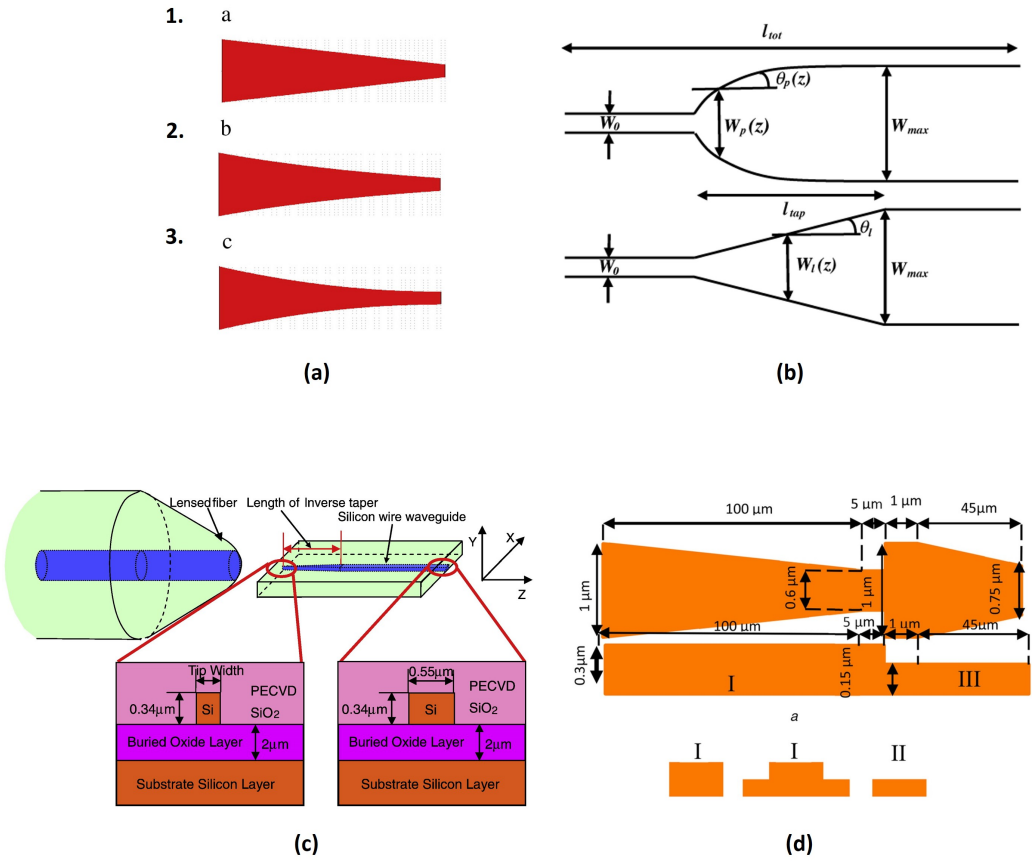

Figure 4.15: Common types of tapers used in literature to enhance the coupling efficiency : (a) schematic comparison of linear, exponential and quadratic taper shape [144] (b) parabolic taper purposed by Hettrick [145] (c) Linear Si inverted taper for butt-coupling setup [144] and Si_xN_y inverted taper [146].

Thèse accessible à l'adresse : https://theses.insa-lyon.fr/publication/2024ISAL0120/these.pdf © [C.B. Chander Bhan], [2024], INSA Lyon, tous droits réservés

In our studies, we employed linear inverted tapers and adiabatic tapers to optimize performance. Inverted tapers were utilized to enhance fiber-to-chip coupling efficiency, ensuring more effective power transfer. Adiabatic tapers were applied both for fiber-to-chip coupling and to ensure smooth transitions of the FM within the racetrack MRRs, particularly from the bending sections to the sensing areas, minimizing losses and maintaining mode integrity.

4.4.1 Inverted tapers

To design inverted tapers, the first crucial step is optimizing the dimensions at the input section. At this point, the cross-section should be carefully chosen to ensure that both TE and TM modes exhibit the same n_{eff}. Additionally, the beam waist at the taper's input must closely match the beam waist of the optical lensed fiber that will be used for coupling light into the chip during the optical bench setup.

At the INL optical bench, we are using lensed fibers with a beam waist of 1.5 μm. Consequently, we optimized the input cross-section to be 300 $\times$ 300 nm of Si_xN_y, buried under a SiO_2 cladding, which exhibits a comparable beam waist. This configuration is shown in the Figure 4.16, which represents the n_{eff} as a function of the waveguide's core width at the input of the inverted tapers.

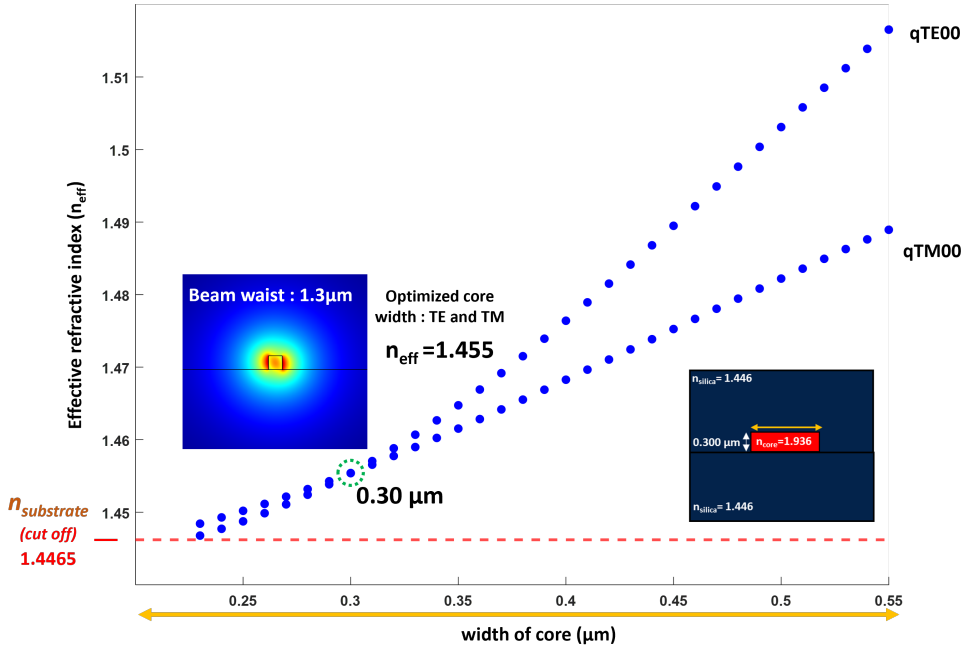

Figure 4.16: n_{eff} as function of core width at the input of inverted tapers with fixed thickness of 0.300 μm.

To further study the coupling efficiency between the optical lensed fiber and the chosen waveguide dimensions, we employ the overlap integral method. This method quantifies the overlap between the optical mode of the lensed fiber and the waveguide mode, allowing us to calculate the coupling efficiency (Γ).

Thèse accessible à l'adresse : https://theses.insa-lyon.fr/publication/2024ISAL0120/these.pdf © [C.B. Chander Bhan], [2024], INSA Lyon, tous droits réservés

$$\Gamma = \frac{\left| \iint \mathbf{E}_{\text{fiber}}(x,y) \cdot \mathbf{E}^*_{\text{waveguide}}(x,y)\, dx\, dy \right|^2}{\left(\iint |\mathbf{E}_{\text{fiber}}(x,y)|^2\, dx\, dy \right) \cdot \left(\iint |\mathbf{E}_{\text{waveguide}}(x,y)|^2\, dx\, dy \right)} \tag{4.7}$$

Using the formula mentioned above 4.7, we calculated a coupling efficiency (Γ) of 75.3 % between the fundamental mode (FM) of the input waveguide cross-section at the inverted tapers (300 $\times$ 300 nm) and the Gaussian source with a spot size of 1.5 μm, representing the lensed fiber mode, as depicted in the Figure 4.17.

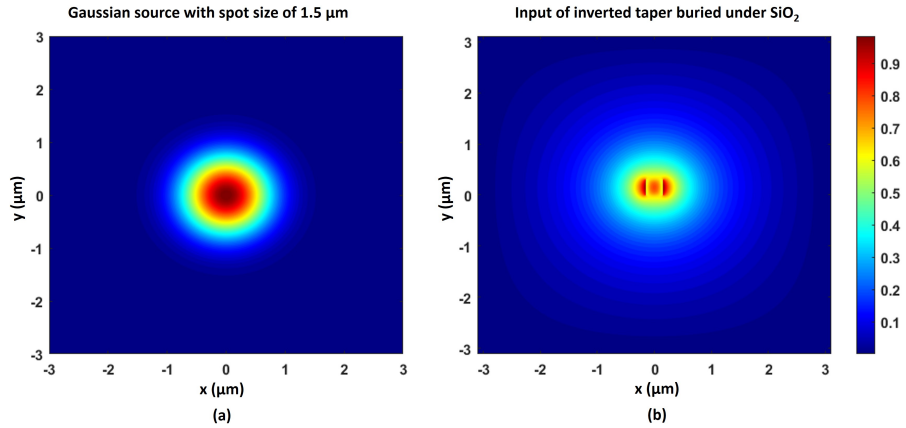

Figure 4.17: X-Y TE Mode-field profile of both input waveguide cross-section at the input of the inverted taper (right side) and Gaussian source (left side) with spot size of 1.5 μm.

Another crucial dimension in the inverted taper design is the taper length. The taper length ensures a smooth transition between the input waveguide and the output waveguide where it couples to the main device. A shorter taper length may result in an abrupt transition, leading to mode mismatch, scattering, and higher losses. A longer taper allows for a more gradual change in waveguide dimensions, ensuring that the optical mode adapts to the new dimensions with minimal disruption. Since we are working with the simplest shape, i.e., a linear taper, a rule of thumb is to consider a taper angle of approximately 1°.

To evaluate the overlap integral between the input and output waveguides in the inverted tapers, we performed FDTD simulations to account for scattering and mode-mismatch losses along the taper length. As shown in the Figure 4.18, a taper length of 35 μm resulted in an overlap efficiency of 92 % and demonstrated convergence.

During the optimization of the inverted tapers, we choose a Si_xN_y thickness of 300 nm. However, this thickness is not compatible with our industrial platform (DAPHNE, STMicroelectronics). Consequently, we designed the device to be fabricated at LN2, 3IT, which provides more space on the wafer and greater flexibility in chip design. For the inverted tapers, we increased the length to 1 mm to achieve maximum coupling efficiency.

4.4.2 adiabatic tapers

Adiabatic tapers were employed for both fiber-to-chip coupling and in racetrack MRRs. Adiabatic tapers are commonly used in photonic chips and are well-documented in the literature. Given the fabrication challenges, such as potential losses during cleaving or

Thèse accessible à l'adresse : https://theses.insa-lyon.fr/publication/2024ISAL0120/these.pdf © [C.B. Chander Bhan], [2024], INSA Lyon, tous droits réservés

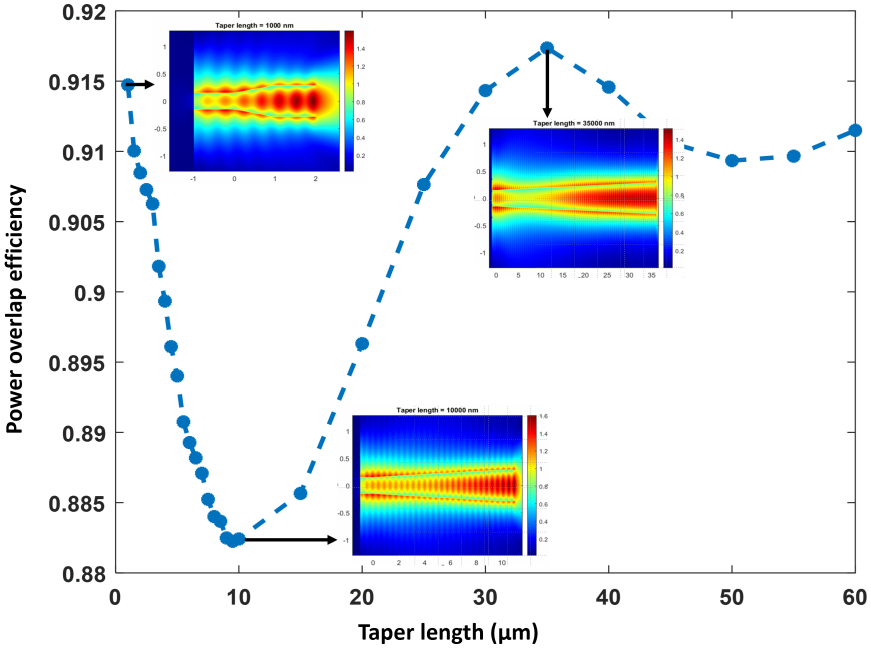

Figure 4.18: Power overlap efficiency as function of the linear taper length.

changes in the RI of Si_xN_y during deposition, which could alter the mode size and reduce coupling efficiency, we opted to use adiabatic tapers for some chips. This approach allows for more reliable characterization of the main device.

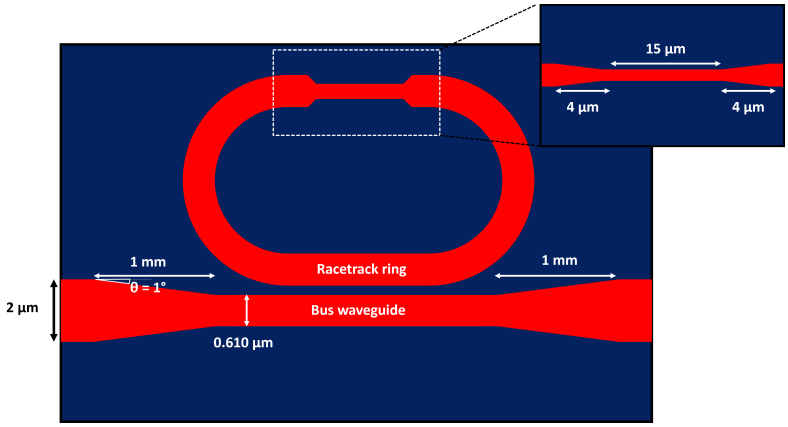

Figure 4.19: Design and schematic diagram of racetrack MRRs using adiabatic tapers with all its critical dimensions.

As described in the previous section, In case of fibre-to-chip coupling the taper angle was chosen to be 1° [147]. The adiabatic tapers were designed with an input width of 2 μm and an output width of 0.570 μm with taper length of 1 mm to effectively couple light into the bus waveguide of the MRRs, as shown in the Figure 4.19.

Thèse accessible à l'adresse : https://theses.insa-lyon.fr/publication/2024ISAL0120/these.pdf © [C.B. Chander Bhan], [2024], INSA Lyon, tous droits réservés

4.5 CAD Layout

Once all the components have been optimized for fabrication, the next step is to design them in a format compatible with lithography machines. Various software tools, such as Klayout, LayoutEditor, CelWIN, and OpenEditor, are available for this purpose. These tools enable the creation of designs in GDS or GDSII formats, which are widely used in the photonic and semiconductor industries for lithography processes.

When designing the Computer-Aided Design (CAD) for photonic chips, several factors must be carefully considered, such as spacing between devices, redundancy, total chip size, alignment of components, and ensuring that there are no breaks or overlaps in the design. Since fabrication reproducibility and errors may alter the final outcome of our devices, it is crucial to account for these possibilities throughout the design process.

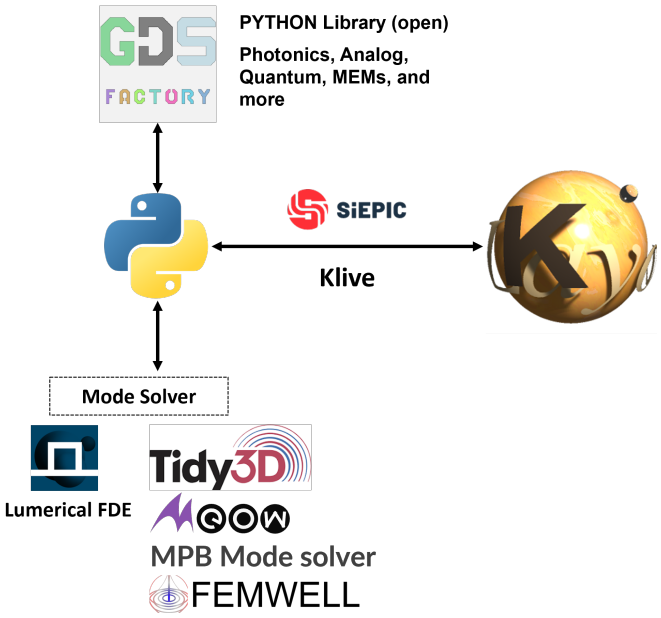

Figure 4.20: GDSfactory package.

Given these challenges, we opted to design 28 photonic chips to cover all potential issues and fabrication variances. This task requires meticulous attention to detail to avoid errors. Fortunately, Klayout offers the ability to create macros or integrate Python scripts, significantly easing the process of designing complex chips. However, the open package GDSFactory, in particular, streamlines this process by providing a rich library of photonic components that can be customized to meet specific design requirements. Additionally, GDSFactory allows integration with various mode solvers for validating the dimensions through simulation, as shown in the Figure 4.20. This helps ensure that the design remains within optimal parameters before fabrication.

Using the GDSFactory package integrated with Klayout, we designed a comprehensive photonic chip that includes key devices such as Circular, Racetrack, and Slot MRRs, as well as Inverted or Adiabatic tapers, Spirals, and Snake bends. This integrated design approach ensures that all essential components are included on a single chip for characterization and testing. An example of one such chip layout, incorporating all these elements, is illustrated in the Figure 4.21

Thèse accessible à l'adresse : https://theses.insa-lyon.fr/publication/2024ISAL0120/these.pdf © [C.B. Chander Bhan], [2024], INSA Lyon, tous droits réservés

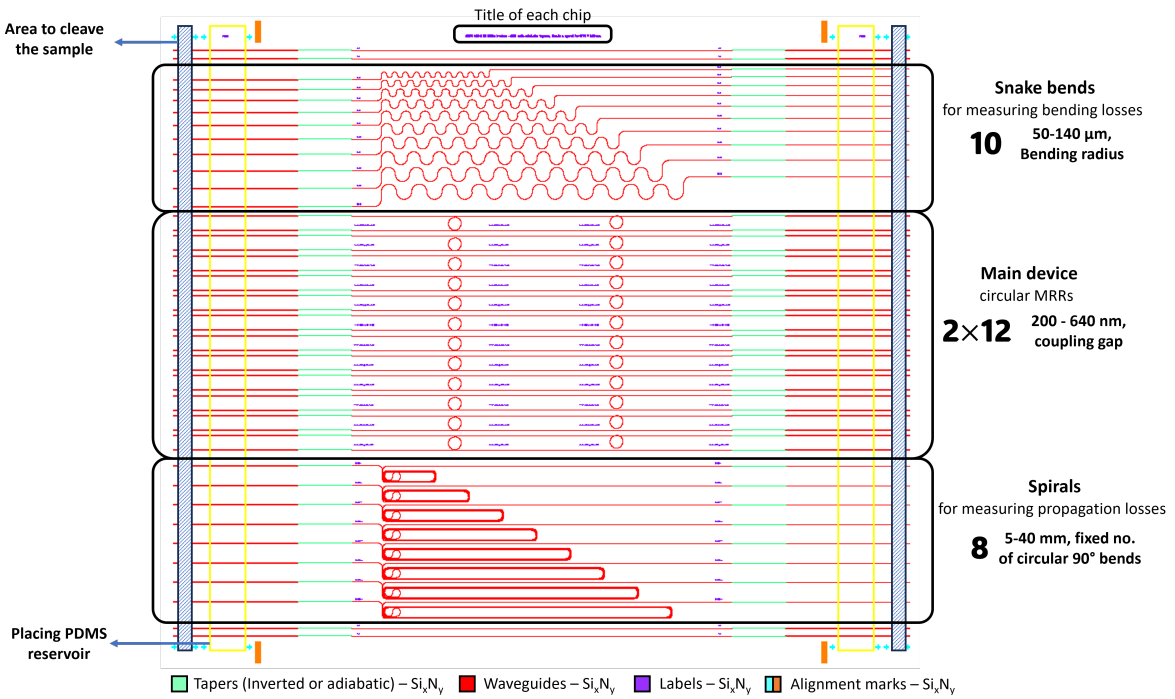

Figure 4.21: Complete CAD for circular MRRs including spiral and snake bend for measuring experimental losses.

The Figure 4.21 displays the CAD design for one of the chips, featuring circular MRRs as the main device. In addition to this, several other chips were designed with different main devices such as Racetrack MRRs, HOM MRRs, and FM MRRs, as discussed earlier during the optimization of each device's dimensions. In the following section, we will present the final structural designs of these devices, created using Klayout. Each design will highlight the critical dimensions and essential elements, ensuring clarity in their fabrication and performance characteristics.

4.5.1 Main devices

The other four main devices, including Racetrack, Slot, HOM, and FM MRRs, are illustrated below in Figure 4.22, each with their critical dimensions. Figure (b) represents the HOM circular MRRs, where the ring has a core width of 1.5 μm and the bus waveguide is 0.55 μm, as optimized in earlier discussions. Additionally, two more chips were designed with variations in these dimensions, accounting for possible fluctuations in the refractive index of the Si_xN_y observed during fabrication. Given that the ring core width is 1.5 μm, the corresponding spirals and bends are fabricated with the same dimensions to maintain consistency across the design. Similarly, the FM MRRs chip is laid out with a detailed schematic as depicted in Figure (c). The slot waveguide MRRs in Figure 4.22.(d) is not an optimized design for any optical trapping or sensitivity. It's an additional device that has been added to try the optical trapping for wider gaps in slot waveguide, as it been never studied in the literature.

Thèse accessible à l'adresse : https://theses.insa-lyon.fr/publication/2024ISAL0120/these.pdf © [C.B. Chander Bhan], [2024], INSA Lyon, tous droits réservés

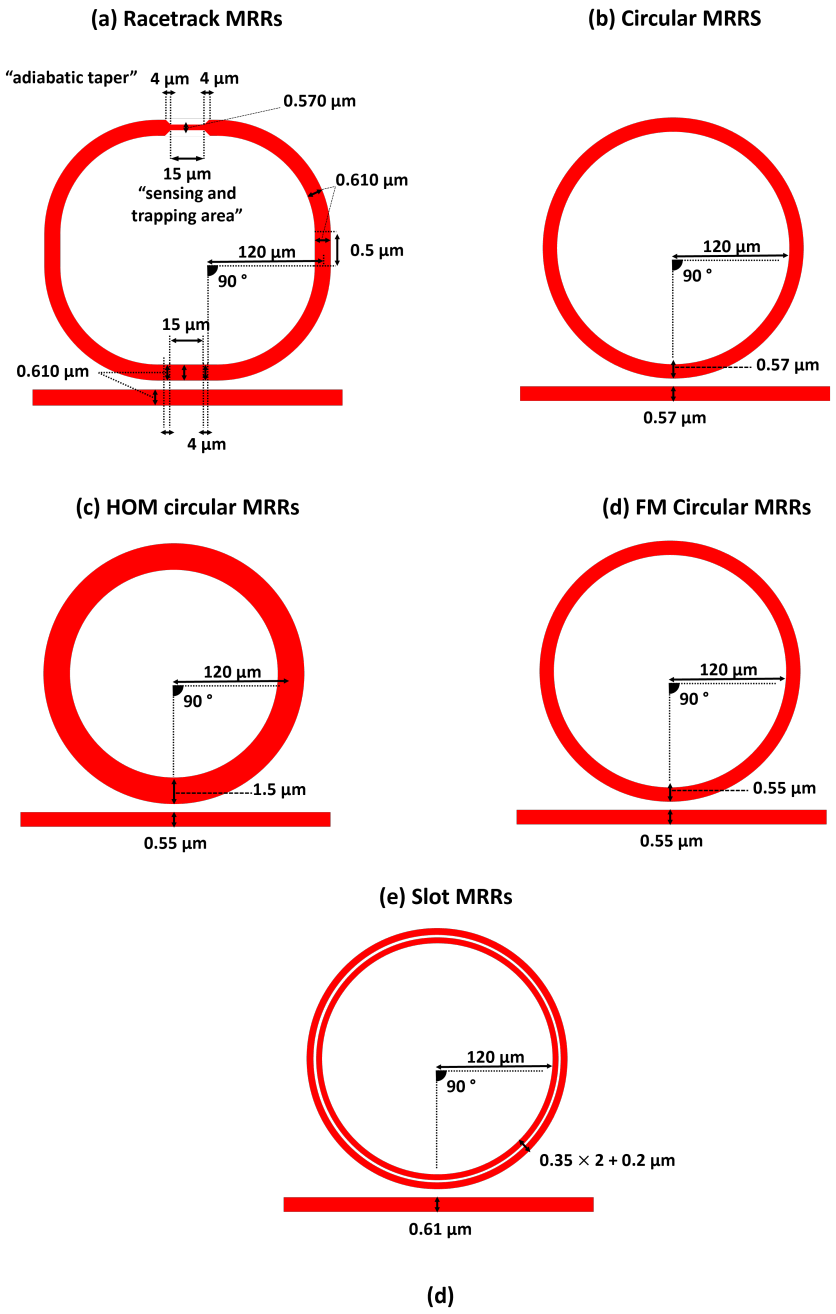

Figure 4.22: Schematic diagram of different MRRs included in the CAD design for different photonic chips.

Thèse accessible à l'adresse : https://theses.insa-lyon.fr/publication/2024ISAL0120/these.pdf © [C.B. Chander Bhan], [2024], INSA Lyon, tous droits réservés

4.5.2 Bends and Spirals

The bends and spirals in each chip are designed to match the dimensions of the main device in order to accurately measure bending and linear propagation losses for the cross-sections utilized in the main device. For instance, in the HOM chip, the bends and spirals have a core width of 1.5 μm, while in the Racetrack MRRs chip, the corresponding dimensions are adjusted to a core width of 0.610 μm.

Furthermore, to precisely calculate the linear propagation losses, a fixed number of circular bends are incorporated into the spirals, with eight spirals included on each photonic chip to account for potential fabrication errors. Additionally, for measuring bending losses, each photonic chip contains 42 circular 90 ° bends. The snake bends are designed with increasing bending radii, starting at 50 μm and progressing in increments of 10 μm, up to 140 μm, as illustrated in the Figure 4.23. This range allows for a comprehensive analysis of bending losses across different radii.

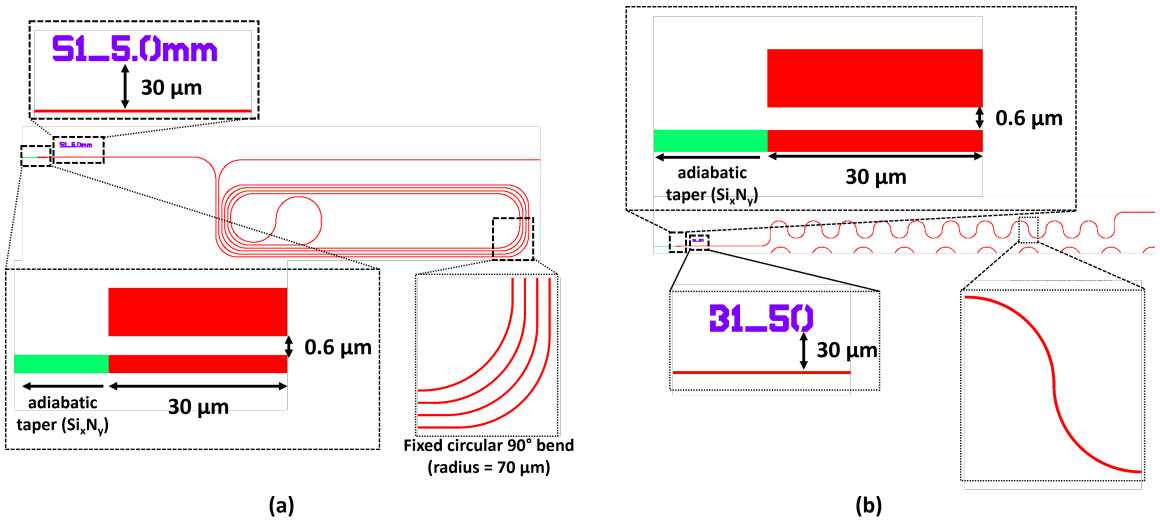

Figure 4.23: Spirals and snake bends: Different colors are used to differentiate the various components within the devices.

4.5.3 Alignment Marks and Labels

Lastly, to streamline post-fabrication processes and minimize errors during characterization, alignment marks and labels play a critical role. These features help reduce the time and effort involved in aligning components and performing measurements. Multiple alignment marks were incorporated, including those for cleaving, PDMS reservoir placement, and larger alignment marks for depositing SiO_2 and creating physical masks (described in Chapter 5) as shown in Figure 4.24. This strategic use of alignment marks as depicted in the figure ensures precise and efficient handling during each stage of the experimental workflow.

Thèse accessible à l'adresse : https://theses.insa-lyon.fr/publication/2024ISAL0120/these.pdf © [C.B. Chander Bhan], [2024], INSA Lyon, tous droits réservés

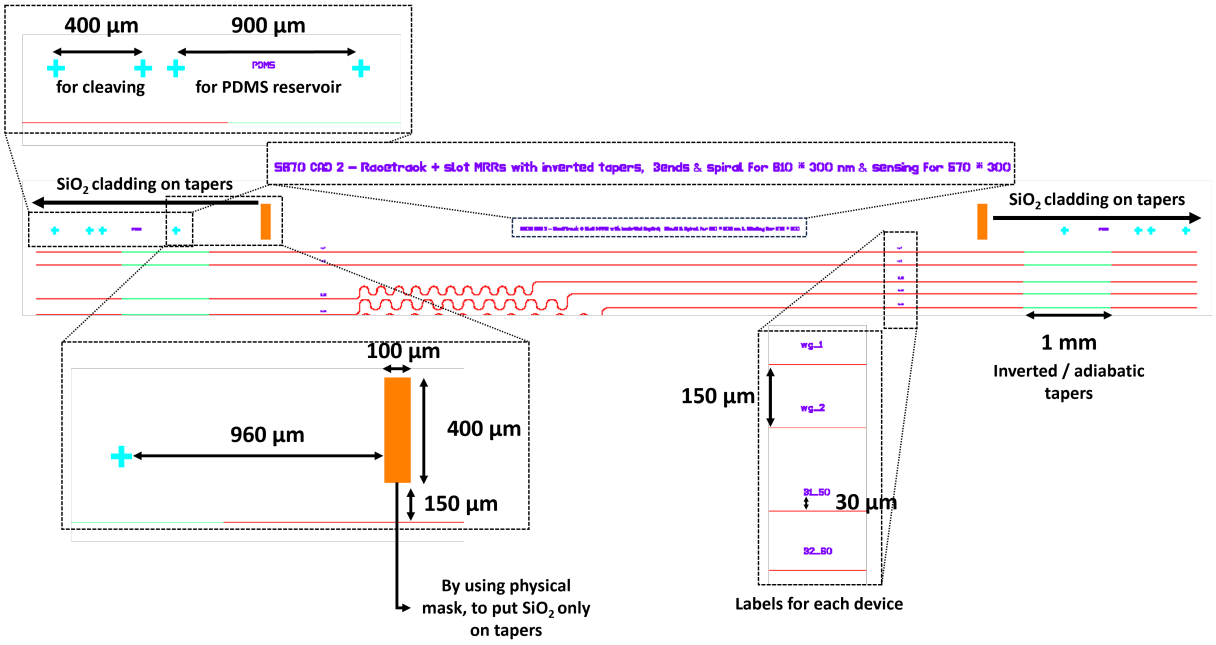

Figure 4.24: Alignment marks.

4.6 Conclusion

In this chapter, we outlined the comprehensive design, optimization, and fabrication processes for various photonic components based on MRRs to enhance their performance in optical trapping and sensing applications. In the initial section's, we optimized both circular and racetrack MRRs, focusing on critical parameters such as coupling gaps, bending radii, and core dimensions to ensure the devices achieved critical coupling with minimal losses. Marcatill's methods, combined with Lumerical varFDTD and FDTD modelling, were employed to model the coupling sections of the MRRs and optimize their performance under various configurations, addressing the unique challenges posed by different waveguide geometries (such as HOM and racetrack MRRs) and mode interactions.

In designing MRRs, significant bending losses results in low Q MRRs and low power in the rings. The implementation of the FDFV mode solver, using TBC, was crucial for accurately predicting these losses and informing design choices for all the MRRs we developed. To support future experimental validation, we incorporated spirals and snake bends into the photonic chips to measure both linear propagation and bending losses experimentally, ensuring that the fabricated devices aligned with the simulated performance.

In the second-to-last section, we focused on enhancing the coupling between optical fibers and the photonic chips by optimizing the design of both inverted and adiabatic tapers. These design elements were crucial for maintaining high coupling efficiencies and preventing parasitic mode excitation as light propagated towards the ring resonators.

Given the inherent uncertainties in the fabrication process, we incorporated redundancy and adaptability into the designs. Multiple photonic chips were created with slight variations in critical dimensions, such as coupling gaps and waveguide widths (with tolerances of $\pm$ 20 nm), to account for potential deviations during fabrication. To simplify the fabrication and

Thèse accessible à l'adresse : https://theses.insa-lyon.fr/publication/2024ISAL0120/these.pdf © [C.B. Chander Bhan], [2024], INSA Lyon, tous droits réservés

characterization process, we employed GDSFactory and Klayout to create precise CAD layouts in GDSII format. These tools enabled scripting and automation, significantly improving the efficiency of designing the 28 photonic chips, each of which included key components such as MRRs, tapers, spirals, and snake bends.

Furthermore, the integration of alignment marks and labels in the chip designs facilitated various post-fabrication processes, including cleaving, the deposition of SiO_2, and the alignment of PDMS reservoirs. These features were essential for minimizing errors and ensuring the accurate characterization of the fabricated devices.

Overall, this chapter highlights the need for robustness and adaptability in photonic chip design, particularly when addressing the practical challenges of fabrication. By carefully considering factors such as coupling efficiencies, bending losses, and redundancy in device dimensions, we ensured that the fabricated devices could meet our requirements for providing the optical trapping and sensing applications. In the next chapter, we will move forward with the fabrication of these devices using the developed CAD layouts. Subsequently, in Chapter 6, we will analyze the experimental results and compare them with the simulation predictions, aiming to validate the design strategies and optimization techniques discussed here.

Thèse accessible à l'adresse : https://theses.insa-lyon.fr/publication/2024ISAL0120/these.pdf © [C.B. Chander Bhan], [2024], INSA Lyon, tous droits réservés

Chapter 5

Device Fabrication

The primary objective of this chapter is to detail the manufacturing steps of the devices designed and studied in this thesis. We will outline the fabrication steps undertaken at the STMicroelectronics DAPHNE platform (Industry cleanroom) and the 3IT platform (University cleanroom) for the fabrication of previous devices, such as Higher Order Modes (HOM) and hybrid plasmonic waveguide (HPWG) Micro ring resonators, as well as the final device developed in this thesis. This chapter will cover the deposition procedures for passive materials, the lithography methods employed, and the etching processes for Si_xN_y and SiO_2. It closely relates to the design chapter 3 & 4. Therefore, some sections will be revisited to bridge the concepts of fabrication and design effectively.

5.1 Device fabrication at DAPHNE, STMicroelectronics

Two of our waveguide structure designs are derived from concepts explored in a previous thesis [97]. Before embarking on the design and fabrication of new structures for our application, it was crucial to characterize the existing devices from prior research to gain insights that could inform and enhance our new designs. Therefore, this section will detail the fabrication steps of these devices.

The HOM ring and dielectric MRRs section of the HPWG were fabricated using the STMicroelectronics Datacom Advanced Photonic Nanoscale Environment (DAPHNE) industrial platform. This platform, initially designed for Datacom applications, is also compatible with biosensing applications [124].

Figure 5.1 shows a schematic diagram of the fabrication steps implemented, including their dimensions. The second step involves the deposition of 2 μm of SiO_2 using Plasma Enhanced Chemical Vapor Deposition (PECVD) and 630 nm of Si_xN_y, which can later be partially etched to achieve a thickness of 350 nm. Equation 5.1 represents the dispersion formulae of real part of the RI of ST PECVD Si_xN_y used here. Step 3 depicts the standard waveguide configuration that can be achieved using the DAPHNE platform. Step 4 illustrates the possibility of obtaining both thicknesses on the same wafer by an additional local Si_xN_y etching step or through separate deposition of Si_xN_y layers with thicknesses of 600 nm and 350 nm.

Thèse accessible à l'adresse : https://theses.insa-lyon.fr/publication/2024ISAL0120/these.pdf © [C.B. Chander Bhan], [2024], INSA Lyon, tous droits réservés

$$n_{Si_xN_y} = 1 - 0.0101\lambda^3 + 0.0459\lambda^2 - 0.0963\lambda + 1.9835 \tag{5.1}$$

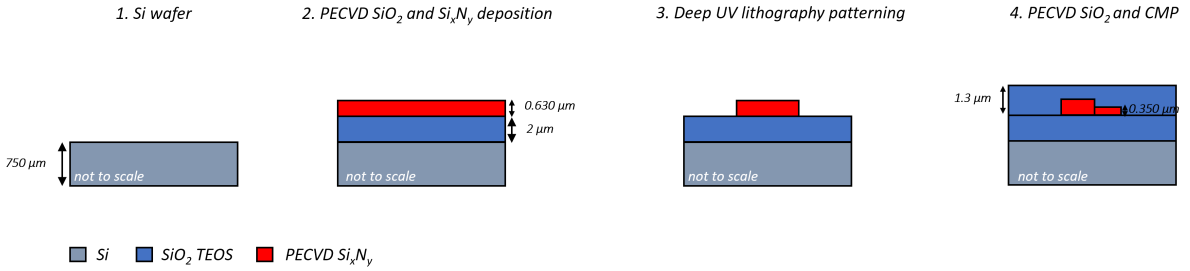

Figure 5.1: Fabrication steps implemented at the photonic platform, DAPHNE, STMicroelectronics, to fabricate HOM microring resonators: The 4 steps illustrated in the figure demonstrate the waveguide configurations that can be achieved with the platform.

Additionally, several other configurations can be realized using PECVD SiO_2 and Chemical Mechanical Planarization (CMP) processes, depending on the waveguide structure (e.g., rib, strip) and cladding requirements (e.g., air, SiO_2, water). For HPWG, the dielectric part of the MRRs was fabricated on the DAPHNE platform. Since the plasmonic part of the MRRs involves metal, which can contaminate the entire platform process, the plasmonic butterfly antenna was fabricated in the cleanroom facillities of NanoLyon platform using e-beam lithography, lift-off processes. The final fabricated devices are shown in Figure 5.2.

The possible configurations with DAPHNE platform and plasmonic parts of the HPWG waveguide structures are thoroughly described in Michele's thesis [97] and will not be repeated here. The width of the waveguide is achieved through inductively coupled plasma (ICP) etching of Si_xN_y, with a standard deviation of 11 nm and a sidewall angle of 85 °.

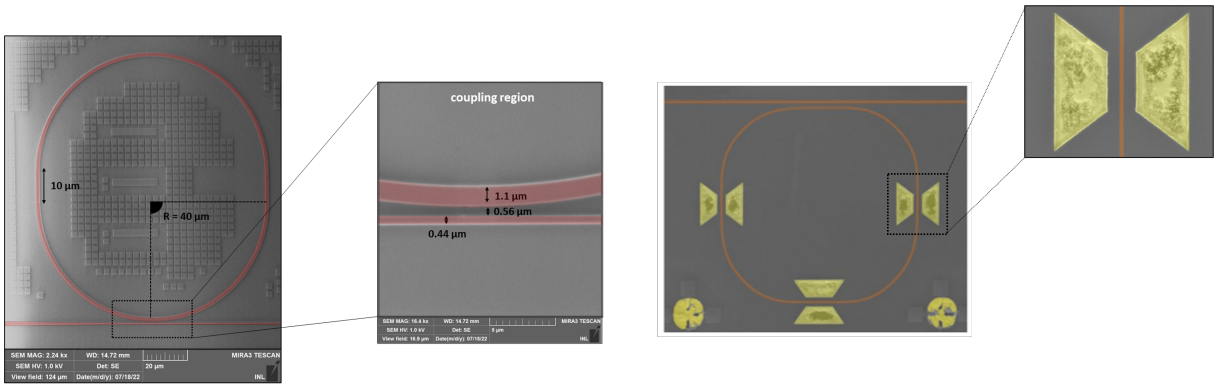

Figure 5.2: Colored SEM Image of HOM and HPWG MRR: (a) HOM MRRS where red strip lines shows the Si_xN_y strip waveguide on the SiO_2 substrate (gray color) (b) HPWG MRRs (taken from Michele Thesis [97]).

Figure 5.2 illustrates colored SEM picture with the measured dimension of HOM MRRs. The red line on the picture shows the Si_xN_y strip waveguide on 2 μm of SiO_2 as the substrate and with open air cladding where later it was replaced by water using a fluidic reservoir for characterisation.

Thèse accessible à l'adresse : https://theses.insa-lyon.fr/publication/2024ISAL0120/these.pdf © [C.B. Chander Bhan], [2024], INSA Lyon, tous droits réservés

5.2 Device fabrication at 3IT University of sherbrooke

The Institut interdisciplinaire d'innovation technologique (3IT) provides a comprehensive platform for research in various fields, including energy on chip, nanoelectronics, photonics, packaging, and their impacts on society. The laboratory features advanced facilities for micro & nanofabrication, metrology, characterization, and nano-biotechnologies. Leveraging these integrated facilities, we fabricated all our photonic chips at 3IT. To initiate the fabrication process, we selected Si-wafers with a thickness of 275 μm, as the final device characterization would involve a butt coupling setup that necessitates clean facets. These clean facets can be precisely achieved through facet etching. However, due to time constraints, we were unable to proceed with the facet etching process and opted instead for the traditional cleaving method.

5.2.1 Deposition of Passive materials

There are several different approach to deposit Si_xN_y such as chemical vapor deposition (CVD), physical vapor deposition (PVD), and atomic layer deposition (ALD). The 3IT platform provides 2 CVD techniques for Si_xN_y deposition, Plasma Enhanced Chemical Vapour Deposition (PECVD) and Low Pressure Chemical Vapour Deposition (LPCVD). The LPCVD Si_xN_y is deposited at 785 °C to avoid the NH defects in the Si_xN_y which reduces the linear propagation losses at infrared wavelength.

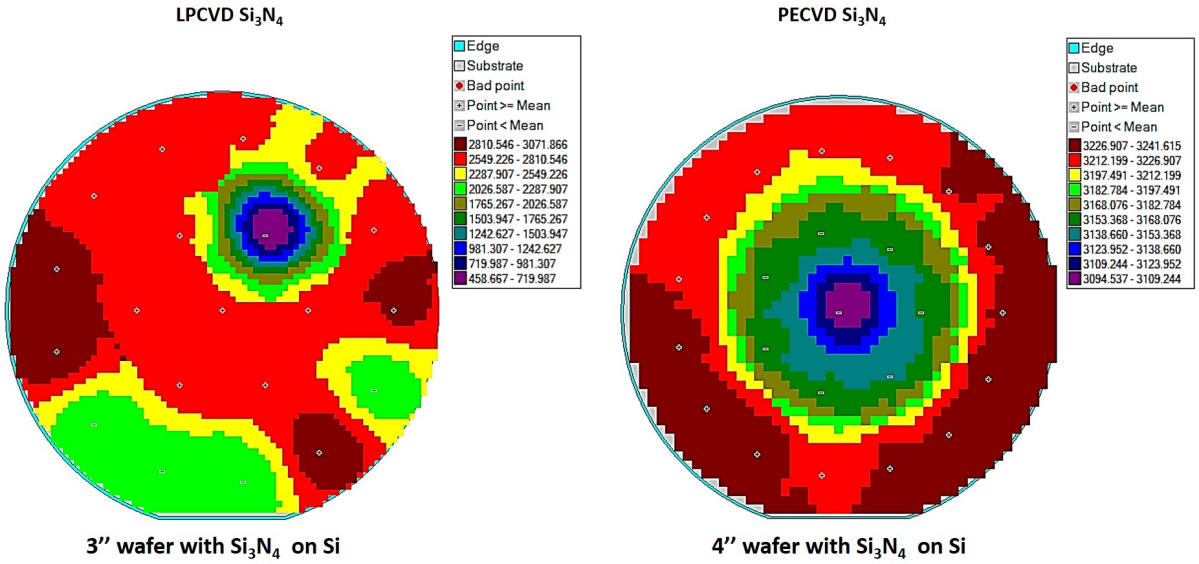

Figure 5.3: 3D mapping thickness of LPCVD and PECVD Si_xN_y film deposited with standard recipes at LN2, 3IT : The legends shown in the pictures represents the thickness measured (in A°) with the responding color to it.

Figure 5.3 shows the surface contour map to illustrates uniformity in deposition of both PECVD and LPCVD Si_xN_y. The contour map here shows the multiple point of thickness measured with ellipsometery (HORIBA UVISEL Plus) from 800 - 1700 nm. As it can be seen that the LPCVD Si_xN_y deposited on 3-inch wafer goes from 45 nm - 300 nm which is a big difference as compare to the PECVD Si_xN_y where its deposition is ranging between

Thèse accessible à l'adresse : https://theses.insa-lyon.fr/publication/2024ISAL0120/these.pdf © [C.B. Chander Bhan], [2024], INSA Lyon, tous droits réservés

300-324 nm with only 20 nm difference throughout the wafer. The reason behind large non-uniformity in the deposition of LPCVD is due to the furnace of the LPCVD system at 3IT which is optimized for 6-inch wafers.

Therefore, for this fabrication, due to the non-uniformity problem in LPCVD Si_xN_y, PECVD Si_xN_y of 300 nm was deposited followed by the deposition of 2 µm of SiO_2 on 4-inch wafers with a thickness of 275 μm. The standard recipes of PECVD Si_xN_y and SiO_2 are mentioned in the Table 5.1. Both depositions were performed by STS MESC Multiplex PECVD tool as shown in Figure 5.4 after solvent and piranha cleaning of the wafer.



Figure 5.4: PECVD Tool for passive material deposition (SiO_2, Si_xN_y) at LN2, 3IT.

PECVD Si_xN_y						
Pressure	Platen power	Frequency	T	NH_3	SiH_4	N_2
900 mTorr	30 W	13.56 MHz	300 $^\circ C$	25 sccm	40 sccm	1960 sccm
PECVD SiO_2						
Pressure	Platen power	Frequency	T	N_2O	SiH_4	N_2
300 mTorr	700 W	380 KHz	300 $^\circ C$	2000 sccm	17 sccm	- sccm

Table 5.1: Standard PECVD Low frequency Si_xN_y and SiO_2 recipes at LN2, 3IT by researcher and engineers.

Its also important to stay close to dimension of the designed waveguide as any change in the dimension can lead to radiation modes or end up with no propagation of light through waveguides. There are 3 scenarios where the dimension of the waveguide can be differ after the fabrication than the designed one. The first comes during the deposition of the material that defines the thickness of the waveguide, the second is the exposure by E-beam or UV lithography that can affect the width of the waveguide and last the etching process. To consider all the fabrication tolerances its important to have corner analysis of the waveguide sensor to make sure that with each steps we lie in the same fabrication tolerance. corner analysis allows to check the propagating waveguide modes with simulation under all the set of parameters belonging to extreme fabrication variations. The corner analysis of the waveguide sensor we designed is shown in the Figure 5.5. As it can be seen that with both $\pm$ 20 nm of width and $\pm$ 15 nm of thickness are in the range of fabrication tolerance i.e. the guided modes are still above the radiation modes ($n_{eff} >$ 1.4462, Refractive index (RI) of the substrate) and moreover the change in the n_{eff} are not that large.

Thèse accessible à l'adresse : https://theses.insa-lyon.fr/publication/2024ISAL0120/these.pdf © [C.B. Chander Bhan], [2024], INSA Lyon, tous droits réservés

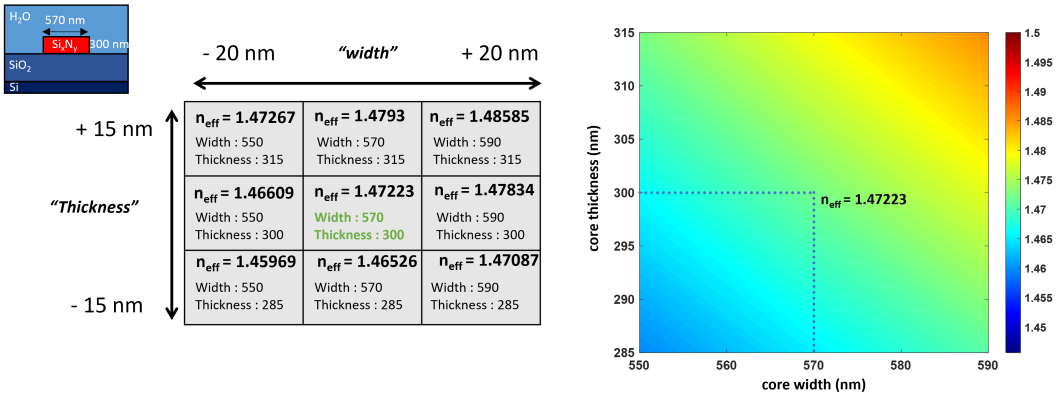

Figure 5.5: Corner analysis of final strip waveguide fabricated with PECVD Si_xN_y (RI = 1.936) of 570 $\times$ 300 nm on SiO_2 (RI = 1.4462) substrate of 2 μm with H_2O (RI = 1.31) superstrate at 1310 nm wavelength.

Throughout the entire fabrication process, we ensured dimensional accuracy at each step. The thicknesses measured by ellipsometry ("alpha-SE [148]") for Si_xN_y and SiO_2 were 1990 nm and 330 nm, respectively, using the recipes mentioned in the Table 5.1. The RI of the Si_xN_y was measured using a ellipsometer ("Horiba UVISEL Plus") in the infrared wavelength range, as shown in the Figure 5.6(b). The figure represents only the real part of the RI of Si_xN_y, as the imaginary part (extinction coefficient) of the RI is very close to zero and the challenging modeling fit made it difficult to detect with ellipsometry. At 1310 nm, the RI of Si_xN_y is 1.936, which was used in all our modeling and device design.

During fabrication, we planned to produce multiple photonic chips, considering all possible variations such as material losses, changes in Si_xN_y thickness, variations in RI, and over-exposure or underexposure of the pattern. Therefore, we accounted for an increment of $\pm$ 20 nm in core width on a few chips. To fabricate multiple chips, we deposited SiO_2 and Si_xN_y on various wafers and measured the thickness using ellipsometry, as illustrated in the Figure 5.6. Figure 5.6(a) shows a slight change in the thickness of SiO_2 as we move towards the edge, with a deposition thickness of 2 μm. However, the Si_xN_y maintained a consistent thickness across the wafer, ensuring no issues in the waveguides at the end.

Once we have all the deposition of the passive materials, the wafer was cleaved into 3 $\times$ 2 cm of the sizes double the size of the pattern we want to expose. Later the sample were exposed followed by spin coating of e-beam resist explained in the next section.

5.2.2 E-beam lithography

To expose the design pattern, both UV and E-Beam lithography (EBL) methods can be used. At LN2, 3IT Sherbrooke, both lithography methods are available. Lithography is a critical part of the fabrication process, as we transfers our pattern on the resist that later will be etched on the material. The advantages of EBL include its high resolution, precise placement, and flexibility. It allows for highly accurate overlaying of different levels of lithography, achieving an alignment accuracy of less than 20 nm. The pattern is defined solely by a software mask, making it easy to change designs without needing to create new physical masks as compare to UV lithography.

Thèse accessible à l'adresse : https://theses.insa-lyon.fr/publication/2024ISAL0120/these.pdf © [C.B. Chander Bhan], [2024], INSA Lyon, tous droits réservés

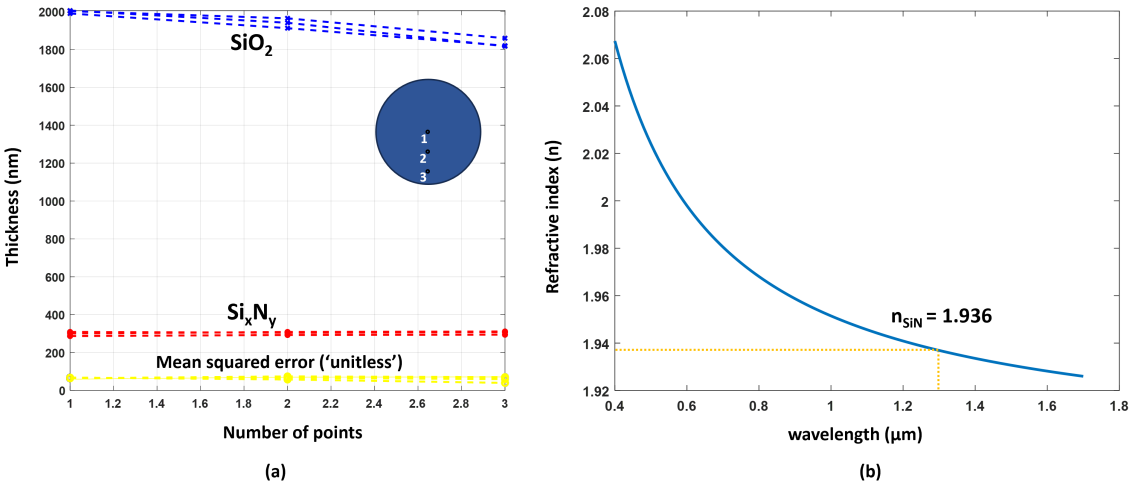

Figure 5.6: PECVD SiO_2 and Si_xN_y material thickness and RI : Deposition of SiO_2 and Si_xN_y on all wafer RI of PECVD Si_xN_y measured with an ellipsometer (HORIBA UVISEL Plus) in the infrared wavelength.

The disadvantage of EBL is its slower speed compared to photo-lithography performed with a mask aligner or a stepper. It is also typically slower than photo-lithography performed with a laser writer such as "Heidelberg μpg101" available at INL. This is because EBL is inherently a serial process, with the pattern being exposed one pixel at a time. Additionally, the pixel size is much smaller than that used in a laser writer, resulting in many more pixels in EBL.

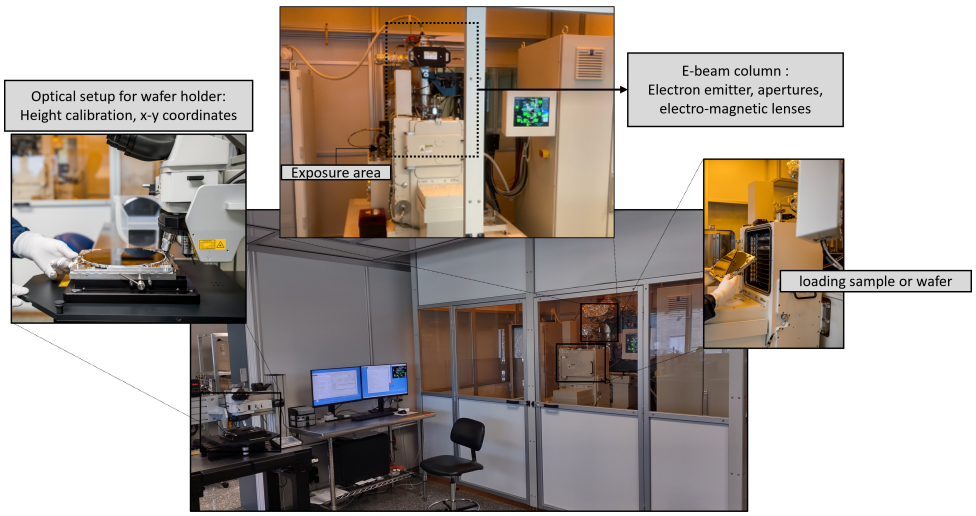

Figure 5.7: Raith 5200 electron pattern beam generator (EPBG) at LN2, 3IT.

The Raith 5200 EPBG was used to expose the pattern on the substrate shown in Figure 5.7, followed by spin coating with negative E-Beam resist ARN7520.17. The ARN7520 resist provides high contrast, better adhesion to the Si_xN_y substrate and offers good resolution and versatility compared to MAN and AZN lift-off resists [149]. Considering the 1.5 etching selectivity between Si_xN_y and ARN7520 (explained below in etching section), the spin coating was performed according to the recipe mentioned in the Table 5.2 to achieve a thickness of 500 nm on all the wafers to be exposed. The speed required for spin coating

Thèse accessible à l'adresse : https://theses.insa-lyon.fr/publication/2024ISAL0120/these.pdf © [C.B. Chander Bhan], [2024], INSA Lyon, tous droits réservés

depends on the density of the resist, which can vary with the age of the resist. The speed mentioned here was used for a fresh bottle and was kept consistent throughout the entire fabrication process.

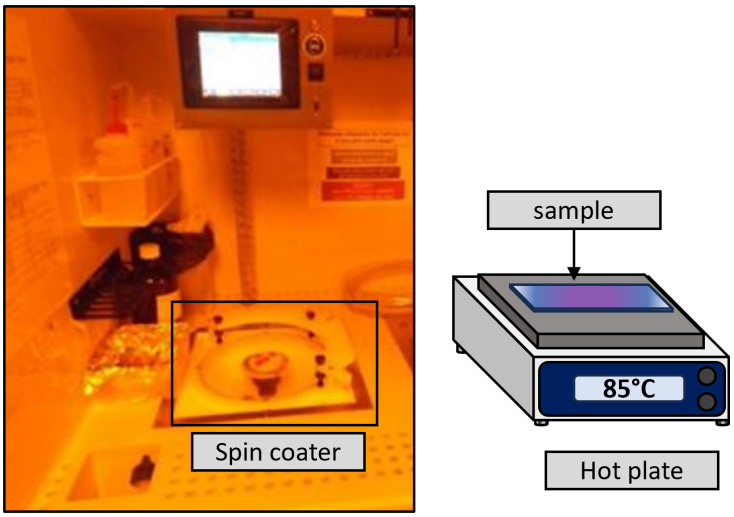

Figure 5.8: spin coater with schematic diagram of hot plate used to spin resist at LN2, 3IT.

Once the spin coating of the resist is completed, the samples can be exposed using EBL. A common issue encountered during pattern writing on the substrate is stitching errors, along with overexposure or underexposure of the pattern. These problems can lead to deviations in the cross-section compared to the design, additional losses, or broken waveguides. Therefore, it is crucial to understand how pattern fracturing works and how it can help avoid stitching errors.

Speed	Spinning time	Baking temp	Baking time
3000 rpm	60 sec	85 $^{\circ}C$	2 min

Table 5.2: Spin coating parameters used to spin the resist ARN7520 on the samples.

Fracturing

In EBL “fracturing” corresponds to the process of breaking down complex patterns into simpler shapes that can be more easily and accurately written and understand by the e-beam. The e-beam writer typically cannot process arbitrarily complex shapes directly so therefore fracturing of the GDSII file is done while following some other crucial steps included such as proximity effect correction (PEC), filling order, writing order, resolution and later its converted into a Generic program format (gpf) file that can be readable by the E-beam writer. The importance of fracturing is further described below in three main categories:

1. **Accuracy and Precision: Resolution, Beam step size, Beam profile**

   The E-beam writer uses focused electron beam shots to expose specific patterns on the substrate. These focused Gaussian beams are produced using circular apertures in the beam column, and the spot size, or full width at half maximum (FWHM), of the beam depends on the supplied current. However, the spot size of the beam does not

Thèse accessible à l'adresse : https://theses.insa-lyon.fr/publication/2024ISAL0120/these.pdf © [C.B. Chander Bhan], [2024], INSA Lyon, tous droits réservés

necessarily imply that the beam will create a feature of the same size in the resist. The size of the exposed feature after development also depends on the dose used, which indicates how long the beam stays in one spot and how far the electron energy is distributed. If the doses exceed the required limit, the printed feature will be larger; if the doses are below the threshold, the printed feature will be smaller. Generally, any beam spot size within the range of 1-100 nm can be created by adjusting the beam current and the aperture size. For practical results, we have selected beam profiles from the calibrated beam profiles that are regularly maintained.

During exposure, the selected beam steps through every pixel of the pattern to be exposed. The size of the pixel, also referred to as "resolution," is defined as the fracturing resolution, which in our fabrication case is 1 nm.

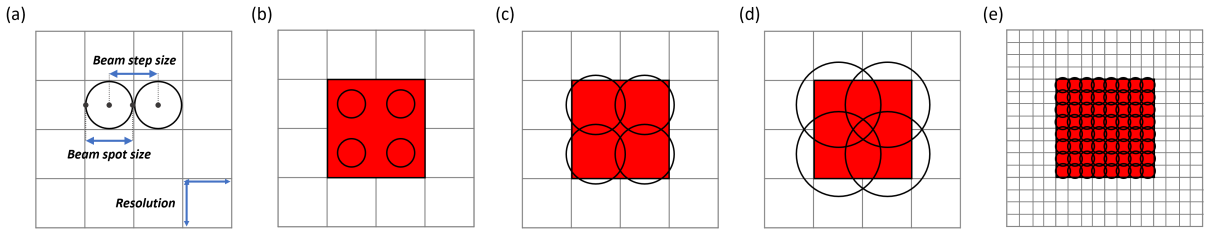

Figure 5.9: correlation between beam step and spot size: (a) represents the underexposed pattern with smaller size of the spot-size and large step size, (b) and (c) represents overexposed pattern in case of large beam spot-sizes (adapted from [150]).

To select the beam step size, it is important to understand that both the beam spot size and step size must be optimized to achieve features close to the intended pattern size on the resist. Figure 5.9 shows several possible combinations of beam step and spot sizes. In this Figure, it is assumed that both resolution and beam step size are equal to clarify the concept of choosing the beam step and beam shot size.

As shown in Figure 5.9 (a), if the beam spot size is significantly smaller than the beam step size, the result will be an array of holes written in the resist. If the beam spot size matches the beam step size, the resulting features will be close to the intended feature size (provided a proper dose is selected), but the line edge roughness may be too high for some applications (e.g., optical waveguides), and some resist "scumming" (leftover resist residue between individual shots) may be present after development. If the beam spot size is significantly larger than the pixel size, the printed feature will be oversized accordingly, the corner rounding will be larger, but the edges will be much smoother, and resist scumming will be minimal or absent [150].

To achieve a clean, well-defined pattern, one could typically select a beam step size to be 0.7 times the spot size and a spot size to be 1/10 of the feature size. Moreover, not all combinations of beam step and spot sizes can be considered, as the maximum frequency of the system is defined as 125 MHz. One can verify the frequency with a simple equation described as:

$$BSS_{min} = \sqrt{\frac{I}{125MHz * D}} \tag{5.2}$$

where BSS_{min} is minimum beam step size that can be considered for the given current beam profile, D represents doses in $\mu C/cm^2$ and I represents the current of the

Thèse accessible à l'adresse : https://theses.insa-lyon.fr/publication/2024ISAL0120/these.pdf © [C.B. Chander Bhan], [2024], INSA Lyon, tous droits réservés

beam profile which is correlated with beam spot size as explained above. Considering all the aspects mentioned above, the beam profile for exposing the waveguide was chosen with a 4 nm spot size (1 nA, 300 µm aperture), a 4 nm step size, and a resolution of 1 nm. For patterning the labels, a larger beam was chosen since high precision was not required and the total writing time can be reduced. Therefore, for the labels, a spot size of 200 nm was selected with a 25 nm step size, maintaining the same resolution of 1 nm for both patterning processes. With a dose of 100 $\mu C/cm^2$, the total frequency would be 60 MHz, which is well below the 125 MHz threshold.

2. **Optimisation of writing : Fracture order, writing order and Shape filling**

   The beam profile we will select will expose the resist according to the pattern provided and it will be stepped through every single pixel. Therefore, its also important to choose the optimized writing strategy to avoid stitching errors, unnecessarily complex movements, high wall roughness, fallacious dimensions.

   Optimizing the writing process in photonic waveguide layouts involves several techniques: fracture order, multipass techniques, field ordering, feature order, and the sizes of main fields and subfields. Fracture order defines the strategy for pattern fracturing, including conventional, Large Rectangle Fine Trapezoid (LRFT), and curved modes. In photonic waveguide layouts, the LRFT mode is particularly beneficial as it provides smoother edges with complete pattern filling. The LRFT technique prioritizes the use of large rectangles first to fill the shape, followed by small trapezoids to complete the filling of smaller areas within the layout as shown in Figure 5.10(a).

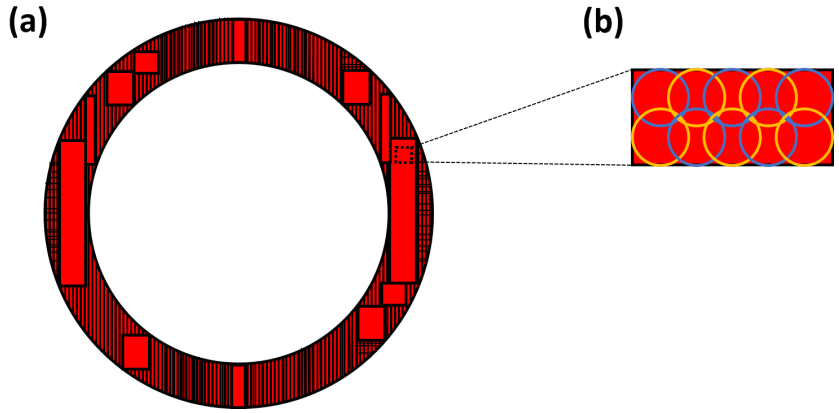

Figure 5.10: Graphical representation of Fracturing and multipass of ring with floating field ordering to avoid the stitching error :(a) LRFT fracturing mode with ring structure (b) the yellow and blue color represents two beam shot in each pass in multipass mode.

To achieve low Line Edge Roughness (LER) and Line Width Roughness (LWR), a two-pass mode was employed within the multipass techniques. This method involves reducing the dose by half in each pass with a small offset, as illustrated in the Figure 5.10 with blue and yellow color beam shots. This ensures a more precise and refined outcome. Floating field ordering was utilized specifically to achieve the writing process described here. By optimizing the order in which fields are written, the overall pattern accuracy and smoothness are significantly improved. The sizes of the main fields and subfields were optimized to 1000 μm $\times$ 1000 μm and 500 nm $\times$ 500 nm, respectively. This optimization ensures that the coupling region of the micro-ring res-

Thèse accessible à l'adresse : https://theses.insa-lyon.fr/publication/2024ISAL0120/these.pdf © [C.B. Chander Bhan], [2024], INSA Lyon, tous droits réservés

onators remains within the same main field, preventing the stiching errors during the exposure process.

3. **Proximity Effect Correction:** When the Gaussian electron beam is exposed to the resist layer, primary electron forward scattering occurs, resulting in the generation of secondary electrons (SE) and backscattered electrons (BSE). This leads to the exposure of the entire area reached by the SE. Consequently, the total exposure is greater in the regions adjacent to the initially exposed pattern. This phenomenon is commonly referred as the Proximity Effect in the literature [151]. The impact of the Proximity Effect depends on the substrate material and the energy distribution. High-density patterns are particularly susceptible to the Proximity Effect, as the proximity of features can lead to merging and loss of structural integrity.

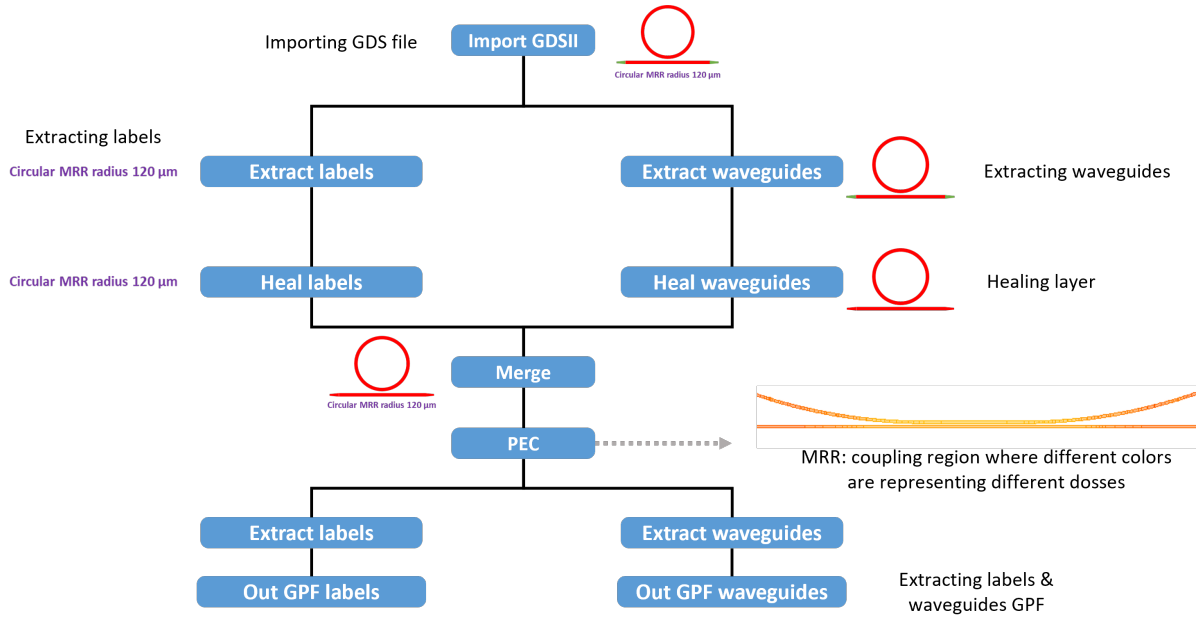

Figure 5.11: Beamer flow chart used in GenISys Beamer application to perform fracturing on the pattern.

To address this, the GenISys Tracer was used to obtain the energy density of the beam and complete the density function. The accompanying Figure 5.11 illustrates the flow chart encompassing all the steps performed during the fracturing process in the GenISys Beamer software. The Figure also highlights the coupling region of micro-ring resonators (MRRs) with proximity effect correction (PEC) applied to the layout. This ensures that the final pattern closely aligns with the intended design.

To calculate the doses required to achieve the desired pattern on the substrate, we utilized a rectangular array pattern on our substrate to evaluate the contrast curve and similarly micro-ring resonator (MRR) array structure was used to confirm the coupling gap that can be achievable with the what exposure dose. Figure 5.12 below illustrates the contrast curve in the first image, while the second image shows the doses that enable us to achieve the defined coupling gaps of 200 nm and 400 nm.

Theoretically, as the dose increases, the exposure to the pattern also increases, leading to larger dimensions that might merge the structures in the case of compact patterns. This

Thèse accessible à l'adresse : https://theses.insa-lyon.fr/publication/2024ISAL0120/these.pdf © [C.B. Chander Bhan], [2024], INSA Lyon, tous droits réservés

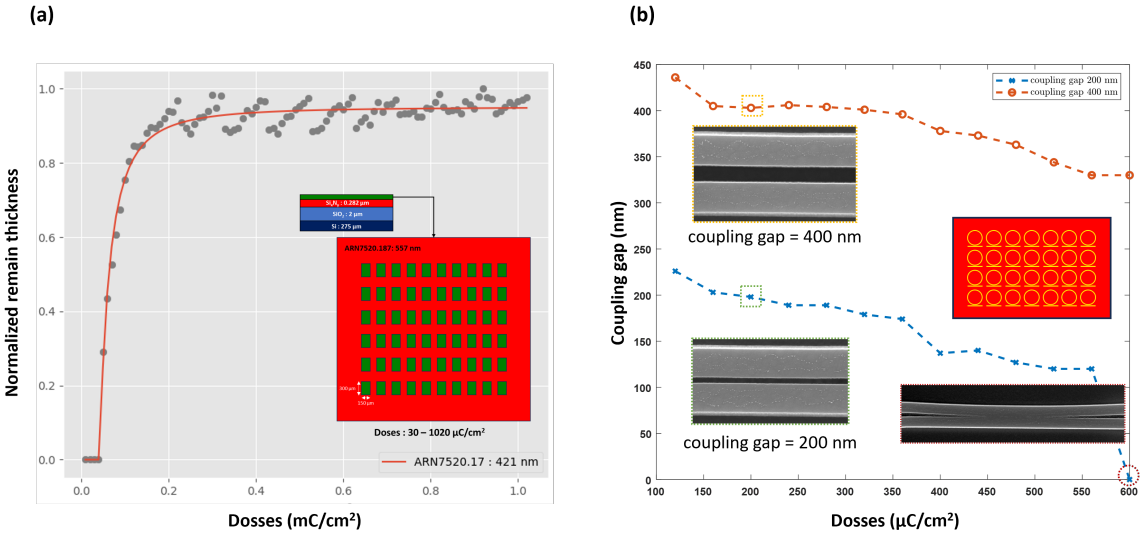

Figure 5.12: Determination of doses required with two samples: (a) resist contrast curve, where the green rectangular structure represents the resist pattern exposed to determine the exposure dosses. (b) Different MRRs with varying doses to achieve clear coupling gaps of 200 and 400 nm.

behavior can be observed in Figure 5.12 (b), where a dose of 600 $\mu C/cm^2$ results in the bus and ring waveguides merging, thus failing to produce the intended pattern compare to coupling region at 200 $\mu C/cm^2$. Therefore considering both results from “contrast curve” and “exposed coupling region” we opted for dosses to be 200 $\mu C/cm^2$ for exposing the patterns.

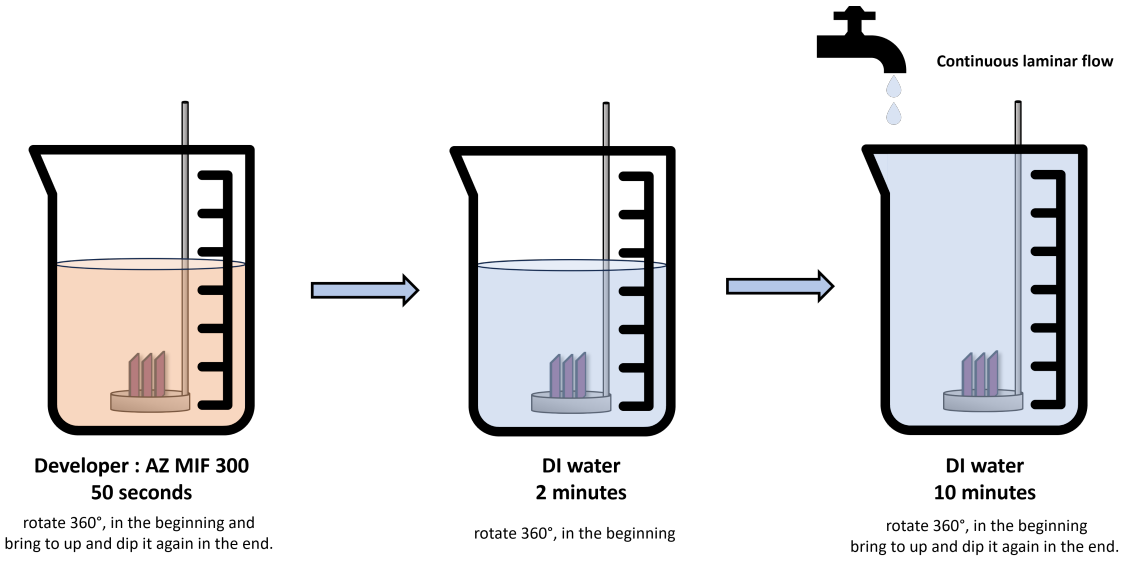

Figure 5.13: Sequential development steps for a photonic chip, including time allocation for each phase.

After the pattern is written onto the resist using EBL, the subsequent resist development process is essential to reveal and transfer the pattern onto the substrate. As we have used the negative resists in our case, therefore the exposed areas become less soluble (or cross-linked) and remain after development, while the unexposed areas are dissolved. For

Thèse accessible à l'adresse : https://theses.insa-lyon.fr/publication/2024ISAL0120/these.pdf © [C.B. Chander Bhan], [2024], INSA Lyon, tous droits réservés

the development of ARN7520 we have used the standard procedure as explained in the data-sheet of the resist [152] but as their will be a bulk amount of resist to remove from the substrate, the time of development was optimized. Moreover, additionally we turned 360 degrees while in the development solution to make sure the solvent reached the coupling regions to get clear the gaps in between bus waveguides and ring.

The SEM cross-section image of the resist pattern shown in Figure 5.14 exhibits a trapezoidal profile. The side angles of the pattern can be improved by adjusting the background doses and actual doses [153]. Furthermore, a similar 73 ° angle was achieved in subsequent etching patterns on the Si_xN_y layer, as illustrated in the Figure 5.17.

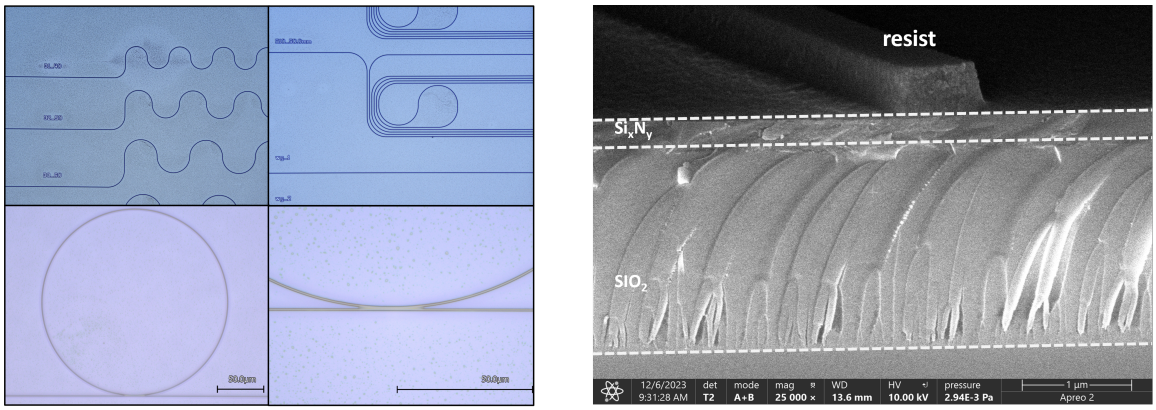

(a) (b)

Figure 5.14: Optical and electron microscopy of the resist profile after development: (a) Optical microscope image of the bending device, spirals, MRRs, and the coupling region of MRRs. (b) SEM cross-section image of the resist waveguide patterned on the Si_xN_y layer after development.

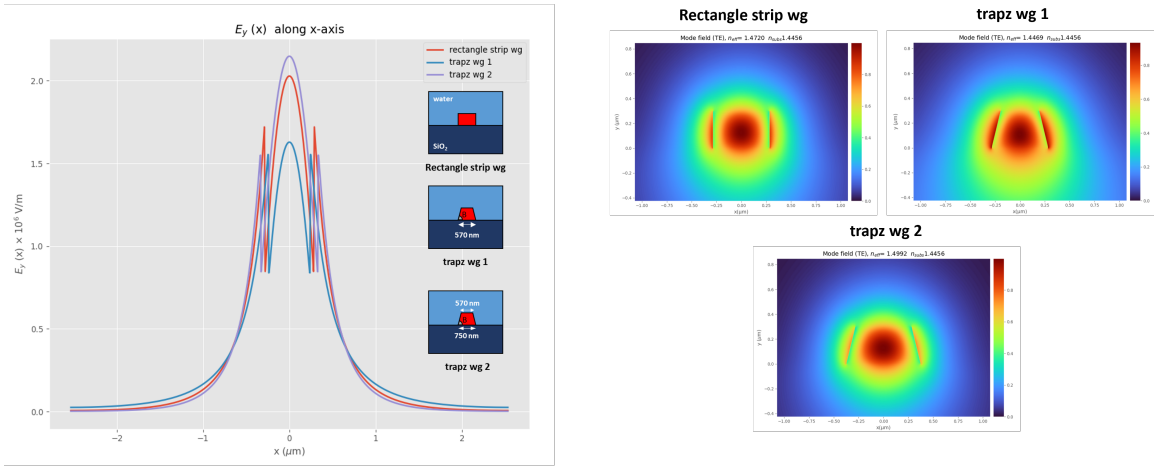

(a) (b)

Figure 5.15: Influence on n_{eff} and evanescent field with trapezoidal profile of waveguide : (a) Electric field on y axis (TE) as a function of length of core width at centre. (b) TE mode-profiles of designed straight waveguide, fabricated design (trapz wg 2) and other option that can be achieved (trapz wg 1).

As we intended to fabricate straight waveguides, we investigated the effect of sidewall angles on the n_{eff} mode before optimizing the etching recipes and EBL exposure. As

Thèse accessible à l'adresse : https://theses.insa-lyon.fr/publication/2024ISAL0120/these.pdf © [C.B. Chander Bhan], [2024], INSA Lyon, tous droits réservés

shown in the Figure 5.15, a sidewall angle of 73 ° does not significantly alter the mode and gradient of the evanescent field compared to the designed one. Considering the time constraints, we decided to proceed with the etching process.

5.2.3 Etching

To transfer the resist pattern onto the material beneath, etching must be performed. In nano-fabrication processes, there are two common methods: dry etching and wet etching. Due to its anisotropic etching capabilities, precise control over process parameters, and ability to create detailed features, dry etching using Inductively Coupled Plasma (ICP) was employed for Si_xN_y etching. Unlike Reactive Ion Etching (RIE), ICP generates a denser plasma because of the RF coil wrapped around the chamber, which enhances the etch rate. Additionally, an independent RF power source can be applied to the substrate electrode, allowing separate control of plasma density and ion energy. This provides a larger process window [154].

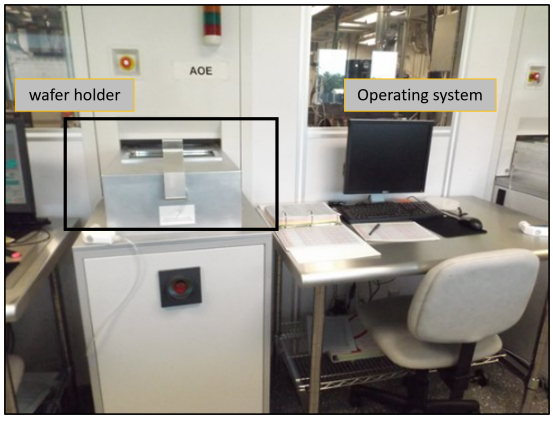

Figure 5.16: STS advance oxide ICP etcher at LN2, 3IT : plasma chamber and all the gases inlets are on the backside of the wall that are controlled by engineers.

Figure 5.16 below shows the Plasma Etcher STS Advanced Oxide used for Si_xN_y etching at LN2, 3IT. This plasma etcher utilizes a static charge wafer holder, which requires a clean wafer backside to avoid high helium (He) leakage. Such leakage can lead to process termination, as He gas is necessary for cooling the platen.

SIN Etching

To etch the Si_xN_y, the “SiNSLOW” recipe developed by engineers at 3IT was used, as shown in Table 5.3. The selectivity between Si_xN_y and ARN7520 resist was measured to be 1.5, with an etching rate of 1.3 nm/s and 0.87 nm/s for Si_xN_y and resist respectively. The recipe was optimized for a temperature of 0℃, with a platen power of 50 W and an RF coil power of 100 W. With this selectivity, after the etch of 230 seconds the roughly 300 nm of resist was left on the top of the waveguide that shows 500 nm of resist was sufficient quantity to achieve the desired pattern of waveguide on Si_xN_y layer.

Once the etching process was completed, the ring-resonator samples shown in Figure 5.12 (b) were examined using a profilometer to measure the thickness of the remaining resist

Thèse accessible à l'adresse : https://theses.insa-lyon.fr/publication/2024ISAL0120/these.pdf © [C.B. Chander Bhan], [2024], INSA Lyon, tous droits réservés

He	CF_4	H_2	Temp	Time
140 sccm	16 sccm	14 sccm	0 °	3min 50sec

Table 5.3: SiNSlow recipe for etching Si_xN_y and resist ARN7520.

on the waveguide. The total thickness of the patterned structure was found to be roughly 600 nm measured by the sides of MRRs as shown in Figure 5.17, which includes both the Si_xN_y and the residual resist layer on top. To remove the leftover resist, a plasma oxidation process was employed with 150 W for 10 mins, followed by immersion in acetone overnight to ensure complete removal of any remaining resist. The cross-sectional profile of the waveguide is illustrated in the SEM image shown in Figure 5.17.

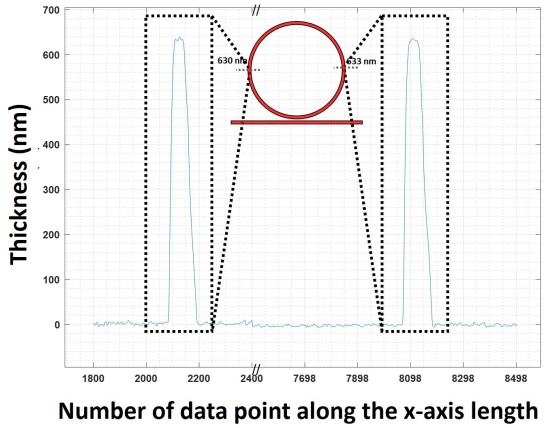

(a)

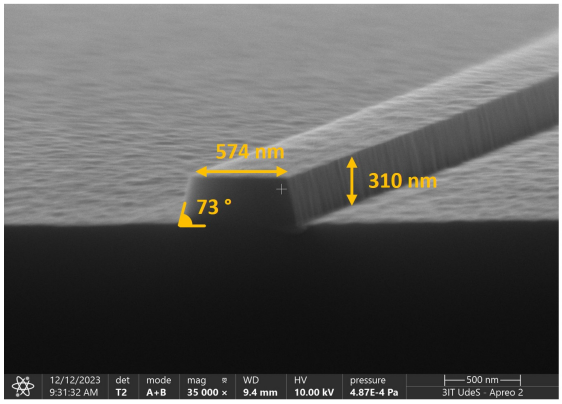

(b)

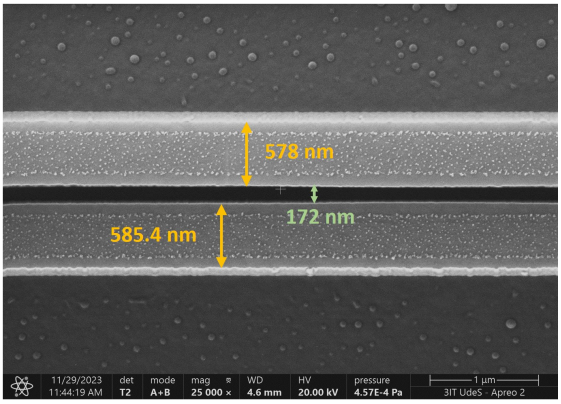

(c)

Figure 5.17: Profilometer profile and electron microscope image of device after etching: (a) illustrates the profilometer profile of the sides of MRRs. (b) the cross-section of the strip waveguide after acetone and plasma oxidation. (c) coupling region after plasma oxidation and acetone cleaning.

The dotted patterns illustrated in the coupling area of the MRRs in Figure 5.17 indicate the residual resist that was not removed by the plasma oxidation process described earlier. To eliminate such resist patterns, a more powerful plasma oxidation process with higher power settings, such as 350 or 400 W, is required. As we fabricated a total of 30 samples, processing them in the etcher tool two at a time would be time-consuming. Therefore, we opted to perform a piranha clean on all the samples at the same time, using a 1:1 ratio of

Thèse accessible à l'adresse : https://theses.insa-lyon.fr/publication/2024ISAL0120/these.pdf © [C.B. Chander Bhan], [2024], INSA Lyon, tous droits réservés

sulfuric acid (H_2SO_4) to hydrogen peroxide (H_2O_2). This piranha solution effectively cleans the waveguides as it does not react with Si_xN_y or SiO_2 on the chip and only reacts with resist. The final cleaned waveguides, along with their dimensions and surface roughness, are shown in the Figure 5.18.

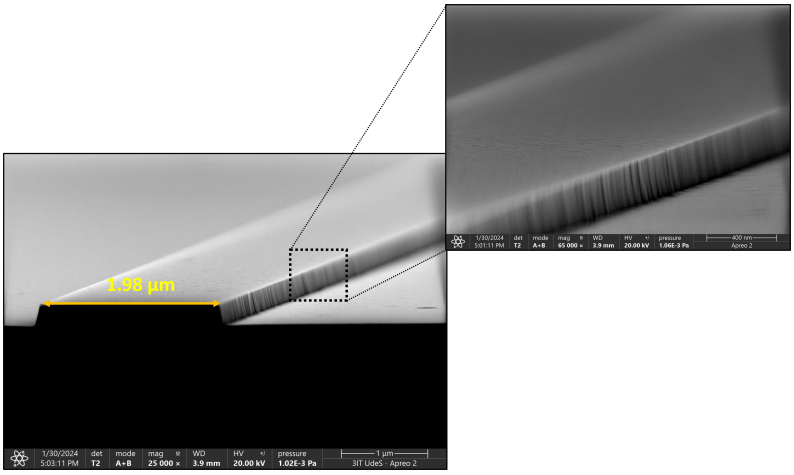

Figure 5.18: SEM image of adiabatic taper (strip waveguide) after piranha to remove the dotten resist pattern on it.

SiO_2 PECVD deposition for Fluidic reservoir and Inverted tapers

This section of the chapter describes the deposition of SiO_2, as discussed in subsection 5.2.1. For the sake of continuity and clarity in the fabrication process, this procedure is detailed here.

As discussed in previous chapters, optical trapping applications require high power in the devices. To enhance coupling efficiency by 75%, we designed inverted tapers (described in chapter 4). These inverted tapers on the chip must be buried beneath a SiO_2 layer of 1-1.5 μm. However, we also require open cladding in the center of the chip to introduce particles and water. In industry, such fabrication steps are typically carried out using lithography and chemical mechanical polishing (CMP) methods, which require a resist thickness double that of the SiO_2 deposition. In our case, this would be approximately 3 μm. Achieving this resist thickness can be accomplished by spin coating the resist twice such as AR-P 3200, CAR 44. Unfortunately, the resist available to us could not withstand the working temperature of SiO_2 PECVD deposition.

Therefore, we engineered a process using a physical silicon mask to cover the center part of the chip and deposited the PECVD SiO_2 at INL shown in Figure 5.19. This was done with the help of two Si supports thick enough to prevent the mask from touching the waveguides. The cross-sectional view of this structure is illustrated in the Figure 5.20, demonstrating the PECVD SiO_2 deposition done at INL following the recipe shown in the Table 5.4. Figure 5.20 (b) and (c) illustrate the point and line EDX on the sample. The line EDX was performed on the edge of the SiO2 layer to observe the edge effect and how far it extends relative to the main devices (bends, spirals, MRRs) on the chip. For the current structure, the edge effect extends to 1200 μm, and the main devices are still 2 mm away from this SiO_2 layer, ensuring that we will be characterizing our device only in the water cladding during characterization.

Moreover, a SiO_2 film at the input and output of chip also helps to prevent reflections

Thèse accessible à l'adresse : https://theses.insa-lyon.fr/publication/2024ISAL0120/these.pdf © [C.B. Chander Bhan], [2024], INSA Lyon, tous droits réservés

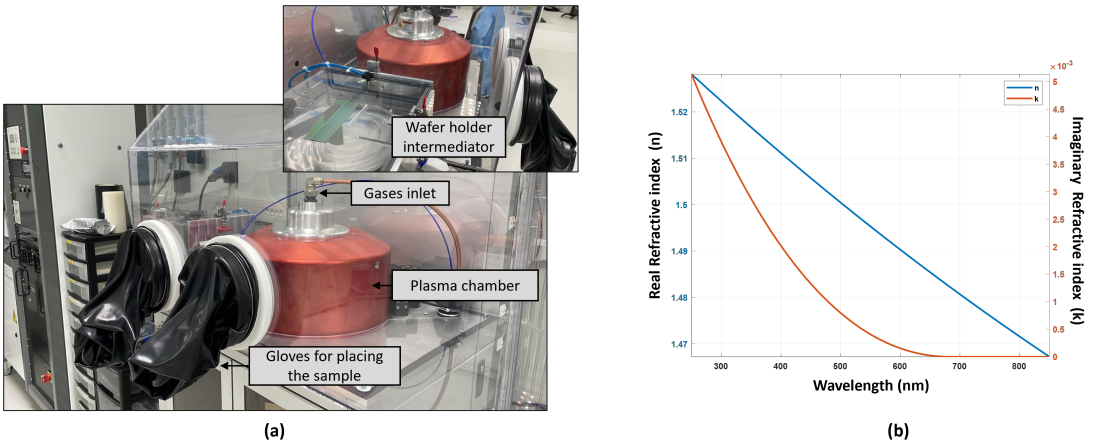

Figure 5.19: PECVD tool at INL used to deposit SiO_2 at the edges of the photonic chip: (a) The PECVD tool (b) The RI graph across the visible wavelength range of PECVD SiO_2 deposited with this tool

between the reservoir and the evanescent field propagating in the waveguide, thereby reducing losses compared to other structures where the PDMS reservoir is directly embedded on the chip.

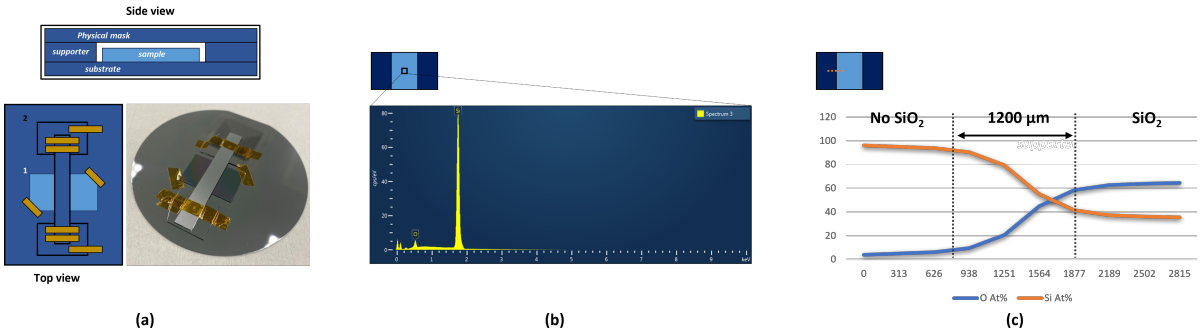

Figure 5.20: PECVD SiO_2 inverted tapers

Pressure	Platen power	Frequency	T	N_2O	SiH_4	N_2
900 mTorr	20 W	13.56 MHz	300 $°C$	1421 sccm	8 sccm	392 sccm

Table 5.4: Standard PECVD high frequency SiO_2 parameters.

5.3 Fluidic setup

To perform our final optical characterisation on the device we need a fluidic setup on the chip to introduce the particles or the analytes to sense by device. In literature, PDMS reservoirs are common for microfluidic reservoirs, channels. PDMS is a combination of a silicone polymer and a curing agent to make the crosslinking in the silicone. The ratio between a silicon polymer and a curing agent can be increased depending on the how strong and hard PDMS is required for the reservoirs and channels. The mold for the reservoir was made by 3D printing based on resin (SLA). The recipe of the PDMS reservoir is illustrated below in Figure 5.21 with all the necessary protocols.

Thèse accessible à l'adresse : https://theses.insa-lyon.fr/publication/2024ISAL0120/these.pdf © [C.B. Chander Bhan], [2024], INSA Lyon, tous droits réservés

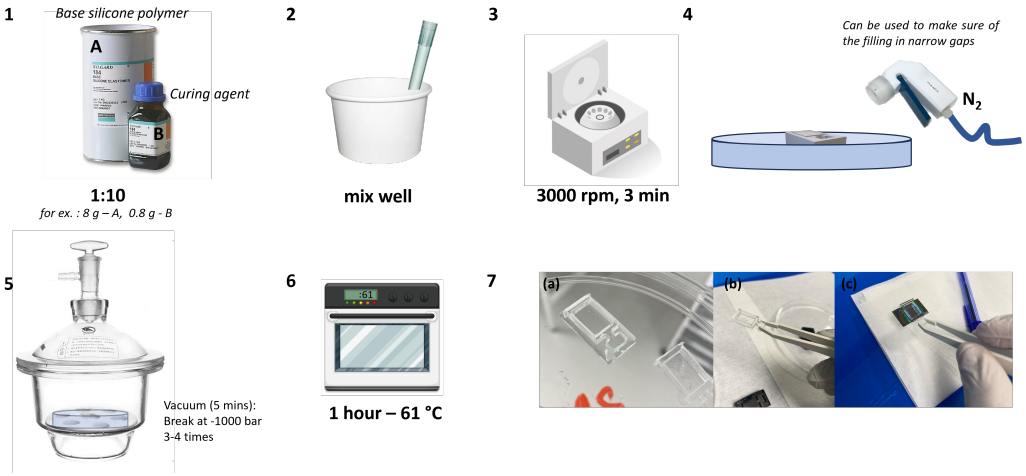

Figure 5.21: Fluidic reservoir fabrication steps using PDMS: Steps 1-6 illustrate all the standard steps involved in fabricating a PDMS reservoir using a mold (shown in step 4). Step 7 represents the adhesion of the reservoir to the SiO_2 substrate, with adhesion strength demonstrated in 7(c).

However, using the PDMS reservoir has three disadvantages in our characterization process. Firstly, it is well-known for releasing its elastomers into water because the curing agent cannot achieve 100% crosslinking efficiency. These elastomers can adhere to the waveguide surface and increase device losses. Secondly, PDMS reservoirs use plasma oxidation to adhere to the silicon chip shown in Figure 5.21 step 7, which complicates solvent cleaning after characterization. Thirdly, due to its softness, aligning PDMS with the silicon chip is challenging. The third issue can be mitigated by increasing the amount of curing agent in the silicone polymer mixture to a 1:8 ratio, but this makes it difficult to remove from molds with narrow sides of 1 mm.

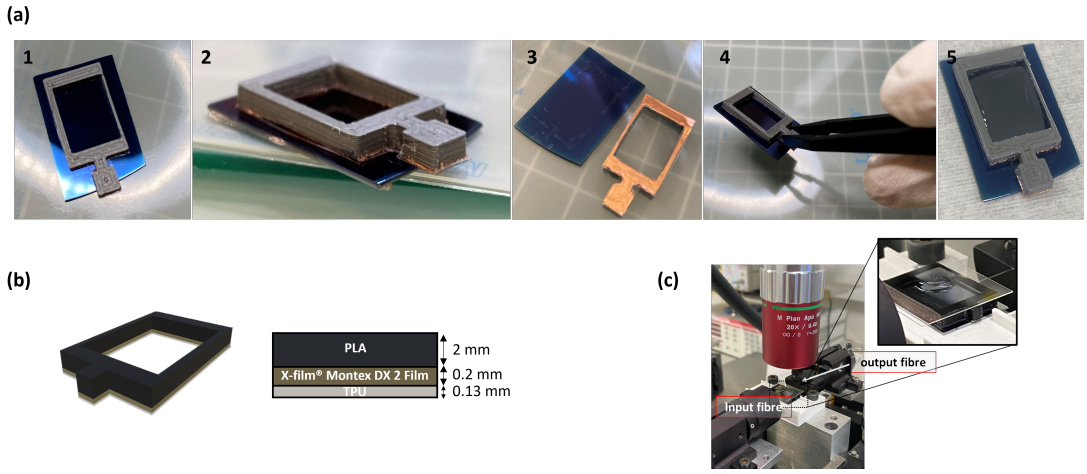

Figure 5.22: Fluidic reservoir fabrication steps using TPU film: (a) Illustration of the fluidic reservoir structure with TPU film, including repositioning and adhesion leakage testing. (b) and (c) Complete schematic diagrams of the reservoir structure and the silicon photonic chip with the reservoir mounted on the optical bench for characterization.

To overcome these problems, “repositionable fluidic” systems using thermoplastic polyurethane (TPU) are becoming popular. TPU features a one-sided adhesive that easily sticks

Thèse accessible à l'adresse : https://theses.insa-lyon.fr/publication/2024ISAL0120/these.pdf © [C.B. Chander Bhan], [2024], INSA Lyon, tous droits réservés

to and detaches from silicon chips shown in Figure 5.22 from 2-4 steps. The adhesion is sufficiently strong to hold fluids inside the structure in step 5 of Figure 5.22 where we have kept the water for more than 4 hours and there wasn't a leakage through it. Furthermore, TPU is increasingly replacing PDMS in microfluidic channels and fluidic structures due to its superior mechanical properties and transparency in the visible range, allowing for clear observation.

We have also combined the TPU reservoir with a 3D-printed PLA material reservoir to add rigidity, which facilitates easier alignment of the reservoir with the samples. Finally, the photonic chip can be filled with water and covered with glass to provide visibility through an IR camera. It can then be mounted on the 3D-printed sample holder shown in Figure 5.22.

5.4 Conclusion

In this chapter, we have presented the various stages in the device fabrication process that were characterized during this thesis. Firstly, we described the STMicroelectronics' photonic platform, DAPHNE, where HOM MRRs were fabricated using photolithography, building on the work of a previous thesis. Secondly, we detailed the technological steps required to fabricate Si_xN_y strip waveguide MRRs at LN2, 3IT Sherbrooke. These steps involve the deposition of PECVD SiO_2 and Si_xN_y, pattern exposure using EBL, and pattern transfer onto the material via ICP etching. Subsequently, we deposited PECVD SiO_2 at both ends of the chip to bury the inverted tapers and to place fluidic reservoirs on them. Profilometry, ellipsometry, and optical and electron microscopy were employed to confirm the dimensions at each step, helping us to avoid fabrication errors.

In Chapter 6, the optical characterization of the various devices studied will be presented.

Thèse accessible à l'adresse : https://theses.insa-lyon.fr/publication/2024ISAL0120/these.pdf © [C.B. Chander Bhan], [2024], INSA Lyon, tous droits réservés

Chapter 6

Characterisation

This chapter focuses on the results of the characterization of the devices designed and fabricated in Chapters 4 and 5. The characterization was conducted at INL, INSA Lyon, using an optical bench with a butt-coupling setup. The chapter is structured into three sections. The first section, “Introduction to Characterization: Optical Setup,” provides a detailed description of the experimental setup used for all characterizations. The second section, “Experimental Results,” discusses the characterization outcomes for device spirals, bends, and microring resonators (MRRs), focusing on linear propagation losses, bending losses, and the frequency spectral characteristics of the MRRs developed in this thesis. The final section, “Optical Trapping and Sensitivity,” explores the results and challenges encountered during the experiments.

6.1 Optical setup

In this section, we examine the optical setup at INL, Lyon, employed for the characterization of the photonic chip developed in this work, as well as for the characterization of devices fabricated in previous studies. Light can generally be coupled into a photonic chip through two methods: grating couplers or edge couplers, as shown in Figure 6.1. Edge couplers typically provide higher coupling efficiency, broader optical bandwidth, and lower polarization-dependent loss compared to grating couplers [155].

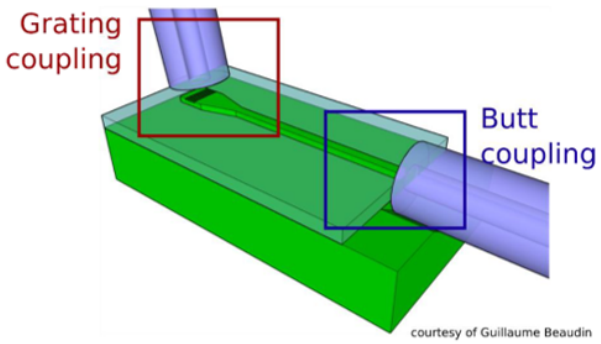

Figure 6.1: Optical coupling mechanism to the photonic chip on optical bench test

Consequently, the photonic chip in this study was designed using adiabatic and inverted

Thèse accessible à l'adresse : https://theses.insa-lyon.fr/publication/2024ISAL0120/these.pdf © [C.B. Chander Bhan], [2024], INSA Lyon, tous droits réservés

tapers to optimize coupling efficiency and to facilitate testing for both transverse electric (TE) and transverse magnetic (TM) modes. In addition, it would be interesting to do the optical trapping characterization for both TE and TM profiles. The evanescent field is quite different for both polarization. So choosing one or the other could lead to better sensitivity and trapping.

Throughout the design process, the operating wavelength of the device was chosen as 1310 nm, owing to the availability of high-power lasers with low material absorption and high energy at this wavelength in both laboratories (Institut des Nanotechnologies de Lyon - INL and Laboratoire Nanotechnologies et Nanosystèmes - LN2, 3IT). Figure 6.2 presents the schematic of the butt-coupling setup at INL, Lyon, detailing all the components necessary for device characterization. At INL, we use a broadband source (BesT LEDs) spanning 1200 – 1700 nm, along with a digital tunable filter to isolate the 1310 nm wavelength from the broadband source for MRR optical sensitivity experiment.

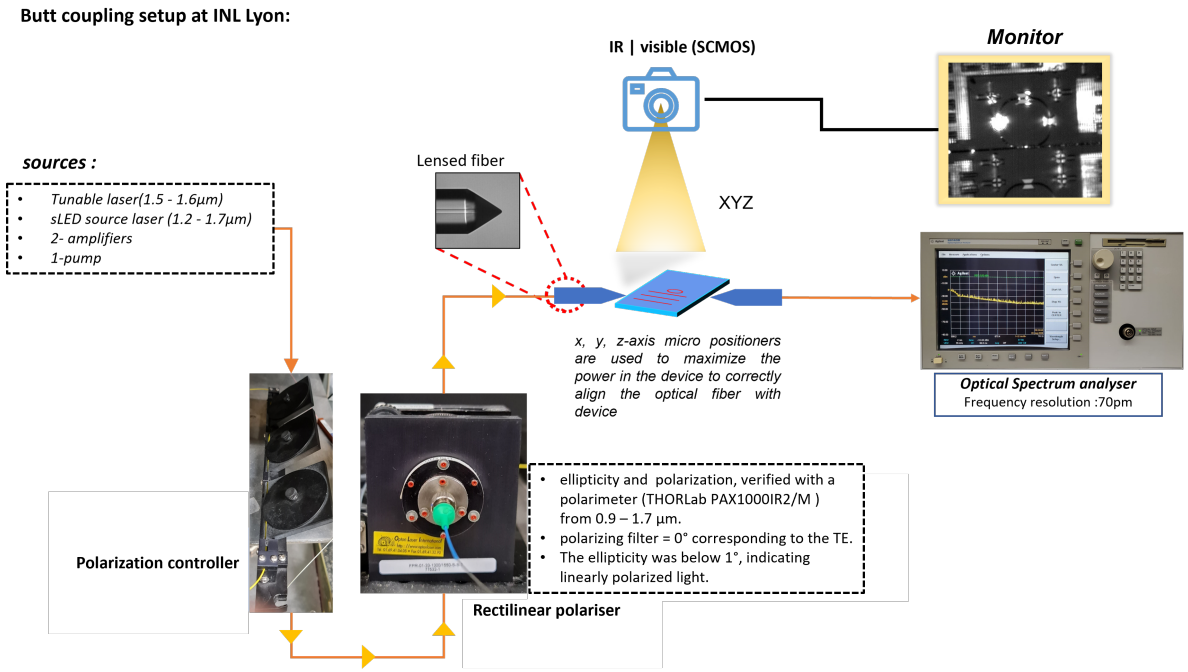

Figure 6.2: Experimental optical bench test at INL,Lyon with butt-coupling mechanism.

The use of a broadband source provides an additional advantage for device characterization, enabling the measurement of losses and resonances in both the O and C bands. Furthermore, the incoherent nature of the broadband source helps bypass the resonances of the Fabry-Pérot cavity formed by the two facets of the waveguide. In most characterizations, broadband light is coupled into the photonic chip using a polarization-maintaining lensed optical fiber, followed by a polarization controller to switch between TE and TM modes. The output light is collected with a non-polarization-maintaining optical fiber and analyzed using an optical spectrum analyzer (OSA). Light coupling into the chip is optimized using mechanical micro-positioners on both the input and output sides of the setup. At INL, two OSAs are available with different resolutions (RBW): 0.07 nm and 0.03 nm.

Furthermore, INL provides additional high-power sources suitable for testing the photonic chip, particularly for optical trapping experiments in this thesis. These sources include a tunable laser at 1550 nm with 10 W of power, a source at 1480 nm with 2 W of power, and

Thèse accessible à l'adresse : https://theses.insa-lyon.fr/publication/2024ISAL0120/these.pdf © [C.B. Chander Bhan], [2024], INSA Lyon, tous droits réservés

another at 980 nm with 10 W of power. Our methodology involved designing the chip for a primary source (1310 nm), after which it can be characterized across the entire O and C bands using a broadband source. If good resonance is observed at other wavelengths, these alternative sources can be employed for optical trapping experiments.

Before presenting the experimental results, It is important to mention that we performed extensive modeling using the FDFV mode solver for validating the experimental findings. This modeling done in the "experimental results" section is based on the dispersion model described in Annex C, which utilizes a custom-made solver employing the Levenberg-Marquardt algorithm to achieve high accuracy in estimating the material dispersion and ensures that the simulated dispersion models closely match the experimental ellipsometry measurements.

6.2 Experimental Results

We began by measuring the propagation and bending losses of the PECVD Si_xN_y ("standard") strip waveguides fabricated at LN2. Initially, we selected samples with adiabatic tapers at the edges to measure losses in waveguides buried under SiO_2, as water absorption could be high and significant material losses could prevent signal detection at the output. Furthermore, the broadband source (BeST LED source) provided only a few mW of output power to couple with the chip, making it preferable to start with waveguides buried under SiO_2. This allows us to observe absorption peaks associated with N-H and O-H defects, which would be more pronounced in water, potentially resulting in a low signal-to-noise ratio (SNR).

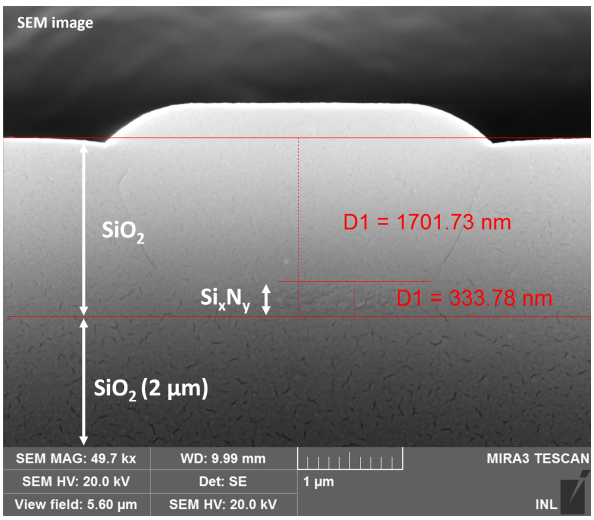

Figure 6.3: SEM image after PECVD deposition of SiO_2 on the edges of a photonics chip with a cross-sectional view of an adiabatic taper with a core width of 2 μm.

The complete photonic chip, comprising racetrack microring resonators (MRRs), spirals, and bends, was fabricated with PECVD Si_xN_y waveguides having cross-sectional dimensions of 610 nm $\times$ 300 nm. To have propagating mode in the waveguides the photonic chip was encapsulated with PECVD SiO_2 at INL followed by a rapid thermal annealing (RTA) process of 5 minutes in N_2 gas was applied to avoid OH bonds that could introduce absorption losses in SiO_2. Figure 6.3 presents a SEM image illustrating the thickness dimension

Thèse accessible à l'adresse : https://theses.insa-lyon.fr/publication/2024ISAL0120/these.pdf © [C.B. Chander Bhan], [2024], INSA Lyon, tous droits réservés

of 1.7 μm, achieved through PECVD SiO_2 deposition on top of the Si_xN_y waveguide at INL. This SEM measurement was done followed by the gold palladium deposition on the sample for 5 mins with 30 mA current using sputter coater (Cressington 208HRD). The thickness of Si_xN_y in the SEM image is not clearly discernible, but an approximate measurement is provided. This falls within the anticipated variation of $\pm$ 30 nm, with all the measured Si_xN_y thicknesses being closely around 300 nm.

For this characterization, a 3D-printed sample holder was used to position the sample on the setup. Figure 6.4.(a) shows the 3D Blender model (.stl file) used for printing with an Anycubic FDM printer, with a nozzle precision of 0.4 mm. Figure 6.4.(b) shows the printed holder integrated into the optical setup. For measurements in a deionized (DI) water cladding, a fluidic reservoir and glass cover were used to prevent evaporation and optical distortion by the meniscus, as depicted in the figure. In contrast, for loss measurements with a SiO_2 cladding, the reservoir and glass cover were unnecessary, as the structure was already embedded in a high-index cladding and could be characterized directly.

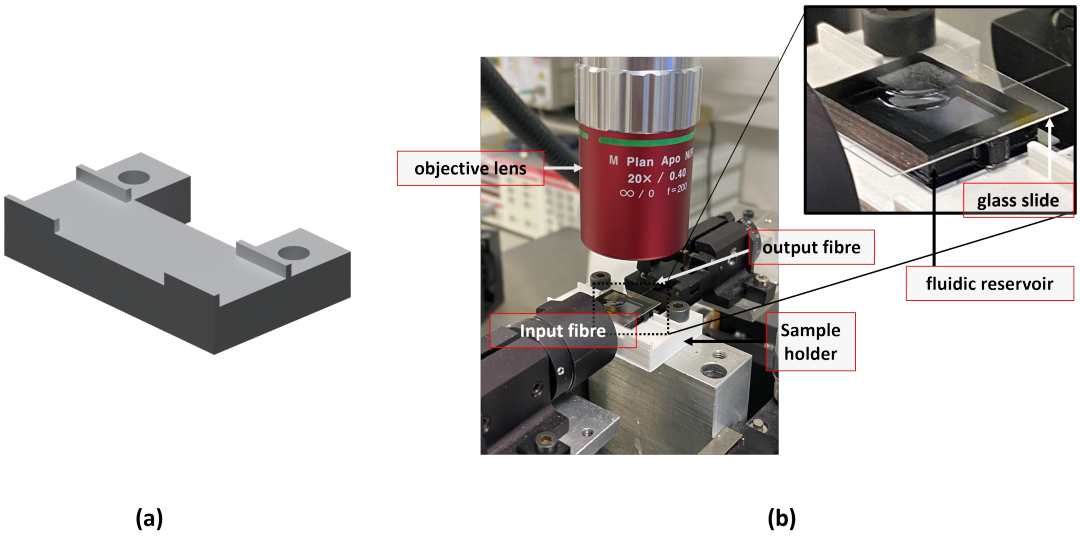

Figure 6.4: Sample holder on the experimental optical bench setup with a fluidic reservoir on top of the chip: (a) 3D Blender model of the sample holder, and (b) a photonic chip with a fluidic reservoir (TPU film + 3D printed reservoir) placed on the sample holder.

6.2.1 Linear propagation losses

As mentioned earlier, each photonic chip was designed and fabricated with 8 spirals and 4 linear waveguides to measure linear propagation losses. The results discussed below are based on measurements from 4 spirals with lengths of 2.78, 3.28, 4.28, and 5.28 cm, and 2 linear waveguides with a length of 1.3 cm. These devices were selected from the total of 8 spirals and 4 linear waveguides due to their minimal or negligible defects.

Figure 6.5(a) shows the output power from the spirals as a function of wavelength for TE polarization, measured using an optical spectrum analyzer, with an average of 5 acquisitions at a sampling frequency of 100 Hz to enhance the signal-to-noise ratio (SNR). The power spectrum represents the power coupled to the spirals with an incoherent broadband source, where the variation in propagation losses as a function of length, is attributed to

Thèse accessible à l'adresse : https://theses.insa-lyon.fr/publication/2024ISAL0120/these.pdf © [C.B. Chander Bhan], [2024], INSA Lyon, tous droits réservés

facet roughness, is gradual. The resolution bandwidth (RBW) of the spectrometer was set to 1 nm to ensure that the signal at each wavelength remained above the spectrometer's integrated detector noise level of 10 pW.

The linear propagation losses (dB/cm) for the Si_xN_y strip waveguide, with critical dimensions indicated in Figure 6.5(b), were evaluated using the linear fit to measurements from the waveguides based on the York method [156]. The propagation losses were calculated using the in-built LINEST function in Excel. The error shown in Figure 6.5(b) represents the standard error (SE) of the beta estimation[1], computed using the INDEX function in combination with LINEST. The resulting linear propagation loss for standard PECVD Si_xN_y of 3IT at 1310 nm is 2.27 $\pm$ 0.054 dB/cm.

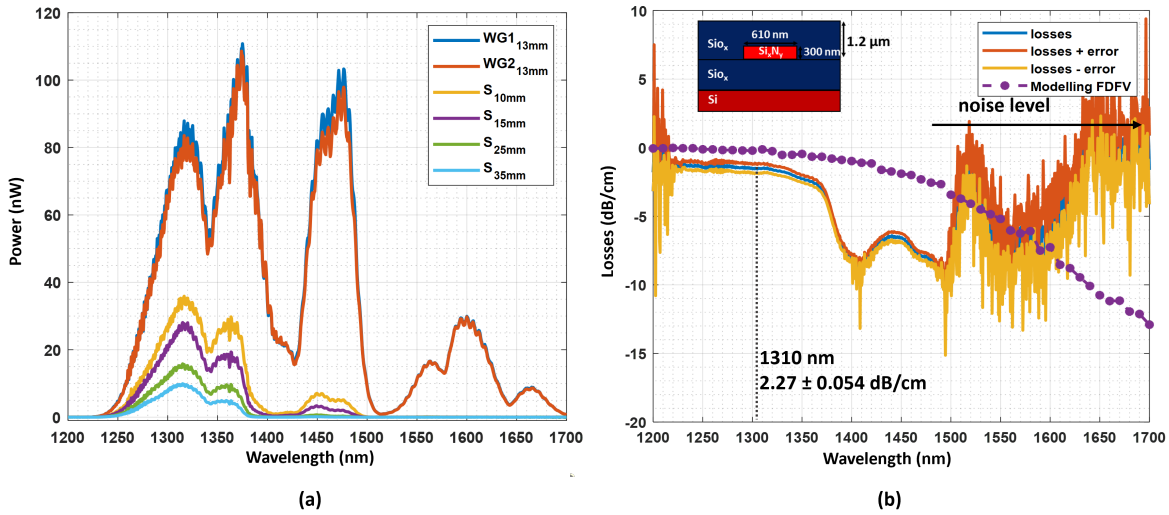

Figure 6.5: Linear propagation losses of a standard PECVD Si_xN_y (3IT) strip waveguide with a cross-sectional width of 610 nm and thickness of 300 nm, buried under PECVD SiO_2: (a) Output power spectrum of spirals and linear waveguides, and (b) Linear propagation losses as a function of wavelength, along with the losses $\pm$ standard error.

The losses above a wavelength of 1400 nm (for E,S,C,L band) were significantly high, as evident in Figure 6.5.(a), resulting in substantial noise in the measurements. The output power from the waveguides and spirals shows that linear waveguides (WG_1 and WG_2) with a length of 1.3 cm still maintain output power at 1550 nm. However, as the waveguide length increases, such as in the spirals S_{15mm} and S_{25mm}, the loss factor rises sharply in the S,C,L band, resulting in very low output power due to absorption losses (NH bonds) and leakage to Silicon substrate. In Figure 6.5.(b), the purple line ('Modelling FDFV') represents the losses due to leakage into the silicon substrate, as evaluated using FDFV modeling. The simulation uses a Si substrate of 0.1 μm thickness sufficient to observe the leakage losses and avoid coupling between the SiO_2 and the Si substrate, which could otherwise induce guided modes due to the presence of boundary conditions in modelling. The leakage losses at a wavelength of 1.5 μm is about 3 dB/cm, which is not negligible. Furthermore, absorption losses associated with NH bonds are also present. These factors, combined, contribute to a significant reduction in signal quality, and leads to noise in our experimental data and making linear regression invalid for range 1200 - 1250 nm and above 1480 nm as shown in Figure 6.5.(b), where the losses are predominantly within the noise range.

[1] is a measure of the standard deviation of the errors in a regression model ($\sigma/\sqrt{n}$)

Thèse accessible à l'adresse : https://theses.insa-lyon.fr/publication/2024ISAL0120/these.pdf © [C.B. Chander Bhan], [2024], INSA Lyon, tous droits réservés

In a previous thesis [134], fabrications performed on both the ST DAPHNE platform and INL, Lyon enabled further investigation of the absorption peak behavior, allowing for a comparative analysis of the losses observed in this study. In that work, Si_xN_y strip microring resonators (MRRs) were fabricated under a SiO_2 buried cladding for gyroscope applications. Figure 6.6 presents the linear propagation loss (dB/cm) measurements as a function of wavelength for each standard PECVD Si_xN_y from 3IT, ST, and INL, along with a schematic diagram of the strip waveguide and their critical dimensions used in the fabrication.

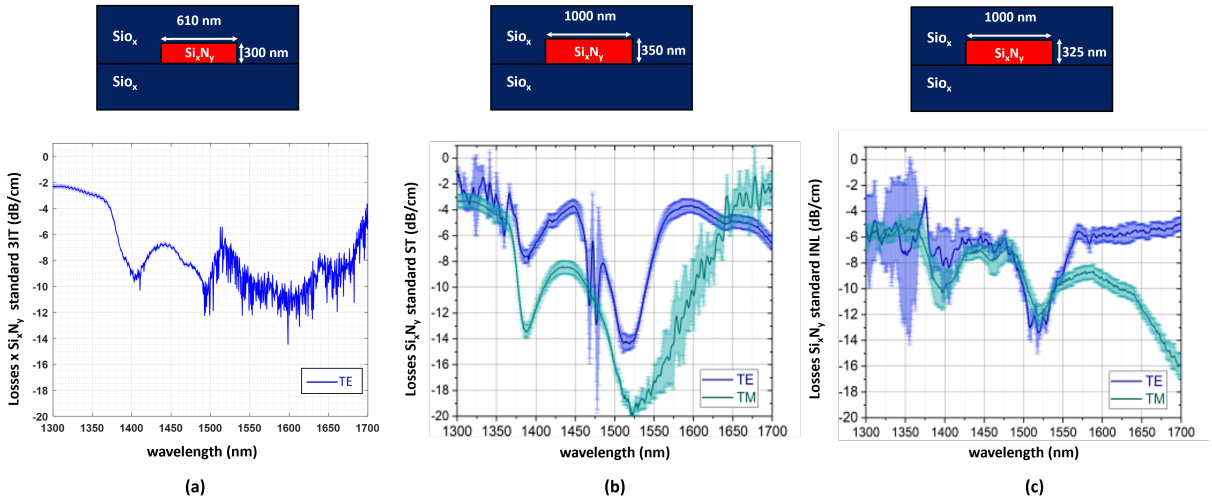

Figure 6.6: A comparative analysis of the linear propagation losses as a function of wavelength, including shaded regions representing the error on independent and dependent variables, is presented for standard Si_xN_y strip waveguides under a SiO_2 cladding. The analysis covers three different cases: (a) standard PECVD Si_xN_y of 3IT, (b) standard PECVD Si_xN_y of ST [134], and (c) standard PECVD Si_xN_y of INL [134].

Figures 6.6(b) and (c) show the propagation losses measured for four waveguides with differential lengths of 0.8 cm, 1.2 cm, 1.6 cm, and 2 cm using the York method, which combines linear regression with the least-squares method by incorporating error bars on both the independent (differential length of the waveguide) and dependent (output optical power) variables. The measurements in Figure 6.6.(b) correspond to the linear Si_xN_y waveguides fabricated at the ST DAPHNE platform with a standard PECVD Si_xN_y thickness of 350 nm, with further processing done at INL. The corresponding losses for the standard Si_xN_y waveguides from ST were 3 dB/cm at 1310 nm and 7.3 ± 0.7 dB/cm at 1550 nm. It is noteworthy that the losses mentioned here were higher in the ST DAPHNE platform samples because they underwent additional processing at INL. In contrast, in Sylvain Guerber's thesis [157], the losses were as low as 0.4 dB/cm for the same thickness and core width of 900 nm, as the waveguides were entirely fabricated at the ST DAPHNE platform using UV photolithography, and the subsequent chemical-mechanical polishing (CMP) step at STMicroelectronics significantly reduced surface roughness.

The measurements in Figure 6.6.(c) correspond to linear Si_xN_y waveguides fabricated at the INL platform with a standard PECVD Si_xN_y thickness of 325 ± 25 nm. The propagation losses for these waveguides were approximately 6 dB/cm at 1310 nm for both TE and TM polarizations.

In contrast, the loss measurements shown in Figure 6.6.(a) correspond to 4 spirals, each with lengths of 2.78, 3.28, 4.28, and 5.28 cm, fabricated at the LN2, 3IT platform with a

Thèse accessible à l'adresse : https://theses.insa-lyon.fr/publication/2024ISAL0120/these.pdf © [C.B. Chander Bhan], [2024], INSA Lyon, tous droits réservés

standard PECVD Si_xN_y thickness of 300 nm. These waveguides were patterned using E-beam lithography, which reduces roughness compared to photolithography. The corresponding propagation losses for the LN2 platform were 2.27 dB/cm for TE polarization. Due to the high absorption peaks associated with NH bonds around 1500 nm in Si_xN_y from LN2, 3IT, a comparison at 1550 nm is not feasible. However, a brief comparison of the losses at 1310 nm is provided in the Table 6.1.

Polarization and losses	ST	INL	3IT
TE	$\approx$ 2.5 dB/cm	$\approx$ 6 dB/cm	$\approx$ 2.2 dB/cm
TM	$\approx$ 3.7 dB/cm	$\approx$ 6 dB/cm	N/A

Table 6.1: Linear propagation losses at wavelength of 1310 nm for standard Si_xN_y strip waveguides under a SiO_2 cladding fabricated at ST, INL and 3IT.

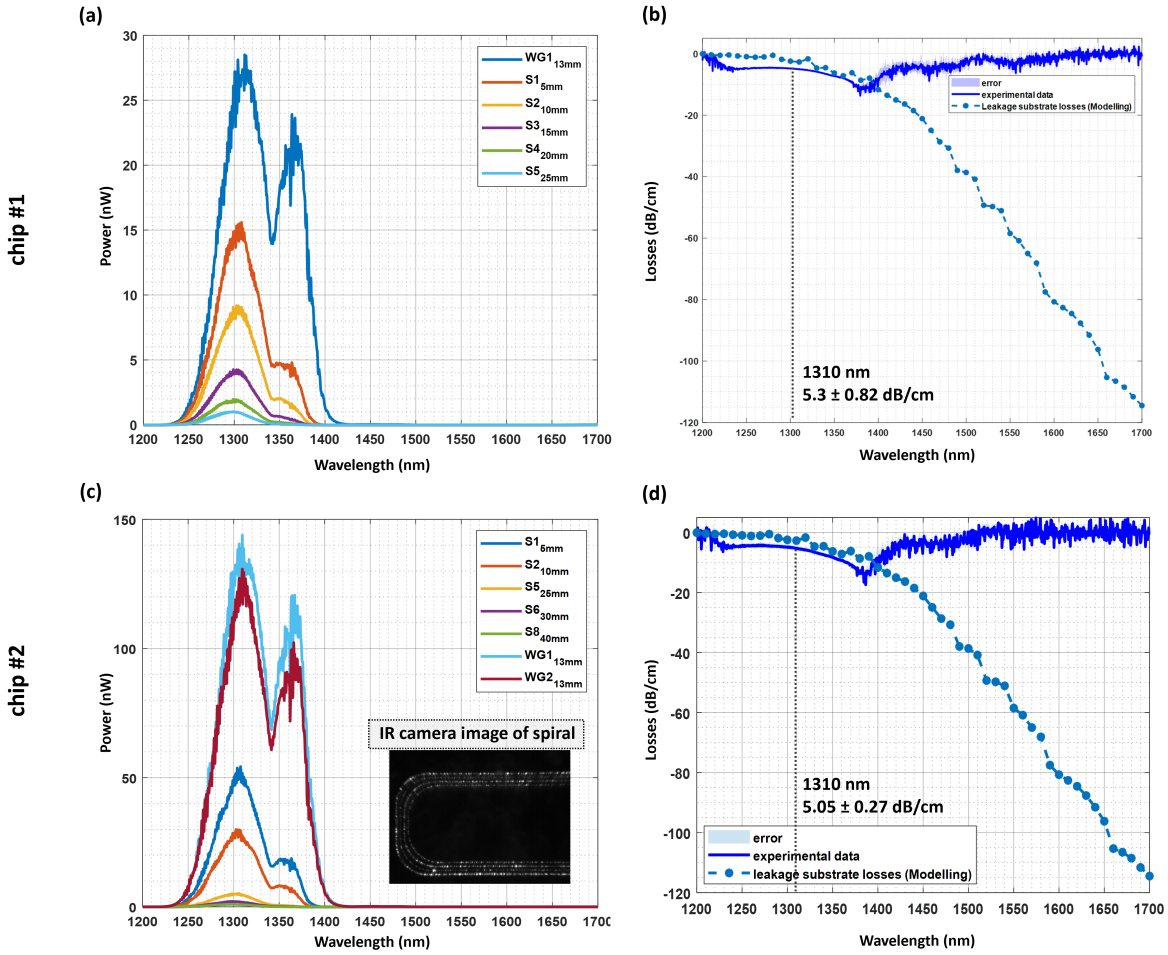

Figure 6.7: Linear propagation losses of a standard PECVD Si_xN_y (3IT) strip waveguide with a cross-sectional width of 610 nm and thickness of 300 nm under water cladding for TE polarization: (a) and (c) output power spectra of spirals and linear waveguides for two different chips, and (b) and (d) Linear propagation losses as a function of wavelength, along with independent and dependent variable errors in water cladding for two different photonic chips.

In this thesis, we optimized the microring resonators (MRRs) for operation in water cladding, as particles will be introduced into water. Consequently, it is essential to investigate the

Thèse accessible à l'adresse : https://theses.insa-lyon.fr/publication/2024ISAL0120/these.pdf © [C.B. Chander Bhan], [2024], INSA Lyon, tous droits réservés

linear propagation losses in a water cladding. The fluidic setup was implemented on the sample, with DI water introduced into the fluidic reservoir using a syringe. The complete fluidic setup on the optical bench is illustrated in Figure 6.4.

The setup employs a Thermoplastic Polyurethane (TPU) film along with a 3D-printed reservoir made of Polylactic acid (PLA) material. This configuration allows for repositioning of the fluidic reservoir and cleaning of the sample before each measurement, enhancing the accuracy and repeatability of the experiment. The 3D-printed reservoir on top of the TPU film provides a firm grip, ensuring proper alignment with the sample. Two samples, characterized with the same waveguide cross-section and fluidic setup approach, were analyzed, and their corresponding linear propagation loss measurements as a function of wavelength are shown in Figure 6.7.

Figure 6.7(a) and (b) show the output power spectra and linear propagation losses as a function of wavelength for linear devices (straight + spirals waveguides) with lengths of 1.3, 2.28, 2.78, 4.28, 4.78, and 5.78 cm in water cladding. The optical spectrum analyzer parameters were kept consistent with those used for the SiO_2 cladding. Similarly, Figure 6.7(c) and (d) present the output power spectra and linear propagation losses as a function of wavelength for linear devices (straight + spirals waveguides) with lengths of 1.3, 2.28, 2.78, 3.28, 3.78, and 4.28 cm. Both sets of measurements correspond to the linear losses of Si_xN_y strip waveguides with a core width of 610 nm and a thickness of 300 nm, for two different photonic chips fabricated using the same process recipes and fluidic setup approach. Furthermore, the shaded regions in the linear loss plots account for errors in both the independent (differential length of the waveguide) and dependent (output optical power) variables. In the both cases, the linear losses corresponds to $\simeq$ 5 dB/cm at 1310 dB for TE polarization.

The absorption peaks caused by OH bonds at 1380 nm in water are significantly stronger than those observed in SiO_2 cladding, making linear regression impractical due to the high noise levels. Similarly, as observed with SiO_2 cladding, NH bond absorption around 1550 nm is also prominent in water cladding. Additionally, leakage into the silicon substrate is more pronounced with water cladding, as demonstrated in Figure 6.8, where leakage losses were estimated using the FDFV solver and compared with those in silicon substrate under SiO_2 cladding. The higher leakage losses in the silicon substrate with water cladding are attributed to the lower RI of water compared to SiO_2. This leads to a reduced mode confinement within the waveguide core, resulting in greater substrate interaction and, consequently, higher losses at longer wavelengths, as evidenced in both the experimental and modeled data in Figure 6.7 and 6.8 respectively. This limits the usable wavelength range and available tunable sources for our optical trapping experiments, making the characterization more challenging.

In previous fabrications on the ST DAPHNE platform, as reported in Michele Calvo's thesis[97], the losses were 1.44 $\pm$ 0.07 dB/cm for the wavelength range of 1.25–1.35 μm for TE polarization, with a cross-sectional width of 700 nm and a thickness of 600 nm in water cladding. Compared to these results, the losses in our devices are higher because the characterized device has a cross-sectional width of 610 nm with thickness of 300 nm, which is closer to the radiation modes (470 nm $\times$ 300 nm). This proximity increases losses due to interactions of the evanescent field with vertical walls and higher water absorption. However, it is important to note that the complete fabrication in this thesis was performed using E-beam lithography, which offers higher resolution than UV lithography. Therefore, further studies

Thèse accessible à l'adresse : https://theses.insa-lyon.fr/publication/2024ISAL0120/these.pdf © [C.B. Chander Bhan], [2024], INSA Lyon, tous droits réservés

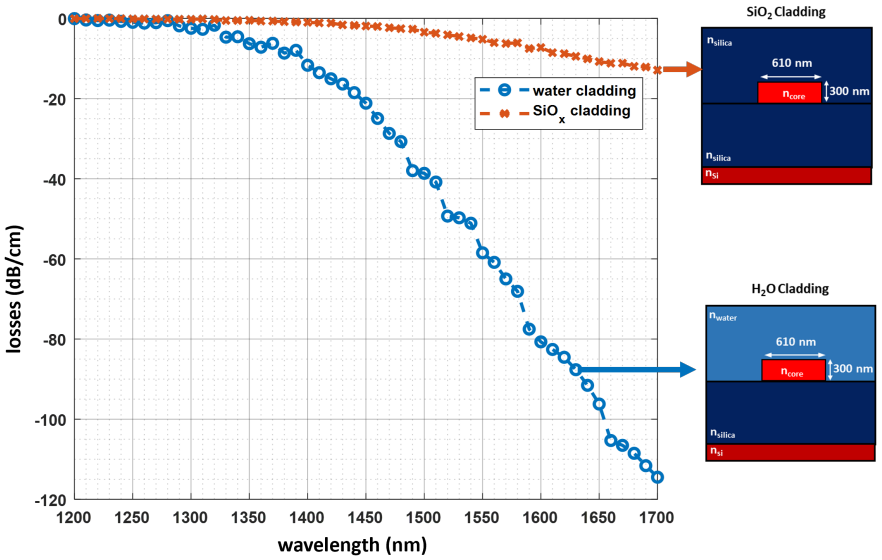

Figure 6.8: Leakage losses estimated with FDFV mode solver due to silicon substrate for both SiO_2 and water cladding of a standard PECVD Si_xN_y (3IT) strip waveguide for TE polarization

are necessary to reduce the losses in the Si_xN_y fabricated at LN2, 3IT.

6.2.2 Bending losses

To measure bending losses, it is important to understand the various factors that affect losses in a bent waveguide. Unlike straight waveguides, bending losses include linear propagation losses, radiation losses, and mode-mismatch losses. These types of losses are thoroughly explained in Chapters 3 and 4. In our characterization, we did not specifically design the bends to measure the mode-mismatch component losses separately. Therefore, the bending losses measured here are assumed to consist primarily of radiation losses combined with all components. Furthermore, it is noteworthy that in high index-contrast waveguides with a large bending radius such as in our case with Si_xN_y waveguides, mode-mismatch losses are negligible. Thus, it was not deemed necessary to measure them separately.

As this was the first time we used the Si_xN_y of 3IT for waveguides in the infrared region, it was crucial to determine the losses for different bending radii and compare them with the simulation model. To achieve this, we designed 10 bending snake structures in our CAD layout to measure bending losses for radii ranging from 50 to 140 μm. The bending waveguides were coupled with a broadband source (BeST sLED), and the power spectra of the different bending waveguides were measured using a power spectrum analyzer with a resolution of 1 nm and a sampling frequency of 100 Hz. The signals acquired were averaged 5 times to reduce noise. The power spectrum for each bending waveguide with core width of 610 nm and thickness of 300 nm in SiO_2 cladding is shown in Figure 6.9, along with a schematic diagram of the bending waveguide structures used for the measurements.

As mentioned earlier, bending losses consist of both linear propagation losses and radi-

Thèse accessible à l'adresse : https://theses.insa-lyon.fr/publication/2024ISAL0120/these.pdf © [C.B. Chander Bhan], [2024], INSA Lyon, tous droits réservés

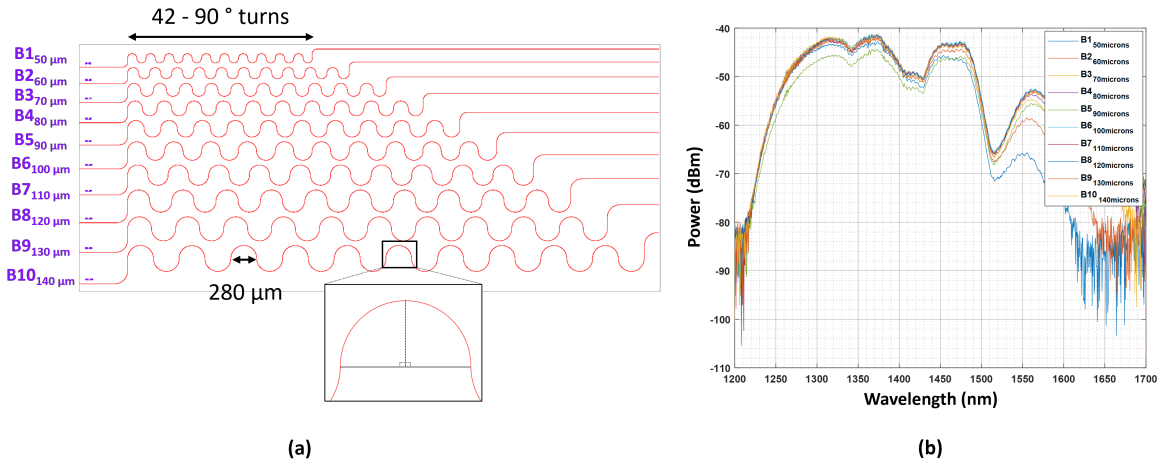

(a) (b)

Figure 6.9: Power spectrum for each bending snake with different bending radii as a function of wavelength: (a) Schematic and CAD diagram of the bending snakes used to measure bending losses, including their dimensions and labels representing the bending radius. (b) Power spectrum as a function of wavelength.

ation losses (assuming mode mismatch losses to be negligible). This results in a parabolic behavior of the total bending losses as a function of the bending radius. If we plot the power spectra at 1310 nm as a function of the bending radius, we should observe this parabolic behavior.

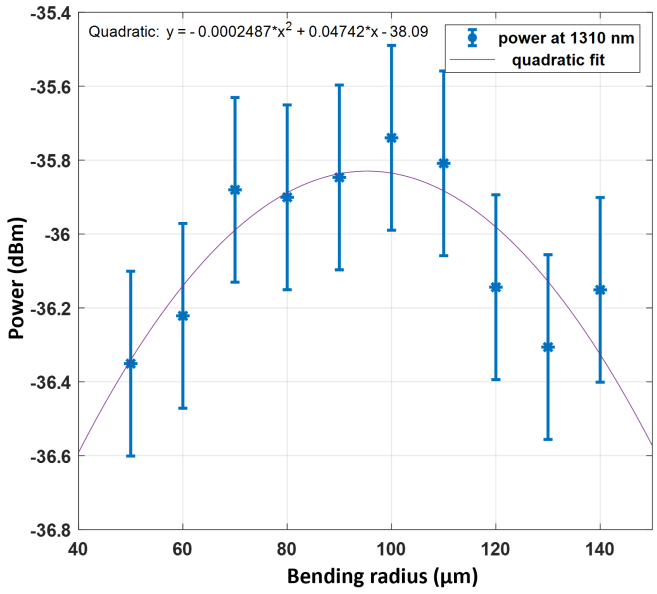

Figure 6.10: Power at 1310 nm wavelength as function of Bending radius to represent the relation between total bending losses as function of bending radius.

The Taylor expansion can be employed to describe the function for experimental data points. When approaching the minimum, the first derivative is zero, and the second derivative provides a quadratic approximation. In this context, as we are near the minimum (i.e., the power coupling for each device has been optimized), a quadratic or parabolic fit can accurately represent the experimental data, with a margin of ± 0.25 dB (half of the measurement accuracy of the spectrum analyzer). From Figure 6.10, it can be observed that

Thèse accessible à l'adresse : https://theses.insa-lyon.fr/publication/2024ISAL0120/these.pdf © [C.B. Chander Bhan], [2024], INSA Lyon, tous droits réservés

the power at 1310 nm indeed shows a parabolic trend as a function of the bending radius. Furthermore, one can easily determine the optimum bending radius from this curve, as it represents the point of minimum total bending losses for the device. Here, the optimum bending radius is found to be around 100 μm, which is very close to the 120 μm radius modeled in our simulations.

The losses induced by surface roughness in bent waveguides can be considered negligible in cases where large bending radii are used. While higher losses may occur at the outer boundary of the bend, these are counterbalanced by lower losses at the inner boundary, resulting in minimal net contribution to the overall loss. Furthermore, If we consider that the bending waveguides are positioned very close to linear waveguides, as shown in Figure 6.11 the linear propagation losses can be subtracted from the bending waveguides' total losses. This process can be normalized by assuming that the same power is coupled into each device. Consequently, the complete equation for calculating the radiation losses is shown in the below figure including the schematic diagram with explanation of the equation.

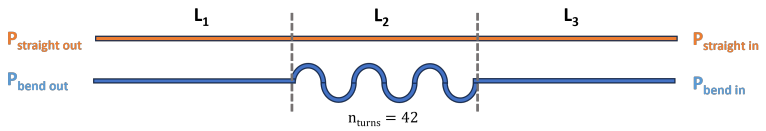

$$\mathbf{P}_{\text{straight out}}(dB) - \mathbf{P}_{\text{bend out}}(dB) = \textit{power lost due to}: \textit{additional linear length (linear propagation losses)} + \textit{radiation losses due to bends}$$

$$\mathbf{P}_{\text{straight out}}(dB) - \mathbf{P}_{\text{bend out}}(dB) = \mathbf{n}_{\text{turns}} \times \left(\frac{\pi}{2} - 1\right) \times \mathbf{R}_{\text{bend}} \times \textbf{linear losses}(dB/cm) + \mathbf{n}_{\text{turns}} \times \textbf{Radiation losses}(\text{dB}/90°)$$

$$\textbf{Radiation losses}\left(\frac{\text{dB}}{90°}\right) = \frac{\mathbf{P}_{\text{bend out}}(dB) - \mathbf{P}_{\text{straight out}}(dB) + \mathbf{n}_{\text{turns}} \times \left(\frac{\pi}{2} - 1\right) \times \mathbf{R}_{\text{bend}} \times \textbf{linear losses}(dB/cm)}{\mathbf{n}_{\text{turns}}}$$

Figure 6.11: Normalization method to estimate radiation losses

Using the equations above, the corresponding radiation losses can be estimated in the range of 1250 - 1480 nm (range where we have only valid experimental data of straight waveguides) for SiO_2 cladding presented in Figure 6.12.(a) for a bending radius of 50 μm as a function of wavelength for TE polarization. As for higher wavelength we observed in Figure 6.5.(b) that due leakage losses (Si substrate) and absorption (NH bonds) the signal are in noise. Therefore, the normalization method utilized in this study is only be valid for lower wavelength ranges (1250 - 1480 nm)as the mode are well confined and behaving more similar to the straight waveguides.

The green and purple solid lines represent the radiation losses calculated using the FDFV mode solver [87] for a 50 μm bending radius and a Si_xN_y thickness of 300 nm, corresponding to configurations without and with the Si substrate, respectively. Figure 6.12.(b) illustrates how the mode profiles of the bending modes shift upwards in the presence of the Si substrate, compared to the configuration without it. The effective refractive index (n_{eff}) of the bending mode at the point of maximum power increases with the Si substrate, resulting in a reduction in radiation losses.

Considering fabrication variations, we also modeled radiation losses for a Si_xN_y thickness of 330 nm, which aligns with the experimental data in the lower wavelength range. The observed discrepancy between experimental and modeled data (eg = 330 nm) at higher wavelengths is attributed to the weaker confinement of the modes, leading to leakage toward the SiO_2 substrate. However, the presence of the Si substrate alters the mode profile,

Thèse accessible à l'adresse : https://theses.insa-lyon.fr/publication/2024ISAL0120/these.pdf © [C.B. Chander Bhan], [2024], INSA Lyon, tous droits réservés

increases the n_{eff}, and reduces the losses. This behavior explains the deviations observed in our experimental results.

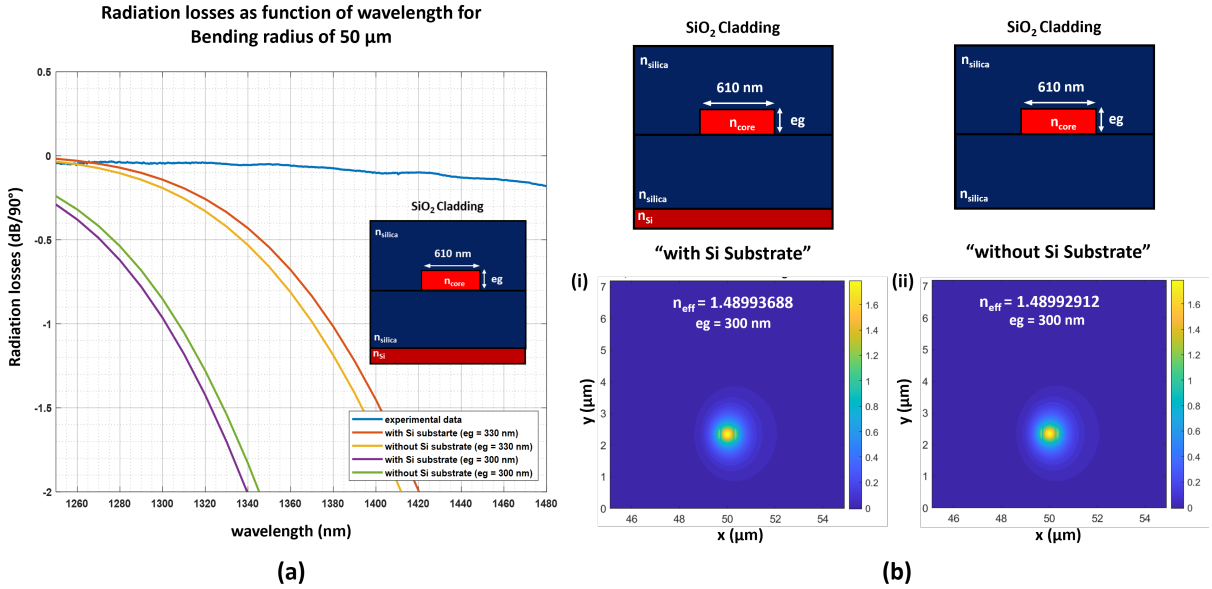

Figure 6.12: Experimental and simulated radiation losses (dB/90°) for a 90° circular bending radius of a strip waveguide under SiO_2 cladding: (a) Radiation losses as a function of wavelength for a bending radius of 50 μm, and (b) Schematic diagram and TE mode profile of bending mode at 1310 nm for 50 µm bending radius.

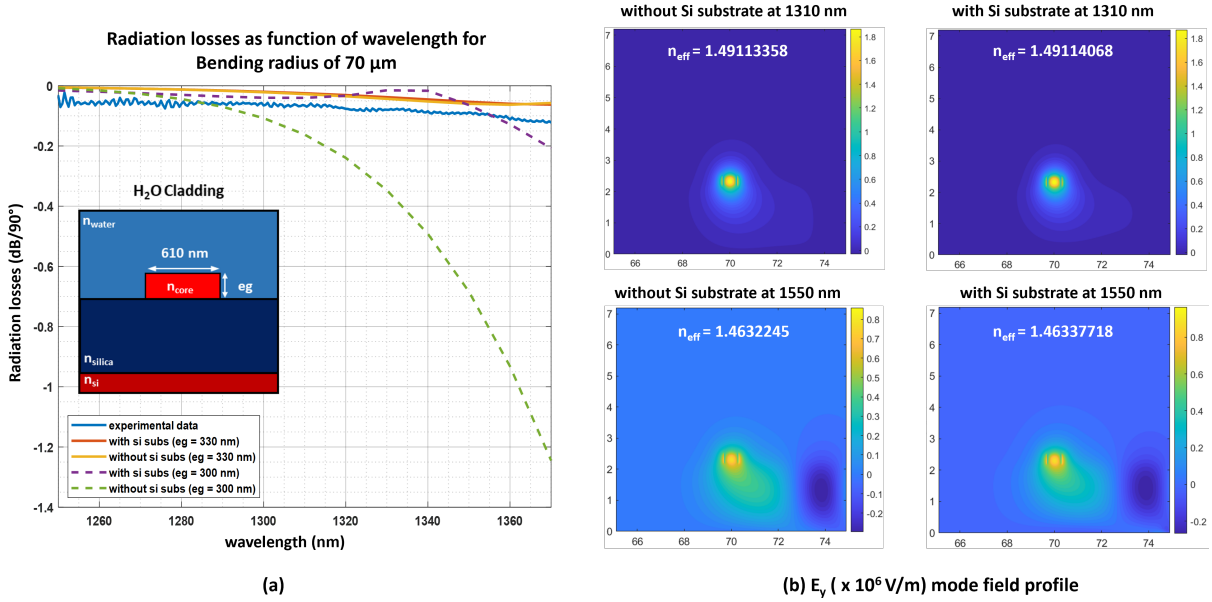

Figure 6.13: Experimental and simulated radiation losses (dB/90°) for a 90° circular bending radius of a strip waveguide under water cladding: (a) Radiation losses as a function of wavelength for a bending radius of 70 μm, and (b) TE mode profile of bending mode of 70 µm bending radius at 1310 nm and 1550 nm.

To measure the bending losses in water cladding, the same fluidic setup method was employed as described earlier for linear propagation losses in water cladding. The corresponding radiation losses for a 70 μm bending radius for TE polarization in the range of 1250 -

Thèse accessible à l'adresse : https://theses.insa-lyon.fr/publication/2024ISAL0120/these.pdf © [C.B. Chander Bhan], [2024], INSA Lyon, tous droits réservés

1370 nm (range where we have only valid experimental data of straight waveguides in water cladding) are shown below in Figure 9.22.(a), along with a schematic diagram of the waveguide dimensions and modelling results of radiation losses in water cladding with and without Si substrate for two waveguide thickness of 300 and 330 nm. In Figure 9.22.(a), the radiation losses are shown for configurations with ('purple dashed line') and without ('green dashed line') a Si substrate, highlighting how the presence of the Si substrate reduces losses. This reduction occurs due to changes in the mode profile, which increases the n_{eff} of the bending mode at the point of maximum power, as illustrated in Figure 9.22.(b), ultimately leading to a decrease in losses.

Additionally, as defined earlier, the Si_xN_y thickness can vary by approximately $\pm$ 30 nm. To account for this variation, we modeled the radiation losses for a thickness of 330 nm, with ('orange solid line') and without ('yellow solid line') the Si substrate. The modeled losses for the 330 nm thickness align closely with the experimental data, as shown in Figure 9.22.(a).

6.2.3 MRRs spectral characteristics

In this section, we present the experimental characterization results of the MRRs designed in Chapter 4, using the optical bench setup shown in Figure 6.2. The focus will be on the spectral characteristics of the MRRs to determine the quality factor, FSR and FWHM of resonance peaks, which are crucial for proceeding with our optical trapping experiments. As we were expecting linear propagation losses of around 3-4 dB/cm in our MRRs, we did not anticipate achieving high quality factors for the rings. Therefore, we continued our characterization using a broadband source with a spectrum analyzer set to a resolution of 0.03 nm. The data were acquired over 20,000 points, averaged over 5 acquisitions, with a sampling frequency of 100 Hz.

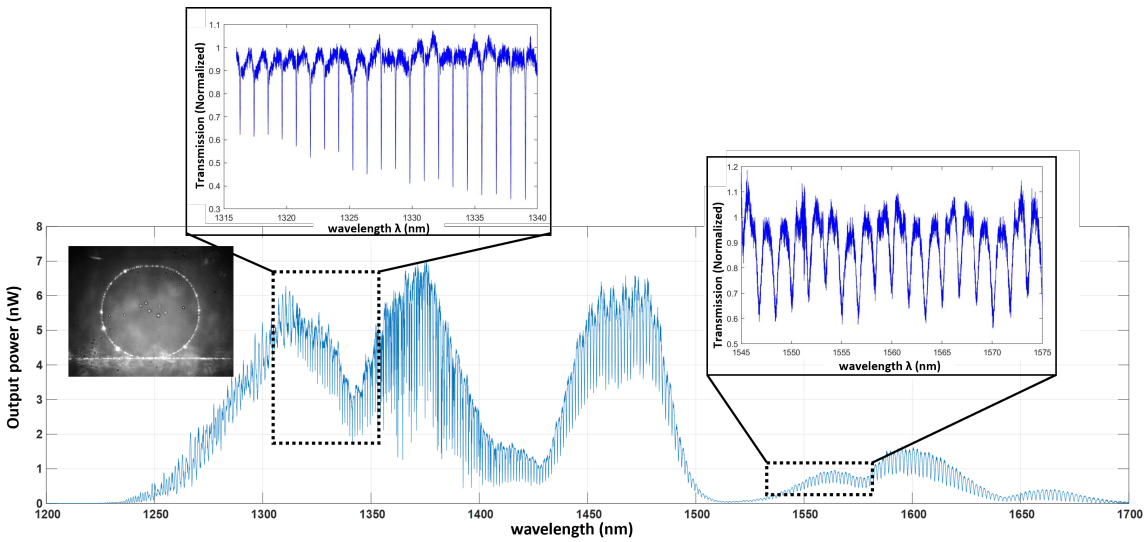

Figure 6.14: Output power spectra observed with an optical spectrum analyzer for a racetrack MRR with coupling gap of 350 nm under SiO_2 cladding, with the normalized transmission spectra highlighted in blue around the wavelength ranges of 1310 nm and 1550 nm.

For a racetrack MRR with a cross-sectional width of 610 nm and a thickness of 300 nm, the

Thèse accessible à l'adresse : https://theses.insa-lyon.fr/publication/2024ISAL0120/these.pdf © [C.B. Chander Bhan], [2024], INSA Lyon, tous droits réservés

transmission spectrum is shown in Figure 6.14 for SiO_2 cladding with coupling gap of 350 nm, along with an IR image of the MRR showing the injected light power circulating within the ring.

From the total power spectrum shown in Figure 6.14, the relevant wavelength ranges of 1315–1340 nm and 1545–1575 nm are shown in details. These normalized resonance peaks are then separated using a peak-detection method and fitted with a Lorentzian curve to extract the Full Width at Half Maximum (FWHM) and Free Spectral Range (FSR) for each resonance. Figure 6.15.(a) shows the selected resonance peaks within the range of 1315–1340 nm, obtained with 20,000 data points and a resolution of 0.03 nm in the optical spectrum analyzer.

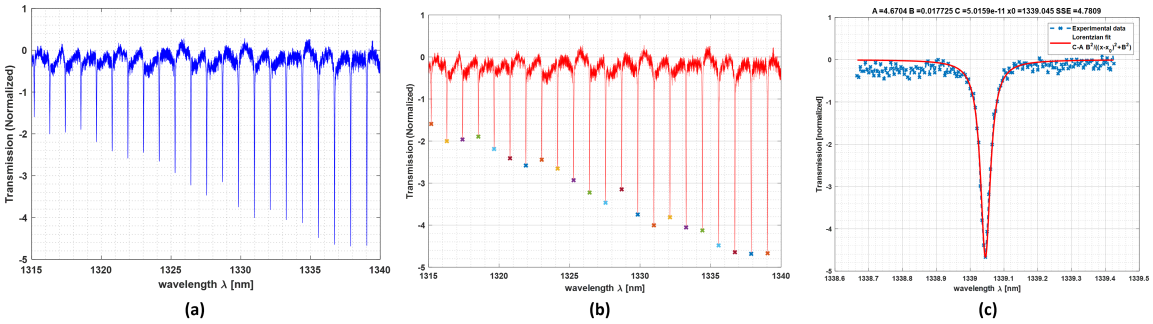

Figure 6.15: Peaks method to determine the frequency spectral characteristics of MRRs: (a) Normalized transmission with respect to wavelength, (b) Selected peaks using peak detection methods, and (c) Lorentzian fit along with the experimental data points.

Using the Lorentzian model as shown in equation 6.1 the data points can be fit as illustrated in Figure 2.(c), The FSR was 1.136 nm were obtained with the FWHM 0.0366 nm which is 2 times of B coefficient .

$$L(x) = C - A \times \frac{B^2}{((x - x0)^2 + B^2)} \tag{6.1}$$

where, L(x) represents Lorentz function; A,B and C represents the coefficients and x_0 resonating wavelength (λ_{res}).

The Q of the MRRs is defined as:

$$Q = \lambda_m / FWHM \tag{6.2}$$

where λ_m is the resonant wavelength. Using this equation, the quality factor (Q) of the MRR is approximately 32,000 for the resonance shown in Figure 6.15 for TE polarization in the wavelength range of 1315–1340 nm. It can be observed that the resonances around 1550 nm are of poor quality due to high absorption and low coupling in this range.

The same methodology was used to measure the spectral characteristics of other MRRs with different coupling gaps. For a coupling gap of 400 nm, a Q of approximately 18,000 was obtained in the wavelength range of 1285–1340 nm, and a Q of about 6,500 was observed in the range of 1485–1575 nm. The transmission spectra of the racetrack MRRs, highlighting the relevant resonance peaks, are shown in Figure 6.16.

Thèse accessible à l'adresse : https://theses.insa-lyon.fr/publication/2024ISAL0120/these.pdf © [C.B. Chander Bhan], [2024], INSA Lyon, tous droits réservés

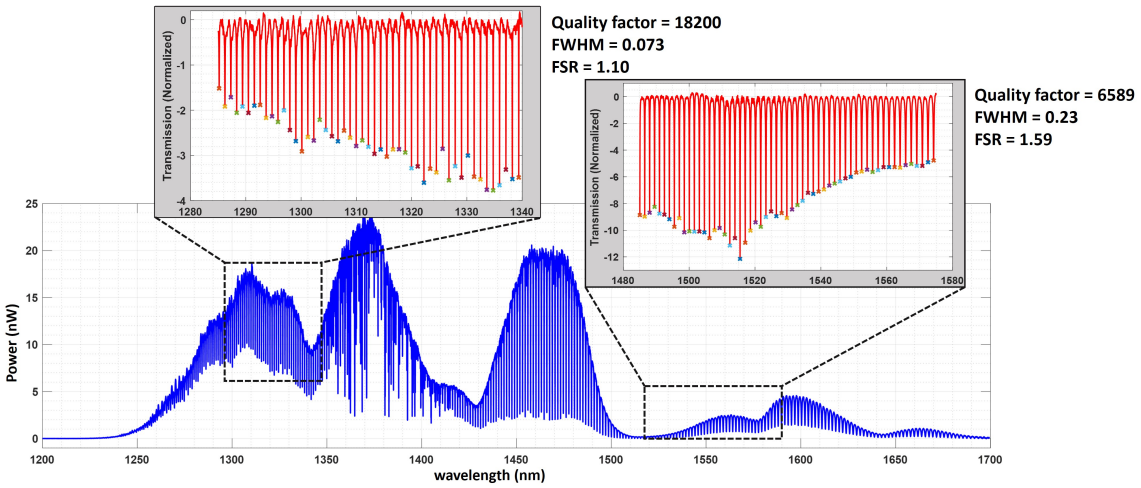

Figure 6.16: Output power spectra observed with an optical spectrum analyzer for a racetrack MRR with coupling gap of 400 nm under SiO_2 cladding, with the normalized transmission spectra highlighted in blue around the wavelength ranges of 1310 nm and 1550 nm.

It is important to note that, as observed in the loss measurements (for SiO_2 cladding) above 1500 nm, a similar trend is seen here. The Quality factor (Q) of the MRRs in the 1300 nm range is significantly higher compared to the 1500 nm range due to the increased losses by NH defects at 1500 nm wavelengths range.

In the case of water cladding, the transmission for the same cross-sectional MRR with a coupling gap of 450 nm, as discussed above, is shown in Figure 6.17 for TE polarization. The figure also presents the frequency spectral characteristics and an image from an IR camera showing the light propagating in the ring as it resonates at different wavelengths.

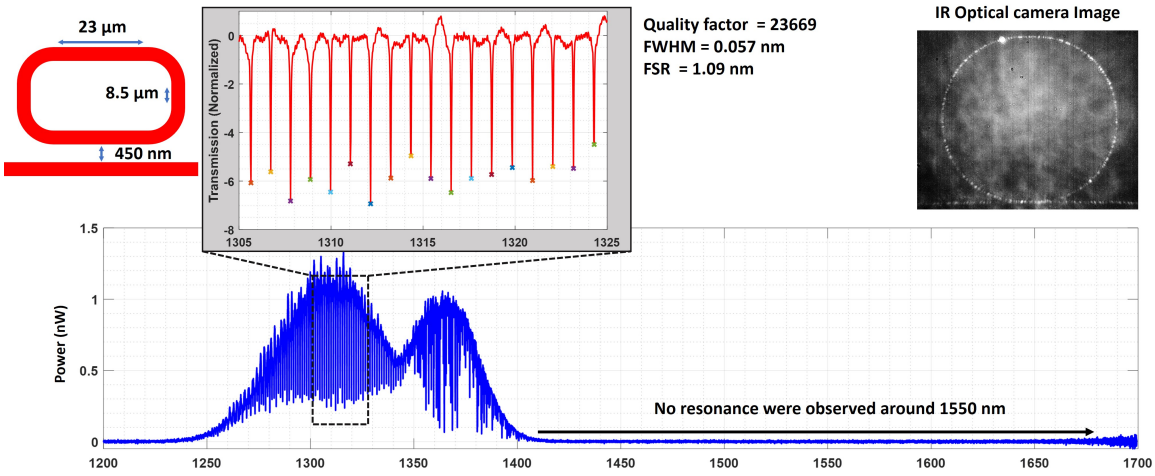

Figure 6.17: Power spectrum observed with an optical spectrum analyzer for a racetrack MRR with coupling gap of 450 nm under water cladding, with the normalized transmission spectrum highlighted in blue around the wavelength ranges of 1310 nm.

Due to the high absorption associated with NH bonds and water, no resonances are observed around the 1550 nm wavelength. The few mW output from the broadband source is insufficient to measure losses and resonances above the 1550 nm range, as the signal

Thèse accessible à l'adresse : https://theses.insa-lyon.fr/publication/2024ISAL0120/these.pdf © [C.B. Chander Bhan], [2024], INSA Lyon, tous droits réservés

remains below the signal-to-noise ratio. To address this, a tunable high-power source will be used to ensure detectable signals in the spectrum.

To validate the experimental data with our modeling, as discussed in Chapter 4, we observed that the racetrack resonator in water cladding achieves critical coupling at 430 nm, which is very close to the 450 nm (experimental data), as shown in Figure 6.17. A resonance at 1312 nm exhibits a resonance contrast of 7 dB, and it can be assumed to be at critical coupling. Therefore, the quality factor (Q) can be estimated using the formula provided in Equation 2 for critical coupling ($a = \tau$):

$$Q = \frac{\lambda_m \pi}{\Delta\lambda_{FSR}} \cdot \frac{a}{1 - a^2} \tag{6.3}$$

where λ_m represents the resonating wavelength, $a = e^{-\frac{\alpha L}{2}}$, L represents the length of the ring, and α is the sum of linear propagation and bending losses. By considering linear propagation losses of 5 dB/cm and a bending loss of 0.09 dB/90 $^\circ$ (experimental data) for a 120 µm bending radius, along with a free spectral range (FSR) of 1.1 nm, the calculated Q-factor of the ring resonator is 46,659. This value significantly exceeds the Q-factor estimated via Lorentzian fitting from the experimental data shown in Figure 6.17.

It can be concluded that, in the case of both SiO_2 and water cladding, the FWHM is very close to the resolution limit of the spectrum analyzer (0.03 nm), suggesting potential undersampling of the resonances. Consequently, this aspect of the characterization remains under investigation, and further findings may be presented in future work.

To characterize the samples in a fluidic environment, it is necessary to deposit SiO_2 on the edges of the photonic chip, specifically on the tapers where the fluidic reservoir is placed. This deposition helps to reduce additional losses due to the interaction of other materials with the evanescent field propagating in the waveguide. It also protects the waveguide in case repositioning or cleaning is needed after measurements. However, due to the technical unavailability of Silane (SiH_4) in our lab, we couldn't prepare our samples further.

As a result, we performed some characterizations on previously fabricated devices to gain more insights. In a previous thesis, higher-order mode (HOM) MRRs fabricated on the DAPHNE platform were used to characterize the spectral characteristics of the MRRs. The normalized transmission between 1285-1340 nm for 600 nm coupling gap of the HOM MRRs at TM polarization under water cladding, along with a schematic diagram illustrating the critical dimensions of the MRRs, is shown in the Figure 6.18.

For the transmission shown in the Figure 6.18, measurements were obtained using a spectrum analyzer with a resolution of 0.07 nm. A total of 10,000 points were recorded, averaging 5 acquisitions to minimize noise. A Q of 3800 was achieved, with a FSR and FWHM of 3.1 nm and 0.31 nm, respectively, for the resonance peak at 1315 nm.

6.3 Optical trapping

In this section, we will discuss the initial trials conducted during this thesis to perform optical trapping experiments using previously fabricated devices. These early experiments

Thèse accessible à l'adresse : https://theses.insa-lyon.fr/publication/2024ISAL0120/these.pdf © [C.B. Chander Bhan], [2024], INSA Lyon, tous droits réservés

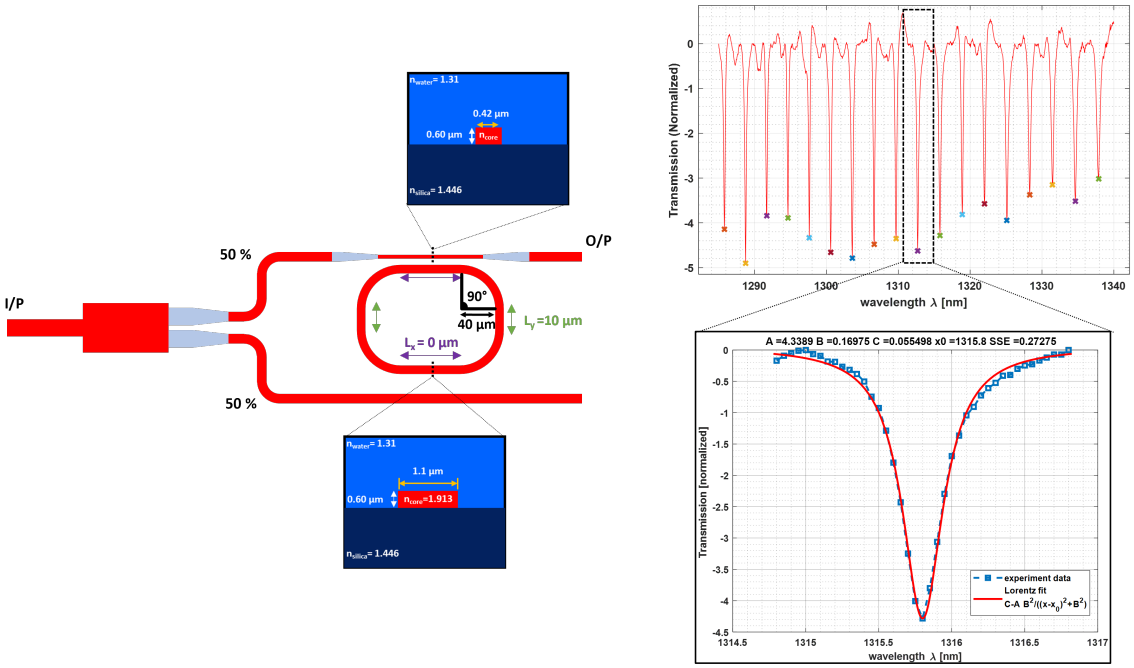

Figure 6.18: Normalized transmission for racetrack HOM MRRs with a coupling gap of 600 nm under water cladding, in the wavelength range of 1290–1340 nm. The schematic diagram illustrates the critical dimensions of the MRRs.

provided valuable insights that helped improve the design for the current work. Fortunately, we managed to design simple dielectric MRRs within this thesis for optical trapping. However, we were unable to continue the experiments due to the unavailability of a high power tunable laser source at 1310 nm, which is necessary for further characterization (further explanation is provided below).

Therefore, we will focus on discussing the experiments performed at the beginning of the thesis using hybrid plasmonic waveguide MRRs fabricated on the DAPHNE platform. Additionally, we will share the protocols followed during these experiments, the challenges encountered, and the current obstacles we are facing.

To perform the optical trapping experiments, fluorescent polystyrene particles with a diameter of 1 μm were selected. However, these polystyrene particles cannot be directly introduced into the fluidic medium (water) due to the risk of aggregation caused by van der Waals forces, which may also lead to their adhesion to the waveguide walls. To mitigate aggregation among the nanoparticles, a surfactant such as sodium dodecyl sulfate (SDS) can be employed. It is crucial to carefully control the concentration of SDS, particularly concerning its critical micelle concentration (CMC), as an excess beyond the CMC can induce further aggregation. For this experiment, a solution of 40 μL of SDS (0.25 mg/L) in 20 mL of water was prepared, to which 200 μL of polystyrene particles (1 μm in diameter) was added.

A similar edge-coupling optical setup, as shown in the figure, was used for this experiment. Since we were working with a broadband source, a digital tunable filter (with a range of 1280–1330 nm) was employed immediately after the broadband source to selectively inject light at specific wavelengths to achieve resonance within the ring and observe optical trapping. Additionally, a semiconductor optical amplifier (SOA) was operated at 700 mA before

Thèse accessible à l'adresse : https://theses.insa-lyon.fr/publication/2024ISAL0120/these.pdf © [C.B. Chander Bhan], [2024], INSA Lyon, tous droits réservés

injecting light into the MRRs to achieve higher power within the ring, thereby enhancing the optical trapping force. The optical trapping setup with a sample used is shown below in the Figure 6.19.

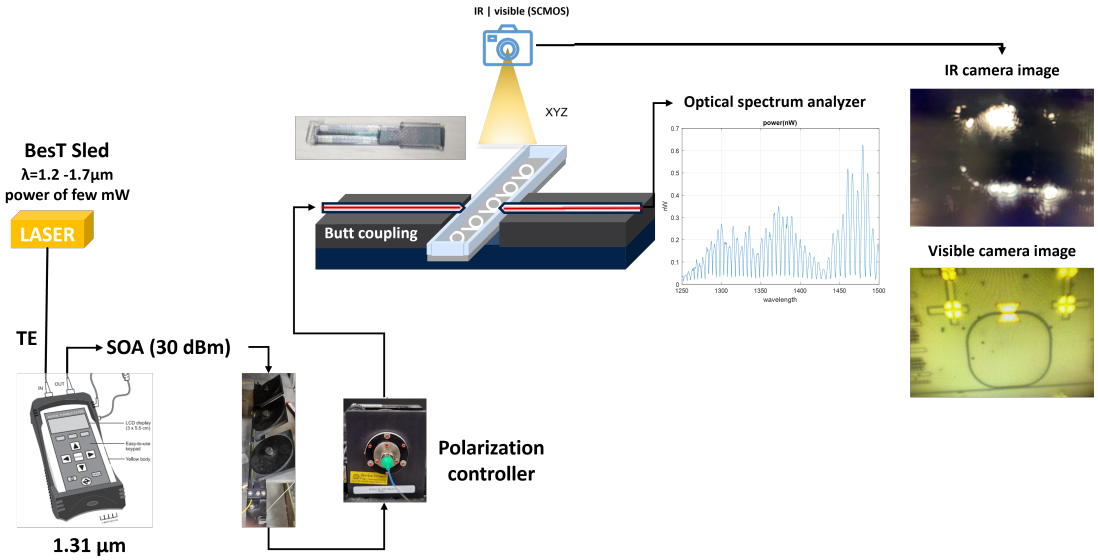

Figure 6.19: Experimental optical trapping setup

Using the optical setup described above, we selected a wavelength of 1310 nm, at which resonance in the microring resonator (MRR) was observed on the spectrum analyzer. Once resonance was confirmed, particles were introduced into the static fluidic reservoir using a syringe. Upon observing particle motion, videos were recorded using the camera installed on the setup. These recorded videos could then be analyzed using the ImageJ software to perform particle tracking from both IR and visible camera recordings. This analysis would enable the determination of particle velocity and motion in the presence of an evanescent field.

We conducted this experiment with two different hybrid plasmonic waveguide (HPWG) microring resonators (MRRs): one with three hybrid plasmonic sensing areas and another with a single hybrid plasmonic sensing area. Each setup was tested with two different particle diameters, 1 μm and 4.8 μm. For each experiment, we recorded a short video using a phone to capture the motion of the particles from the live video playing by CMOS visible camera on monitor (unfortunately, we couldn't record the video from the camera software due to lots of complexities during the experiment). We relied on Brownian motion to bring the particles close to the waveguides for trapping by the ring. This setup required careful management of the micropositioners, which sometimes shifted and had to be adjusted simultaneously.

Due to these complexities and challenges, we were unable to record the experiment with camera software that could have provided high frame rate and resolution, which would have allowed for a clearer observation of particle motion. However, from the figure below, which shows different time frames from the videos, it is evident that no optical trapping phenomena were observed. In the frames of the MRRs with particle size 4.8 μm, there might be an indication that a particle became trapped in the sensing areas. However, for optical trapping to occur, the gradient force must be accompanied by a scattering force that pushes other particles in the direction of light propagation. As no such phenomena were

Thèse accessible à l'adresse : https://theses.insa-lyon.fr/publication/2024ISAL0120/these.pdf © [C.B. Chander Bhan], [2024], INSA Lyon, tous droits réservés

observed for either particle size, we unfortunately did not observe any optical trapping with these devices.

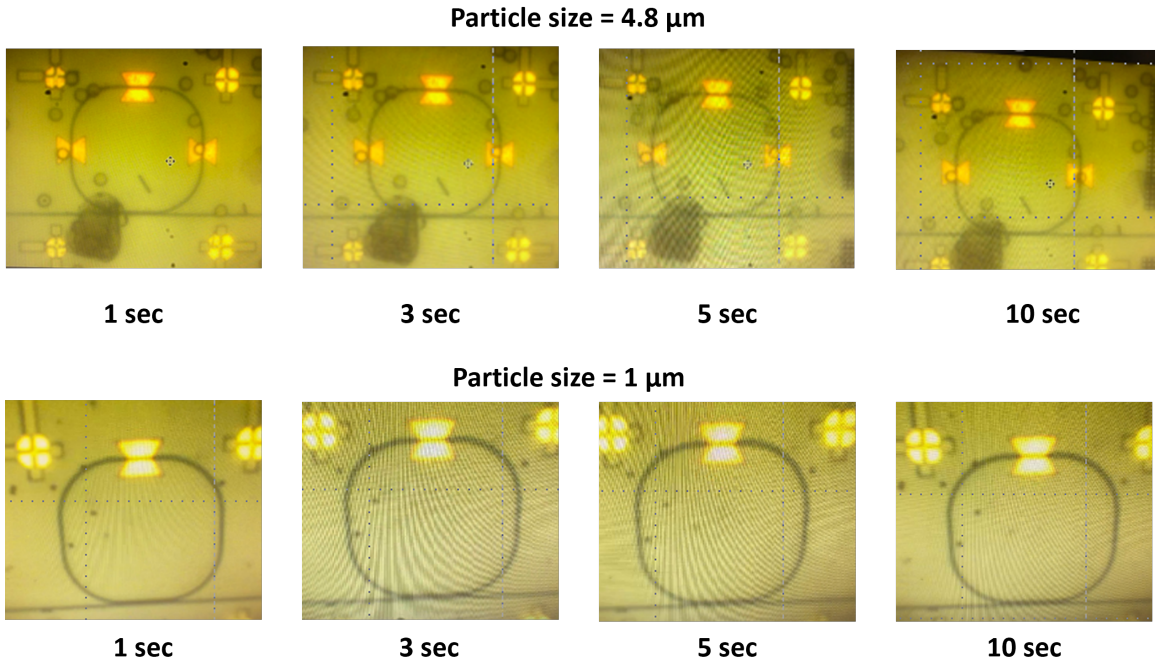

Figure 6.20: Images extracted from a recorded video (using a phone) displayed on a monitor, at different time frames, for the characterization of two devices with dielectric polystyrene particles of 4.8 μm and 1 μm.

The experiment described above faced several challenges and potential reasons for its lack of success, including the following:

1. Visible and Infrared Information monitoring : When particles interact with an evanescent field, the strong light observed through the IR camera can obscure the particle motion and behavior. To address this issue, a CMOS (visible) camera should be added to the setup to clearly observe particle motion, while the IR camera can continue to monitor IR-specific information, such as light coupling levels on the device. Therefore, both cameras must be installed on the setup to enable simultaneous use. Currently on the experiment we performed, we were changing the camera in the middle of the experiment to observe the particle and observing the power spectra at spectrum analyzer we made sure that we are coupling to the ring.

2. Low Power in the ring : The HPWG ring resonator used here had a very low quality factor around 1000 due to high losses introduces by the plasmonic metal. This led to very low power in the ring to observe any optical trapping.

3. Thermophoretic forces : Thermophoresis is a phenomenon arising from the Brownian motion of particles in fluids subjected to a constant temperature gradient. In such a gradient, particle dispersion increases in the hotter region. The differential dispersion results in a collective motion of particles from the hotter region towards the colder region, an effect commonly referred to as thermophoresis. The speed at which particles

Thèse accessible à l'adresse : https://theses.insa-lyon.fr/publication/2024ISAL0120/these.pdf © [C.B. Chander Bhan], [2024], INSA Lyon, tous droits réservés

move due to this effect is termed the thermophoretic velocity [158]. In the case of hybrid plasmonic waveguides (HPWGs), gold nanoantennas act as a heat source, causing nanoparticles to resist optical trapping and move away from the sensing area.

4. coupling efficiency : Edge couplers, such as adiabatic tapers, generally exhibit low coupling efficiency. In this particular experiment, linear adiabatic tapers were used. For our current fabrication, we designed inverted tapers as edge couplers on the chip to improve coupling efficiency. However, these devices have not yet been characterized due to the unavailability of Silane (SiH_4) needed for SiO_2 deposition on the inverted tapers.

In the previous subsections, we discussed the preliminary results obtained and the initial experiments conducted, providing a brief summary of the challenges faced. Currently, we are encountering difficulties in characterizing devices due to the limitations of the available tools. The current broadband laser source with an optical amplifier provides high power at 1340 nm, which is filtered using a digital tunable filter that operates only up to 1330 nm. Thus, the 1300 nm range cannot be utilized with the current setup. Additionally, at 1500 nm, the losses are too high to observe any resonances, making characterization with a tunable laser source unfeasible in this range. As a result, we are refining our experimental protocols and exploring potential collaborations with other labs to continue the characterization of the remaining devices. Further findings will be included in the thesis at a later stage.

6.4 Conclusion

In this chapter, we discussed the optical characterization results of the devices fabricated during this thesis, as well as those from previous fabrications on the ST DAPHNE platform. We began by detailing the experimental optical bench setup with edge coupling, along with the available tools used for device characterization. In the experimental results section, we presented measurements of linear propagation and bending losses of the Si_xN_y strip waveguides fabricated at 3IT, both in SiO_2 and water cladding. These loss characterizations were then compared with those of Si_xN_y waveguides reported in previous studies. We observed a good agreement between the modeled and experimental results for radiation losses at different bending radii.

Subsequently, we introduced the preliminary results of the MRRs characterized using an incoherent broadband source. We found that the FWHM measured with the optical spectrum analyzer was very close to its resolution of 0.03 nm. This suggests that we may have underestimated the MRRs' quality factors, prompting us to refine our experimental protocols and explore potential collaborations with other laboratories to continue the characterization of the remaining devices.

Lastly, we addressed the optical trapping experiments, which could not be completed due to the limitations of the available tools. However, we have outlined the protocols and challenges encountered at the beginning of the thesis while conducting optical trapping experiments with previously fabricated devices. These challenges provided valuable insights during the design of our current devices and will be instrumental in refining our methodologies for ongoing optical trapping characterizations.

Thèse accessible à l'adresse : https://theses.insa-lyon.fr/publication/2024ISAL0120/these.pdf © [C.B. Chander Bhan], [2024], INSA Lyon, tous droits réservés

Chapter 7

Conclusion and Summary

The number of mortalities is increasing each year due to air pollution, which causes severe health issues such as acute respiratory infections, chronic obstructive pulmonary disease, stroke, heart disease, and lung cancer. This is largely due to inhalation of air containing high levels of pollutants, particularly polyaromatic hydrocarbons (PAHs). Particulate matter such as fluoranthene and pyrene, with sizes around 0.1 µm, are identified as significant PM2.5 pollutants (PM2.5 are the fine inhalable particles, with diameters that are generally 2.5 μm and smaller). These particles are commonly found in vehicle emissions, industrial discharges, cigarette smoke, and the combustion of organic matter (e.g., wildfires). Hence, it is crucial to accurately measure such particles in the air.

Through a state-of-the-art review, we identified that current technological solutions, like optical particle counters and MEMS devices using light scattering principles, are unreliable with approximately 50% sensitivity for fine particles ($<$ 0.1 μm) in the air. Therefore, it is pertinent to explore alternative approaches, such as photonic integrated platforms, for studying such dielectric particles. Optical trapping via light offers a precise solution for size-specific particle trapping, enabling more accurate measurements.

In this thesis, we proposed using photonic integrated circuit devices on a silicon nitride (Si_xN_y) platform as an air quality index (AQI) sensor. The high sensitivity of microring resonators (MRRs) can detect even very small concentration particles, while the optical forces enable trapping of specific particle sizes. The Si_xN_y platform demonstrated strong potential in various sensing applications, including chemical, biomedical, physical, and environmental sensing.

As part of this thesis, we examined various waveguide structures, such as hybrid plasmonic waveguides, higher-order modes, slot waveguides, and dielectric strip waveguides, through modeling. Our initial modeling studies focused on ensuring compatibility with STMicroelectronics Datacom Advanced Photonic Nanoscale Environment (DAPHNE), an industrial platforms. Resonant devices like ring resonators offer significant field enhancement and spatial confinement, making them advantageous for nanoparticle trapping. Given their compatibility with industrial platforms, we studied different waveguides with consideration of design and fabrication constraints for MRRs on an industrial scale.

We conducted a study of optical forces in cavities using well-known methods, such as Maxwell stress tensor (MST) and discrete dipole approximation (DDA), to define device

Thèse accessible à l'adresse : https://theses.insa-lyon.fr/publication/2024ISAL0120/these.pdf © [C.B. Chander Bhan], [2024], INSA Lyon, tous droits réservés

parameters for the design process. This thesis focused on four major components:

1. **Dielectric Strip Waveguide:** Using MST and DDA methods, we studied the simplest dielectric strip waveguide, easily fabricated on any industrial platform, to trap particles around 100 nm. We determined the minimum force and power required for trapping and optimized the strip waveguide with a cross-section width of 570 nm and a thickness of 300 nm.

2. **Higher-Order Mode (HOM) Ring Resonators:** HOMs have multiple intensity maxima and minima, allowing for the trapping of multiple particles and offering better tolerance to fabrication errors due to their wider core. These were optimized for design and fabrication in Chapters 3, 4, and 5.

3. **Inverted Taper Coupling:** Trapping a dielectric particle requires approximately 25 mW of power in the waveguide. To enhance coupling efficiency with the current characterization setups available at INL laboratories, we designed and optimized a simple linear inverted taper, achieving a coupling efficiency of 75%, as demonstrated in our FDTD and FDE Lumerical models in Chapter 3.

4. **Hybrid Plasmonic Ring Resonators:** Previous literature and research have demonstrated the high sensitivity of hybrid plasmonic ring resonators. Our modeling showed that these designs can generate substantial optical forces, such as 50 pN for 100 nm dielectric nanoparticles, which is 10-15 times higher than that achieved by strip waveguides. However, these come with high losses. We optimized the design to reduce losses by a factor of six, achieving roughly 2-3 times better performance compared to silicon nitride (Si_xN_y) slot and strip waveguides in terms of optical trapping, while maintaining high sensitivity. Due to fabrication complexity and time constraints, this design was not fabricated in this thesis. Instead, we approached a simpler dielectric strip waveguide prototype to demonstrate optical trapping of dielectric particles around 100 nm.

In Chapter 5, we used the inverted taper in our design, optimized for a 300 nm thickness of silicon nitride. We fabricated the devices using the 3IT platform, which provided more flexibility and an integrated platform with electron-beam lithography (E-beam lithography). This helped reduce losses compared to UV lithography methods. The 3IT integrated platform also enabled the fabrication of multiple chips simultaneously, allowing us to account for all fabrication possibilities and incorporate redundancy and design variations. We then characterized the devices fabricated during this thesis, beginning with the explanation of the experimental optical bench used and the available tools that assisted in our characterization. Subsequently, we discussed the experimental results, including the linear propagation and bending loss measurements for the Si_xN_y strip waveguide under SiO_2 and water cladding, along with a comparison to standard silicon nitride devices fabricated in previous theses using the ST DAPHNE and INL platforms.

During characterization, we encountered challenges with polydimethylsiloxane (PDMS) fluidic reservoirs, which degrade in water, adding extra losses and complicating cleaning after each measurement. Using research conducted by other researchers in the laboratory, we employed a repositionable fluidic reservoir made of TPU film and a 3D-printed reservoir, which allowed easy repositioning and cleaning after each measurement. The 3D-printed

Thèse accessible à l'adresse : https://theses.insa-lyon.fr/publication/2024ISAL0120/these.pdf © [C.B. Chander Bhan], [2024], INSA Lyon, tous droits réservés

reservoir provided a stable alignment on the sample. Using this repositionable fluidic reservoir, we demonstrated two loss measurements on different photonic chips, showing the repeatability and ease of the reservoir compared to the PDMS reservoir.

Toward the end of the characterization chapter, we presented preliminary results for the MRRs fabricated in both SiO_2 and water cladding. We achieved Q-factors close to 30,000 in SiO_2 cladding and around 20,000 in water cladding. Unfortunately, the Full Width at Half Maximum (FWHM) of both measurements was very close to the optical spectrum analyzer's resolution bandwidth (RBW) of 0.03 nm. As a result, we are still in the process of refining our characterization protocols and seeking potential collaborations that could allow us to continue the experiments on other fabricated devices. Finally, we discussed the current challenges faced in our optical trapping experiments but also provided insights gained from previous optical trapping experiments conducted at the beginning of the thesis with previously fabricated devices.

From a modeling perspective, designs such as HOM and HPWG show significant potential for optical trapping and could be promising for future sensing and AQI applications. Given that optical forces alone are not sufficient to trap large numbers of particles, future work could explore combining dielectrophoresis and optical force physics. Such hybrid designs could capture numerous particles while maintaining high sensitivity, thereby competing effectively with the current state-of-the-art commercialized devices.

This thesis proposes a simplified dielectric microring resonator (MRR) design capable of trapping dielectric particles in water (principle will be same for air) at a size of 0.1 µm. The design can be readily fabricated on any CMOS-integrated platform, in conjunction with laser sources and photodetectors. Additionally, the development of repositionable fluidic channels, which can be easily integrated into CMOS lab-on-chip systems, enables reusable measurements, thereby improving practicality and cost-efficiency. Based on the ongoing characterization, we are confident in demonstrating the proof of concept for optical trapping using the proposed design. Transferring this design to the STMicroelectronics platform, combined with the inverted taper design and low-loss silicon nitride waveguides developed at STMicroelectronics, offers a promising solution to enhance sensor performance and sensitivity.

Thèse accessible à l'adresse : https://theses.insa-lyon.fr/publication/2024ISAL0120/these.pdf © [C.B. Chander Bhan], [2024], INSA Lyon, tous droits réservés

Thèse accessible à l'adresse : https://theses.insa-lyon.fr/publication/2024ISAL0120/these.pdf © [C.B. Chander Bhan], [2024], INSA Lyon, tous droits réservés

Chapter 8

Annexes

Annexe A : Brownian Motion:

The motion was first described by Einstein analytically in 1905 after Robert Brown observed it in a microscope in 1837. This Brownian motion is the result of all the collisions between molecules of fluid and particles. Molecules in fluids have velocities, which depend on their temperature, of up to 1,000 m/s.

Random molecular collisions with particles occur at molecular timescales, which are shorter than the time scales of the particles and the order of femtoseconds (10^{-15} s). The effects of molecular collisions on nanoparticles are very small due to the small mass of molecules compared to nanoparticles. However, because the number of impacts per unit time is very large, the aggregate effect of molecular impacts is noticeable on the movement of particles with sizes less than $10\mu m$ and is considered negligible for larger particles[158, 159].

Brownian movement in a continuum framework, without the stipulation of the molecular motion, and draw conclusions in a mechanistic, Newtonian framework, is that the particle movement is the consequence of a random force, which continuously acts on the individual particles.

Let us consider the motion of a small particle under the influence of the random molecular.

$$\overrightarrow{F_{Br}} = \overrightarrow{R}\sqrt{\frac{12\pi K_B T \alpha \mu_f}{\Delta t}} \tag{8.1}$$

where,
K_B = 1.380648 $\times$ $10^{-23} m^2 K g s^{-2} K^{-1}$ Boltzmann constant
α = $0.05 \times 10^{-6} m$ size of the particle
μ_f = $0.01\ pascals\ second$ (Dynamic Viscosity)

where $\overrightarrow{R}$ is a random vector with Gaussian random number components of zero mean and unit variance and Δ t is the time interval of action of the random force. It must be noted that when this random force is integrated over a long-time t (t $>>$ Δt) the results of the particle dispersion are independent of the choice of the interval Dt and yield the Stokes–Einstein diffusion coefficient

Thèse accessible à l'adresse : https://theses.insa-lyon.fr/publication/2024ISAL0120/these.pdf © [C.B. Chander Bhan], [2024], INSA Lyon, tous droits réservés

Dispersion coefficient in isothermal fluid

$$D \overset{def}{=} \frac{d}{2dt} < \overrightarrow{\chi} \cdot \overrightarrow{\chi} >= K_B T 6\pi\alpha\mu_f \tag{8.2}$$

For each particle we have the following equation of motion:

$$\frac{m_p d^2\vec{x}}{dt^2} = \overrightarrow{R}\sqrt{\frac{12\pi K_B \alpha T \mu_f}{\delta t}} - 6\pi f_{Kn}\alpha\mu_f \overrightarrow{v} \tag{8.3}$$

The integration of 8.3 are independent of the choice of the time interval Δ t provided that t $>>$ Δ t.

A Brownian force is a time-dependent, random force that causes particles to move transiently. The form of the Brownian force, as given in equation 8.3, has been derived and has been demonstrated in unsteady particulate flow. Applied to particle dispersion, aggregation kinetics, and Stokes-Einstein diffusion, equation 8.3 yields accurate results [159, 160, 161].

$$f_{Kn} = \frac{1}{1 + AK_n} \tag{8.4}$$

$$A = 1.165 + 0.483\, e^{-\frac{0.997}{K_n}} \tag{8.5}$$

Here coefficient f_{Kn} represents the drag reduction on the particle because of the velocity slip at the interface [78, 77]. In liquids the Knudsen number is very low even for nanoparticles (e.g., in water $K_n = 0.05$ for α = 5nm) the coefficient f_{Kn} is approximately equal to 1 for most of the nanoparticles of interest.

The choice of Δ t given by equation (5) generates stable numerical integration's that are reasonably fast and accurate

$$\Delta t = \frac{1}{10}\tau_p = \frac{1}{10}\frac{2\alpha^2\rho_p}{9\mu_f} \tag{8.6}$$

During the computation time step Δ t, the Brownian force is assumed to be constant, so equation 8.3 can be integrated directly to determine the particle's velocity and position:

$$\overrightarrow{v}(t + \Delta t) = \overrightarrow{v}(t) exp(-\Delta t \frac{f_{Kn}}{\tau_p} + \frac{\overrightarrow{F_{Br}}}{2m_p}(\Delta t)) \tag{8.7}$$

$$\overrightarrow{x}(t + \Delta t) = \overrightarrow{x}(t) + \overrightarrow{v}(t)[-\Delta t - \frac{\tau_p}{f_{Kn}} exp(-\frac{\Delta t f_{Kn}}{\tau_p})] + \frac{\overrightarrow{F_{Br}}}{2m_p}(\Delta t)^2 \tag{8.8}$$

It is significant to note that the immobile fluid layer on the liquid–particle interface plays a role in calculating the particle's inertial mass: in addition to the particle's mass, the particle's inertial mass is also affected by the mass of the immobile liquid layer that surrounds it. In

Thèse accessible à l'adresse : https://theses.insa-lyon.fr/publication/2024ISAL0120/these.pdf © [C.B. Chander Bhan], [2024], INSA Lyon, tous droits réservés

the case of an immobile liquid layer with a width of δa, then the inertial mass of the particle is [162]:

An approximate value of interfacial fluid layer was determined by Gerardi et al. [162] through Nuclear magnetic resonance (NMR) measurements in aqueous solution's δa = 1.4nm.

simulations performed in the study are by assuming a dielectric sphere in a fluid. However, in the case of irregular particles, the measure of this equivalent radius for the motion of particles is the area equivalent radius,

$$\alpha_{eq} = (\frac{A}{\pi})^{0.5} \tag{8.9}$$

where A is the total surface area of the irregular particles.

Thèse accessible à l'adresse : https://theses.insa-lyon.fr/publication/2024ISAL0120/these.pdf © [C.B. Chander Bhan], [2024], INSA Lyon, tous droits réservés

Annexe B : Marcatilli's method for Directional coupler

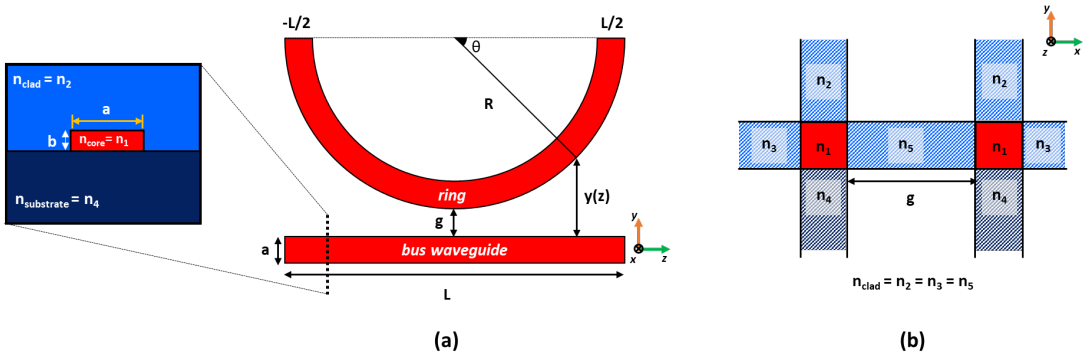

Figure 8.1: Schematic diagram of the coupling region of MRR (a) top view (b) cross-section view at z=0 (redrawn from Pauline girault article [141])

In between Ring and bus waveguide the distance separation in y direction is varying along the z direction as shown in Figure 8.1 and can be expressed as :

$$y(z) = g + R(1 - cos(\theta)) \tag{8.10}$$

where g is the coupling gap between the straight bus waveguide and ring, R is the raidus of the ring and $\theta = arcsin(\frac{z}{R})$ varying between $-\pi/2$ to $\pi/2$.

The coupling coefficient (C_{TE}) for z abscissa given by Marcatili method [84] and Kuznetsov [139] for the mode TE is :

$$C_{TE} = \frac{\frac{2k_x^2\xi_5 e^{-\frac{y(z)}{\xi_5}}}{k_z a(1+k_x^2+\xi_5^2)} + \frac{2k_x^2\xi_5 e^{-\frac{g}{\xi_5}}}{k_z a(1+k_x^2+\xi_5^2)} L}{1 + \frac{\xi_3}{a} + \frac{\xi_5}{a}} \tag{8.11}$$

where, a is the core width, k_Z is the propagation constant along the z direction depending upon transverse propagation constant k_x and k_y

$$k_z = \sqrt{k_1^2 - k_x^2 - k_y^2} \tag{8.12}$$

$$k_x = \frac{\pi}{a}(1 + \frac{2n_3^2 A_3 + 2n_5^2 A_5}{\pi n_1^2 a})^{-1} \tag{8.13}$$

$$k_y = \frac{\pi}{a}(1 + \frac{A_3 + A_5}{\pi b})^{-1} \tag{8.14}$$

$$k_1 = \frac{2\pi}{\lambda} n_1 \tag{8.15}$$

Thèse accessible à l'adresse : https://theses.insa-lyon.fr/publication/2024ISAL0120/these.pdf © [C.B. Chander Bhan], [2024], INSA Lyon, tous droits réservés

In Equation 8.11, ξ_3 and ξ_5 represents penetration depth along x and y respective to polarization.

$$\xi_{(3,5)} = \frac{A_{(3,5)}}{\pi}(1 - (\frac{A_{(3,5)}k_x}{\pi})^2)^{1/2} \tag{8.16}$$

Where, constants A is :

$$A_i = \frac{\pi}{\sqrt{k_1^2 - k_i^2}} \tag{8.17}$$

A significant portion of this work was accomplished with the assistance of Pauline Girault, whose previous contributions, as mentioned in her article [141, 142], were instrumental in solving the Marcatilli's equation and developing the corresponding Python script.

Thèse accessible à l'adresse : https://theses.insa-lyon.fr/publication/2024ISAL0120/these.pdf © [C.B. Chander Bhan], [2024], INSA Lyon, tous droits réservés

Annexe C : Dispersion of PECVD Silicon nitride, 3IT

A 350 nm layer of PECVD Si_xN_y was deposited using standard recipes described in Chapter 5, followed by a 2 μm SiO_2 layer on a 4-inch silicon wafer with a thickness of 275–300 μm. The ellipsometry measurements, taken with the Alpha-SE during the deposition, confirmed the deposited thicknesses of Si_xN_y and silicon oxide, which were 325 nm and 2007 nm, respectively.

To estimate the refractive index (RI) of Si_xN_y, ellipsometry measurements were performed using the HORIBA (UVISEL PLUS) system at 3IT, over a wavelength range of 400–1700 nm with incident angle of 70 °. In order to achieve an accurate fit between the raw ellipsometry data and the dispersion models, two approaches were used: either cross-polarization measurements or adjustments of Psi and Delta by subtracting 360 ° from Delta and 90 ° from Psi, as shown in the Figure 8.2. These modifications provide a closer match to the material's dispersion behavior and help eliminate errors that occurred during the measurements.

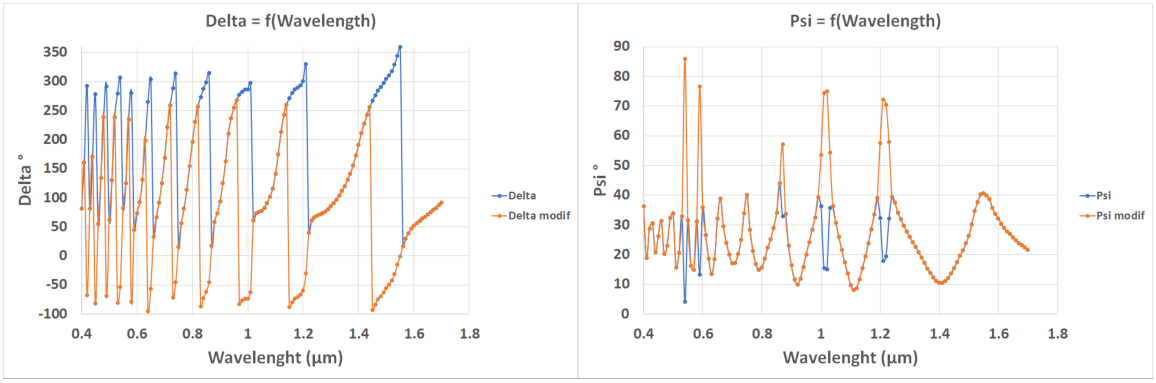

Figure 8.2: Comparison between experimental and Modified Psi (right) and delta (left): (a) modified delta (delta-360 °) as function of wavelength, (b) modified delta (delta-90 °) as function of wavelength.

Using the modified Psi and Delta values described above, regression was performed using a custom MATLAB script. The refractive indices of SiO_2 and Si were fixed according to the Sellmeier model with three harmonics and the Forouhi-Bloomer model with four harmonics respectively. The Sellmeier model was used with two harmonics to find the RI of the Si_xN_y. After applying the Levenberg-Marquardt algorithm for regression, the resulting parameters were of the same order as the initial values considered : Si_xN_y (0.324612176 μm), SiO_2 (2.017162171 μm), incident angle (69.999503079 °). The comparison between experimental data and the model's results is shown in the below Figure 8.3.

The dispersion model of the Si_xN_y and SiO_2 including all the coefficient is illustrated below in the Figure 8.4 that were found with the above algorithm.

For dispersion model of Si, the Forouhi-Bloomer model with all the coefficient is provided below in the Figure 8.5:

Thèse accessible à l'adresse : https://theses.insa-lyon.fr/publication/2024ISAL0120/these.pdf © [C.B. Chander Bhan], [2024], INSA Lyon, tous droits réservés

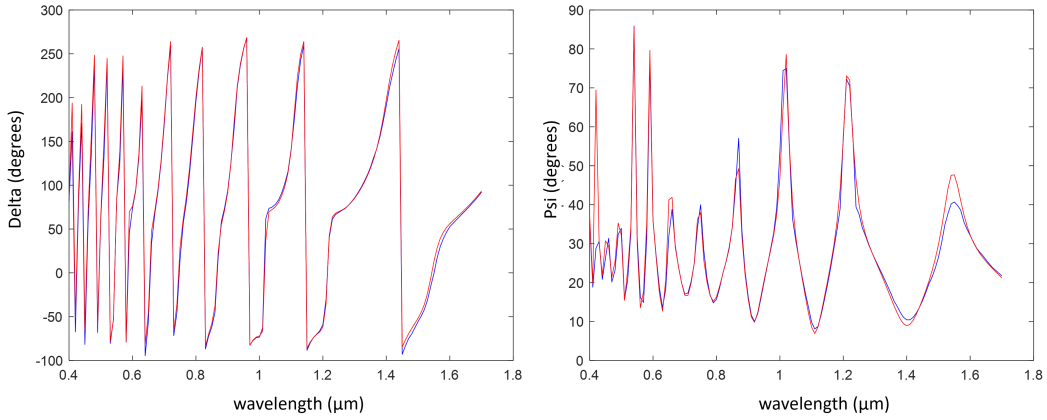

Figure 8.3: Comparison between experimental and model's results for Psi (right) and delta (left).

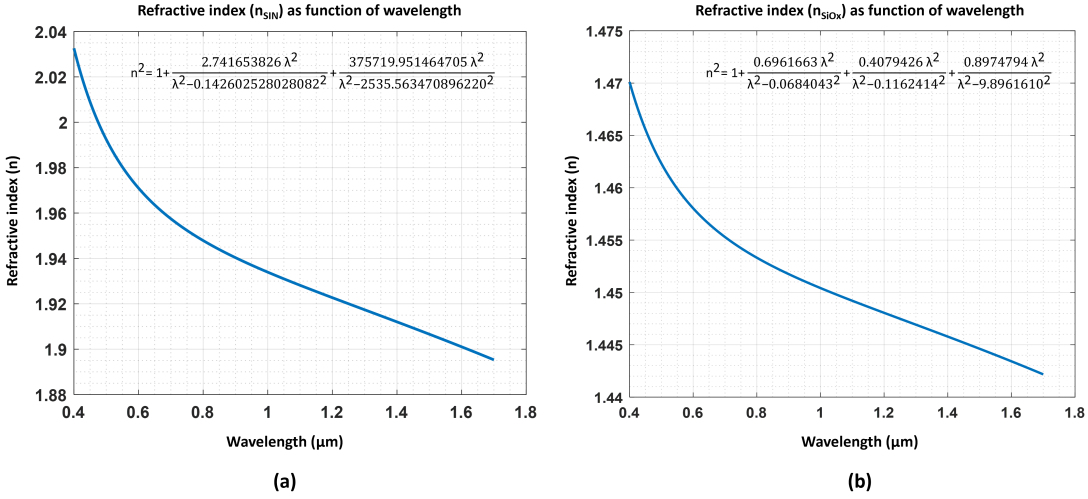

Figure 8.4: Sellmeier dispersion model of Si_xN_y (left) and SiO_2 (right) as function of wavelength.

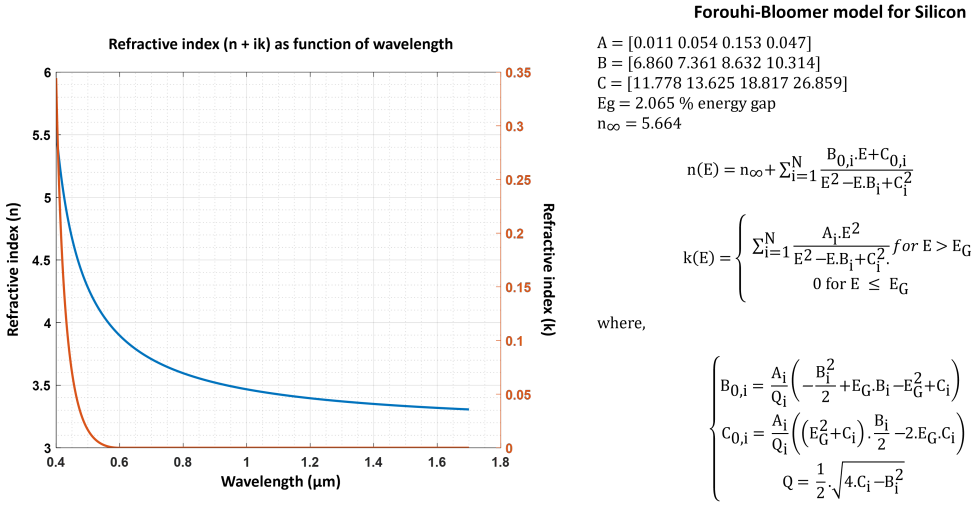

Figure 8.5: Forouhi-Bloomer model of Si as function of wavelength.

Thèse accessible à l'adresse : https://theses.insa-lyon.fr/publication/2024ISAL0120/these.pdf © [C.B. Chander Bhan], [2024], INSA Lyon, tous droits réservés

Thèse accessible à l'adresse : https://theses.insa-lyon.fr/publication/2024ISAL0120/these.pdf © [C.B. Chander Bhan], [2024], INSA Lyon, tous droits réservés

Chapter 9

RÉSUMÉ LONG EN FRANCAIS

Introduction

À l'échelle mondiale, la pollution de l'air tue environ sept millions de personnes par an. Les données de l'OMS indiquent que neuf personnes sur dix respirent un air contenant un niveau élevé de polluants qui dépasse les recommandations de l'OMS [1]. La pollution de l'air, qu'elle provienne de sources ambiantes (extérieures) ou domestiques, est responsable de 7 millions de décès prématurés chaque année et représente une menace majeure pour la santé et le climat [1, 2, 3]. La cause de cette mortalité est l'exposition aux particules en suspension (PM) présentes dans l'air à cause de la pollution. Les infections respiratoires aiguës, les maladies pulmonaires obstructives chroniques, les accidents vasculaires cérébraux, les maladies cardiaques et le cancer du poumon peuvent tous être liés de manière causale à la pollution de l'air. Les PM se composent de produits chimiques tels que les sulfates, les nitrates, le carbone ou la poussière minérale, ainsi que de composés organiques comme les hydrocarbures aromatiques polycycliques (HAP). Les diverses sources de PM comprennent les émissions des véhicules, les émissions industrielles, la fumée de cigarette et la combustion de matières organiques (comme les feux de forêt).

Plus de 95% des émissions issues de la combustion du diesel, de l'essence et du gaz naturel, de la pollution liée à la combustion de déchets à l'air libre, de la combustion de biomasse et de la combustion du charbon dans les cuisinières et chaudières relèvent de la catégorie des PM2.5[1]. La figure 9.1 illustre la comparaison de taille entre les particules fines et un cheveu humain. Par rapport à un cheveu humain, les particules PM2.5 sont 30 fois plus petites.“

La Table 9.1 présente une comparaison des techniques de détection des PM les plus courantes rapportées dans la littérature (La description complète est fournie en version anglaise dans le chapitre 1 avec les principes détaillés de chaque technologie). On peut observer que les méthodes basées sur les principes gravimétriques et de diffusion de la lumière présentent une faible sensibilité aux particules de taille inférieure à 100 nm. La littérature actuelle met en avant des solutions émergentes qui utilisent la manipulation de fluides sur

[1] Les PM2.5 sont des particules fines inhalables, dont le diamètre est généralement de 2,5 micromètres ou moins

Thèse accessible à l'adresse : https://theses.insa-lyon.fr/publication/2024ISAL0120/these.pdf © [C.B. Chander Bhan], [2024], INSA Lyon, tous droits réservés

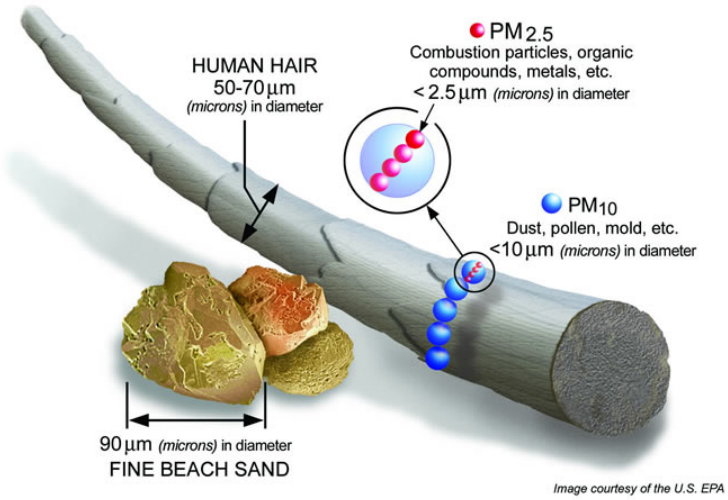

Figure 9.1: Comparaison de taille entre un cheveu humain et les particules en suspension [2].

puce par la lumière, offrant de nouvelles approches pour améliorer la sensibilité aux particules de taille inférieure à 100 nm. En tirant parti de la plateforme CMOS, les mesures peuvent être effectuées plus rapidement avec des puces photoniques intégrées, car cette plateforme permet une intégration complète des lasers, photodétecteurs et canaux microfluidiques sur une seule puce. Par conséquent, dans cette thèse, nous nous concentrons sur le développement d'un prototype capable de piéger des particules diélectriques de 100 nm à l'aide d'un dispositif photonique intégré compatible avec les plateformes industrielles existantes.

Manipulation de fluides sur puce par la lumière Une pince optique est un instrument utilisé pour manipuler et mesurer de petites particules. Deux des principaux avantages des pinces optiques sont leur précision et leur résolution, qui permettent des mesures détaillées de la taille, de la forme et de la position des particules. De plus, les pinces optiques peuvent manipuler et trier les particules en fonction de leurs propriétés physiques, telles que la charge ou l'indice de réfraction [27]. Cependant, les pinces optiques présentent plusieurs inconvénients, notamment la nécessité d'un laser à haute puissance, les limitations imposées par la diffraction et la diffusion thermique des nanoparticules. Ces facteurs les rendent coûteuses et difficiles à utiliser.

La manipulation optique en champ proche offre des avantages par rapport aux pinces optiques classiques. Par exemple, l'utilisation d'une cavité, comme un résonateur en anneau, renforce le champ circulant, qui peut être considérablement plus fort que le champ incident [28]. Récemment, les microcavités optiques ont gagné en popularité en tant que ≪ capteurs sur puce ≫ en raison de leur capacité à détecter des nanoparticules et des molécules sans nécessiter de marqueurs [29, 30, 31]. Plusieurs chercheurs ont démontré la manipulation de nanoparticules et de microparticules en utilisant le piégeage optique en champ proche intégré, basé sur les champs évanescents des dispositifs photoniques et plasmoniques sur des plateformes lab-on-a-chip, comme illustré dans la figure ci-dessous, qui sont des systèmes peu coûteux, portables et très sensibles [32, 33, 34, 35, 36].

Thèse accessible à l'adresse : https://theses.insa-lyon.fr/publication/2024ISAL0120/these.pdf © [C.B. Chander Bhan], [2024], INSA Lyon, tous droits réservés

Types de capteur	Gammes de taille	Avantage	Inconvénient
Gravimétrique	$>$ 150 nm	bon marché, simple à déployer	temps d'analyse long
M & NEMS	$>$ 5 nm	mesure en temps réel, compatibilité CMOS	sensible aux températures
APS	0.5 - 20 μm	haute précision et résolution	cher et encombrant
SMPS	2.5 nm - 1 μm	haute précision et résolution	cher
Principe de diffusion de la lumière	300 nm - 10 μm	bon marché, haute portabilité	faible sensibilité aux particules sub-microniques ($<$ 0.1 μm)
Compteur de particules optique	300 nm - 10 μm	bon marché	faible sensibilité aux particules sub-microniques ($<$ 0.1 μm)
Holographie	500 nm - 10 μm	haute portabilité	l'analyse est coûteuse en calcul
Diélectrophorèse	$<$ 10 nm	forces de piégeage élevées, compatibilité CMOS	nécessite des champs électriques alternatifs à haute fréquence
Manipulation de fluides sur puce par la lumière	$<$ 5 nm	compatibilité CMOS	les forces optiques diminuent avec la taille des particules

Table 9.1: Comparaison des techniques de détection des PM les plus courantes (adapté de [23])

Plusieurs chercheurs ont démontré le piégeage optique de nanoparticules (à l'échelle du μm) et le commutateur optofluidique en utilisant des structures de guides d'ondes et de résonateurs en anneau [163, 164, 106]. Cependant, des défis surgissent lorsqu'il s'agit de particules dans le régime de Rayleigh, en particulier pour les particules de taille inférieure à 100 nm.

Piégeage des nanoparticules inférieures à 100 nm :

1. Le potentiel de piégeage diminue considérablement, car la force optique est proportionnelle au volume des particules (ou, plus précisément, à leur polarisabilité).

2. Le mouvement thermique réduit la force de traînée visqueuse, augmentant ainsi la probabilité que les particules s'échappent du piège.

Ainsi, il devient essentiel de maintenir une forte force de gradient optique pour obtenir un piégeage stable des nanoparticules. Les structures résonantes nanophotoniques ou plas-

Thèse accessible à l'adresse : https://theses.insa-lyon.fr/publication/2024ISAL0120/these.pdf © [C.B. Chander Bhan], [2024], INSA Lyon, tous droits réservés

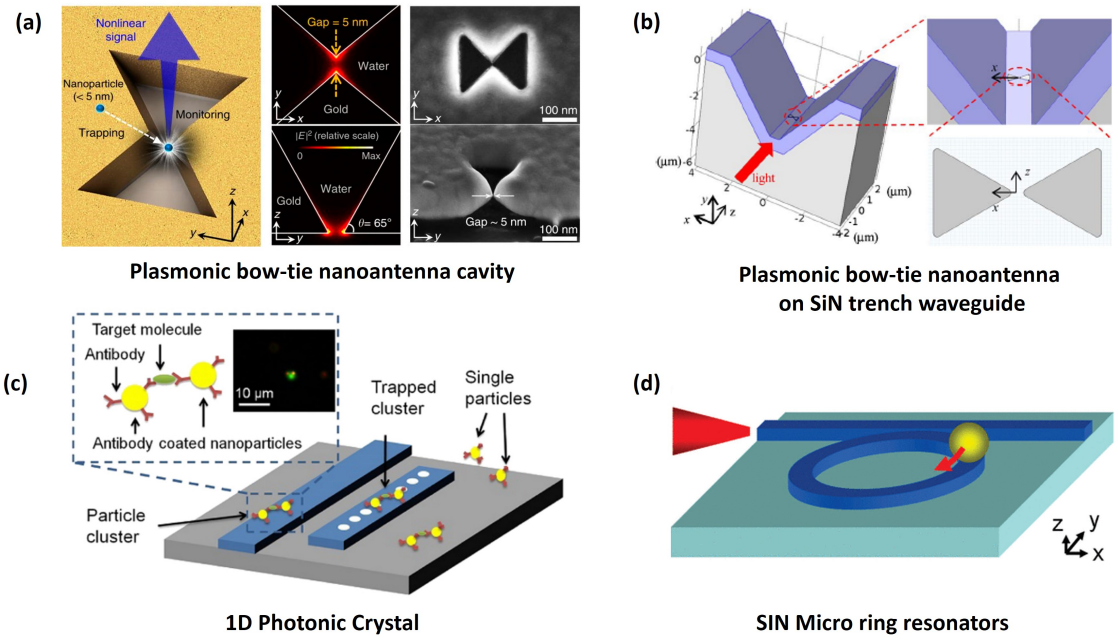

Figure 9.2: Manipulation optique par la lumière : (a) Piégeage d'une particule de 5 nm avec une nanoantenne plasmonique en forme de nœud papillon, (b) Conception d'une nanoantenne plasmonique en forme de nœud papillon sur un guide d'onde en tranchée SIN pour le piégeage optique de particules de Rayleigh, (c) Piégeage de particules de 320 nm avec un cristal photonique 1D, et (d) Piégeage de particules de 1 μm avec des résonateurs à anneaux en silicium (MRRs).

moniques sont préférées aux pinces optiques en espace libre pour le piégeage des nanoparticules en raison de leur confinement spatial serré, comme montré à la Figure 9.2.(a). Cependant, les structures purement plasmoniques présentent un inconvénient majeur : elles souffrent de pertes élevées et, en raison de leurs petites régions de confinement, sont généralement utilisées pour le piégeage de particules ponctuelles plutôt que pour le piégeage de grandes concentrations de particules, ce qui est l'objectif dans les études d'indices de qualité de l'air.

Dans cette perspective, les guides d'ondes hybrides plasmoniques (HPWG) offrent des avantages significatifs pour le piégeage optique. Les HPWG résultent du couplage entre les modes diélectriques et plasmoniques. Lorsque ces deux types de guides d'ondes sont placés suffisamment près, la structure combinée supporte à la fois des super-modes TE et TM, exploitant efficacement les forces des deux technologies [165, 166]. Pour augmenter la force de gradient optique, certains chercheurs ont utilisé des structures en forme de rainure en V en Si_xN_y combinées avec des nano-antennes plasmoniques comme montré à la Figure 1.10.(b) [7, 167, 168]. Cependant, la fabrication de ces types de guides d'ondes est difficile, et le couplage de la lumière dans de telles structures pose des difficultés expérimentales et pratiques.

Dans les guides d'ondes à fente, il est crucial que les deux guides d'ondes soient très proches (généralement à moins de 100 nm) pour garantir qu'une partie significative de l'énergie optique soit concentrée dans le revêtement (entre les guides d'ondes) et interagisse avec l'analyte ou l'échantillon, fournissant ainsi un dispositif MRR à haute sensibilité. Les guides d'ondes hybrides plasmoniques avec le concept de ≪mode lift≫ récemment

Thèse accessible à l'adresse : https://theses.insa-lyon.fr/publication/2024ISAL0120/these.pdf © [C.B. Chander Bhan], [2024], INSA Lyon, tous droits réservés

breveté qui consiste à augmenter l'indice effectif au dessus de la coupure. [125], dans le cadre de travaux antérieurs, présentent une approche prometteuse pour renforcer la force de piégeage optique avec des particules dans le régime de Rayleigh. Un guide d'ondes plasmonique hybride utilisant un concept de ≪mode lift≫, où un guide d'ondes diélectrique à cœur étroit conçu pour ne supporter que des modes de rayonnement est placé suffisamment près d'une interface métal/diélectrique, de sorte que le mode plasmonique puisse augmenter l'indice effectif du mode hybridé, résultant en un mode guidé global (super-mode). De plus, le fort gradient du champ évanescent renforce la force de piégeage pour piéger des particules de moins de 100 nm avec suffisamment d'énergie potentielle pour surmonter le mouvement brownien.

L'introduction de métal à proximité du guide d'ondes, où les modes du guide d'ondes sont proches de leur coupure, génère des super-modes qui renforcent l'énergie entre le guide d'ondes et le métal. En plus d'améliorer la sensibilité du revêtement, l'utilisation de métaux renforce le champ électrique, entraînant de fortes forces de gradient optique pour le piégeage. Pour plus de détails, voir la section suivante.

Pour assurer la compatibilité avec les processus de fabrication CMOS, le dispositif sera modélisé et conçu en tenant compte de ces exigences. La détection optique basée sur la technologie CMOS a suscité un intérêt significatif en raison de ses avantages inégalés, notamment une grande sensibilité, une compacité, un faible coût et une compatibilité avec les systèmes électroniques intégrés [169, 170]. Compte tenu de ces considérations, la question de recherche suivante émerge :

Question de recherche : *Comment concevoir et fabriquer un dispositif de piégeage optique intégré capable de piéger des particules diélectriques de moins de 100 nm, tout en assurant la compatibilité avec un environnement de fabrication industrielle de 300 mm ?*

Pour répondre à cette question générale, les sous-questions suivantes doivent être abordées :

1. *Quels paramètres de conception sont cruciaux pour obtenir un piégeage optique efficace en utilisant des méthodes de calcul ? (par exemple, force de gradient, couplage critique, énergie potentielle de piégeage K_BT)*

2. *Quel indicateur de performance peut être établi pour prendre en compte à la fois la sensibilité et l'efficacité du piégeage optique ?*

3. *Quelle technologie de guide d'ondes offre le plus d'avantages pour le piégeage optique : guides d'ondes monomodes, guides d'ondes multimodes, ou HPWG avec ou sans le concept de levée de mode ?*

4. *Comment obtenir une puissance suffisante dans le résonateur en anneau pour permettre la caractérisation des échantillons ? (par exemple, une investigation sur les rétrécissements inversés)*

Etat de l'art

Cette section présente un aperçu de la théorie des forces optiques, des avancées récentes dans les méthodes de piégeage optique pour la manipulation des nanoparticules diélectriques,

Thèse accessible à l'adresse : https://theses.insa-lyon.fr/publication/2024ISAL0120/these.pdf © [C.B. Chander Bhan], [2024], INSA Lyon, tous droits réservés

ainsi que des différentes approches de modélisation utilisées pour évaluer les forces optiques et résoudre les modes des guides d'ondes.

Force optique

Une particule subit une force optique lorsque la pression de radiation de la lumière interagit avec elle sous forme d'absorption, de réflexion ou de réfraction. Les forces optiques résultent de la conservation de la quantité de mouvement et comprennent trois forces principales : ***la force de gradient, les forces de diffusion, et les forces de spin-curl***. La force de spin-curl agit lorsque la polarisation du champ n'est pas homogène. Comparées aux forces de diffusion et de gradient, les forces de spin-curl sont généralement relativement faibles. Par conséquent, dans la plupart des cas, nous ne calculons pas la force de spin-curl à moins qu'un champ non homogène ne soit présent.

1. **Force de gradient (force de piégeage)** : lorsqu'une particule est positionnée dans un champ électrique non uniforme, la polarisation de la particule change en fonction de l'emplacement. Cela résulte en une force conservative. Les forces de gradient sont orientées dans la direction du gradient spatial de la lumière.

2. **Force de diffusion (pression de radiation)** : La quantité de mouvement du rayonnement électromagnétique est transférée aux particules par diffusion et absorption optiques. Il s'agit donc d'une force non conservative. Les forces de diffusion sont dirigées dans le sens de la propagation de la lumière.

Méthode Modélisation numérique

La modélisation des forces optiques exercées sur une particule, découlant de la conservation de la quantité de mouvement électromagnétique, est essentielle pour comprendre la physique sous-jacente et optimiser les paramètres de conception. Avec l'avancée rapide des pinces optiques, le cadre théorique pour le calcul des forces optiques a également évolué de manière significative. Au cours des dernières décennies, plusieurs méthodes ont été proposées dans la littérature pour déterminer les forces optiques sur des particules de tailles et de formes variées. Chaque méthode présente ses propres avantages et limitations. Ces méthodes sont classées en fonction de leur applicabilité à différents régimes de piégeage optique, qui dépendent du paramètre de taille ($k_m a$), comme détaillé ci-dessous.

Régime de piégeage optique

Les chercheurs ont proposé diverses techniques de piégeage optique pour piéger et manipuler des objets à l'échelle nanométrique, comme illustré à la Figure 9.3. Dans cette figure, les objets sont classés en différents régimes de piégeage optique pour simplifier la compréhension de leur taille par rapport à la longueur d'onde. Il existe trois principaux régimes de piégeage optique :

- Régime de Rayleigh ($k_m a < 1$)
- Régime de Lorenz-Mie ou régime intermédiaire ($k_m a \sim 1$)
- Régime optique géométrique ou optique des rayons ($k_m a >> 1$)

Thèse accessible à l'adresse : https://theses.insa-lyon.fr/publication/2024ISAL0120/these.pdf © [C.B. Chander Bhan], [2024], INSA Lyon, tous droits réservés

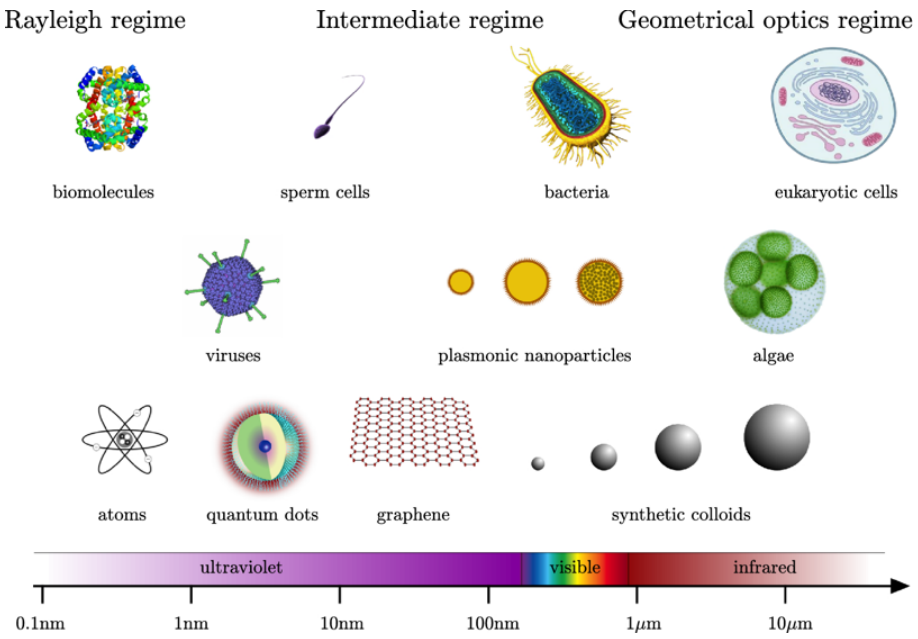

Figure 9.3: Régimes de piégeage optique : La barre d'échelle horizontale montre la taille moyenne des objets et la longueur d'onde correspondante (figure tirée des recherches d'Onofrio M. Maragò [48]).

En général, un calcul électromagnétique complet est nécessaire pour prédire avec précision le comportement du piégeage optique d'objets microscopiques de différentes tailles et formes. Ces calculs électromagnétiques complets peuvent être résolus en utilisant des méthodes telles que la méthode des différences finies dans le domaine temporel (FDTD) ou la méthode des éléments finis (FEM). Cependant, des modèles d'approximation peuvent fournir rapidement des informations physiques sur des problèmes complexes et simplifier leur résolution numérique [47], bien qu'ils présentent souvent des limitations. Il est crucial de comprendre les limites de validité de ces modèles d'approximation avant de les appliquer [49].

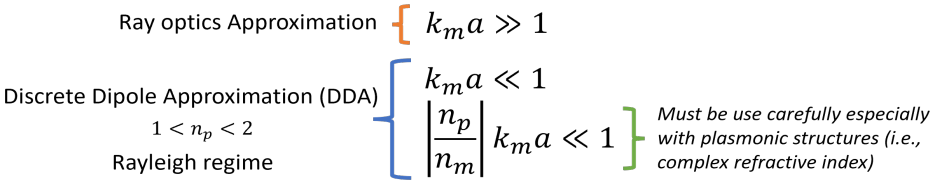

Figure 9.4: Condition d'application des modèles d'approximation.

Le *paramètre de taille* ($K_m a$) dans l'équation 9.1 est souvent utilisé pour déterminer la plage de validité d'une méthode d'approximation.

$$k_m a = \frac{2\pi n_m}{\lambda_0} a \tag{9.1}$$

où k_m est le vecteur d'onde ou la constante de propagation du front d'onde lumineuse dans le milieu, λ_0 est la longueur d'onde de fonctionnement, n_m et a sont respectivement l'indice

Thèse accessible à l'adresse : https://theses.insa-lyon.fr/publication/2024ISAL0120/these.pdf © [C.B. Chander Bhan], [2024], INSA Lyon, tous droits réservés

de réfraction (IR) et le rayon d'une nanoparticule sphérique [48]. La figure 9.4 illustre la condition pour choisir les modèles d'approximation appropriés.

Dans nos études, nous nous concentrons sur des particules sphériques diélectriques de taille 0.1μm, où les champs sont considérés comme homogènes à l'intérieur des particules. Comme illustré dans la Figure 9.4, pour étudier les forces optiques dans cette gamme de tailles de particules, la méthode DDA (valide pour $k_m a < 1$) fournit une approximation raisonnable pour calculer les forces optiques et est efficace d'un point de vue numérique.

Une comparaison complète des différentes méthodes de calcul pour déterminer les forces optiques est fournie dans le Tableau 9.2, mettant en évidence leurs avantages et inconvénients respectifs. Cependant, puisque l'Approximation Dipolaire Discrète (DDA) est limitée à une plage spécifique de tailles de particules, des calculs plus complets sont nécessaires pour étudier les effets de la variation des tailles de particules et des structures complexes, telles que les guides d'ondes plasmoniques hybrides (décrits dans le Chapitre 3). Par conséquent, la fonction intégrée de Tensor de Contrôle de Maxwell (MST) de COMSOL a été utilisée pour des calculs de force optique précis. La méthode DDA (décrits dans le Chapitre 2) sera utilisée pour approximer les forces optiques sur des particules de la gamme de 100 nm et pour des études impliquant plusieurs points de calcul de force optique. Cette approche double facilitera l'examen des puits d'énergie potentielle, nous permettant d'estimer la force minimale et la distance minimale requises pour piéger une particule en surmontant le mouvement brownien.

Méthode	Avantage	Inconvénient
Optique géométrique	Simple, rapide et adapté aux grandes particules ($k_m a >> 1$)	Pas précis pour les petites particules + ignore les phénomènes d'onde comme la diffraction et l'interférence
Théorie de Lorenz-Mie généralisée	Très précise pour les particules sphériques de toute taille [54]	Moins flexible pour les géométries non sphériques ou les matériaux complexes.
Approximation des dipôles discrets (régime de Rayleigh)	Bon pour les particules de forme arbitraire	Limité à la taille de Rayleigh et à l'erreur de discrétisation
Méthode T-matrice	Précise pour les particules axysymétriques (cylindriques) et efficace pour les problèmes de diffusion multiple	Moins précise pour les formes très irrégulières
Tenseur de contrainte de Maxwell	Précis pour les particules de toute taille ; peut modéliser des formes, des polarisations et des matériaux complexes.	Coûteux en calcul et nécessite des ressources significatives pour des géométries complexes et de grands domaines

Table 9.2: Méthodes de calcul les plus courantes pour le calcul des forces optiques.

Thèse accessible à l'adresse : https://theses.insa-lyon.fr/publication/2024ISAL0120/these.pdf © [C.B. Chander Bhan], [2024], INSA Lyon, tous droits réservés

Méthodes de Modélisation : Dans ce travail, la modélisation et la simulation de composants photoniques intégrés tels que les guides d'ondes rectangulaires, les études de piégeage optique, les analyses de sensibilité et les modes de flexion sont essentielles pour concevoir et optimiser les dispositifs photoniques. Avec l'expansion de la recherche dans les plateformes photoniques intégrées, de nombreuses méthodes analytiques, semi-analytiques et numériques ont été développées pour résoudre les problèmes de guides d'ondes optiques, y compris la Méthode de l'Indice Effectif [82, 83], la Méthode de Marcatili [84], le domaine temporel par différences finies (FDTD) [85], la Méthode des Éléments Finis (FEM) [86], la résolution aux valeurs propres par différences finies (FDE) et finite difference fully vectorial (FDFV) [87, 88], la méthode de Correspondance de Modes [89], et la Méthode des Moments (MoM) [90], entre autres. Ces différentes méthodes sont expliquées et comparées en détail dans la littérature [91, 92, 93].

Cette section fournit des tableaux concis et résumés des méthodes clés utilisées dans les simulations de nos diverses études. Le Tableau 9.3 présente un aperçu des approches FDTD, FEM, FDE, FDFV et de Marcatili, ainsi que leurs avantages, inconvénients et les cas spécifiques où elles ont été appliquées.

Méthode	**Avantage**	**Inconvénient**	**Utilisation dans cette étude**	**Outils**
FDTD	Haute précision, peut être utilisé pour des structures 1D, 2D et 3D	Intensif en calcul	Taper inversé, section de couplage dans les MRRs	Lumerical
FEM	Flexible, haute précision	Exigence élevée en ressources computationnelles	Étude de piégeage optique	COMSOL
FDE	solveur 2D, maillage rectangulaire	Temps de calcul moyen	Étude de la profondeur de puits potentiels pour l'évaluation des forces optiques minimales et de la puissance	Intégré avec l'API Lumerical et fonction python
Approche de Marcatili	Simple, facile à utiliser	Géométries rectangulaires uniquement	Coupleurs directionnels	Scripté en Python
FDFV	solveur 2D avec moyennage aux frontières, conditions aux limites transparentes	Fournit une estimation de beta	Modes optiques de bande, fente, HPWG, modes de flexion, forces optiques	Scripté en MATLAB [87]

Table 9.3: Tableau de comparaison des méthodes de modélisation utilisées dans cette thèse.

Thèse accessible à l'adresse : https://theses.insa-lyon.fr/publication/2024ISAL0120/these.pdf © [C.B. Chander Bhan], [2024], INSA Lyon, tous droits réservés

Structures de guides d'ondes optiques utilisées pour la manipulation optique

Selon la littérature, le Tableau 9.4 compare les différentes structures de guides d'ondes utilisées pour étudier les forces optiques sur des particules diélectriques en polystyrène. Les forces optiques ($\approx 100pN/\mu m/mW$) générées par des structures plasmoniques hybrides sont beaucoup plus élevées que celles des autres structures de guides d'ondes. Pour atteindre ces forces dans cette étude [98], ils ont minimisé l'écart entre le métal plasmonique et la structure diélectrique jusqu'à 20 nm. Cela a introduit des pertes élevées de 1 dB/μm dans le dispositif. De plus, l'écart étroit de 20 nm ne permet pas d'introduire une particule de taille 100 nm à l'intérieur de cet écart.

type de guide d'ondes	matériaux du guide d'ondes	matériau de la particule, taille	force optique / raideur
Réseau de paires de nervures [99]	silicium	Polystyrène, 200 nm	$\sim 55pN/W$
Guide d'ondes à nervure [72]	nitrure de silicium	verre, 500 nm	$\sim 153pN/W$
Guide d'ondes fente (g = 100 nm) [100]	silicium	ADN, Polystyrène, 100 nm	$\sim 25pN/W$
Bande plasmonique [33]	or	Polystyrène, 1 ou $2\mu m$	$\sim 1.7pN/\mu m$
Hybride plasmonique (écart = 20 nm) [98]	diélectrique et or	mesuré par rapport au bruit thermomécanique et normalisé aux forces optiques	$\sim 100pN/\mu m/mW$

Table 9.4: Forces optiques dans différentes structures de guides d'ondes.

Il est également important de noter que les forces optiques dans les structures de guides d'ondes sont influencées par la puissance optique qui leur est couplée. À mesure que la puissance augmente, les forces augmentent également. Dans les cavités résonantes, la longueur d'onde confinée accumule de l'intensité au cours de multiples allers-retours en raison de l'interférence constructive. Cela entraîne une puissance plus élevée dans la cavité que dans le guide d'onde qui couple la lumière. La puissance dans la cavité est directement liée au facteur de qualité Q de la cavité.

Amélioration par Cavité Résonante

Au cours de nos études, nous avons considéré le résonateur en anneau comme une cavité pour piéger des particules diélectriques. Il est important de noter que la théorie de perturbation de la cavité (comme l'effet SIBA [171]) s'applique à toutes les cavités de manière similaire, sauf que les formules peuvent varier en fonction de leur configuration structurelle.

Le Tableau 9.5 ci-dessous fournit une comparaison des forces optiques obtenues à partir de diverses cavités résonantes utilisées dans les dispositifs photoniques. D'un point de

Thèse accessible à l'adresse : https://theses.insa-lyon.fr/publication/2024ISAL0120/these.pdf © [C.B. Chander Bhan], [2024], INSA Lyon, tous droits réservés

la littérature, les cavités de cristal photoniques, en raison de leur facteur de qualité élevé (Q-factor) et de leur petit volume mode, présentent des forces optiques plus fortes par rapport aux résonateurs en anneau. Cependant, atteindre de tels facteurs Q élevés dans les cavités de cristal photoniques est un défi en pratique. Les complexités de fabrication, les plages de réglage limitées, la sensibilité aux imperfections et les difficultés à coupler la lumière dans et hors des cavités rendent les cavités de cristal photoniques moins pratiques pour notre application. De plus, améliorer le facteur de qualité des résonateurs en anneau (MRRs) en utilisant des guides d'onde à faibles pertes et en minimisant les pertes de flexion présente une solution plus réalisable.

Une autre solution couramment utilisée est celle des cavités plasmoniques, qui offrent un confinement étroit et des volumes modaux extrêmement faibles, ce qui les rend adaptées au piégeage de nanoparticules très petites. Cependant, leurs champs évanescents sont confinés à des régions hautement localisées, ce qui limite leur applicabilité dans des scénarios où une grande concentration de particules piégées est requise, comme dans cette thèse. D'un autre côté, les cavités photoniques comme les résonateurs en anneau (MRRs) offrent des avantages significatifs par rapport aux cavités plasmoniques, notamment en termes d'intégration avec des plateformes CMOS industrielles (les métaux plasmoniques introduisent des contaminations dans le processus de fabrication). Les MRRs peuvent être intégrés de manière transparente avec d'autres composants optiques tels que des modulateurs, des détecteurs et des multiplexeurs, ce qui est crucial pour les systèmes lab-on-chip et l'optofluidique.

type de cavités	matériau du guide d'ondes	particule : matériau, taille	force optique / raideur
Résonateur en anneau [28]	silicium	polystyrène, 1.1 μm	$\sim 150 pN/W$
Cristal photoniques (mode guidé) [103]	silicium	polystyrène, 520 nm	$\sim 500 pN/W$
Cristal photoniques (mode de défaut) [104]	silicium	polystyrène, 100 nm	$\sim 700 pN/W$
Résonateur en anneau (add-drop) [106]	Si_xN_y	polystyrène, 1 μm	N/A

Table 9.5: Forces optiques dans des cavités photoniques.

Les deux configurations les plus courantes pour les résonateurs en anneau optiques sont all-pass et add-drop. Une description complète de ces deux types fondamentaux de résonateurs en anneau (MRRs), ainsi que des caractéristiques spectrales clés et des paramètres critiques pour la performance des MRR, est bien documentée dans la littérature et brièvement introduite dans le Chapitre 2. Dans cette thèse, nous avons opté pour un design plus simple et concentré nos études sur les résonateurs en anneau all-simple.

Thèse accessible à l'adresse : https://theses.insa-lyon.fr/publication/2024ISAL0120/these.pdf © [C.B. Chander Bhan], [2024], INSA Lyon, tous droits réservés

Modélisation et conception

Dans cette section, nous ne détaillons pas les modèles 3D et 2D développés dans COMSOL, FDFV, utilisant les fonctions de Tenseur de Stress Maxwell (MST) et d'Approximation Dipolaire Discrète (DDA). Ces modèles sont décrits en détail au début du Chapitre 3 et comparés à la littérature pour fournir une preuve substantielle de l'exactitude de nos résultats. Il n'est pas crucial de détailler la conception du modèle ici, nous nous concentrons plutôt sur la présentation des résultats importants dérivés des études menées dans cette thèse.

1. **Différents modes optiques : Modes fondamentaux et d'ordre supérieur dans les guides d'ondes**

   Le F_{grad} est plus fort vers l'intensité maximale du mode. Les modes d'ordre supérieur (HOM) dans les guides d'ondes diélectriques avec plusieurs maxima peuvent faciliter le piégeage d'un grand nombre de particules. De plus, en raison du noyau plus large des guides d'ondes, cela réduit les tolérances de fabrication lors de la réalisation de tels dispositifs. Dans cette thèse, nous étudions le mode de premier ordre et le mode fondamental pour des applications de piégeage optique. La Figure 9.5 ci-dessous montre le une vue en coupe du guide d'onde, le profil en intensité du mode guidé et le tracé du vecteur F_{grad} pour les deux modes afin de les comparer.

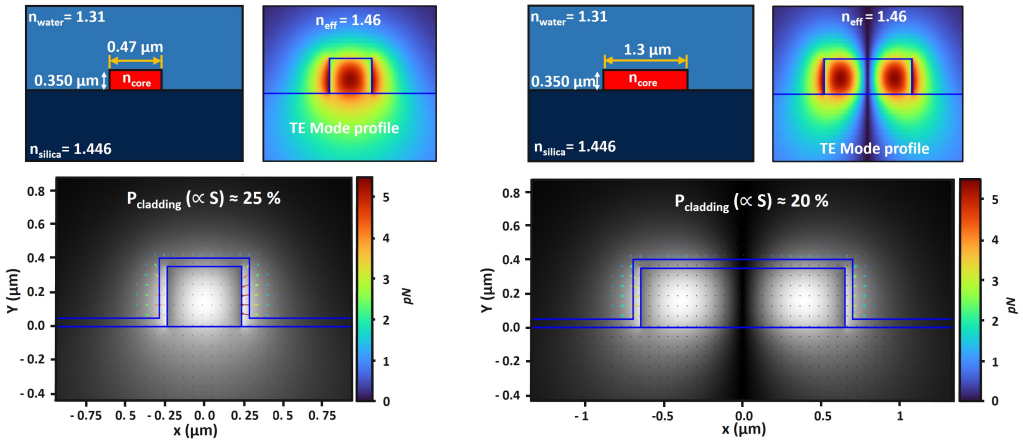

(a) Fundamental mode *(b) Higher order mode*

Figure 9.5: Tracé du vecteur F_{grad} dans les profils XY pour les guides d'ondes HOM et FM avec une vue en coupe et le profil en intensité du mode des deux guides d'onde schématique de la structure des deux guides d'ondes (évalué avec le modèle FDE de Lumerical).

   Comme on peut le voir, les guides d'ondes à largeur faible étroit (FM) et à section plus large (HOM) présentent le même F_{grad} sur leurs parois verticales. Les forces optiques ici sont calculées à l'aide de la méthode DDA, qui évalue la force au centre de la particule. Par conséquent, près du mur du guide d'ondes, les valeurs de force ont été intentionnellement fixées à zéro jusqu'au centre de la particule (rayon), comme le montre la ligne bleue de contour dans la Figure 9.5. De plus, dans cette figure, les modes des deux guides d'onde sont montrés avec des tracés de contour noir et blanc pour distinguer le comportement du tracé du vecteur F_{grad} et les intensités des modes.

Thèse accessible à l'adresse : https://theses.insa-lyon.fr/publication/2024ISAL0120/these.pdf © [C.B. Chander Bhan], [2024], INSA Lyon, tous droits réservés

Remarque : Étant donné que la présence de plusieurs maxima dans les modes d'ordre supérieur (HOM) peut être bénéfique pour piéger plusieurs particules, nous avons intégré cette structure dans notre conception de fabrication et l'avons optimisée (décrite dans le chapitre 4) avec une épaisseur de Si_xN_y de 300 nm.

2. **Guides d'ondes plasmoniques hybrides (HPWG)** Les métaux plasmoniques sont populaires dans la littérature pour améliorer le piégeage optique et la sensibilité car ils permettent une forte amélioration résonante de la densité locale des états de photon à la surface, ce qui augmente le gradient du champ électrique [121].

   Nous avons considéré une structure similaire (HPWG avec le concept de "mode-lift" : décrite plus tôt dans la section d'introduction) utilisée dans une thèse précédente pour augmenter la sensibilité. Dans notre étude, nous avons utilisé de l'or (Au) comme métal plasmonique dans l'infrarouge. Malgré l'amélioration du champ électrique, il présente des caractéristiques uniques sous-jacentes à leur forte absorption et diffusion de lumière dans les études biomédicales [126]. L'indice de réfraction de l'Au utilisé dans la modélisation est de 0.550 + 9.81i à une longueur d'onde de 1310 nm. Pour garantir des modes de polaritons de surface plasmoniques (SPP) dans les murs parois verticales, nous avons délibérément sélectionné des structures plasmoniques avec des largeurs de 0.430 μm dépassant la profondeur de peau.

   Pour des raisons pratiques, nous avons optimisé la conception des HPWG en sélectionnant le mode de rayonnement, se produisant à une largeur du guide d'onde diélectrique de 430 nm, avec des pertes associées de 3000 dB/cm.

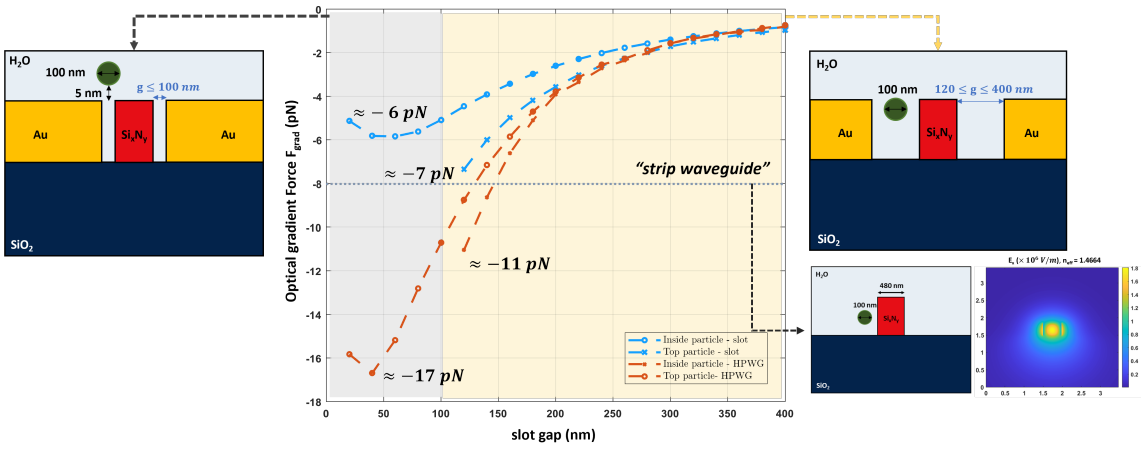

Figure 9.6: Comparaison de F_{grad} en fonction de la taille de l'ouverture pour les HPWG. Les lignes en pointillés bleue et orange représentent F_{grad} pour les guides d'onde classiques fente et HPWG, respectivement, dans la plage d'écart $120 \leq g \leq 400$ nm (arrière-plan jaune) et $g \leq 120$ nm (arrière-plan gris). La ligne en pointillés grise représente F_{grad} pour le guide d'onde classique à nervure, comme illustré dans le diagramme schématique de la figure.

Il est impératif de comprendre le rôle crucial de la taille de l'ouverture, car des largeurs plus petites facilitent des interactions lumière-matière plus fortes, amplifiant ainsi les forces optiques dans les HPWG par rapport aux guides d'onde diélectriques à fente. Par exemple, comme l'illustre la Figure 9.6, pour des écarts inférieurs à 100 nm, la force optique maximale exercée sur un HPWG avec un écart de 20 nm est de 17 pN, trois fois plus élevée que celle d'un guide d'onde diélectrique à fente. En revanche,

Thèse accessible à l'adresse : https://theses.insa-lyon.fr/publication/2024ISAL0120/these.pdf © [C.B. Chander Bhan], [2024], INSA Lyon, tous droits réservés

pour des écarts supérieurs à 100 nm, la force optique maximale est environ 1,5 fois plus grande que celle d'un guide d'onde diélectrique à fente, et cette comparaison diminue davantage à mesure que l'on augmente la taille de l'écart jusqu'à 400 nm. Par rapport aux guides d'ondes standard, les forces de gradient optique dans les HPWG sont deux fois plus élevées.

La sensibilité de masse est définie comme suit [127] :

$$S = \frac{\Delta\lambda_{res}}{\Delta n_{clad}} = \frac{\lambda_{res}}{n_g}\frac{\delta n_{eff}}{\delta n_{clad}} \tag{9.2}$$

où $\frac{\delta n_{eff}}{\delta n_{clad}}$ définit le changement dans le n_{eff} dû au changement de l'indice de réfraction (RI) du milieu extérieur $(\delta n_{clad} = 0.0073)$, et n_g est défini comme l'indice de groupe. λ_{res} est la longueur d'onde résonante. Le $\frac{\delta n_{eff}}{\delta n_{clad}}$ augmente à mesure que la puissance dans le milieu extérieur augmente.

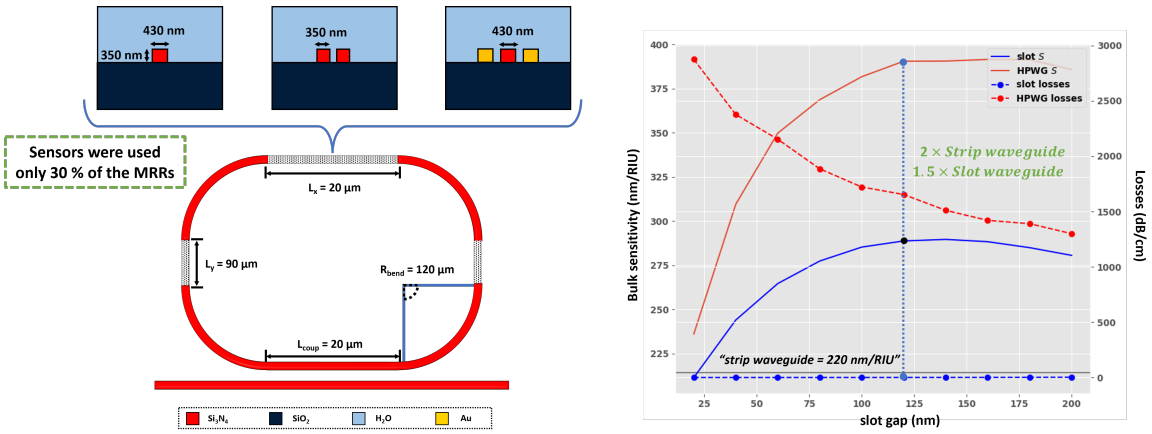

Figure 9.7: Comparaison de S pour les HPWG, les guides d'onde diélectriques à fente et standard : a) Diagramme schématique des MRRs en forme de piste où le motif en pointillés montre la zone où trois types de guides d'ondes différents sont utilisés pour évaluer S ; b) Courbes de S et de pertes en fonction de la taille de l'écart pour les guides d'onde diélectriques à fente et HPWG. Les lignes noires pleines représentent la sensibilité du guide d'ondes à standard de 220 nm/RIU.

Il convient de noter que les guides d'ondes HPWG et diélectrique à fente présentent une sensibilité minimale S avec un écart de 20 nm par rapport à un écart de 120 nm, tandis que les F_{grad} sont relativement plus élevés pour la configuration de 20 nm. Ce phénomène découle de la nature du F_{grad}, qui s'aligne vers le gradient d'intensité maximal, induisant une charge sur les particules et dirigeant les forces vers le pic d'intensité, indépendamment du volume d'interaction du champ avec l'analyte. En revanche, S repose sur un volume interactif plus important avec un champ électrique élevé, améliorant la sensibilité du capteur. Par conséquent, dans notre étude, nous avons opté pour un espacement de 120 nm en adéquation avec l'optimisation conception optimisée de l'HPWG pour des comparaisons pratiques. Avec une largeur de coeur de 430 nm et un espacement de 120 nm, l'HPWG proposé dans cette étude surpasse les guides d'onde diélectrique à fente de 1,5 fois et les guides d'onde standard de 2 fois. De plus, en incorporant des MRRs en forme de piste avec des pertes HPWG, un facteur Q respectable de 3000 peut être atteint en utilisant l'équation

Thèse accessible à l'adresse : https://theses.insa-lyon.fr/publication/2024ISAL0120/these.pdf © [C.B. Chander Bhan], [2024], INSA Lyon, tous droits réservés

décrite au chapitre 2. En outre, selon l'application, une telle conception d'HPWG peut être adaptée avec des largeurs de coeur diélectrique plus étroites et des écarts plus petits pour renforcer les forces optiques, au prix d'augmenter les pertes du dispositif.

Remarque : Étant donné la complexité, les contraintes de temps et les exigences étendues en matière de conception et de fabrication associées aux guides d'ondes plasmoniques hybrides (HPWG), nous avons choisi de ne pas inclure cette structure dans notre conception finale pour la fabrication.

3. **Coupeurs effilés:**

   Les coupleurs effilés ont été utilisés pour améliorer l'efficacité de couplage fibre-à-puce, garantissant un transfert de puissance plus efficace vers les guides d'ondes. Sur le banc optique de l'INL, nous utilisons des fibres à lentille avec un diamètre de faisceau de 1,5 μm. Par conséquent, nous avons optimisé la section transversale d'entrée à 300 $\times$ 300 nm de Si_xN_y, enterrée sous un revêtement en SiO_2, qui présente un diamètre de faisceau comparable. Cette configuration est illustrée dans la Figure 9.8, qui représente le n_{eff} en fonction de la largeur du cœur du guide d'onde dans le coupleur effilé.

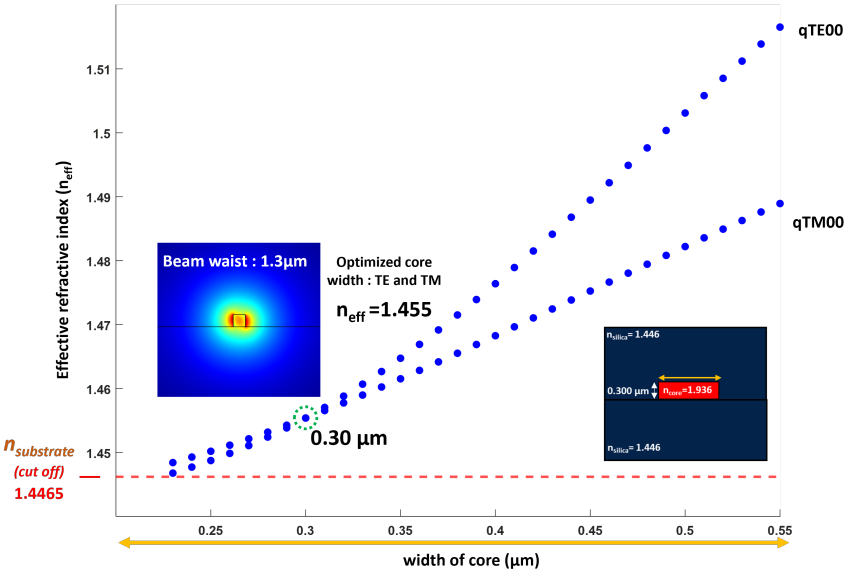

Figure 9.8: n_{eff} en fonction de la largeur du coupleur effilé avec une épaisseur fixe de 0,300 μm.

Pour étudier plus avant l'efficacité du couplage entre la fibre à lentille optique et les dimensions choisies du guide d'ondes, nous utilisons la méthode de l'intégrale de recouvrement. Cette méthode quantifie le recouvrement entre le mode optique de la fibre à lentille et le mode du guide d'ondes, nous permettant de calculer l'efficacité de couplage (Γ).

$$\Gamma = \frac{\left|\iint \mathbf{E}_{fiber}(x,y) \cdot \mathbf{E}^*_{waveguide}(x,y), dx, dy\right|^2}{\left(\iint \left|\mathbf{E}_{fiber}(x,y)\right|^2, dx, dy\right) \cdot \left(\iint \left|\mathbf{E}_{waveguide}(x,y)\right|^2, dx, dy\right)} \tag{9.3}$$

En utilisant la formule mentionnée ci-dessus 9.3, nous avons calculé une efficacité de couplage (Γ) de 75,3 $\%$entre le mode fondamental (FM) de la section transversale du

Thèse accessible à l'adresse : https://theses.insa-lyon.fr/publication/2024ISAL0120/these.pdf © [C.B. Chander Bhan], [2024], INSA Lyon, tous droits réservés

guide d'onde d'entrée aux cônes inversés (300 $\times$ 300 nm) et la source gaussienne avec une taille de spot de 1,5 μm.

Une autre dimension cruciale dans la conception des cônes inversés est la longueur du cône. La longueur du cône assure une transition adiabatique en douceur entre le guide d'onde d'entrée et le guide d'ondes de sortie où il se couple au dispositif principal. Une longueur de la transition plus courte peut entrainer des pertes de diffraction plus élevées. Comme nous travaillons avec la forme la plus simple, c'est-à-dire un cône linéaire, une règle empirique consiste à considérer un angle d'environ 1°.

Pour évaluer l'intégrale de recouvrement entre les guides d'ondes d'entrée et de sortie dans les coupleurs inversés, nous avons réalisé des simulations FDTD pour tenir compte des pertes de diffraction dues à la diffusion et au décalage de mode le long de la longueur du coupleur. Comme le montre la Figure 9.9, une longueur du coupleur de 35 μm a entraîné une efficacité de recouvrement de 92 $\%$.

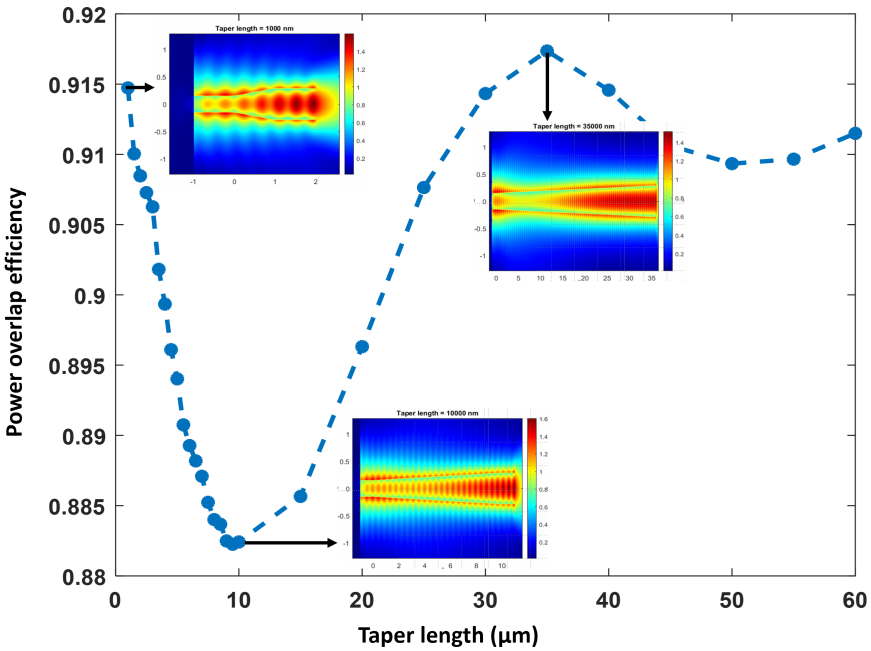

Figure 9.9: Efficacité de recouvrement de puissance en fonction de la longueur linéaire du coupleur.

Lors de l'optimisation des coupleurs effilés, nous avons choisi une épaisseur de Si_xN_y de 300 nm. Cependant, cette épaisseur n'est pas compatible avec notre plateforme industrielle (DAPHNE, STMicroelectronics). Par conséquent, nous avons conçu le dispositif pour être fabriqué à LN2, 3IT, ce qui offre plus d'espace sur la plaquette et une plus grande flexibilité dans la conception des puces. Pour les coupleurs effilés, nous avons augmenté la longueur à 1 mm pour atteindre une efficacité de couplage maximale.

4. **Etude de la stabilité du piégeage optique : F_{min} et D_{min}**

   Il est pertinent de comprendre que pour le piégeage de nanoparticules, à mesure que la taille diminue, le potentiel de piégeage diminue drastiquement, augmentant

Thèse accessible à l'adresse : https://theses.insa-lyon.fr/publication/2024ISAL0120/these.pdf © [C.B. Chander Bhan], [2024], INSA Lyon, tous droits réservés

ainsi la probabilité que les particules échappent au piège en raison du mouvement brownien. Pour surmonter cela, il est nécessaire de maintenir une force de gradient optique forte, c'est-à-dire suffisamment élevée pour atteindre une énergie potentielle (10 K_BT) supérieure à trois fois l'énergie cinétique du mouvement brownien dans chaque degré de liberté (1/2 K_BT), comme l'indique la règle empirique décrite par Ashkin [45].

On peut trouver l'énergie potentielle ($U(x)$) à partir de la force calculée ci-dessus le long de l'axe x avec l'équation suivante :

$$U(x) = \int_0^{\infty} F_{grad} \cdot dx \tag{9.4}$$

Intégrer le F_{grad} jusqu'à l'infini conduirait à un potentiel infini, ce qui est irréaliste dans n'importe quel scénario. Par conséquent, l'intégration doit être limitée à la profondeur de pénétration (x_e) du champ évanescent, où 37 $\%$ du champ est confiné dans la région du milieu extérieur. Par conséquent, l'équation de champ 9.4 se présentera comme suit :

$$U(x) = \int_0^{x_e} F_{grad} \cdot dx \tag{9.5}$$

La Figure 9.10.(a) ci-dessous montre le F_{grad} calculé pour différentes puissances optiques pour une particule diélectrique de 100 nm le long de l'axe x, juste au-delà du mur vertical du guide d'onde. Les valeurs de F_{grad} sont présentées pour le profil central du mode TE E_y (hauteur du cœur = 150 nm). La Figure 9.10.(b) illustre la profondeur potentielle du F_{grad} en utilisant l'équation ci-dessus 9.5. Comme montré, le F_{grad} calculé pour 24, 30 et 36 mW n'a que suffisamment de $U(x)$ pour dépasser la condition minimale de piégeage stable de 10 K_BT. Cependant, il est également crucial de déterminer la quantité de puissance requise pour remplir la proportion de particules dans la taille du piège, qui est définie par la profondeur de pénétration du champ évanescent dans le revêtement. Pour évaluer cela, il faut évaluer la densité de probabilité en fonction de l'énergie de piégeage en utilisant la distribution de Maxwell-Boltzmann et la fonction de partition, comme montré ci-dessous dans l'Équation 9.6. Par la suite, la proportion de particules peut être évaluée pour la taille du piège (x_e) en utilisant l'Équation 9.7.

$$p(x) = \frac{e^{-\frac{u(x)}{K_BT}}}{e^{\int_0^{\infty} \frac{u(x)}{K_BT}}} \tag{9.6}$$

$$D(x) = \frac{\int_0^{x_e} p(x)dx}{\int_0^{\infty} p(x)dx} \tag{9.7}$$

5. **Structure finale optimisée du guide d'onde**

Nous avons conçu des coupleurs inversés optimisés pour une épaisseur (eg_{core}) de 300 nm en utilisant Si_xN_y. Étant donné que la plateforme industrielle DAPHNE est optimisée uniquement pour deux eg_{core} de Si_xN_y, 350 nm et 600 nm, nous avons préféré continuer à concevoir et à fabriquer au sein des installations du Laboratoire

Thèse accessible à l'adresse : https://theses.insa-lyon.fr/publication/2024ISAL0120/these.pdf © [C.B. Chander Bhan], [2024], INSA Lyon, tous droits réservés

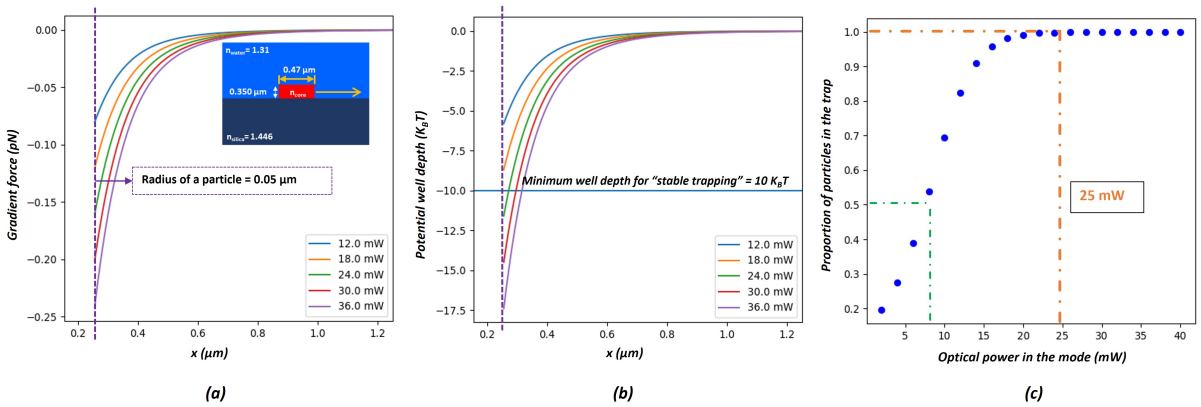

Figure 9.10: Courbe de la valeur du puit de potentiel en fonction de la distance x dans le milieu extérieur d'eau : (a) F_{grad} en fonction de la distance par rapport à l'interface cœur/extérieur à différents niveaux de puissance optique (b) Profondeur du puits potentiel (U_x) en fonction de la distance par rapport à l'interface cœur/extérieur à différents niveaux de puissance optique (c) Proportion de particules piégées (D_x) dans la taille du piège (e_x) en fonction de la puissance optique.

Nanotechnologies et Nanosystèmes (LN2) et de l'Institut interdisciplinaire d'innovation technologique (3IT), où une plus grande flexibilité est offerte pour nos exigences de conception.

Comme $\Delta\lambda_{res}$ est directement proportionnel à la sensibilité, nous considérons $\Delta\lambda_{res}$ comme un paramètre de sensibilité et le rappelerons comme sensibilité dans les discussions ultérieures. Pour optimiser le guide d'onde à la fois pour les applications de sensibilité et de piégeage optique, on peut observer directement la relation entre $\Delta\lambda_{res}$ et le F_{grad} par rapport à la largeur du cœur, comme montré dans la Figure 9.11.

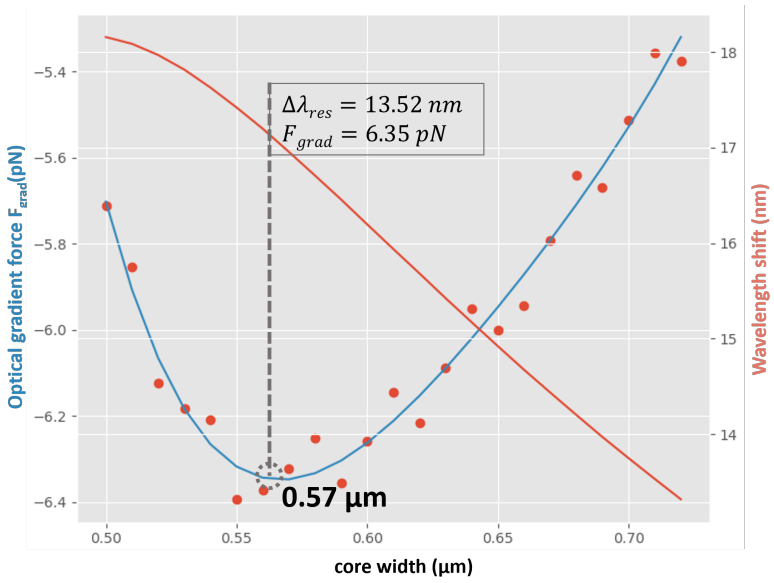

Figure 9.11: Optimisation de la largeur finale du cœur du guide d'onde : F_{grad} (ligne bleue solide) et décalage de longueur d'onde (ligne orange) pour différentes largeurs de cœur : les valeurs de F_{grad} calculées ici sont pour une particule diélectrique de 100 nm avec une puissance normalisée de 1 W.

Thèse accessible à l'adresse : https://theses.insa-lyon.fr/publication/2024ISAL0120/these.pdf © [C.B. Chander Bhan], [2024], INSA Lyon, tous droits réservés

Il est évident d'après la Figure 9.11 qu'une largeur de cœur plus étroite (500 nm) fournit une sensibilité plus élevée, tandis qu'un gradient prononcé augmente le F_{grad} jusqu'à 590 nm de la largeur du cœur. Si l'un des paramètres est essentiel, il peut facilement être choisi, mais au final, il est important que le dispositif ait une forte force de piégeage et soit sensible. Dans ce cas, le pourcentage de gain dans le F_{grad} doit être égal au pourcentage de perte en sensibilité pour déterminer la largeur de cœur optimale. Par conséquent, au lieu de perdre le maximum de l'un ou l'autre paramètre, il serait préférable de trouver le point optimal où le gain égalise la perte.

Cela pourrait être réalisé en trouvant le pourcentage de différence relative entre deux F_{grad} (passant de la position initiale à la position que l'on souhaite évaluer) et les niveaux de sensibilité pour les deux positions. La moindre différence entre le changement relatif sera la largeur optimisée où la force est maximisée sans compromettre le paramètre de sensibilité. Nous avons optimisé notre largeur de cœur à 570 nm pour des guides d'onde à base de Si_xN_y avec un eg_{core} de 300 nm.

Les dispositifs élémentaires optimisés du GDS des premiers composants de test sont présentés sur la Figure ci-dessous 9.12, avec toutes les dimensions critiques clairement définies. De plus, les courbes et spirales sur chaque puce sont conçues pour correspondre aux dimensions du dispositif principal, afin de mesurer avec précision les pertes de courbure et de propagation linéaire pour les sections transversales utilisées dans la structure principale. Compte tenu des incertitudes inhérentes au processus de fabrication, la redondance et l'adaptabilité ont été intégrées dans les conceptions. Plusieurs puces photoniques ont été fabriquées avec de légères variations dans les dimensions critiques, telles que les espaces de couplage et les largeurs de guides d'onde, en tenant compte des écarts potentiels avec des tolérances de $\pm$ 20 nm.

Thèse accessible à l'adresse : https://theses.insa-lyon.fr/publication/2024ISAL0120/these.pdf © [C.B. Chander Bhan], [2024], INSA Lyon, tous droits réservés

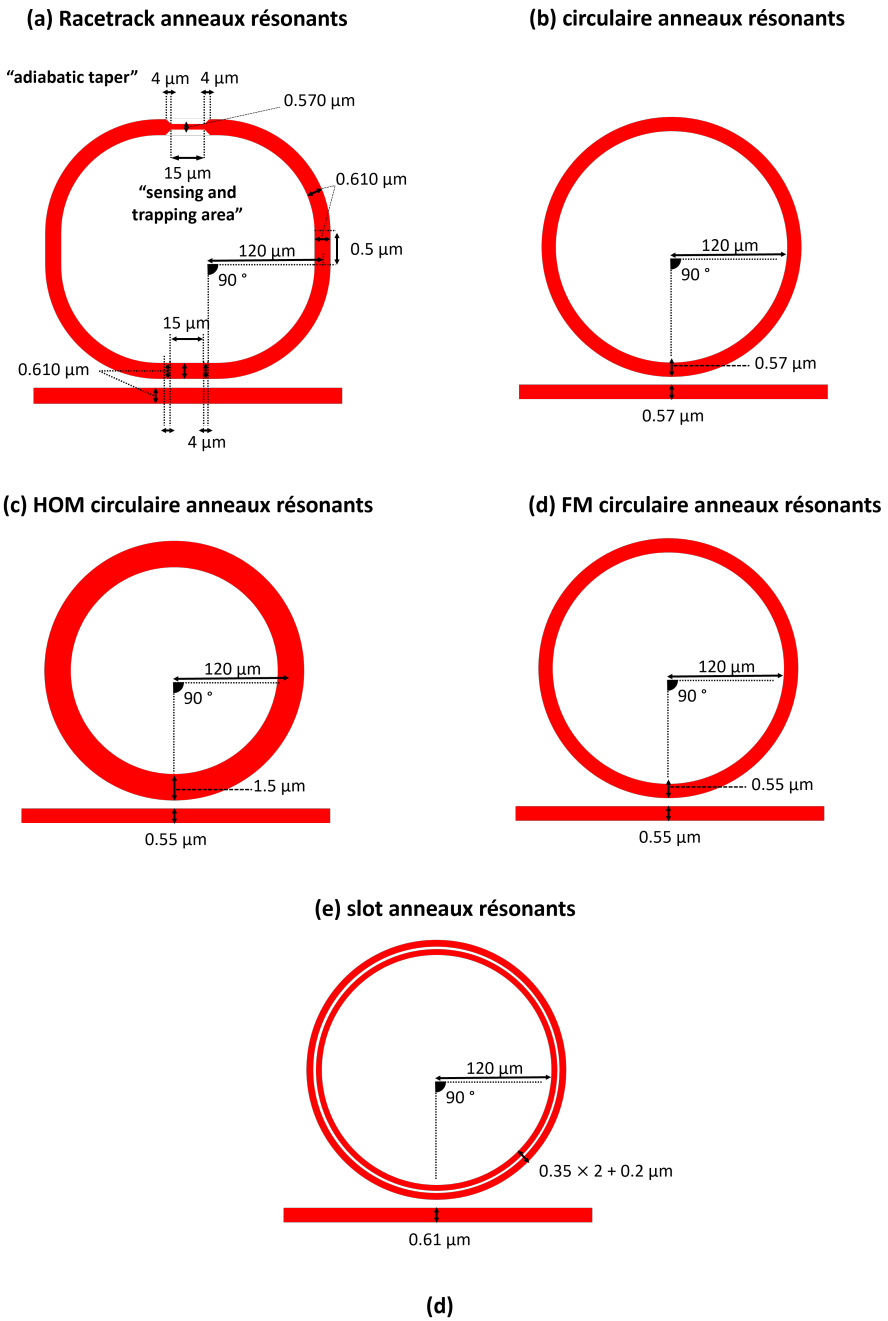

Figure 9.12: Schéma des différents MRRs inclus dans la conception CAO pour différents puces photoniques.

Thèse accessible à l'adresse : https://theses.insa-lyon.fr/publication/2024ISAL0120/these.pdf © [C.B. Chander Bhan], [2024], INSA Lyon, tous droits réservés

Fabrication

Tous les puces photoniques ont été fabriquées à l'Institut interdisciplinaire d'innovation technologique (3IT). Le processus de fabrication a suivi des recettes standard établies par les ingénieurs de l'institut. Étant donné que ces étapes de fabrication sont des recettes bien documentées, une description détaillée n'est pas nécessaire à ce stade. Un organigramme complet des étapes de fabrication, comme indiqué dans la Figure 9.13, illustre le processus utilisé pour la fabrication des puces.

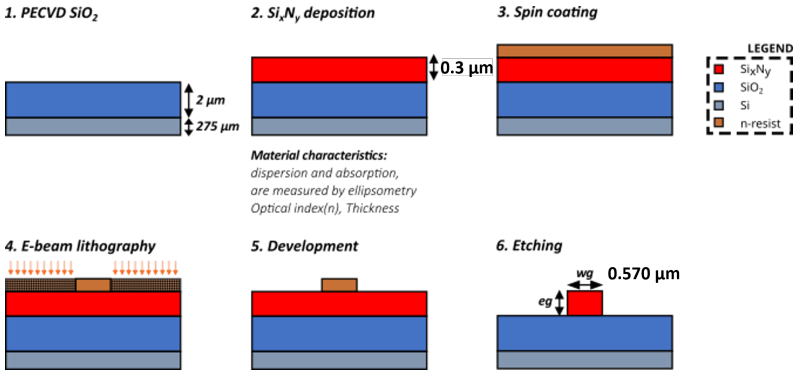

Figure 9.13: Processus de fabrication : guide d'onde en Si_xN_y.

De plus, il est important de souligner deux points cruciaux et conclusions tirées du processus de fabrication :

1. **Profil final du guide d'onde :**

   Une fois le processus de gravure terminé, l'épaisseur totale de la structure a été mesurée à environ 600 nm au niveau des côtés des MRRs, comme montré dans la Figure 9.14. Cela inclut à la fois la couche de Si_xN_y et la couche résiduelle de résine photosensible sur le dessus. Pour éliminer les résidus de résine, un processus d'oxydation plasma a été appliqué à 150 W pendant 10 minutes, suivi d'une immersion dans de l'acétone pendant la nuit afin d'assurer l'élimination complète de la résine restante. Le profil en coupe transversale du guide d'onde est illustré dans l'image SEM présentée dans la Figure 9.14.

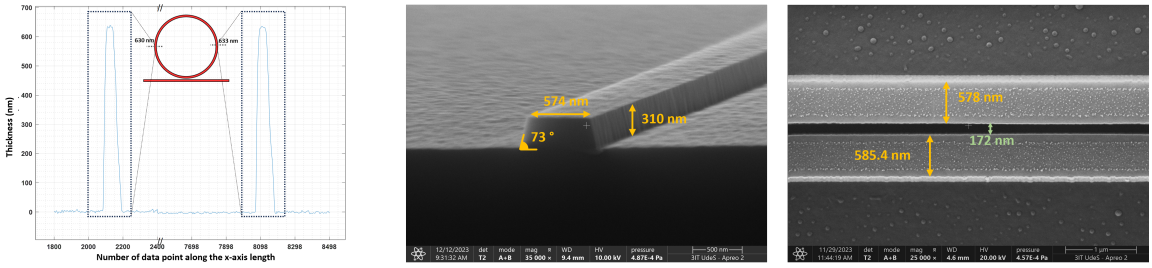

Figure 9.14: Profil au profilomètre et image au microscope électronique du dispositif après gravure : (a) illustre le profil au profilomètre des côtés des MRRs. (b) la coupe transversale du guide d'onde après nettoyage à l'acétone et oxydation plasma. (c) région de couplage après nettoyage à l'acétone et oxydation plasma.

   Comme illustré dans la Figure 9.14.(b), un angle de 73 ° a été obtenu dans les motifs de gravure subséquents sur la couche de Si_xN_y. Nous avons étudié l'effet des

Thèse accessible à l'adresse : https://theses.insa-lyon.fr/publication/2024ISAL0120/these.pdf © [C.B. Chander Bhan], [2024], INSA Lyon, tous droits réservés

angles de parois latérales sur le mode n_{eff} avant d'optimiser les recettes de gravure et l'exposition EBL. Comme le montre la Figure 9.15, un angle de paroi latérale de 73 ° n'altère pas significativement le mode et le gradient du champ évanescent par rapport à la conception initiale. Compte tenu des contraintes de temps, nous avons décidé de continuer avec la même recette de gravure (décrite au chapitre 5) pour toutes les puces.

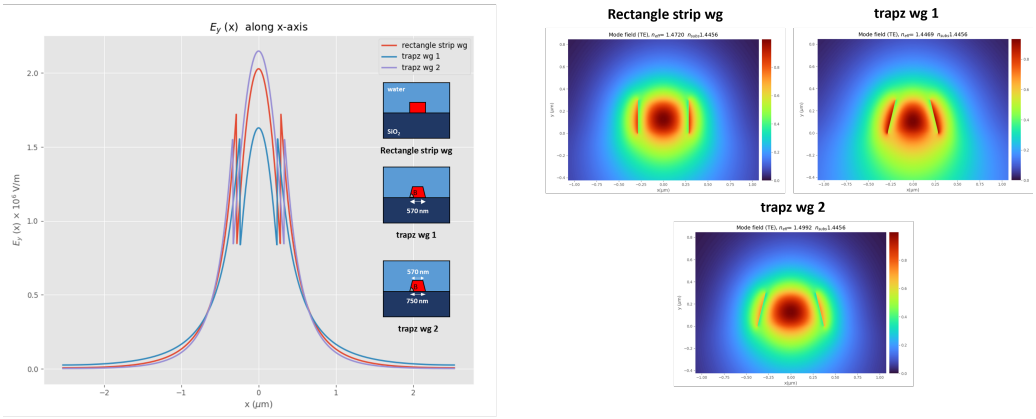

Figure 9.15: Effet sur n_{eff} et champ évanescent avec un profil trapézoïdal du guide d'onde : (a) Champ électrique E_y (TE) en fonction de la largeur du noyau au centre. (b) Profils de mode TE du guide d'onde droit conçu, du design fabriqué (trapz wg 2) et d'autres options possibles (trapz wg 1).

2. **Système fluidique :**

   Pour réaliser notre caractérisation optique finale du dispositif, il est nécessaire d'intégrer un système fluidique sur la puce afin d'introduire les particules ou les analytes à détecter par le dispositif. Dans la littérature, les réservoirs en PDMS sont couramment utilisés pour les réservoirs et canaux microfluidiques. Cependant, l'utilisation du réservoir en PDMS présente trois inconvénients dans notre processus de caractérisation. Tout d'abord, il est bien connu que le PDMS libère ses élastomères dans l'eau car l'agent de réticulation ne peut pas atteindre une efficacité de réticulation de 100 $\%$. Ces élastomères peuvent adhérer à la surface du guide d'onde et augmenter les pertes du dispositif. Deuxièmement, les réservoirs en PDMS utilisent l'oxydation plasma pour adhérer à la puce en silicium, ce qui complique le nettoyage par solvants après la caractérisation. Troisièmement, en raison de sa souplesse, il est difficile d'aligner correctement le PDMS avec la puce en silicium. Ce troisième problème peut être atténué en augmentant la quantité d'agent de réticulation dans le mélange de polymères de silicone à un rapport de 1:8, mais cela complique son retrait des moules ayant des côtés étroits de 1 mm.

   Pour surmonter ces problèmes, des systèmes fluidiques « repositionnables » utilisant du polyuréthane thermoplastique (TPU) deviennent populaires. Le TPU possède une surface adhésive qui se fixe et se détache facilement des puces en silicium, comme montré dans la Figure 9.16 de l'étape 2 à 4. L'adhésion est suffisamment forte pour retenir des fluides à l'intérieur de la structure à l'étape 5 de la Figure 9.16, où nous avons maintenu de l'eau pendant plus de 4 heures sans qu'il y ait de fuite. De plus, le TPU remplace de plus en plus le PDMS dans les canaux microfluidiques et structures

Thèse accessible à l'adresse : https://theses.insa-lyon.fr/publication/2024ISAL0120/these.pdf © [C.B. Chander Bhan], [2024], INSA Lyon, tous droits réservés

fluidiques en raison de ses meilleures propriétés mécaniques et de sa transparence dans le domaine visible, permettant une observation claire.

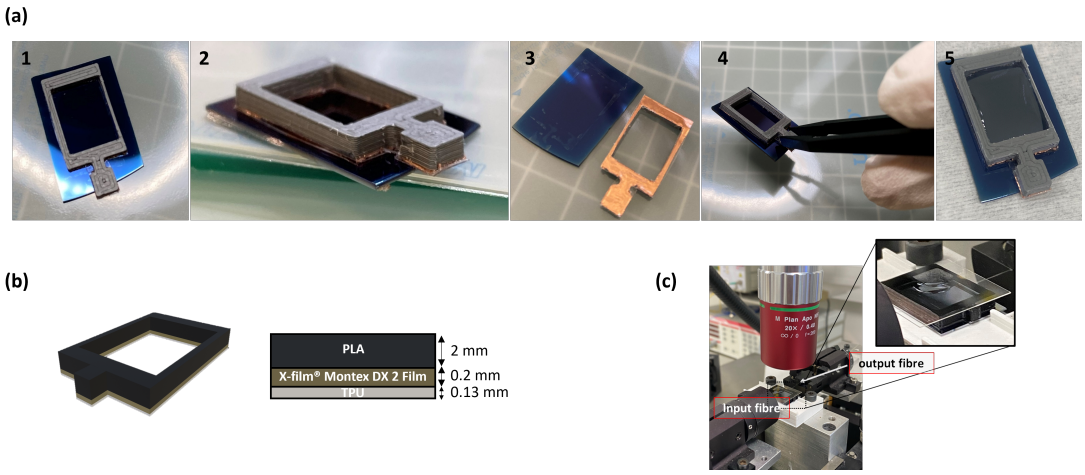

Figure 9.16: Étapes de fabrication du réservoir fluidique utilisant un film TPU : (a) Illustration de la structure du réservoir fluidique avec film TPU, comprenant les tests de repositionnement et d'étanchéité. (b) et (c) Schémas complets de la structure du réservoir et de la puce photonique en silicium avec le réservoir monté sur le banc optique pour la caractérisation.

Thèse accessible à l'adresse : https://theses.insa-lyon.fr/publication/2024ISAL0120/these.pdf © [C.B. Chander Bhan], [2024], INSA Lyon, tous droits réservés

Caractérisation

La figure 9.17 présente le schéma du montage de couplage en bout à l'INL, à Lyon, détaillant tous les composants nécessaires à la caractérisation du dispositif. À l'INL, nous utilisons une source large bande (BesT LEDs) s'étendant de 1200 à 1700 nm, ainsi qu'un filtre numérique accordable pour isoler la longueur d'onde de 1310 nm de la source large bande pour l'expérience de sensibilité optique MRR.

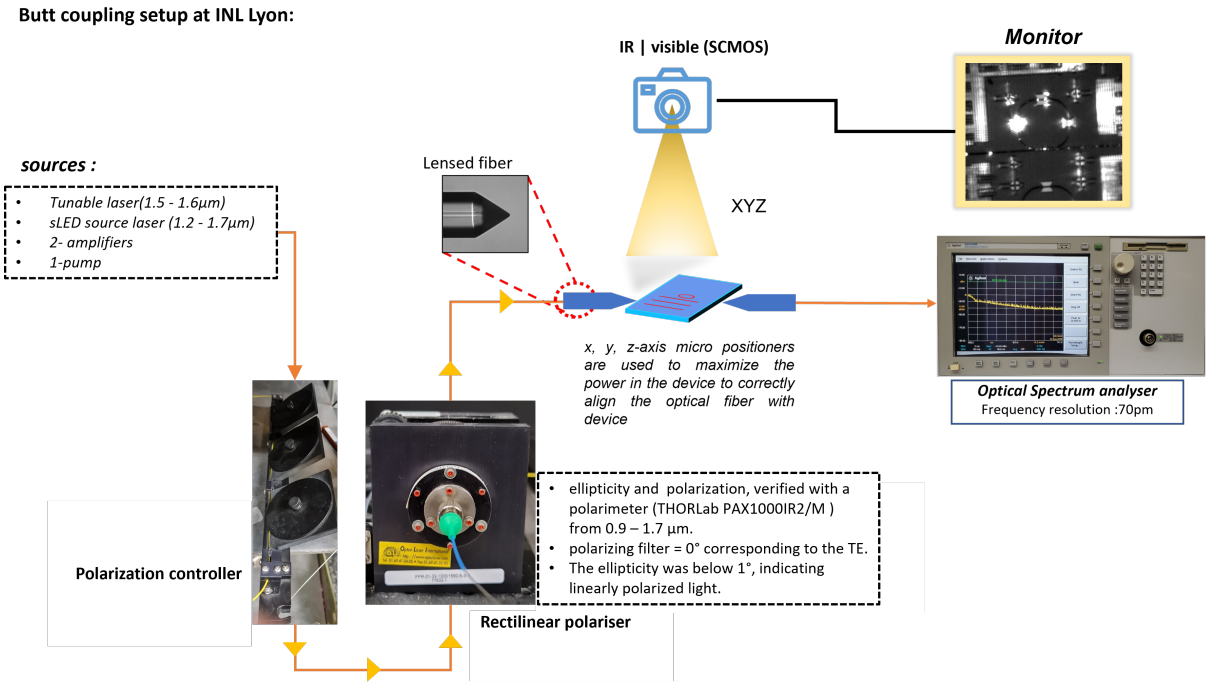

Figure 9.17: Test optique expérimental sur banc à INL, Lyon, avec un mécanisme de couplage par la tranche.

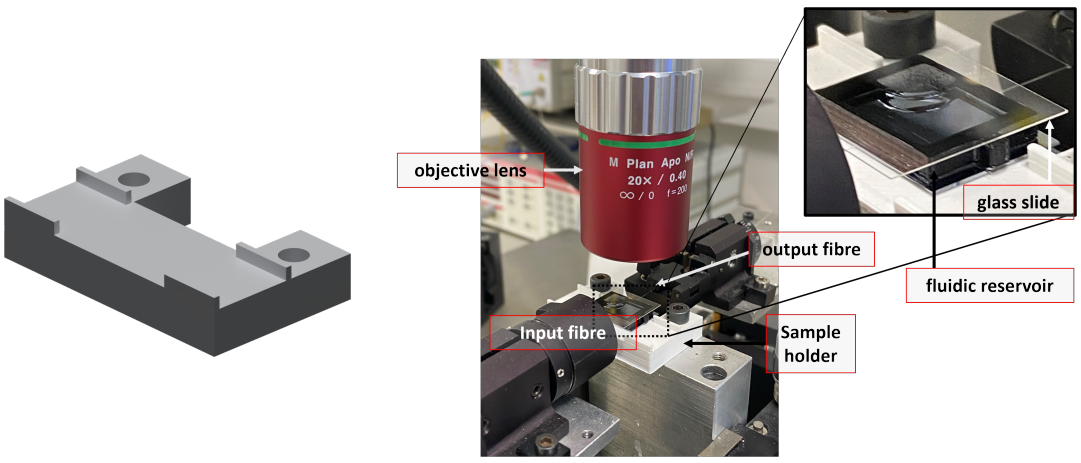

Figure 9.18: Support d'échantillon sur le dispositif optique expérimental avec un réservoir fluidique sur le dessus de la puce : (a) modèle 3D du support d'échantillon créé avec Blender, et (b) une puce photonique avec un réservoir fluidique (film TPU + réservoir imprimé en 3D) placé sur le support d'échantillon.

Thèse accessible à l'adresse : https://theses.insa-lyon.fr/publication/2024ISAL0120/these.pdf © [C.B. Chander Bhan], [2024], INSA Lyon, tous droits réservés

Pour les résultats de caractérisation présentés dans cette thèse, un support d'échantillon imprimé en 3D a été utilisé pour positionner l'échantillon dans le dispositif. Pour les mesures dans une enveloppe en eau déionisée (DI), un réservoir fluidique et un couvercle en verre ont été utilisés pour prévenir l'évaporation et la distorsion optique due au ménisque, comme illustré dans la figure 9.18. En revanche, pour les mesures de pertes avec une enveloppe en SiO_2, le réservoir et le couvercle en verre n'étaient pas nécessaires, car la structure était déjà intégrée dans une enveloppe à indice de réfraction élevé et pouvait être caractérisée directement.

Résultats expérimentaux

1. **Perte de propagation linéaire pour le guide d'onde en Si_xN_y sous un gaine en SiO_2**

   Les résultats discutés ci-dessous sont basés sur des mesures de 4 spirales ayant des longueurs de 2,78, 3,28, 4,28 et 5,28 cm, et de 2 guides d'ondes linéaires d'une longueur de 1,3 cm. La figure 9.19.(a) montre la puissance de sortie des spirales en fonction de la longueur d'onde pour la polarisation TE, mesurée à l'aide d'un analyseur de spectre optique, avec une moyenne de 5 acquisitions à une fréquence d'échantillonnage de 100 Hz pour améliorer le rapport signal sur bruit (SNR). Les pertes de propagation linéaires (dB/cm) pour le guide d'onde en Si_xN_y, avec des dimensions critiques indiquées dans la figure 9.19(b), ont été évaluées à l'aide de l'ajustement linéaire aux mesures des guides d'ondes basé sur la méthode de York [156].

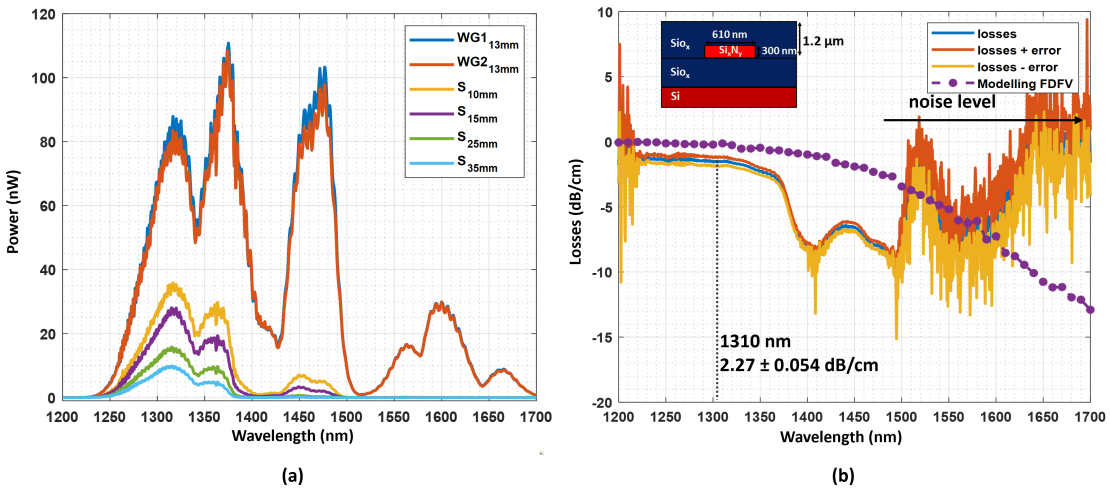

Figure 9.19: Pertes de propagation linéaires d'un guide d'ondes en Si_xN_y standard PECVD (3IT) avec une largeur de section transversale de 610 nm et une épaisseur de 300 nm, enfoui sous du SiO_2 PECVD : (a) Spectre de puissance de sortie des spirales et des guides d'ondes linéaires, et (b) Pertes de propagation linéaires en fonction de la longueur d'onde, accompagnées des pertes $\pm$ erreur standard

Les pertes au-delà d'une longueur d'onde de 1400 nm (pour les bandes E, S, C, L) étaient significativement élevées, comme le montre la Figure 9.19.(a), ce qui a entraîné un bruit important dans les mesures. La puissance de sortie des guides d'ondes et des spirales montre que les guides d'ondes linéaires (WG_1 et WG_2)

Thèse accessible à l'adresse : https://theses.insa-lyon.fr/publication/2024ISAL0120/these.pdf © [C.B. Chander Bhan], [2024], INSA Lyon, tous droits réservés

d'une longueur de 1,3 cm maintiennent toujours une puissance de sortie à 1550 nm. Cependant, à mesure que la longueur des guides d'ondes augmente, comme dans les spirales S_{15mm} et S_{25mm}, le facteur de perte augmente fortement dans les bandes S, C, L, entraînant une très faible puissance de sortie en raison des pertes par absorption (liées aux liaisons NH) et des fuites vers le substrat en silicium. Dans la Figure 9.19.(b), la ligne violette (≪ Modelling FDFV ≫) représente les pertes dues aux fuites dans le substrat en silicium, telles qu'évaluées à l'aide de la modélisation FDFV. La simulation utilise un substrat de Si d'une épaisseur de 0,1 μm, suffisante pour observer les pertes par fuite et éviter le couplage entre le SiO_2 et le substrat en Si, qui pourrait autrement induire des modes guidés en raison de la présence de conditions aux limites dans la modélisation. Les pertes par fuite à une longueur d'onde de 1,5 μm sont d'environ 3 dB/cm, ce qui n'est pas négligeable. De plus, des pertes par absorption associées aux liaisons NH sont également présentes. Ces facteurs combinés contribuent à une réduction significative de la qualité du signal, ce qui conduit à du bruit dans nos données expérimentales et rend la régression linéaire invalide pour la plage de 1200-1250 nm et au-delà de 1480 nm, comme le montre la Figure 9.19.(b), où les pertes sont principalement dans la plage de bruit.

2. **Pertes de propagation linéaires pour le guide d'onde à bande Si_xN_y sous un gaine d'eau**

   La figure 9.20 (a) et (b) montre les spectres de puissance de sortie et (c) et (d) les pertes de propagation linéaires en fonction de la longueur d'onde pour des dispositifs linéaires (guides d'onde droits + spirales) dans un gainage d'eau pour deux puces photoniques différentes.

   Les deux ensembles de mesures correspondent aux pertes linéaires des guides d'onde en Si_xN_y avec une largeur de cœur de 610 nm et une épaisseur de 300 nm, pour deux puces photoniques différentes fabriquées en utilisant les mêmes recettes de processus et approche de configuration fluidique. De plus, les zones ombragées dans les graphiques des pertes linéaires tiennent compte des erreurs dans les variables indépendantes (longueur différentielle du guide d'onde) et dépendantes (puissance optique de sortie). Dans les deux cas, les pertes linéaires correspondent à $\simeq$ 5 dB/cm à 1310 nm pour la polarisation TE.

Thèse accessible à l'adresse : https://theses.insa-lyon.fr/publication/2024ISAL0120/these.pdf © [C.B. Chander Bhan], [2024], INSA Lyon, tous droits réservés

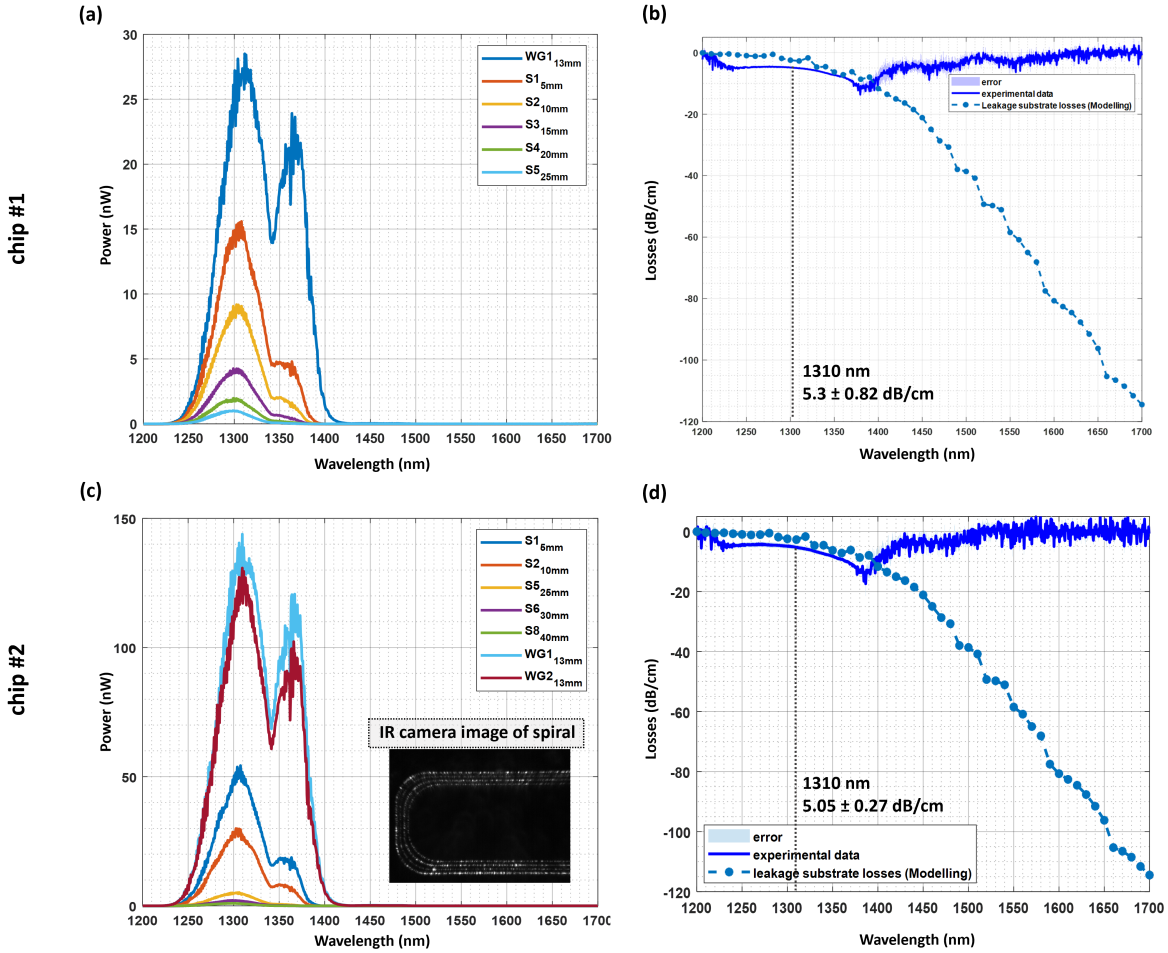

Figure 9.20: Pertes de propagation linéaires d'un guide d'onde en Si_xN_y standard PECVD (3IT) avec une largeur de section transversale de 610 nm et une épaisseur de 300 nm sous gainage d'eau pour la polarisation TE : (a) et (c) spectres de puissance de sortie des spirales et des guides d'onde linéaires pour deux puces différentes, et (b) et (d) pertes de propagation linéaires en fonction de la longueur d'onde, ainsi que les erreurs des variables indépendantes et dépendantes dans un gainage d'eau pour deux puces photoniques différentes.

Thèse accessible à l'adresse : https://theses.insa-lyon.fr/publication/2024ISAL0120/these.pdf © [C.B. Chander Bhan], [2024], INSA Lyon, tous droits réservés

3. **Pertes de courbure pour les guides d'onde en Si_xN_y sous un gaine en SiO_2**

   Les pertes par rayonnement correspondantes peuvent être estimées dans la plage de 1250 à 1480 nm (plage où nous avons uniquement des données expérimentales valides pour des guides d'ondes droits) pour un revêtement en SiO_2, comme présenté dans la Figure 9.21.(a) pour un rayon de courbure de 50 μm en fonction de la longueur d'onde pour la polarisation TE. Pour des longueurs d'onde plus élevées, nous avons observé dans la Figure 9.19.(b) que, du fait des pertes par fuite (substrat en Si) et de l'absorption (liaisons NH), le signal est noyé dans le bruit. Par conséquent, la méthode de normalisation utilisée dans cette étude n'est valable que pour les plages de longueurs d'onde inférieures (1250 - 1480 nm) où les modes sont bien confinés et se comportent de manière similaire aux guides d'ondes droits.

   Les lignes solides verte et violette représentent les pertes par rayonnement calculées à l'aide du solveur de modes FDFV [87] pour un rayon de courbure de 50 μm et une épaisseur de Si_xN_y de 300 nm, correspondant aux configurations sans et avec substrat en Si, respectivement. La Figure 9.21.(b) illustre comment les profils des modes de courbure se décalent vers le haut en présence du substrat en Si, comparé à la configuration sans substrat. L'indice de réfraction effectif (n_{eff}) du mode courbé au point de puissance maximale augmente avec le substrat en Si, entraînant une réduction des pertes par rayonnement.

   En tenant compte des variations de fabrication, nous avons également modélisé les pertes par rayonnement pour une épaisseur de Si_xN_y de 330 nm, ce qui correspond aux données expérimentales dans la plage de longueurs d'onde inférieures. L'écart observé entre les données expérimentales et modélisées (par exemple pour 330 nm) à des longueurs d'onde plus élevées est attribué au confinement plus faible des modes, entraînant une fuite vers le substrat en SiO_2. Cependant, la présence du substrat en Si modifie le profil du mode, augmente le n_{eff} et réduit les pertes. Ce comportement explique les écarts observés dans nos résultats expérimentaux. De plus, la même méthodologie peut être utilisée pour déterminer les pertes par rayonnement pour tous les rayons de courbure, comme montré dans la Figure 9.21.(b) pour la polarisation TE à 1310 nm.

Thèse accessible à l'adresse : https://theses.insa-lyon.fr/publication/2024ISAL0120/these.pdf © [C.B. Chander Bhan], [2024], INSA Lyon, tous droits réservés

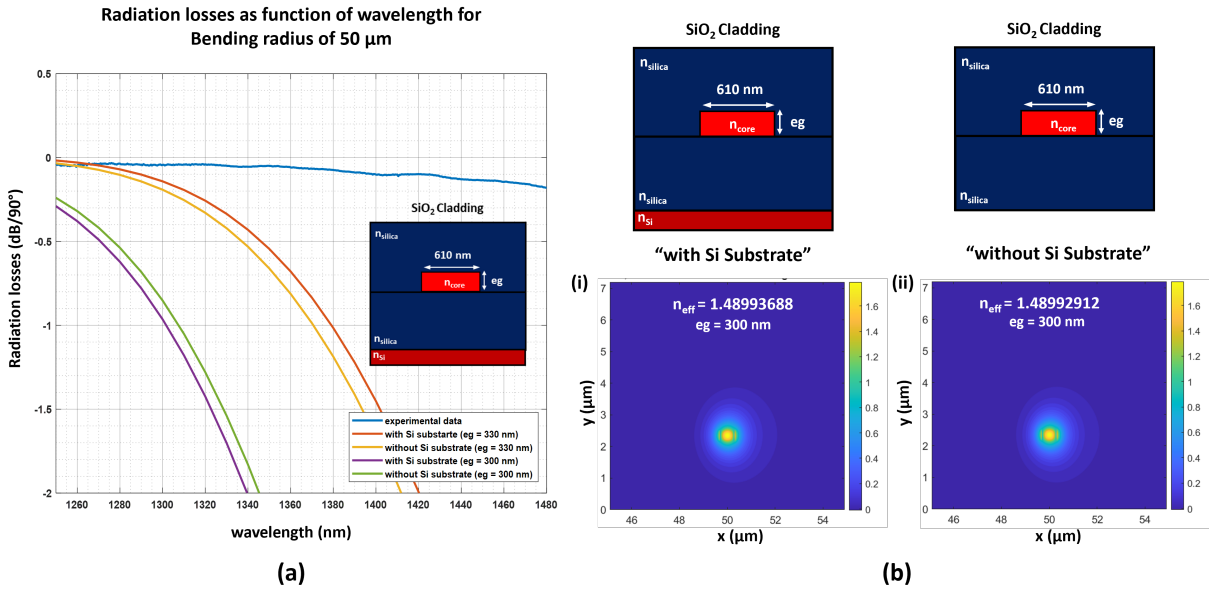

Figure 9.21: Pertes de radiation expérimentales et simulées (dB/90°) pour un rayon de courbure circulaire de 90° d'un guide d'onde à bande étroite sous revêtement de SiO_2 : (a) Pertes de radiation en fonction de la longueur d'onde pour un rayon de courbure de 50 μm, et (b) Schéma et profil du mode TE de la courbure à 1310 nm pour un rayon de courbure de 50 µm.

Thèse accessible à l'adresse : https://theses.insa-lyon.fr/publication/2024ISAL0120/these.pdf © [C.B. Chander Bhan], [2024], INSA Lyon, tous droits réservés

4. **Pertes de courbure pour un guide d'onde à bande étroite Si_xN_y sous gaine d'eau**

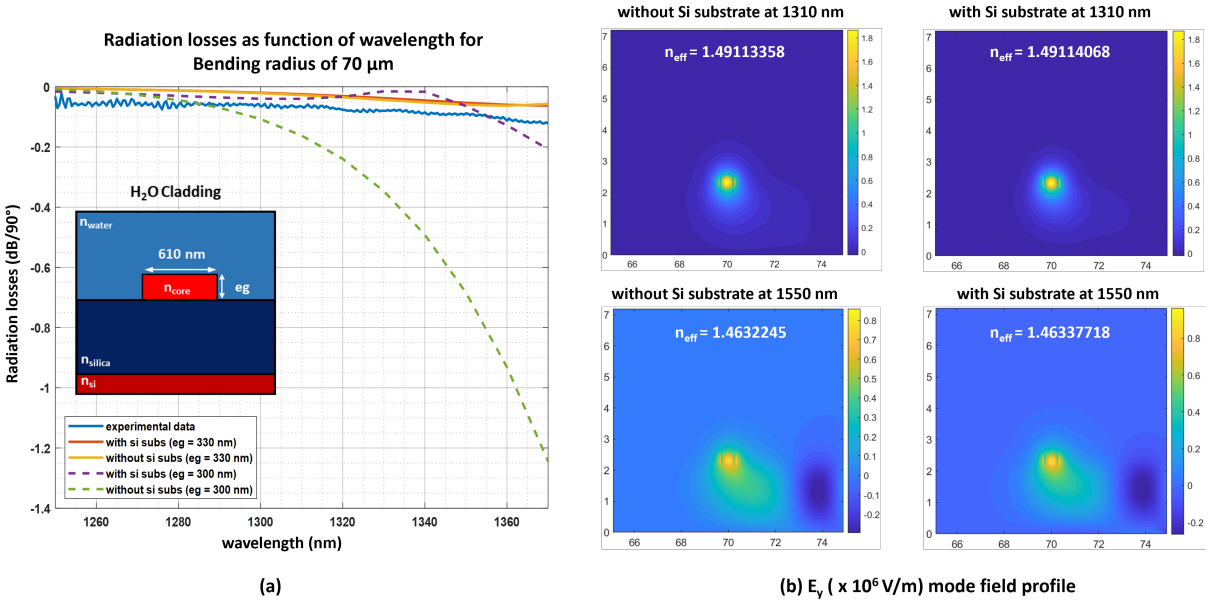

Figure 9.22: Pertes de radiation expérimentales et simulées (dB/90°) pour un rayon de courbure circulaire de 90° d'un guide d'onde sous gaine d'eau : (a) Pertes de radiation en fonction de la longueur d'onde pour un rayon de courbure de 70 μm, et (b) Profil du mode TE de la courbure pour un rayon de courbure de 70 µm à 1310 nm et 1550 nm.

5. **Résonateurs à anneau micro-racetrack avec guide d'onde Si_xN_y sous gaine d'eau**

   Dans le cas du revêtement en eau, la transmission pour le même résonateur à anneau (MRR) avec un écart de couplage de 450 nm est montrée dans la Figure 9.23 pour la polarisation TE. La figure présente également les caractéristiques spectrales en fréquence ainsi qu'une image d'une caméra IR montrant la lumière se propageant dans l'anneau alors qu'elle résonne à différentes longueurs d'onde.

   En raison de la forte absorption associée aux liaisons NH et à l'eau, aucune résonance n'est observée autour de la longueur d'onde de 1550 nm. La faible puissance de quelques mW provenant de la source à large bande est insuffisante pour mesurer les pertes et les résonances au-dessus de la plage de 1550 nm, car le signal reste en dessous du rapport signal sur bruit. Pour remédier à cela, une source haute puissance ajustable sera utilisée pour garantir des signaux détectables dans le spectre.

   Pour valider les données expérimentales avec notre modélisation, comme discuté dans le Chapitre 4, nous avons observé que le résonateur en forme de piste dans un revêtement d'eau atteint un couplage critique à 430 nm, ce qui est très proche de 450 nm (données expérimentales), comme le montre la Figure 9.23. Une résonance à 1312 nm présente un contraste de résonance de 7 dB, et il peut être supposé qu'elle est en couplage critique. Par conséquent, le facteur de qualité (Q) peut être estimé à l'aide de la formule fournie dans l'Équation 2 pour le couplage critique ($a = \tau$):

$$Q = \frac{\lambda_m \pi}{\Delta\lambda_{FSR}} \cdot \frac{a}{1 - a^2} \tag{9.8}$$

Thèse accessible à l'adresse : https://theses.insa-lyon.fr/publication/2024ISAL0120/these.pdf © [C.B. Chander Bhan], [2024], INSA Lyon, tous droits réservés

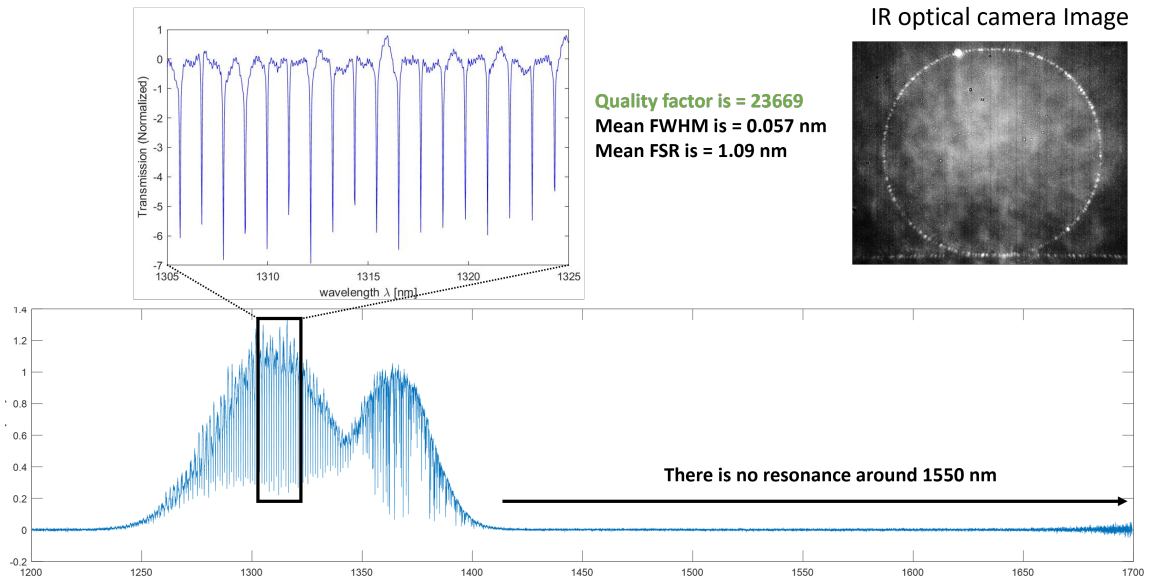

Figure 9.23: Spectre de puissance observé avec un analyseur de spectre optique pour un résonateur à anneau en forme de piste (MRR) avec un écart de couplage de 450 nm sous un revêtement en eau, avec le spectre de transmission normalisé mis en évidence en bleu autour des plages de longueurs d'onde de 1310 nm.

où λ_m représente la longueur d'onde résonante, $a = e^{-\frac{\alpha L}{2}}$, L représente la longueur de l'anneau et α est la somme des pertes de propagation linéaires et des pertes par courbure. En considérant des pertes de propagation linéaires de 5 dB/cm et une perte par courbure de 0,09 dB par 90° pour un rayon de courbure de 120 µm, ainsi qu'une plage spectrale libre (FSR) de 1,1 nm, le facteur Q calculé du résonateur en anneau est de 46,659. Cette valeur dépasse largement le facteur Q estimé par ajustement lorentzien à partir des données expérimentales montrées dans la Figure 9.23.

On peut conclure que, dans le cas d'un milieu de gaine en eau, la largeur à mi-hauteur (FWHM) est très proche de la limite de résolution de l'analyseur de spectre (0,03 nm), suggérant un potentiel sous-échantillonnage des résonances. Par conséquent, cet aspect de la caractérisation reste à l'étude, et de nouvelles découvertes pourraient être présentées dans de futurs travaux.

Thèse accessible à l'adresse : https://theses.insa-lyon.fr/publication/2024ISAL0120/these.pdf © [C.B. Chander Bhan], [2024], INSA Lyon, tous droits réservés

Conclusion

Dans cette thèse, nous avons proposé l'utilisation de circuits photoniques intégrés sur une plateforme en nitrure de silicium (Si_xN_y) comme capteur d'indice de qualité de l'air (AQI). La haute sensibilité des résonateurs en anneau micrométrique (MRR) permet de détecter même de très faibles concentrations de particules, tandis que les forces optiques permettent de piéger des particules de tailles spécifiques. La plateforme Si_xN_y a démontré un fort potentiel dans diverses applications de détection, notamment dans les domaines chimique, biomédical, physique et environnemental.

Dans le cadre de cette thèse, nous avons examiné diverses structures de guides d'onde, telles que les guides d'ondes plasmoniques hybrides, les modes d'ordre supérieur, les guides diélectrique, et les guides diélectriques à standards, à travers la modélisation. Nos premières études de modélisation se sont concentrées sur la compatibilité avec la plateforme industrielle STMicroelectronics Datacom Advanced Photonic Nanoscale Environment (DAPHNE). Les dispositifs résonants, comme les résonateurs en anneau, offrent un renforcement significatif du champ et un confinement spatial, ce qui les rend avantageux pour le piégeage de nanoparticules. Compte tenu de leur compatibilité avec les plateformes industrielles, nous avons étudié différents guides d'onde en tenant compte des contraintes de conception et de fabrication pour les MRRs à une échelle industrielle.

Nous avons réalisé une étude des forces optiques dans des cavités en utilisant des méthodes bien connues, telles que le tenseur des contraintes de Maxwell (MST) et l'approximation dipolaire discrète (DDA), pour définir les paramètres du dispositif pour le processus de conception. Cette thèse se concentre sur quatre composants principaux :

1. **Guides d'onde diélectriques standards :** En utilisant les méthodes MST et DDA, nous avons étudié le guide d'ondes diélectrique à bande le plus simple, facilement fabriqué sur toute plateforme industrielle, pour piéger des particules d'environ 100 nm. Nous avons déterminé la force et la puissance minimales nécessaires pour le piégeage et optimisé le guide d'ondes à bande avec une largeur de section de 570 nm et une épaisseur de 300 nm.

2. **Résonateurs en anneau à modes d'ordre supérieur (HOM) :** Les HOM ont plusieurs maxima et minima d'intensité, permettant le piégeage de plusieurs particules et offrant une meilleure tolérance aux erreurs de fabrication en raison de leur cœur plus large. Ceux-ci ont été optimisés pour la conception et la fabrication dans les chapitres 3, 4 et 5.

3. **Couplage par effilement inversé :** Le piégeage d'une particule diélectrique nécessite environ 25 mW de puissance dans le guide d'ondes. Pour améliorer l'efficacité du couplage avec les dispositifs de caractérisation actuels disponibles dans les laboratoires INL, nous avons conçu et optimisé un simple effilement linéaire inversé, atteignant une efficacité de couplage de 75%, comme démontré dans nos modèles FDTD et FDE Lumerical dans le chapitre 3.

4. **Résonateurs en anneau plasmoniques hybrides :** La littérature et les recherches antérieures ont démontré la haute sensibilité des résonateurs en anneau plasmoniques hybrides. Nos modélisations ont montré que ces conceptions peuvent générer des forces optiques substantielles, telles que 50 pN pour des nanoparticules diélectriques

Thèse accessible à l'adresse : https://theses.insa-lyon.fr/publication/2024ISAL0120/these.pdf © [C.B. Chander Bhan], [2024], INSA Lyon, tous droits réservés

de 100 nm, soit 10 à 15 fois plus que celles obtenues avec des guides d'ondes à bande. Cependant, ces structures présentent des pertes élevées. Nous avons optimisé la conception pour réduire les pertes par un facteur de six, atteignant une performance environ 2 à 3 fois meilleure par rapport aux guides d'ondes en nitrure de silicium (Si_xN_y) à fente et à bande en termes de piégeage optique, tout en maintenant une haute sensibilité. En raison de la complexité de la fabrication et des contraintes de temps, cette conception n'a pas été fabriquée dans cette thèse. Nous avons plutôt opté pour un prototype de guide d'ondes à bande diélectrique plus simple pour démontrer le piégeage optique de particules diélectriques autour de 100 nm.

Dans le chapitre 5, nous avons utilisé l'effilement inversé dans notre conception, optimisé pour une épaisseur de 300 nm de nitrure de silicium. Nous avons fabriqué les dispositifs en utilisant la plateforme 3IT, qui offrait plus de flexibilité et une plateforme intégrée avec la lithographie par faisceau d'électrons (E-beam lithography). Cela a permis de réduire les pertes par rapport aux méthodes de lithographie UV. La plateforme intégrée 3IT a également permis la fabrication de plusieurs puces simultanément, nous permettant de prendre en compte toutes les possibilités de fabrication et d'incorporer la redondance et les variations de conception. Nous avons ensuite caractérisé les dispositifs fabriqués au cours de cette thèse, en commençant par une explication de la configuration expérimentale et des outils disponibles qui ont assisté à notre caractérisation. Ensuite, nous avons discuté des résultats expérimentaux, y compris les mesures de propagation linéaire et de pertes de courbure pour le guide d'ondes à bande en Si_xN_y sous revêtement de SiO_2 et d'eau, avec une comparaison aux dispositifs standard en nitrure de silicium fabriqués dans des thèses précédentes en utilisant les plateformes ST DAPHNE et INL.

Au cours de la caractérisation, nous avons rencontré des défis avec les réservoirs fluidiques en polydiméthylsiloxane (PDMS), qui se dégradent dans l'eau, ajoutant des pertes supplémentaires et compliquant le nettoyage après chaque mesure. En nous basant sur les recherches menées par d'autres chercheurs au laboratoire, nous avons utilisé un réservoir fluidique repositionnable en film TPU et un réservoir imprimé en 3D, ce qui a permis un repositionnement et un nettoyage faciles après chaque mesure. Le réservoir imprimé en 3D offrait un alignement stable sur l'échantillon. En utilisant ce réservoir fluidique repositionnable, nous avons démontré deux mesures de perte sur différentes puces photoniques, montrant la répétabilité et la facilité d'utilisation du réservoir par rapport au réservoir PDMS.

Vers la fin du chapitre de caractérisation, nous avons présenté les résultats préliminaires pour les MRRs fabriqués avec des revêtements en SiO_2 et en eau. Nous avons atteint des facteurs de qualité proches de 30 000 sous revêtement SiO_2 et autour de 20 000 sous revêtement en eau. Malheureusement, la largeur à mi-hauteur (FWHM) des deux mesures était très proche de la bande passante de résolution (RBW) de l'analyseur de spectre optique, soit 0,03 nm. En conséquence, nous sommes toujours en train de peaufiner nos protocoles de caractérisation et de rechercher des collaborations potentielles pour continuer les expériences sur d'autres dispositifs fabriqués. Enfin, nous avons discuté des défis actuels rencontrés dans nos expériences de piégeage optique, mais également des perspectives offertes par les expériences antérieures de piégeage optique menées au début de la thèse avec des dispositifs fabriqués précédemment.

D'un point de vue modélisation, des conceptions telles que les HOM et les HPWG montrent un potentiel significatif pour le piégeage optique et pourraient être prometteuses pour les

Thèse accessible à l'adresse : https://theses.insa-lyon.fr/publication/2024ISAL0120/these.pdf © [C.B. Chander Bhan], [2024], INSA Lyon, tous droits réservés

applications futures de détection et d'AQI. Étant donné que les forces optiques seules ne sont pas suffisantes pour piéger un grand nombre de particules, les travaux futurs pourraient explorer la combinaison de la diélectrophorèse et des forces optiques. De telles conceptions hybrides pourraient capturer de nombreuses particules tout en maintenant une haute sensibilité, concurrençant ainsi efficacement les dispositifs commercialisés actuels.

Cette thèse propose une conception simplifiée de résonateur en anneau micrométrique (MRR) diélectrique capable de piéger des particules diélectriques dans l'air d'une taille de 0,1 µm. La conception peut être facilement fabriquée sur n'importe quelle plateforme intégrée CMOS, en conjonction avec des sources laser et des photodétecteurs. De plus, le développement de canaux fluidiques repositionnables, pouvant être facilement intégrés dans des systèmes lab-on-chip CMOS, permet des mesures réutilisables, améliorant ainsi la praticité et l'efficacité des coûts. Sur la base de la caractérisation en cours, nous sommes convaincus de démontrer la preuve de concept pour le piégeage optique en utilisant la conception proposée. Le transfert de cette conception sur la plateforme STMicroelectronics, combiné à la conception par effilement inversé et aux guides d'ondes en nitrure de silicium à faibles pertes développés chez STMicroelectronics, offre une solution prometteuse pour améliorer les performances et la sensibilité des capteurs.

Thèse accessible à l'adresse : https://theses.insa-lyon.fr/publication/2024ISAL0120/these.pdf © [C.B. Chander Bhan], [2024], INSA Lyon, tous droits réservés

CONTRIBUTION

Conference:

1. **Enhanced optical forces for trapping dielectric nanoparticles with hybrid plasmonic waveguides**, Oral presentation, Chander Bhan, G. Beaudin, S. Monfray, F. Boeuf, R. Orobtchouk, P.G. Charette, Photonic Europe 2024, Apr 2024, Strasbourg, France.
2. **Higher order mode ring resonator for trapping dielectric particulate matter in air**, Poster presentation, Chander Bhan, M Calvo, G Beaudin, S Monfray, F Boeuf, M. Canva, P.G. Charette, R. Orobtchouk,

Paper in progress:

1. **Improving optical trapping for dielectric particulate matter by using hybrid plasmonic waveguide with larger gaps while maintaining sensitivity**, Chander Bhan, M. Calvo, G. Beaudin, S. Monfray, F. Boeuf, R. Orobtchouk, P.G. Charette.

Thèse accessible à l'adresse : https://theses.insa-lyon.fr/publication/2024ISAL0120/these.pdf © [C.B. Chander Bhan], [2024], INSA Lyon, tous droits réservés

Thèse accessible à l'adresse : https://theses.insa-lyon.fr/publication/2024ISAL0120/these.pdf © [C.B. Chander Bhan], [2024], INSA Lyon, tous droits réservés

Bibliography

[1] United States Environmental Protection Agency Office of Health and Environmental Assessment. *Health assessment document for 2, 3, 7, 8-tetrachlorodibenzo-p-dioxin (TCDD) and related compounds*. Vol. 92. US Environmental, Protection Agency, Office of Research and Development . . ., 1994.

[2] *Size comparisons for PM particles*. Science Learning Hub. URL: https://www.sciencelearn.org.nz/images/1869-size-comparisons-for-pm-particles (visited on 13th Dec. 2022).

[3] Prof. S.P. Gautham and Prof. H. B. Mathur. *Air quality monitoring, emission inventory and source apportionment study for Indian cities*. National summary Report. Delhi: NEERI, IITK, IITM, TERI, ARAI, Feb. 2011, p. 290. URL: https://cpcb.nic.in/displaypdf.php?id=RmluYWxOYXRpb25hbFN1bW1hcnkucGRm.

[4] J Li et al. 'Source seasonality of polycyclic aromatic hydrocarbons (PAHs) in a subtropical city, Guangzhou, South China'. In: *Science of the Total Environment* 355.1-3 (2006), pp. 145–155.

[5] Adrián Garrido, Pedro Jiménez-Guerrero and Nuno Ratola. 'Levels, trends and health concerns of atmospheric PAHs in Europe'. In: *Atmospheric Environment* 99 (2014), pp. 474–484.

[6] Akihiro Fushimi et al. 'Chemical composition and source of fine and nanoparticles from recent direct injection gasoline passenger cars: Effects of fuel and ambient temperature'. In: *Atmospheric Environment* 124 (2016), pp. 77–84.

[7] Mahdi Sahafi and Amir Habibzadeh-Sharif. 'Robust increase of the optical forces in waveguide-based optical tweezers using V-groove structure'. In: *JOSA B* 35.8 (2018), pp. 1905–1909.

[8] Stephen Sakai and David Rothamer. 'Impact of ethanol blending on particulate emissions from a spark-ignition direct-injection engine'. In: *Fuel* 236 (2019), pp. 1548–1558.

[9] Yan Lv et al. 'Size distributions of polycyclic aromatic hydrocarbons in urban atmosphere: sorption mechanism and source contributions to respiratory deposition'. In: *Atmospheric Chemistry and Physics* 16.5 (2016), pp. 2971–2983.

[10] Senlin Lü et al. 'Size distribution of chemical elements and their source apportionment in ambient coarse, fine, and ultrafine particles in Shanghai urban summer atmosphere'. In: *Journal of Environmental Sciences* 24.5 (2012), pp. 882–890.

[11] Craig Dunbar and Jolyon Mitchell. 'Analysis of cascade impactor mass distributions'. In: *Journal of aerosol medicine* 18.4 (2005), pp. 439–451.

Thèse accessible à l'adresse : https://theses.insa-lyon.fr/publication/2024ISAL0120/these.pdf © [C.B. Chander Bhan], [2024], INSA Lyon, tous droits réservés

[12] P P. Hairston. *Apparatus for measuring particle sizes and velocities*. US Patent US5 561 515. May 1995. URL: https://permalink.orbit.com/RenderStaticFirstPage?XPN=ZhkC%252BIS0MLvjCoOEB2EWlnfDUqlXTJ5uwQdFuycu4uk%3D%26n%3D1&id=0&base=.

[13] Simon Clavaguera, Michel Pourprix and Quentin Renot. *Device for collecting particles contained in an aerosol, comprising electrometres to determine nanoparticle concentration and particle size*. 2017.

[14] Simon Clavaguera et al. *Selective aerosol particle collecting method and device, according to particle size*. US Patent 10,814,335. Oct. 2020.

[15] 1405-F TEOM™ Continuous Ambient Air Monitor. URL: https://www.thermofisher.com/order/catalog/product/TEOM1405F (visited on 22nd Jan. 2023).

[16] Navpreet Singh, Mohannad Y Elsayed and Mourad N El-Gamal. 'Towards the World's Smallest Gravimetric Particulate Matter Sensor: A Miniaturized Virtual Impactor with a Folded Design'. In: *Sensors* 22.5 (2022), p. 1727.

[17] Igor Paprotny et al. 'Microfabricated air-microfluidic sensor for personal monitoring of airborne particulate matter: Design, fabrication, and experimental results'. In: *Sensors and Actuators A: Physical* 201 (2013), pp. 506–516.

[18] Jiuling Liu et al. 'A novel particulate matter 2.5 sensor based on surface acoustic wave technology'. In: *Applied Sciences* 8.1 (2018), p. 82.

[19] Harold G Craighead. 'Nanoelectromechanical systems'. In: *Science* 290.5496 (2000), pp. 1532–1535.

[20] Eric Sage et al. 'Neutral particle mass spectrometry with nanomechanical systems'. In: *Nature communications* 6.1 (2015), p. 6482.

[21] Sanju Thomas et al. 'High frequency surface acoustic wave resonator-based sensor for particulate matter detection'. In: *Sensors and Actuators A: Physical* 244 (2016), pp. 138–145.

[22] PH McMurry. 'Chapter 17 A review of atmospheric aerosol measurements'. In: *Developments in Environmental Science* 1.C (2002), pp. 443–517.

[23] Gabirel Jobert. 'Contribution to the development and miniaturization of optical particulate matter sensors'. Theses. Université de Lyon, Oct. 2021. URL: https://dumas.ccsd.cnrs.fr/INSA-LYON-THESES/tel-03389025v2.

[24] Haoqing Zhang, Honglong Chang and Pavel Neuzil. 'DEP-on-a-chip: Dielectrophoresis applied to microfluidic platforms'. In: *Micromachines* 10.6 (2019), p. 423.

[25] Avijit Barik, Xiaoshu Chen and Sang-Hyun Oh. 'Ultralow-power electronic trapping of nanoparticles with sub-10 nm gold nanogap electrodes'. In: *Nano letters* 16.10 (2016), pp. 6317–6324.

[26] Florian Patocka et al. 'Novel resonant MEMS sensor for the detection of particles with dielectric properties in aged lubricating oils'. In: *Sensors and Actuators A: Physical* 315 (2020), p. 112290.

[27] Arthur Ashkin. 'History of optical trapping and manipulation of small-neutral particle, atoms, and molecules'. In: *IEEE Journal of Selected Topics in Quantum Electronics* 6.6 (2000), pp. 841–856.

Thèse accessible à l'adresse : https://theses.insa-lyon.fr/publication/2024ISAL0120/these.pdf © [C.B. Chander Bhan], [2024], INSA Lyon, tous droits réservés

[28] Shiyun Lin, Ethan Schonbrun and Kenneth Crozier. 'Optical manipulation with planar silicon microring resonators'. In: *Nano letters* 10.7 (2010), pp. 2408–2411.

[29] Satoshi Kawata and T Tani. 'Optically driven Mie particles in an evanescent field along a channeled waveguide'. In: *Optics letters* 21.21 (1996), pp. 1768–1770.

[30] Tao Lu et al. 'High sensitivity nanoparticle detection using optical microcavities'. In: *Proceedings of the National Academy of Sciences* 108.15 (2011), pp. 5976–5979.

[31] Katrien De Vos et al. 'SOI optical microring resonator with poly (ethylene glycol) polymer brush for label-free biosensor applications'. In: *Biosensors and Bioelectronics* 24.8 (2009), pp. 2528–2533.

[32] J Patrick Hole et al. 'Velocity distribution of gold nanoparticles trapped on an optical waveguide'. In: *Optics Express* 13.10 (2005), pp. 3896–3901.

[33] Kai Wang et al. 'Scannable plasmonic trapping using a gold stripe'. In: *Nano letters* 10.9 (2010), pp. 3506–3511.

[34] Adel Rahmani and Patrick C Chaumet. 'Optical trapping near a photonic crystal'. In: *Optics express* 14.13 (2006), pp. 6353–6358.

[35] Mathieu L Juan et al. 'Self-induced back-action optical trapping of dielectric nanoparticles'. In: *Nature Physics* 5.12 (2009), pp. 915–919.

[36] Poul Martin Hansen et al. 'Expanding the optical trapping range of gold nanoparticles'. In: *Nano letters* 5.10 (2005), pp. 1937–1942.

[37] Pierre Dugac. 'Euler, d'Alembert et les fondements de l'analyse'. In: *Leonhard Euler 1707–1783*. Springer, 1983, pp. 171–184.

[38] Poynting J.H. 'XV. On the transfer of energy in the electromagnetic field'. en. In: *Royal Society* (Jan. 1884), pp. 1–19. ISSN: 2053-9223. DOI: https://doi.org/10.1098/rstl.1884.0016. URL: https://royalsocietypublishing.org/doi/10.1098/rstl.1884.0016.

[39] Arther E Woodruff. 'William Crookes and the radiometer'. In: *Isis* 57.2 (1966), pp. 188–198.

[40] Peter Lebedew. 'Untersuchungen über die Druckkräfte des Lichtes'. In: *Annalen der Physik* 311.11 (1901), pp. 433–458.

[41] Ernest Fox Nichols and Gordon Ferrie Hull. 'The pressure due to radiation.(second paper.)' In: *Physical Review (Series I)* 17.1 (1903), p. 26.

[42] Ernest Fox Nichols and Gordon Ferrie Hull. 'A preliminary communication on the pressure of heat and light radiation'. In: *Physical Review (Series I)* 13.5 (1901), p. 307.

[43] Charles H Townes. *How the laser happened: Adventures of a scientist*. Oxford University Press, 2002.

[44] Arthur Ashkin. 'Acceleration and trapping of particles by radiation pressure'. In: *Physical review letters* 24.4 (1970), p. 156.

[45] Arthur Ashkin and JM Dziedzic. 'Optical levitation by radiation pressure'. In: *Applied Physics Letters* 19.8 (1971), pp. 283–285.

[46] Arthur Ashkin. 'Optical trapping and manipulation of neutral particles using lasers'. In: *Proceedings of the National Academy of Sciences* 94.10 (1997), pp. 4853–4860.

Thèse accessible à l'adresse : https://theses.insa-lyon.fr/publication/2024ISAL0120/these.pdf © [C.B. Chander Bhan], [2024], INSA Lyon, tous droits réservés

[47] Ya Sha Yi. *Integrated Nanophotonic Resonators: Fundamentals, Devices, and Applications*. CRC Press, 2015.

[48] Onofrio M Maragò et al. 'Optical trapping and manipulation of nanostructures'. In: *Nature nanotechnology* 8.11 (2013), pp. 807–819.

[49] Maxim A Yurkin, Valeri P Maltsev and Alfons G Hoekstra. 'Can the Discrete Dipole Approximation simulate scattering of particles with size parameter equal to 100?' In: *9th International Conference*. 2006, p. 279.

[50] Gérard Gouesbet and Gérard Gréhan. *Generalized lorenz-mie theories*. Vol. 31. Springer, 2011.

[51] Hendrik Christoffel Hulst and Hendrik C van de Hulst. *Light scattering by small particles*. Courier Corporation, 1981.

[52] Giuseppe Pesce et al. 'Optical tweezers: theory and practice'. In: *The European Physical Journal Plus* 135 (2020), pp. 1–38.

[53] Xiaoqiong Qi et al. 'Comparison of T-matrix calculation methods for scattering by cylinders in optical tweezers'. In: *Optics letters* 39.16 (2014), pp. 4827–4830.

[54] Wenqiang Li et al. 'Numerical analysis on the optical force calculation in the Rayleigh scattering regime'. In: *Optical Review* 28 (2021), pp. 1–7.

[55] Edward M Purcell and Carlton R Pennypacker. 'Scattering and absorption of light by nonspherical dielectric grains'. In: *The Astrophysical Journal* 186 (1973), pp. 705–714.

[56] Evgenij Zubko et al. 'Validity criteria of the discrete dipole approximation'. In: *Applied optics* 49.8 (2010), pp. 1267–1279.

[57] Patrick C Chaumet and Manuel Nieto-Vesperinas. 'Time-averaged total force on a dipolar sphere in an electromagnetic field'. In: *Optics letters* 25.15 (2000), pp. 1065–1067.

[58] Karel Svoboda and Steven M Block. 'Biological applications of optical forces'. In: *Annual review of biophysics and biomolecular structure* 23.1 (1994), pp. 247–285.

[59] Juejun Hu et al. 'Optical trapping of dielectric nanoparticles in resonant cavities'. In: *Physical Review A* 82.5 (2010), p. 053819.

[60] Arthur Ashkin et al. 'Observation of a single-beam gradient force optical trap for dielectric particles'. In: *Optics letters* 11.5 (1986), pp. 288–290.

[61] Bruce T Draine. 'The discrete-dipole approximation and its application to interstellar graphite grains'. In: *The Astrophysical Journal* 333 (1988), pp. 848–872.

[62] Alexander Rohrbach, Ernst-Ludwig Florin and Ernst HK Stelzer. 'Photonic Force Microscopy: Simulation of principles and applications'. In: *Photon Migration, Optical Coherence Tomography, and Microscopy*. Vol. 4431. SPIE. 2001, pp. 75–86.

[63] Clifton E Dungey and Craig F Bohren. 'Light scattering by nonspherical particles: a refinement to the coupled-dipole method'. In: *JOSA A* 8.1 (1991), pp. 81–87.

[64] Jack Vanderlinde. *Classical electromagnetic theory*. Vol. 145. Springer Science & Business Media, 2006.

[65] Hermann Minkowski. *Space and Time: Minkowski's papers on relativity*. Minkowski Institute Press, 2013.

Thèse accessible à l'adresse : https://theses.insa-lyon.fr/publication/2024ISAL0120/these.pdf © [C.B. Chander Bhan], [2024], INSA Lyon, tous droits réservés

[66] Julius Adams Stratton. *Electromagnetic theory*. Vol. 33. John Wiley & Sons, 2007.

[67] Hermann Minkowski. 'The fundamental equations for electromagnetic processes in moving bodies'. In: *Nachr. Ges. Wiss. Gottingen, Mathematisch-Physikalische Klasse, pp53-111* (1908).

[68] Bruno Anghinoni et al. 'On the formulations of the electromagnetic stress–energy tensor'. In: *Annals of Physics* 443 (2022), p. 169004.

[69] Lip Ket Chin, Yuzhi Shi and Ai-Qun Liu. 'Optical forces in silicon nanophotonics and optomechanical systems: science and applications'. In: *Advanced Devices & Instrumentation* 2020 (2020).

[70] Veerachart Kajorndejnukul et al. 'Linear momentum increase and negative optical forces at dielectric interface'. In: *Nature Photonics* 7.10 (2013), pp. 787–790.

[71] Balpreet Singh Ahluwalia, Øystein Ivar Helle and Olav Gaute Hellesø. 'Rib waveguides for trapping and transport of particles'. In: *Optics express* 24.5 (2016), pp. 4477–4487.

[72] Stephanie Gaugiran et al. 'Optical manipulation of microparticles and cells on silicon nitride waveguides'. In: *Optics Express* 13.18 (2005), pp. 6956–6963.

[73] Hong Cai and Andrew W Poon. 'Optical trapping of microparticles using silicon nitride waveguide junctions and tapered-waveguide junctions on an optofluidic chip'. In: *Lab on a Chip* 12.19 (2012), pp. 3803–3809.

[74] K Grujic et al. 'Sorting of polystyrene microspheres using a Y-branched optical waveguide'. In: *Optics Express* 13.1 (2005), pp. 1–7.

[75] Olav Gaute Hellesø. 'Optical pressure and numerical simulation of optical forces'. In: *Applied optics* 56.12 (2017), pp. 3354–3358.

[76] A Renoux and D Boulaud. 'Physique des aérosols, Partie 1, Techniques de l'Ingénieur, traité Science fondamentales'. In: *Vol. AF4., No. AF3612* (2003), pp. 1–15.

[77] Robert A Millikan. 'The general law of fall of a small spherical body through a gas, and its bearing upon the nature of molecular reflection from surfaces'. In: *Physical Review* 22.1 (1923), p. 1.

[78] Jung Hyeun Kim et al. 'Slip correction measurements of certified PSL nanoparticles using a nanometer differential mobility analyzer (nano-DMA) for Knudsen number from 0.5 to 83'. In: *Journal of Research of the National Institute of Standards and technology* 110.1 (2005), p. 31.

[79] Stéphanie Gaugiran. 'Déplacement de particules et d'objets biologiques sur des guides d'ondes'. fr. In: (), p. 186.

[80] Yasuhiro Harada and Toshimitsu Asakura. 'Radiation forces on a dielectric sphere in the Rayleigh scattering regime'. In: *Optics communications* 124.5-6 (1996), pp. 529–541.

[81] Arthur Ashkin. 'Forces of a single-beam gradient laser trap on a dielectric sphere in the ray optics regime'. In: *Biophysical journal* 61.2 (1992), pp. 569–582.

[82] G Benjamin Hocker and William K Burns. 'Mode dispersion in diffused channel waveguides by the effective index method'. In: *Applied optics* 16.1 (1977), pp. 113–118.

Thèse accessible à l'adresse : https://theses.insa-lyon.fr/publication/2024ISAL0120/these.pdf © [C.B. Chander Bhan], [2024], INSA Lyon, tous droits réservés

[83] JENS Buus. ‘Application of the effective index method to nonplanar structures’. In: *IEEE journal of quantum electronics* 20.10 (1984), pp. 1106–1109.

[84] Enrique AJ Marcatili. ‘Dielectric rectangular waveguide and directional coupler for integrated optics’. In: *Bell System Technical Journal* 48.7 (1969), pp. 2071–2102.

[85] Kane Yee. ‘Numerical solution of initial boundary value problems involving Maxwell’s equations in isotropic media’. In: *IEEE Transactions on antennas and propagation* 14.3 (1966), pp. 302–307.

[86] Klaus-Jurgen Bathe and Edward Wilson. ‘Numerical methods in finite element analysis’. In: (1976).

[87] Marco Masi et al. ‘Towards a realistic modelling of ultra-compact racetrack resonators’. In: *Journal of Lightwave Technology* 28.22 (2010), pp. 3233–3242.

[88] Zhaoming Zhu and Thomas G Brown. ‘Full-vectorial finite-difference analysis of microstructured optical fibers’. In: *Optics express* 10.17 (2002), pp. 853–864.

[89] Alvin Wexler. ‘Solution of waveguide discontinuities by modal analysis’. In: *IEEE Transactions on Microwave Theory and Techniques* 15.9 (1967), pp. 508–517.

[90] A Rubio Bretones, R Mittra and R Gómez Martın. ‘A hybrid technique combining the method of moments in the time domain and FDTD’. In: *IEEE Microwave and Guided wave letters* 8.8 (1998), pp. 281–283.

[91] KS Chiang. ‘Review of numerical and approximate methods for the modal analysis of general optical dielectric waveguides’. In: *Optical and Quantum Electronics* 26 (1994), S113–S134.

[92] R Scarmozzino et al. ‘Numerical techniques for modeling guided-wave photonic devices’. In: *IEEE Journal of Selected Topics in Quantum Electronics* 6.1 (2000), pp. 150–162.

[93] AW Snyder. *Optical Waveguide Theory*. 1983.

[94] Vilson R Almeida et al. ‘Guiding and confining light in void nanostructure’. In: *Optics letters* 29.11 (2004), pp. 1209–1211.

[95] Tomoya Taniguchi et al. ‘Detection of antibody-antigen reaction by silicon nitride slot-ring biosensors using protein G’. In: *Optics Communications* 365 (2016), pp. 16–23.

[96] Stefan A Maier et al. *Plasmonics: fundamentals and applications*. Vol. 1. Springer, 2007.

[97] Michele Calvo. ‘Study and manufacturing of biosensors based on plasmonic effects and built on silicon’. Theses. Université de Lyon, July 2020. URL: https://theses.hal.science/tel-03125744.

[98] Huan Li et al. ‘Enhanced optical forces in integrated hybrid plasmonic waveguides’. In: *Optics express* 21.10 (2013), pp. 11839–11851.

[99] Yuzhi Shi et al. ‘Optical potential-well array for high-selectivity, massive trapping and sorting at nanoscale’. In: *Nano Letters* 20.7 (2020), pp. 5193–5200.

[100] Allen HJ Yang et al. ‘Optical manipulation of nanoparticles and biomolecules in sub-wavelength slot waveguides’. In: *Nature* 457.7225 (2009), pp. 71–75.

[101] Kerry J Vahala. ‘Optical microcavities’. In: *nature* 424.6950 (2003), pp. 839–846.

Thèse accessible à l'adresse : https://theses.insa-lyon.fr/publication/2024ISAL0120/these.pdf © [C.B. Chander Bhan], [2024], INSA Lyon, tous droits réservés

[102] Christophe Pin, Hideki Fujiwara and Keiji Sasaki. ‘Controlled Optical Manipulation and Sorting of Nanomaterials Enabled by Photonic and Plasmonic Nanodevices’. In: *Journal of Photochemistry and Photobiology C: Photochemistry Reviews* (2022), p. 100534.

[103] Eric Jaquay et al. ‘Light-assisted, templated self-assembly using a photonic-crystal slab’. In: *Nano letters* 13.5 (2013), pp. 2290–2294.

[104] Sudeep Mandal, Xavier Serey and David Erickson. ‘Nanomanipulation using silicon photonic crystal resonators’. In: *Nano letters* 10.1 (2010), pp. 99–104.

[105] Shoubao Han and Yaocheng Shi. ‘Systematic analysis of optical gradient force in photonic crystal nanobeam cavities’. In: *Optics Express* 24.1 (2016), pp. 452–458.

[106] Hong Cai and Andrew W Poon. ‘Optical manipulation and transport of microparticles on silicon nitride microring-resonator-based add–drop devices’. In: *Optics letters* 35.17 (2010), pp. 2855–2857.

[107] Wim Bogaerts et al. ‘Silicon microring resonators’. In: *Laser & Photonics Reviews* 6.1 (2012), pp. 47–73.

[108] Youngchul Chung and Nadir Dagli. ‘An assessment of finite difference beam propagation method’. In: *IEEE Journal of quantum electronics* 26.8 (1990), pp. 1335–1339.

[109] Allan W Snyder and William R Young. ‘Modes of optical waveguides’. In: *JOSA* 68.3 (1978), pp. 297–309.

[110] Wouter J Westerveld et al. ‘Extension of Marcatili’s analytical approach for rectangular silicon optical waveguides’. In: *Journal of Lightwave Technology* 30.14 (2012), pp. 2388–2401.

[111] Raj K Narisetti, Michael J Leamy and Massimo Ruzzene. ‘A perturbation approach for predicting wave propagation in one-dimensional nonlinear periodic structures’. In: *J. Vib. Acoust.* (2010).

[112] Jian-Ming Jin. *The finite element method in electromagnetics*. John Wiley & Sons, 2015.

[113] Arman B Fallahkhair, Kai S Li and Thomas E Murphy. ‘Vector finite difference modesolver for anisotropic dielectric waveguides’. In: *Journal of lightwave technology* 26.11 (2008), pp. 1423–1431.

[114] Pierre Berini and Ke Wu. ‘Modeling lossy anisotropic dielectric waveguides with the method of lines’. In: *IEEE Transactions on Microwave Theory and Techniques* 44.5 (1996), pp. 749–759.

[115] A Sv Sudbo. ‘Film mode matching: a versatile numerical method for vector mode field calculations in dielectric waveguides’. In: *Pure and Applied Optics: Journal of the European Optical Society Part A* 2.3 (1993), p. 211.

[116] Stéphanie Gaugiran. ‘Déplacement de particules et d’objets biologiques sur des guides d’ondes’. Pierre Benech président Frédérique de Fornel rapporteur Sylvia jeney rapporteur Patrick Tabeling examinateur Stéphane Getin co-encadrant Jacques Derouard directeur de thèse. Theses. Université Joseph-Fourier - Grenoble I, Sept. 2005. URL: https://theses.hal.science/tel-00010904.

[117] Xiaoyan Ma et al. ‘Determination of complex refractive index of polystyrene microspheres from 370 to 1610 nm’. In: *Physics in medicine & biology* 48.24 (2003), p. 4165.

Thèse accessible à l'adresse : https://theses.insa-lyon.fr/publication/2024ISAL0120/these.pdf © [C.B. Chander Bhan], [2024], INSA Lyon, tous droits réservés

[118] A Melloni et al. ‘The role of index contrast in dielectric optical waveguides’. In: *International Journal of Materials and Product Technology* 34.4 (2009), pp. 421–437.

[119] Carsten Schinke et al. ‘Uncertainty analysis for the coefficient of band-to-band absorption of crystalline silicon’. In: *Aip Advances* 5.6 (2015).

[120] Roel Baets et al. ‘Silicon Photonics: silicon nitride versus silicon-on-insulator’. In: *Optical fiber communication conference*. Optica Publishing Group. 2016, Th3J–1.

[121] Stefan A Maier. ‘Plasmonics: The promise of highly integrated optical devices’. In: *IEEE Journal of selected topics in Quantum Electronics* 12.6 (2006), pp. 1671–1677.

[122] Hassan MG Wassel et al. ‘Opportunities and challenges of using plasmonic components in nanophotonic architectures’. In: *IEEE Journal on Emerging and Selected Topics in Circuits and Systems* 2.2 (2012), pp. 154–168.

[123] Svetlana V Boriskina et al. ‘Losses in plasmonics: from mitigating energy dissipation to embracing loss-enabled functionalities’. In: *Advances in Optics and Photonics* 9.4 (2017), pp. 775–827.

[124] Michele Calvo et al. ‘Ring resonator designed for biosensing applications manufactured on 300 mm SOI in an industrial environment’. In: *Japanese Journal of Applied Physics* 58.SB (2019), SBBE02.

[125] Michele CALVO et al. *Wave guide sensor*. B18040PCT-8-GR3CO-0364. Apr. 2019. URL: https://patents.google.com/patent/WO2020221964A1/en?inventor=Michele+calvo&oq=Michele+calvo.

[126] Jin-Ho Lee et al. ‘Application of gold nanoparticle to plasmonic biosensors’. In: *International journal of molecular sciences* 19.7 (2018), p. 2021.

[127] Kenneth B Crozier. ‘Quo vadis, plasmonic optical tweezers?’ In: *Light: Science & Applications* 8.1 (2019), p. 35.

[128] Chih-Wei Tseng et al. ‘Study of coupling loss on strongly-coupled, ultra compact microring resonators’. In: *Optics express* 21.6 (2013), pp. 7250–7257.

[129] Chih-Wei Tseng et al. ‘Narrow gap width induced radiation loss on waveguide coupled microring’. In: *The 9th International Conference on Group IV Photonics (GFP)*. IEEE. 2012, pp. 291–293.

[130] Mordehai Heiblum and Jay Harris. ‘Analysis of curved optical waveguides by conformal transformation’. In: *IEEE Journal of Quantum Electronics* 11.2 (1975), pp. 75–83.

[131] D Marcuse. ‘Bending losses of the asymmetric slab waveguide’. In: *Bell System Technical Journal* 50.8 (1971), pp. 2551–2563.

[132] Vien Van. *Optical microring resonators: theory, techniques, and applications*. CRC Press, 2016.

[133] Zhanghua Han, Pu Zhang and Sergey I Bozhevolnyi. ‘Calculation of bending losses for highly confined modes of optical waveguides with transformation optics’. In: *Optics Letters* 38.11 (2013), pp. 1778–1780.

[134] Eva Kempf. ‘Développement d’un gyroscope intégré en technologie de guide d’onde SiN’. Theses. Université de Lyon, June 2022. URL: https://theses.hal.science/tel-03860457.

Thèse accessible à l'adresse : https://theses.insa-lyon.fr/publication/2024ISAL0120/these.pdf © [C.B. Chander Bhan], [2024], INSA Lyon, tous droits réservés

[135] Meisam Bahadori et al. ‘Universal design of waveguide bends in silicon-on-insulator photonics platform’. In: *Journal of Lightwave Technology* 37.13 (2019), pp. 3044–3054.

[136] Frank P Payne and Jonathan PR Lacey. ‘A theoretical analysis of scattering loss from planar optical waveguides’. In: *Optical and Quantum Electronics* 26 (1994), pp. 977–986.

[137] Wei-Ping Huang. ‘Coupled-mode theory for optical waveguides: an overview’. In: *JOSA A* 11.3 (1994), pp. 963–983.

[138] Hermann A Haus and Weiping Huang. ‘Coupled-mode theory’. In: *Proceedings of the IEEE* 79.10 (1991), pp. 1505–1518.

[139] M Kuznetsov. ‘Expressions for the coupling coefficient of a rectangular-waveguide directional coupler’. In: *Optics letters* 8.9 (1983), pp. 499–501.

[140] Arun Kumar, AN Kaul and Ajoy K Ghatak. ‘Prediction of coupling length in a rectangular-core directional coupler: an accurate analysis’. In: *Optics letters* 10.2 (1985), pp. 86–88.

[141] Pauline Girault et al. ‘Integrated polymer micro-ring resonators for optical sensing applications’. In: *Journal of applied Physics* 117.10 (2015).

[142] Miguel Diez Garcia et al. ‘An analytical approach to predict maximal sensitivity of microring resonators for absorption spectroscopy’. In: *Journal of Lightwave Technology* 37.21 (2019), pp. 5500–5506.

[143] Xin Mu et al. ‘Edge couplers in silicon photonic integrated circuits: A review’. In: *Applied Sciences* 10.4 (2020), p. 1538.

[144] Guanghui Ren et al. ‘Study on inverse taper based mode transformer for low loss coupling between silicon wire waveguide and lensed fiber’. In: *Optics Communications* 284.19 (2011), pp. 4782–4788.

[145] SJ Hettrick et al. ‘An experimental comparison of linear and parabolic tapered waveguide lasers and a demonstration of broad-stripe diode pumping’. In: *Journal of lightwave technology* 22.3 (2004), p. 845.

[146] Juan Fernández et al. ‘Low-loss inverted taper edge coupler in silicon nitride’. In: *IET Optoelectronics* 13.2 (2019), pp. 62–66.

[147] T Tamir. ‘Beam and waveguide couplers’. In: *Integrated Optics*. Springer, 1975, pp. 83–137.

[148] *Alpha-SE*. URL: https://www.qd-latam.com/site/en/products/company/j-a-woollam/alpha-se/. (accessed: 12-07-2024).

[149] R Andok et al. ‘Study and comparison of resist characteristics for different negative tone electron beam resists’. In: *Journal of Physics: Conference Series*. Vol. 2443. 1. IOP Publishing. 2023, p. 012006.

[150] *Ebeam – Writing Strategy*. URL: https://www.epfl.ch/research/facilities/cmi/equipment/ebeam-lithography/raith-ebpg5000/writing-strategy/. (accessed: 25-07-2024).

[151] Geraint Owen and Paul Rissman. ‘Proximity effect correction for electron beam lithography by equalization of background dose’. In: *Journal of Applied Physics* 54.6 (1983), pp. 3573–3581.

Thèse accessible à l'adresse : https://theses.insa-lyon.fr/publication/2024ISAL0120/these.pdf © [C.B. Chander Bhan], [2024], INSA Lyon, tous droits réservés

[152] *E-Beam Resist AR-N 7520 series*. e-beam-resist-ar-n-7520-series. Rev. 1. All Resist AR. May 2019.

[153] Corinna Kaspar et al. 'Adjustable sidewall slopes by electron-beam exposure layout'. In: *Journal of Vacuum Science & Technology B* 35.6 (2017).

[154] *Inductively Coupled Plasma – Reactive Ion Etching (ICP-RIE)*. URL: https://corial.plasmatherm.com/en/technologies/icp-rie-inductively-coupled-plasma-reactive-ion-etching. (accessed: 24-07-2024).

[155] Yiding Lin et al. 'Low-loss broadband bi-layer edge couplers for visible light'. In: *Optics express* 29.21 (2021), pp. 34565–34576.

[156] Derek York et al. 'Unified equations for the slope, intercept, and standard errors of the best straight line'. In: *American journal of physics* 72.3 (2004), pp. 367–375.

[157] Sylvain Guerber. 'Intégration d'un deuxième niveau de guidage photonique par dépôt de SiN au-dessus du SOI traditionnel'. PhD thesis. Université Paris Saclay (COmUE), 2019.

[158] Efstathios E Stathis Michaelides. 'Heat and mass transfer in particulate suspensions'. In: (2013).

[159] Efstathios E Michaelides. 'Brownian movement and thermophoresis of nanoparticles in liquids'. In: *International Journal of Heat and Mass Transfer* 81 (2015), pp. 179–187.

[160] Clayton Crowe, Martin Sommerfeld, Yutaka Tsuji et al. *Multiphase Flows with*. Ž, 1998.

[161] EE Michaelides. 'Nanofluidics'. In: *Cham: Springer International Publishing* (2014).

[162] Craig Gerardi et al. 'Nuclear magnetic resonance-based study of ordered layering on the surface of alumina nanoparticles in water'. In: *Applied Physics Letters* 95.25 (2009), p. 253104.

[163] Allen HJ Yang and David Erickson. 'Stability analysis of optofluidic transport on solid-core waveguiding structures'. In: *Nanotechnology* 19.4 (2008), p. 045704.

[164] Yang, Allen HJ and David Erickson. 'Optofluidic ring resonator switch for optical particle transport'. In: *Lab on a Chip* 10.6 (2010), pp. 769–774.

[165] MZ Alam, J Stewart Aitchison and Mo Mojahedi. 'Theoretical analysis of hybrid plasmonic waveguide'. In: *IEEE Journal of Selected Topics in Quantum Electronics* 19.3 (2013), pp. 4602008–4602008.

[166] Xiao Sun. *Hybrid plasmonic waveguides and devices: Theory, modeling and experimental demonstration*. University of Toronto (Canada), 2013.

[167] Qiancheng Zhao et al. 'Plasmon optical trapping using silicon nitride trench waveguides'. In: *JOSA B* 33.6 (2016), pp. 1182–1189.

[168] Qiancheng Zhao, Yuewang Huang and Ozdal Boyraz. 'Optical properties of V-groove silicon nitride trench waveguides'. In: *JOSA A* 33.9 (2016), pp. 1851–1859.

[169] C Ciminelli et al. 'High performance SOI microring resonator for biochemical sensing'. In: *Optics & laser technology* 59 (2014), pp. 60–67.

[170] Alireza Kargar and Chung-Yen Chao. 'Design and optimization of waveguide sensitivity in slot microring sensors'. In: *JOSA A* 28.4 (2011), pp. 596–603.

Thèse accessible à l'adresse : https://theses.insa-lyon.fr/publication/2024ISAL0120/these.pdf © [C.B. Chander Bhan], [2024], INSA Lyon, tous droits réservés

[171] Lukas Neumeier, Romain Quidant and Darrick E Chang. ‘Self-induced back-action optical trapping in nanophotonic systems’. In: *New Journal of Physics* 17.12 (2015), p. 123008.

Thèse accessible à l'adresse : https://theses.insa-lyon.fr/publication/2024ISAL0120/these.pdf © [C.B. Chander Bhan], [2024], INSA Lyon, tous droits réservés

FOLIO ADMINISTRATIF

THESE DE L'INSA LYON, MEMBRE DE L'UNIVERSITE DE LYON

NOM : **CHANDER BHAN** DATE de SOUTENANCE : **19-12-2024**
(avec précision du nom de jeune fille, le cas échéant)

Prénoms : **Chander Bhan**

TITRE : **Capteurs environnementaux à base de dispositifs photonique pour la surveillance de la qualité de l'air dans l'automobile**

NATURE : **Doctorat** Numéro d'ordre : 2024ISAL0120

École Doctorale : **Électronique, Électrotechnique et Automatique**

Spécialité : **Nanophotonique**

RÉSUMÉ :
Cette thèse explore les dispositifs de circuits photoniques intégrés (PIC) basés sur une plateforme en nitrure de silicium (Si_xN_y), en mettant l'accent sur leur potentiel pour la détection de particules dans l'air, un élément clé des capteurs de l'indice de qualité de l'air (AQI). La haute sensibilité de masse des résonateurs microracetrack (MRR) dans ces dispositifs permet de détecter de faibles concentrations de particules, tandis que les forces optiques permettent le piégeage de particules de tailles spécifiques. Pour surmonter les défis associés au piégeage de particules diélectriques de moins de 100 nm, la recherche explore diverses structures photoniques, notamment des guides d'onde diélectriques standards, des résonateurs en anneau à modes d'ordre supérieur (HOM) et des guides d'ondes plasmoniques hybrides. L'étude se concentre sur quatre composants clés de la photonique intégrée : les guides d'ondes en ruban diélectriques, les résonateurs en anneau HOM, les couplages par effilement inversé, et les résonateurs en anneau plasmoniques hybrides.

MOTS-CLÉS : capteur PM, optique intégrée, photonique sur silicium, résonateur en anneau, piégeage optique

Laboratoire(s) de recherche : Institut des Nanotechnologies de Lyon (INL), Université de Sherbrooke, STMicroelectronics

Directeur de thèse : **Régis Orbotchouk, Paul G. Charette**

Président du Jury : **Yves Jourlin**

Composition du Jury : Emmanuel Hadji, Elise Ghibaudo, Michael Canva, Yves Jourlin, Aurore Vicet, Stéphane Monfray, Paul G. Charette, Régis Orobtchouk

Thèse accessible à l'adresse : https://theses.insa-lyon.fr/publication/2024ISAL0120/these.pdf © [C.B. Chander Bhan], [2024], INSA Lyon, tous droits réservés